A New Fatigue Test for Composite Rings

Master Thesis

Zia Ahmad Ansari

Delft University of Technology

SYENSQO TUDelft TOYOTA

A New Fatigue Test for Composite Rings

Master Thesis

by

Zia Ahmad Ansari

to obtain the degree of Master of Science in Aerospace Engineering
at the Delft University of Technology,
to be defended publicly on Tuesday 26 August, 2025 at 13:30.

Student number:	5916151	
Project duration:	January 2, 2025 – August 26, 2025	
Thesis committee:	Dr.ir. Saullo G. P. Castro	TU Delft, Chair
	Prof.dr.ir. René C. Alderliesten	TU Delft, Supervisor
	Dr.ir. Otto K. Bergmsa	TU Delft, External
	Dr.ir. Siebe W. F. Spronk	Syensqo, Supervisor
	Dr.ir. Martin Kerschbaum	Toyota, Supervisor

Cover:	Close-up of the Polyurethane Ring and Composite Specimen
Style:	TU Delft Report Style, with modifications by Daan Zwaneveld

An electronic version of this thesis is available at http://repository.tudelft.nl/.

SYENSQO TU Delft TOYOTA

Preface

You could not live with your own failure. Where did that bring you? Back to me - Python.

I thought choosing a more practical topic would give me a break from Python, but imagine my surprise, when I needed it in almost every step anyway. My thesis was a culmination of my work at Syensqo. I started there as an intern, developing specialized mechanical tests. To continue, my supervisor, Dr.ir. Siebe Spronk, posited this topic to develop a new fatigue test. I wanted to work on this as it gave me the opportunity to apply everything I had learnt so far to develop something tangible. It was also really fun to get to break stuff.

This challenge had to be approached from scratch. It would have not been possible without the constant guidance and insightful questions from Prof.dr.ir. René Alderliesten. Siebe's unvarying support and confidence was the foundation of this thesis. I am truly grateful for his help in navigating both the technical and practical challenges in this work. Also valuable was the technical guidance and suggestions from Dr.ir. Martin Kerschbaum. I am also thankful for the valuable knowledge and critical feedback from Prof.dr.ir. Wim van Paepegem, who took the time to guide this thesis at some of its crucial stages. Through them, I also got the opportunity to present my work at the ComfHy consortium meetings, which was a great learning experience.

There were multiple partners involved, and looking back, I am still surprised everything went according to plan. I am truly grateful for the support of my Syensqo colleagues. They were crucial in procuring and manufacturing the parts. Without them and Sharp Composites, we might not even have had specimens to test in time. The support of the lab technicians at TU Delft was also greatly appreciated in preparing the test bench and equipment as planned.

My family has always shone through with their unwavering love and support. My friends, both here and abroad, were always available for weekend breaks. I am also grateful to my peers who were with me in the same boat. I found solace in sharing the challenges and victories that were interspersed in our work. I loved that we could help each other focus, while at times, providing some much-needed distractions.

Syensqo and Toyota Motor Europe completely funded this thesis. Syensqo, in particular, generously hosted me in Brussels, giving me full access to the labs and equipment, which really helped me focus more on the work. Lastly, I would like to thank the TU Delft's Mobility Team for facilitating the Erasmus+ traineeship grant.

Zia Ahmad Ansari
Delft, August 2025

Contents

List of Figures

List of Tables

List of Symbols and Abbreviations

Abbreviations

Notation	Description	Page List
AFP	Automated Fibre Placement	2, 3, 7, 32, 33, 86
ASTM	American Society for Testing and Materials	6–12, 33, 104, 105
CF	Carbon Fiber	2, 15, 26, 35
CFCC	Continuous fibre-Reinforced Ceramic Composite	7, 11, 12
CLT	Classical Laminate Theory	27, 39, 48, 55
COPV	Composite Over-wrapped Pressure Vessel	2–4, 6, 7, 15, 19, 27, 36–38, 84, 131, 134
CVT	continuously variable transmission	20
DIC	Digital Image Correlation	11, 12, 73, 84, 88–92, 94, 96, 98, 100, 103, 104, 106–109, 115, 119, 120, 122, 124, 128, 131, 133, 137
DOF	degree of freedom	55
EDM	electrical discharge machining	29
EPDM	Ethylene propylene diene monomer	40
FEA	finite-element analysis	48, 59
FEM	finite-element model	19, 42, 47, 50, 51, 53, 54, 56–61, 64, 83, 84, 110–113, 126, 131
GRE	glass-reinforced epoxy	8, 9, 19, 33, 35
HDPE	High Density Polyethylene	2
NWP	Nominal Working Pressure	6
PA	Polyamide	2, 35
PCD	Polycrystalline Diamond	33, 135
PH	precipitation hardening	38
PTFE	Polytetrafluoroethylene	14, 16, 19, 107, 136, 137
PU	polyurethane	40–45, 47, 48, 51, 53, 54, 61, 64, 74, 75, 77, 78, 84, 85, 90–93, 96–98, 100, 101, 103, 111, 112, 114, 119, 121, 122, 124, 126–129, 131, 132, 136, 137, 145, 148
PVDF	Polyvinylidene fluoride	15
ROI	Region of Interest	105, 108, 115
UD	uni-directional	7, 8
UHMWPE	ultra-high molecular weight polyethylene	26, 41, 65, 136, 137, 146

Symbols

Notation	Description	Page List
A	Area	32, 43, 59, 108
C_B	Compression set	43, 63, 85
E_c	Young's modulus (compressive)	38, 48, 56
E	Young's modulus	13, 27, 32, 38–41, 43, 46, 48, 55, 65, 106, 109
F_{CY}	Yield compressive strength	38, 66, 70, 71, 147, 148
F_{SU}	Ultimate shear strength	38
F_{TU}	Ultimate tensile strength	38, 66
F_{TY}	Yield tensile strength	38
F	Force	9, 12–14, 16–18, 20–23, 25, 43, 44, 59, 105, 107, 108, 110, 148
G	Shear modulus	38, 55
K_t	Stress concentration factor	50, 59
MS	Margin of Safety	66, 67, 70, 71, 147, 148
N	Normal reaction force	23, 25
P	Pressure	9, 12, 13, 16–18, 20, 21, 27, 32, 44, 65, 108
R	Reaction force	25
SF	Safety factor	147, 148
S	Shear strength	38
V_f	Volume fraction	38, 86, 87
V	Volume	14, 17
X_C	Axial/hoop compressive strength	38
X_T	Axial/hoop tensile strength	38, 65, 106, 109, 110
Y_C	Transverse compressive strength	38
Y_T	Transverse tensile strength	38
$\dot{\epsilon}$	Strain rate	vi, ix, 40, 41, 51, 52, 145, 146
ϵ_T	True strain	52
ϵ	Strain	vi, 13, 32, 38, 40, 61, 65, 96, 110, 112, 155
μ	Coefficient of Friction	9, 13, 17, 18, 20–25, 107, 108, 113
ν	Poisson's ratio	32, 38, 40, 41, 46, 47, 55, 56, 61, 112, 126, 137
σ_N	Nominal stress	52
σ_T	True stress	52
σ	Stress	13, 27, 32, 34, 50, 59, 65–68, 70, 71, 105, 108, 147, 148
τ	Shear stress	34
d	Diameter	9, 12–14, 16–18, 20, 27, 31, 32, 43, 46, 51, 65, 96, 108
f	Frequency	51
h	Height	9, 14, 17, 18, 20, 21, 23, 25, 51, 105, 108
k	Stiffness	43
l	Length	25, 26, 32, 43
r	Radius	23–25, 61, 65
t	Thickness	9, 27, 32, 65, 105, 108
u	Displacement	60, 61
v	Velocity	51

Abstract

Composite over-wrapped pressure vessels (COPVs) are the state-of-the-art for Hydrogen storage. Current type IV pressure vessels, made with filament winding, comprise a thermoplastic polymer liner wrapped with a thermoset composite. The liner acts as an impermeable barrier, while the composite withstands both static and cyclic internal pressures. The next latent innovation is the Type V pressure vessel, where a thermoplastic composite over-wrap, made using automated fibre placement (AFP), serves both functions.

This requires the development of novel thermoplastic polymers and composites. The goal is to improve the barrier properties, impact strength, and life of the vessels. The materials developed need to be tested to characterize their mechanical properties. Manufacturing processes such as filament winding and AFP introduce several process parameters which influence the same. The effects of these parameters are simply not captured in standard coupon tests.

One way to overcome this challenge is to test ring specimens, made with the same process. It allows the study of the effects of the manufacturing process, layup, and geometry. An accurate characterization of the static strength, fatigue life, and residual strength of the composite is critical for a safe pressure vessel design.

The standard split-disk test used for composite rings under-predicts the strength and life of the material. Its results are influenced by stress concentration and friction that lead to an uneven hoop strain distribution in the specimen. Attempts with non-standard tests address these drawbacks for static strength estimations. However, they are not viable in fatigue. Hence, there was a need for a fatigue test which could improve upon the standard in both static and fatigue tests.

From an extensive literature review, a concept was developed analytically. It used a polyurethane ring, which when compressed axially, applied radial internal pressure to the specimen placed around its circumference. Preliminary tests and finite-element analyses were used to create a detailed design. Extensive tests were performed to study the test itself and fine-tune its parameters. The results were used to improve the accuracy of the finite-element model for future design iterations.

The test developed was easy to assemble and perform. It showed a 2.6% improvement in the failure strain over the standard split-disk test. The hoop strain distribution was practically free from stress concentrations. The polyurethane performed consistently over the 22000 $cycles$ tested. It was even tested with COPV-layup specimens and performed well up to 70 MPa of pressure. In the scope of this thesis, it reached its minimum goal of being able to perform comparative residual strength tests. It demonstrated potential capability to perform more accurate static and fatigue tests for wound composites. Overcoming its challenges with specimen alignment and uneven friction could further improve its accuracy.

1

Introduction

1.1. Motivation for Alternative Fuels

To combat climate change, the European Union (EU) aims to achieve climate neutrality by 2050. This implies that greenhouse gas (GHG) emissions into the atmosphere should not exceed what can be absorbed by nature. To achieve this goal, countries must cut emissions by at least 55% by 2030[1], compared to 2014. A key aspect of this goal is to reduce the use of fossil fuels in transportation, which is responsible for 25% of GHG emissions in the EU[2]. The main proponent of this change is to switch to electric or alternative fuels as energy sources.

This change is rapidly being adopted by the aerospace and automotive industries. Currently, there are 13.4 million cars running on alternative fuels in the EU. This number is estimated to grow ten times by 2050, meaning nearly 50% of cars in the EU would be running on alternative fuels[2]. Airbus, the leading aircraft manufacturer in the EU, plans to introduce hydrogen-powered commercial aircraft by 2035, with its ZEROe project. The concepts use propulsion systems that are either hybrid hydrogen-electric fuel cells, or direct hydrogen combustion[3].

1.2. Hydrogen as an Energy Source

Hydrogen is a key enabler in the switch to alternative fuels and thereby, achieving the climate goals [1]. Produced hydrogen is classified based on its method of production, from green having no harmful emissions, to black, being the most polluting. Green hydrogen is produced by electrolysis of water, where the electricity for the process comes from renewable sources. It produces hydrogen and oxygen, and hence, is pollution free. Blue hydrogen is produced from methane, using steam reforming, where carbon dioxide is a by-product. If > 85% of the carbon dioxide is captured, the hydrogen produced is classified as blue, else it is gray[4].

For application in mobility, hydrogen is typically stored in its gaseous form. This allows the storage system to achieve high gravimetric and volumetric energy densities. Gravimetric energy density is the ratio of energy produced by hydrogen, to the total weight of the storage system. Volumetric energy density is the ratio of the energy produced by hydrogen, to the total storage system volume. Typically, at room temperature and pressure, hydrogen can have a gravimetric energy density of $143 MJ/kg$, but a volumetric energy density of just $0.01 MJ/L$ [2]. By compressing it to 70 MPa (700 bar), the volumetric energy density increases to $5.6 MJ/L$. Hence, storing it Hydrogen in a compressed gas state is preferred. This is also beneficial for weight-critical applications such as in the aerospace and automotive industries.

[1] https://www.consilium.europa.eu/en/policies/climate-change/#2050

[2] https://www.consilium.europa.eu/en/infographics/fit-for-55-afir-alternative-fuels-infrastructure-regulation/

[3] https://www.airbus.com/en/innovation/energy-transition/hydrogen/zeroe

[4] https://www.weforum.org/agenda/2021/07/clean-energy-green-hydrogen/

For comparison, Kerosene, Diesel, and Petrol have gravimetric and volumetric energy densities of $45 - 47\ MJ/kg$ and $34 - 37\ MJ/L$, respectively [2].

1.3. Pressure Vessels for Hydrogen Storage

Pressure vessel development for hydrogen storage has been gaining traction in the past few decades. Currently, Type IV pressure vessels are used. These consist of a polymer liner with a full composite over-wrap. The lining is typically made of High Density Polyethylene (HDPE) or Polyamide (PA) [3]. This leads to a lighter construction, thereby increasing the gravimetric efficiency to 5.7 $wt\%$ [4]. It also solves the problem of hydrogen embrittlement. Hydrogen absorbed into the polymers do not dissociate into atoms. However, hydrogen can permeate through the polymer. As explained by [3], the process of hydrogen permeation consists of dissolution and diffusion. Dissolution of hydrogen into a polymer has a "plasticizing effect". It increases its toughness but reduces the strength. Diffusion is the random motion of hydrogen molecules within the polymer. Hence, the barrier properties of the polymer liner need to be considered. Since the tanks have a metallic polar boss at the opening, the interface properties of the polymer with the metal also needs to be taken into account. Common types of pressure vessels are shown in Figure 1.1.

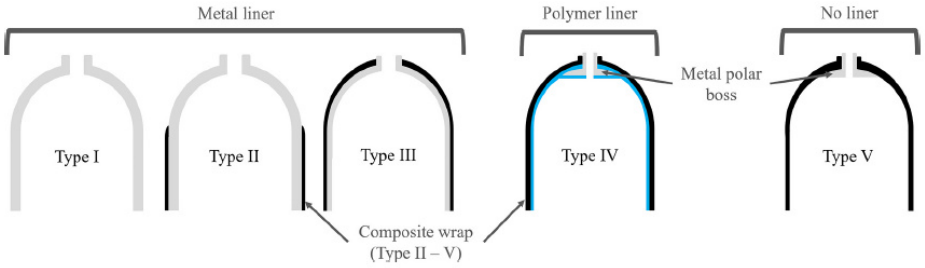

Figure 1.1: Types of Pressure Vessels [5]

Type V pressure vessels consist only of the composite, with the polymer matrix acting as the hydrogen barrier. However, the current state of Type V pressure vessels do not meet the standards set by the automotive and aerospace industries. Challenges exist in reaching the operating pressure, burst pressure, and permeability targets [5]. Hence, it is a topic for future development.

1.4. Manufacturing and Materials

Traditionally, COPVs are manufactured using filament winding. This is owing to its precision and low cost. However, the drawbacks are its limited flexibility and its optimization capability. The fibres, being in tension, follow a geodesic path; and as it has to be a continuous tow, the thickness at the domes cannot be changed independently of the cylinder thickness [5].

Currently, at Syensqo, AFP is used to manufacture the COPVs. The width of the tow can be varied. It can also be steered to achieve non-geodesic paths. At the domes, a lower width tow can be used to better conform to the shape, as well as allowing for a higher thickness. However, AFP is prone to defects such as overlaps and gaps. The processing parameters such as compaction pressure and temperature can also affect the void content [5].

Commercially available COPVs use Carbon Fiber (CF) and a thermoset matrix. This is owing to its low cost, especially in the highly competitive automotive industry. However, the current focus at Syensqo is on the research and development of thermoplastic COPVs. The aim is to provide better impact and damage resistance, leading to safer tanks. A life cycle assessment also shows it to be sustainable, having a lower environmental impact. However, the cost of the tanks is expected to be higher in comparison to thermoset ones.

1.5. Mechanical Test Development

The role of mechanical tests in the development of COPVs is to characterize the mechanical properties of the new materials being developed. These include stiffness and strength in the longitudinal, transverse, and shear loading conditions. The goal is to use test results for characterization of both the static and fatigue performance of the materials. This can then be used to design vessels through accurate material models.

As the COPVs are made through filament winding or AFP, ring specimens best represent the final structure [6]. Coupon tests cannot capture the effects of the variability in the uni-directional tape material or the effects of the processing parameters used. On the other hand, testing complete COPVs to failure is extremely expensive. Owing to the size of the vessels, it is also difficult to observe the failure, or to setup instrumentation for measurements. Hence, tests need to be done on specimens that are representative of the COPVs but use less material, while allowing for observation and measurement.

The NOL tensile test method [6], published in 1964, is still used as the standard for testing ring specimens [7]. It has been used extensively for both static and fatigue tests. It has seen incremental improvements over the years, but its main drawbacks are inherent to its design and are yet to be overcome. Several researchers have developed alternative novel methods to test the hoop performance of rings or tube sections. Other test setup designs and non-standard methods are limited to static strength tests.

The standard method has inherent drawbacks that under-predict the test results, and the non-standard methods are not feasible in fatigue. Hence, a gap is identified, where there is no effective method to study the fatigue performance of ring specimens. Hence, leading to this research to develop a novel hoop fatigue test for composite rings.

1.6. Research Objectives

The primary objective of this research is to develop a fatigue test for tubular composite specimens. The test method should, at the minimum, be able to apply cyclic loading to the specimen, then determine the burst-after-fatigue strength. The ultimate objective for the test is to characterize the hoop fatigue life of the material by generating un-notched S-N curves.

A secondary objective is to demonstrate the test setup's capability to perform fatigue tests on representative COPV specimens. The purpose of the tests would be to study the gap between testing a ring specimen and a full pressure vessel. The result of the future study could be an assessment of the differences and an engineering relation to bridge the same.

1.7. Report Outline

The thesis was focused on the development of a new test method. Since it was done in collaboration with a consortium, the second chapter briefly introduces each partner and explains their involvement in this thesis.

The subsequent chapters detail the complete methodology of the test development. It starts with a detailed literature review, which includes an analytical assessment of each concept, to define a research proposal. The next chapter documents the complete analysis and design process used to refine the concept into a manufacturable setup.

Subsequent chapters give detailed descriptions of the tests performed, and the methodology used to study and fine-tune the test developed. It leads to a discussion of the tests capabilities, challenges, and limitations, based on comparisons with the standard test. Lastly, there is a brief conclusion which summarizes the results and answers the research questions formulated in the proposal. It is followed by recommendations for future work and studies, to improve the setup's accuracy.

2

Partners Involved

2.1. Syensqo

Syensqo is a Belgian materials company with its headquarters in Brussels. On paper, it is relatively new, existing since December 2023. However, it was formed when Solvay split into two companies[1].

Solvay was founded in 1863 by two brothers, Ernest and Alfred Solvay. It grew as a chemical company, making sodium bicarbonate (soda ash). As of 2023, it also specialized in chemicals, polymers, and composites. After the split, Solvay retained the traditional business of making sodium bicarbonate, adhesives, and hydrogen peroxide. The part specializing in polymers and composites became Syensqo. Hence, Syesnqo jump-started with 13,200 employees and an annual turnover of 7.9 billion euros[1].

It is one of the major suppliers of composite materials and polymers for the aerospace, automotive, and healthcare industries. The current projects focus mainly on renewable materials, battery materials, thermoplastic composites, and green hydrogen[2]. With these growth platforms, the goal is to help decarbonize the aerospace, automotive, and energy industries, in keeping with the EU's goal to reach climate neutrality by 2050.

2.2. Toyota Motor Europe

Toyota Motor Europe (TME) oversees operations of Toyota across Europe and West Asia. Based in Brussels, it encompasses research & development, manufacturing and sales across these regions. TME began in 1963 in Europe, has nine manufacturing plants, and employs approximately 90,000 people.

It is a major manufacturer of automobiles in Europe, holding 7.3% of the market share [3]. As of 2023, it had an annual revenue of 229 billion euros[4]. Apart from selling consumer vehicles, it also has a major involvement in motor-sports, which is used as a test-bed for alternative fuels and energy diversification.

TME has made substantial efforts towards developing Hydrogen engines and, along with Syesnqo, is supporting the development of thermoplastic COPVs for Hydrogen storage. The goal of this effort is to make sustainable energy sources such as Hydrogen more viable, and to help reduce emissions to meet the 2050 carbon neutrality target.

[1] https://www.solvay.com/en/press-release/solvay-and-syensqo-revealed-new-company-names
[2] https://www.syensqo.com/en/innovation/growth-platforms
[3] https://newsroom.toyota.eu/toyota-motor-europes-market-share-increases-to-a-record-73-in-2022-09-points-year-on-year/
[4] https://www.annualreports.com/HostedData/AnnualReports/PDF/NYSE_TM_2023.pdf

2.3. ComFHy Consortium

ComFHy (COMposite solutions for Future Hydrogen storage tanks) is a consortium of five industrial partners based in Belgium. They fund and support academic research and engineering projects at their academic partner, Ghent University. This research is supported financially by Vlaio in Flanders and Innoviris in Brussels. Syensqo and Toyota Motor Europe are among the five industrial partners that contribute to this project. The other partners are namely OP Mobility (Plastic Omnium), Sharp Composites, and AMS Robotics.

There are three main goals of the project, divided in work packages between partners [8],

1. Accurate analytical models for manufacturing and tank design (OP Mobility), and better finite-element simulations for burst, impact, and fatigue (Ghent University).
2. Full-tank test methods (Sharp Composites) and representative small-scale test developments (Syensqo).
3. Development of new tank concepts (Toyota Motor Europe).

This thesis contributes towards the second goal, to develop a ring fatigue test that could potentially be representative of a full tank test.

2.4. Involvement

The thesis topic was posited by Dr.ir. Siebe Spronk from Syensqo. As it contributed to the ComFHy project, it was funded by the same. The budget was approved by Dr.ir. Martin Kerschbaum from Toyota Motor Europe. It was supervised by Prof.dr.ir. René Alderliesten from the Faculty of Aerospace Engineering, TU Delft. The thesis was jointly supervised and guided by the three through weekly meetings. Their individual contributions are attributed throughout the text. They also offered valuable feedback to improve and refine the thesis.

After the literature review, the work was carried out at Syensqo, which offered complete support of its mechanical testing lab, workshop, and cafeteria. Siebe's support was instrumental in preparing the tests. Colleagues from Syensqo's workshop were crucial in procuring raw materials, refining the design for manufacturing, and preparing the specimens.

Prof.dr.ir. René Alderliesten gave valuable inputs to ensure a thorough literature review and test development methodology. TU Delft's mechanical testing lab allowed to test at the high force requirements in-house. The support of the lab technicians was critical in preparing the test bench for the compression tests in time. Their continued support ensured that the tests were not delayed.

Prof.dr.ir. Wim van Paepegem from the Department of Materials, Textiles, and Chemical Engineering, Ghent University offered valuable guidance during the initial concept stage. Along with his team of doctoral candidates, he gave valuable suggestions to improve the axisymmetric finite-element model. His critical feedback was also appreciated and addressed.

3

Literature Review

3.1. Introduction

The primary objective was to develop an effective fatigue test for composite rings. It should ultimately be capable of generating S/N curves for the material. An additional objective was to be able to test rings cut from COPVs. Since the latter demands higher requirements, it was used to decide the limits of the test setup.

According to the EU's directive for the performance requirements for COPVs [9], the Nominal Working Pressure (NWP) of the vessel should be 70 MPa. It's burst pressure should be greater than 225% NWP, which is 157.5 MPa. For it's fatigue performance, the vessel should be able to withstand a pressure cycle from 2 MPa to 87.5 MPa for up to 22.000 cycles, without failure.

The test had to use a smaller, cylindrical composite specimen that could be representative of the vessel's performance. The COPV in this study had an inner diameter of 170 mm, within which was a 4 mm thick polymer liner. The aforementioned pressures and dimensions were used as the design limits. It would allow testing specimens from COPVs.

A literature review was done to study current standard test methods, non-standard tests, and concepts from other disciplines. The goal was to find ways to apply uniform internal pressure to a cylindrical composite specimen. Attention was paid to the setups used, the test conditions and limitations, purpose of the tests, and failure mechanisms. Exploring existing test methods was a way to generate ideas that could be adapted to the needs of the project. It was also to note their shortcomings, and to see whether they could be overcome or avoided in the current development.

Concepts were developed simultaneously during the review and were analysed to quantify their performance. An objective assessment of each setup and the derived concepts are presented. Then, in section 3.5, their challenges and feasibility are discussed to determine the most promising way forward.

3.2. Standard Test Methods

ASTM and ISO standards were studied to see relevant tests that could be implemented. The implementations of these standards in previous literature were reviewed as well. Particular attention was given to modifications, test conditions, and specimen preparation methods.

An overview of the standard tests studied is shown in Table 3.1.

Table 3.1: Equivalent Test Standards

Test Description	ASTM	ISO
Tensile strength of composites	D3039	527-1
Tension-tension fatigue strength of composites	D3749	13003
Hoop tensile strength (split-disk test)	D2290	8521
Hydraulic internal pressure resistance of composite tubes	D1599	1167-1
Cyclic pressure resistance of composite tubes	D2143	15306
Hoop tensile strength of CFCC tubes	C1819	21971

3.2.1. Coupon Test

ASTM D3479/D3479M-19 [10] describes the standard for tension-tension fatigue testing of composite specimens. It advises the use of an un-notched rectangular specimen. To promote failure in the gauge section, tabs must be adhesively bonded to the specimen, to reduce the stress concentration at the location of the grips. Recommendations for specimen geometry and setup preparation are given in ASTM D3039/D3039M-17 [11]. The equivalent International Standards ISO 527-5:2021 [12] and ISO 13003:2003 [13] describe the method of preparation of uni-directional (UD) fibre-reinforced plastic composites and the tension-tension fatigue testing method, respectively. The standard suggests a minimum R-ratio of 0.1 to prevent unloading the wedge grips completely, leading to slipping. This test has the benefit of being easy to prepare, perform, and monitor. However, for the objective of representing the performance of a COPV, a coupon test presents certain limitations. Although flat, rectangular specimens can be manufactured using AFP [14], the effect of processing parameters and geometry will not represent that of a pressure vessel [15]. This could be overcome by testing specimens that are closer to the final product.

Coupon Specimen Preparation

Kastenmeier *et al.* [16] studied the effect of specimen preparation on the stiffness and strength of filament wound specimens. The specimens were made from glass-fibre/epoxy using three methods, shown in Figure 3.1 (a). The goal was to see how the processing conditions can influence mechanical properties in composites. It was noted that when the filaments are wound over a cylinder, the radial force, resulting from the tension over the curvature, was constant throughout. It resulted in ring specimens that had a consistent fibre volume content. When winding over the hexagonal mandrel, the radial force peaked over the corners and dropped over the flat surfaces. This resulted in a thinner composite over the corners, leading to a higher fibre volume content. However, the section formed over the flat surfaces had higher void content.

The results of longitudinal strength tests are shown in Figure 3.1 (b). For the ring specimen, the split-disk test was used [7]. The lower strength reported was due to the presence of the bending moment at the split. The transverse strength was also measured for the different specimens. The specimens made using the octagonal mandrel had the lowest transverse strength due to the aforementioned high void content. These observations may not be entirely applicable to specimens produced using AFP. To better capture the layup and thermal history of a cylindrical part, a tubular specimen was decided upon for the current research.

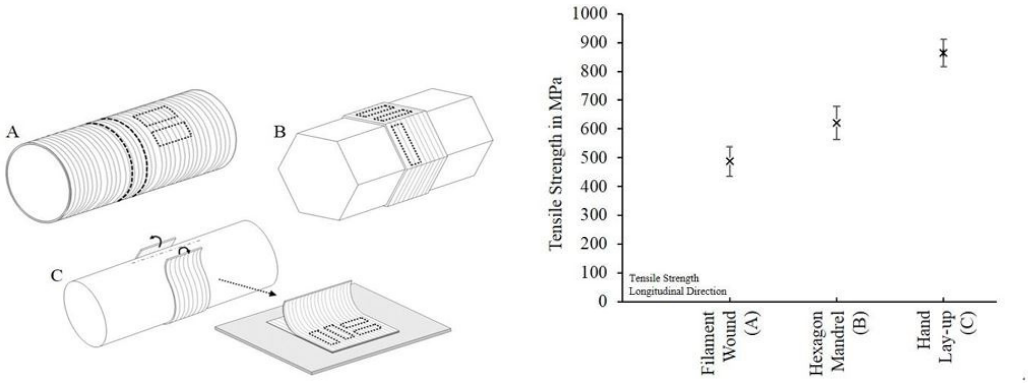

(a) Specimen Preparation Methods **(b)** Longitudinal Tensile Strength

Figure 3.1: Strength Varies by up to 80% Depending on the Manufacturing Process [16]

3.2.2. Split-disk Test

For the hoop tensile strength of composite cylinders, the standard test method is given by ASTM D2290-19a [7]. It describes using a split-disk to load a composite ring specimen. It recommends that the specimen should have a notch, to create a section of reduced area, where the failure should occur. By pulling apart the two half-disks, the section of the specimen that lies at the split experiences a hoop tensile stress. The schematic for this setup is shown in Figure 3.2.

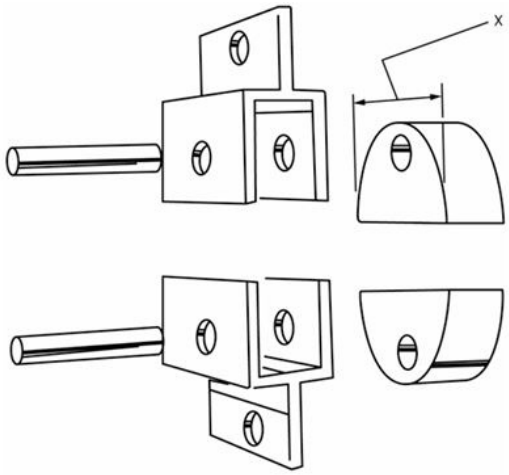

Figure 3.2: Split-Disk Setup [7]

It can be used for both static and fatigue tests [17]. ASTM D2992-24 [18] procedure A gives the guidelines for the fatigue strength estimation. The International Standard ISO 8521:2020 [19] describes an identical setup, as method B. It further specifies that the test is meant to determine the initial circumferential tensile strength and it is not effective for specimens with helically wound layers. These standards evolved from ring tests developed by Kinna [6].

Implementations in Literature

Shabani *et al.* [17] studied the behaviour of glass-reinforced epoxy (GRE) rings under fatigue loading using the split-disk test. Un-notched UD rings were used for static tests, while notched rings were used for fatigue tests. The layup of the notched rings was $[90_2, +45_2, -45_2, 90_2]$. The goal of the tests was to develop a numerical prediction tool for the fatigue life of the material, using the test results as input. The model over-predicted the static strength by 9%, but under-predicted the fatigue life by 16%. Hence, a finite-element based approach could be used to bridge the gap between the test and reality ([17], [20]), it would introduce its own intrinsic errors into the fatigue life estimation.

Static and fatigue tests were performed using the split-disk test by Mahdavi *et al.* [21]. The specimens were cut from [±55°] filament-wound GRE pipes. The diameter was 209 mm and the thickness was 6.7 mm (18 $layers$). Rings were cut to a width of 25 mm and were notched, having a reduced area width of 15 mm. As per ASTM D2992-24 [18], the frequency of loading was 25 $cycles/min$ (0.42 Hz) and the stress ratio was 0.05. Static tests were done to estimate the hoop strength of the specimen, which was on average 260 MPa. In static tests, it was reported that the failure initiated with fibre-matrix interface de-bonding and matrix cracking, followed by delamination, and finally, fibre breakage. In the fatigue tests, the specimens were loaded till 60, 70, 80, *and* 90% of the hoop strength. The cycles till failure were recorded and the focus was on studying the failure mechanisms. For the GRE rings, in fatigue, it was reported that the initial failure was at the fibre-matrix interface, parallel to the fibre direction. The de-bonding created stress concentrations, which promoted further de-bonding. When the fatigue of the epoxy was exceeded, it created delamination which progressed through the thickness. Towards the end, fibre failure occurred [21]. Based on these observations, it would be necessary to judge the quality of the specimen through an ultrasonic scan before testing. It would be important in understanding the failure mechanisms and separating the failures observed cyclic loading from existing defects in the specimens.

Calculations

Preliminary calculations for the effectiveness of this test were done. The specimen in this case has an inner diameter, $d_i = 170\ mm$ and thickness, $t = 10\ mm$. To keep the amount of material used at a minimum and also to reduce the required force, the height of the specimen is $h = 10\ mm$. As per the requirements mentioned in section 3.1, the radial pressure target for the fatigue test was 87.5 MPa. Equation 3.1 was used to calculate the radial force required to reach the target pressure.

$$F_{radial} = P_{radial}\frac{\pi d_i h}{2} \tag{3.1}$$
$$F_{radial} = 87.5\frac{\pi \times 170 \times 10}{2} = 233.66\ kN$$

Equation 3.2 was then used to calculate the applied force required. Where μ is the coefficient of friction between steel and the specimen's surfaces, which in this case was 0.11[1].

$$F_{applied} = \frac{F_{radial}}{1-\mu} \tag{3.2}$$
$$F_{applied} = \frac{233.66}{1-0.11} = 262.53\ kN$$

The mechanical advantage ($F_{radial}/F_{applied}$) for this setup is ideally 1. However, due to friction, it reduced, in this case, to 0.89.

Drawbacks

The benefits of this method are that it uses relatively simple components, can be set up on an existing electromechanical test bench, and allows for easy data acquisition. However, there are considerable drawbacks,

1. At the split, a bending moment will be generated, as the specimen will bend over the edge of the disks. The interaction of the tensile and bending stresses will result in a higher stress along the cross-section thickness. This would cause premature failure in the specimen, under-predicting the hoop tensile strength by at least 20% [20]. In case of cyclic loading, it would promote faster crack growth on the outer layers of the specimen, under-predicting the fatigue life.
2. The bending moment will also cause an uneven strain distribution along the circumference and the thickness. As per to Zhao *et al.* [20], measuring the strain at an angle 10° away from the split results in a modulus value closer to the prediction. However, for strength there is no such mitigation.
3. Friction between the specimen and the split disks can also affect the strain distribution along the circumference. For a cyclic loading case, this friction would generate heat. An increase in

[1] https://www.engineeringtoolbox.com/friction-coefficients-d_778.html

temperature over time would lower the strength of the thermoplastic composite, affecting fatigue life and damage estimations. By using a lubricated surface, the effect of friction on strain could be mitigated [20]. However, its effectiveness would likely reduce over the duration of the fatigue test.

4. The standard recommends using a notched specimen to promote failure at a certain cross-section. For the purpose of this project, the specimens used would have hoop-wound layers, with a winding angle greater than ±88°. Zhao *et al.* [20] observed that for such specimens, the presence of a notch created matrix splits parallel to the fibres. This happened due to the stress concentration created at the notch location. Under cyclic loading, the matrix splits could occur before failure in the reduced section.

Although few of the drawbacks of this method can be overcome, the presence of the local bending moment still affects the results from this test. The modulus can be estimated by picking a suitable location for strain measurements. However, the static strength and fatigue life are still under-predicted. As the strain distribution would vary across the thickness due to the bending moment, having a thicker specimen would exacerbate this problem. Overcoming these drawbacks is one of the goals of the current research.

3.2.3. Hydraulic Internal Pressure Test

ASTM standards D1598-24 [22] and D1599-18 [23] give the guidelines for testing pipes under hydrostatic pressure. The standards suggest that for a pipe specimen shorter than 150 mm, its length should not be less than five times its outer diameter. The pipes must be sealed at the ends, and a fluid, such as water, can be used to apply internal pressure. D1598 focuses on applying a constant internal pressure and estimating the time to failure. D1599 focuses on linearly increasing the internal pressure till burst failure or leakage occurs. The purpose of the test is to estimate the hoop strength of a pipe specimen. Hence, the two aforementioned standards focus on quasi-static tests. Method 'A' described in ISO 8521:2020 [19] describes a hydraulic internal pressure test for fibre-reinforced pipes. ISO 1167-1:2006 [24] details a similar test specific to thermoplastic pipes. Both ASTM and ISO standards detail two types of end cap assemblies. The first type, named type A, is not constrained longitudinally, and hence, allows both hoop and longitudinal deformation of the tube specimen. The second, type B, has one or more longitudinal connections between the end caps, allowing only radial deformation of the specimen.

The aforementioned standards extend to cyclic loading in ASTM D2143-21 [25]. It adds an additional requirement that the specimens' outer diameter to wall thickness ratio should be 10 : 1. It is used to measure the performance of pipes under cyclic internal pressure. The setup includes solenoid valves and oil pumps, together with pressure relief valves to cycles the fluid. The recommended cycling rate is 25 ± 2 $cycles/min$. The pressure should be monitored using gauges. ISO 15306:2003 [26] details a similar test. It further recommends the mean and alternating pressures to be the nominal pressure and 25% of the nominal pressure, respectively. The cycling rate is also recommended depending on the nominal diameter of the pipe. For a diameter > 150 mm, the frequency is 8 ± 2 $cycles/min$. The test is meant only a pass/fail test and the cycles to failure should be recorded. The benefit is that multiple specimens can be tested simultaneously. However, it is complicated and will require an extensive hydraulic and electrical setup. Similar to other hydraulic tests, the use of fittings and valves will create more risk of leakages in the system. The use of solenoid valves will also limit the maximum pressure that could be applied through the system. Switching to bigger valves will then limit the cycling rate. Hence, owing to its complexity and requirements, this method was not feasible to implement for this project.

Implementation in Literature

Mahdavi *et al.* [27] set up a hydraulic internal pressure test for a glass fibre-reinforced epoxy pipe as per D1599-18 [23]. The purpose was to test the ultimate hoop strength of the pipes. The specimens were made with filament winding with the layup $[\pm 55°]_9$. The results of the test were compared with the results from a split-disk test. The test setup is shown in Figure 3.3. End caps and O-rings were used to seal the specimen against the caps. Rings were added over the ends of the specimen to prevent radial expansion at the ends, making an effective seal.

Under hydrostatic pressure, matrix cracks were observed parallel to the fibre direction. The specimens were tested till leakage. The hoop strength calculated was similar to what was obtained for notched

rings in a split-disk test. However, the failure mechanism in the notched ring was a mix of matrix cracks and fibre failure.

Figure 3.3: Hydrostatic Pressure Test Setup [27]

3.2.4. Elastomer Expansion Test

ASTM C1819-21 [28] details a method to apply internal pressure through the radial expansion of elastomer inserts. It is meant for Continuous fibre-Reinforced Ceramic Composite (CFCC) tubes, which may be because of their high stiffness, ensuring small deformations. The setup consists of two pushrods, which compress an elastomer placed at the centre of a composite tube specimen. The pushrods compress the elastomer longitudinally, guided by the specimen. Longitudinal compression causes the elastomer to expand radially, applying uniform radial pressure to the specimen.

This setup was first developed by Mosley [29] for testing brittle materials. The schematic for the setup is shown in Figure 3.4 (a). For the elastomers, common materials such as urethane, neoprene, or silicone rubber are suggested, as they have a wide range of hardnesses available. The hardness of the elastomer chosen also limits the maximum pressure that can be applied to it. The elastomers are positioned only in the centre of the specimen such that the rest of the specimen can act as guides for the pushrods, and the ends of the specimen do not experience significant stress. A high-pressure lubricant is suggested to be used to reduce friction. The benefits of this setup are that it requires simple components, can be set up on an existing test bench, and can be used to test up to high internal pressures without using any hydraulic systems, eliminating the risk of leakage.

ISO 21971:2024 [30] details a different setup, also for CFCCs. It recommends an elastomeric bladder that conforms to the inner surface of the tube. The bladder is pressurized by injecting oil through a piston, moving at a constant rate. It further recommends a specimen length $\geq 60 \pm 2\ mm$, and an external diameter $\geq 7 \pm 0.2\ mm$, for this test. The schematic is shown in Figure 3.4 (b). For both tests, the applied pressure can be recorded and the hoop tensile strain can be measured using either Digital Image Correlation (DIC) or strain gauges.

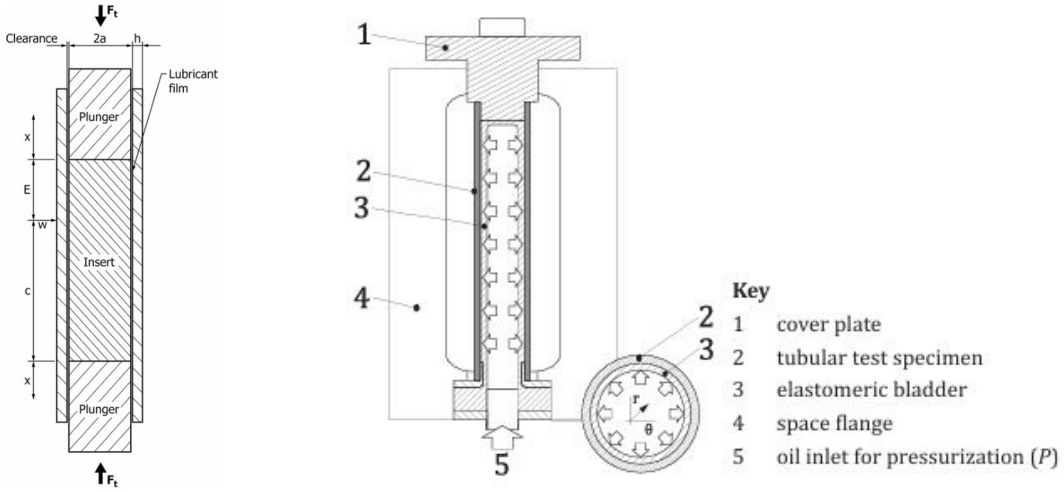

(a) Elastomeric Insert Compression [28] **(b)** Hydraulic Pressurization of an Elastomeric Bladder [30]

Figure 3.4: Internal Pressurization using Elastomer Compression and Elastomer Bladder Expansion

Implementations in Literature

ASTM C1819-21 [28] was implemented by Xiao *et al.* [31]. The objective was to study the hoop tensile properties and the crack propagation behaviour in CFCC tubes. Static strength tests were conducted where the maximum hoop strength of the specimens was approximately 80 MPa. However, the specimens tested were relatively small, being 7 mm in internal diameter and 30 mm in length. The polyurethane insert was 10 mm in height. The failure mechanism noted was cracks originating from and connecting pore regions between the woven fibres.

Madrid *et al.* [32] adapted the same for filament wound specimens. The goal was to test the effectiveness of C1819 on these specimens in measuring the hoop strength. The test was performed for six specimens with winding angles from 35° to 90°. The specimens were 110 mm long with the pressurized region being 60 mm. Silicone rubber elastomers were used with a Shore hardness of 40 A, and were checked to have a Poisson's ratio of 0.5. They were 10 mm in height and 50 mm in diameter. DIC was used to monitor radial displacement of the specimen, as well as axial and hoop strains. The failure mechanism of the specimen with winding angle 90° was noted to be matrix cracking. Due to the elastomer pressurizing only the central part of the specimen, and the high hoop stiffness of the unpressurised surrounding regions, bending stresses were induced. These stresses were significant enough to cause matrix failure parallel to the fibre direction before fibre failure could happen. Under cyclic loading, the same could be expected.

Derived Concept and Calculations

The force required for this setup and its effectiveness were estimated. To apply a radial pressure of 87.5 MPa, the applied force was calculated by rearranging Equation 3.3.

$$P_{radial} = P_{applied} = \frac{4F_{applied}}{\pi d_i^2} \tag{3.3}$$

$$F_{applied} = \frac{87.5 \times 170^2 \times \pi}{4} = 1986.08\ kN$$

The high force requirement was impractical. However, owing to the ease of implementation of this setup, a concept was devised. A schematic is shown in Figure 3.5.

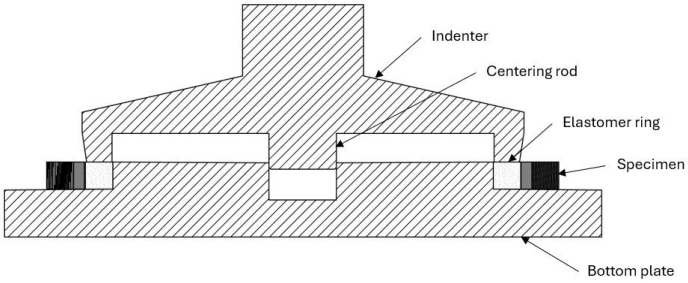

Figure 3.5: Elastomer Expansion Setup Concept

To seal the edge of the specimen against the indenter, the outer face is tapered. This would be required to prevent the elastomer from squeezing through the gaps that would form due to the radial expansion of the specimen. The angle of the taper would be calculated by estimating the radial expansion and axial contraction of the specimen. As the elastomer is compressed along the specimen height, the area of the specimen being pressurized would also reduce. The edge of the specimen should not be loaded through the tapered face.

For a ring of 10 mm thickness, the applied pressure was calculated using Equation 3.4. It was then used to calculate the ideal force by neglecting the effect of friction.

$$P_{applied} = \frac{4F_{applied}}{\pi(d_i^2 - d_{core}^2)} \tag{3.4}$$

$$P_{radial} = P_{applied} = \frac{4 \times 100000}{\pi(170^2 - 150^2)} = 19.89\ MPa$$

$$F_{radial-ideal} = 19.89 \times (\pi \times 170 \times 10) = 106226.67\ N$$

To account for friction on the top and bottom surfaces of the elastomer, $\mu = 0.05$[1] was used to calculate the actual radial force, through Equation 3.5.

$$F_{radial} = F_{radial-ideal} - 2\mu F_{applied} \tag{3.5}$$

$$F_{radial} = 106226.67 - 2 \times 0.05 \times 100000 = 96226.67\ N$$

To calculate the hoop strain at 87.5 MPa, the hoop stress under this pressure was first calculated using Equation 3.6. Then the modulus, $E_{11} = 129\ GPa$, was used to estimate the hoop strain, using Equation 3.7.

$$\sigma_\theta = \frac{P_{radial} d_{mean}}{2t} \tag{3.6}$$

$$\sigma_\theta = \frac{87.5 \times 180}{2 \times 10} = 787.50\ MPa$$

$$\epsilon_\theta = \frac{P_\theta}{E_{11}} \tag{3.7}$$

$$\epsilon_\theta = \frac{787.50}{129000} = 6.10 \times 10^{-3}$$

From the hoop strain, the increase in diameter was calculated using Equation 3.8.

$$\Delta d = d_i \epsilon_\theta \tag{3.8}$$

$$\Delta d = 180 \times 6.10 \times 10^{-3} = 1.04\ mm$$

To calculate the cross-head displacement, the elastomer was assumed to be incompressible. With a

constant volume, the increase in diameter was used to calculate the decrease in height using Equation 3.9.

$$
\begin{aligned}
V &= \frac{\pi(d_i^2 - d_{core}^2)h}{4} \\
\Delta h &= h - \frac{4V}{\pi((d_i + \Delta d)^2 - d_{core}^2)} \\
\Delta h &= 10 - \frac{4 \times 16000\pi}{\pi(171.04^2 - 150^2)} = 0.52\ mm
\end{aligned}
\tag{3.9}
$$

As the mechanical advantage, (F_{radial}/F_{radial}) was 0.96, this setup would need at least a 500 kN test bench.

3.3. Non-standard Test Methods

Setups developed by researchers for the similar applications were studied. The setups ranged from hydraulic to purely mechanical.

3.3.1. Hydraulic Setups

Etemad *et al.* [33] devised a hydraulic setup to characterize the hoop strength of carbon fibre composites. Tubes were made using filament winding. The outer diameter was 81.6 mm and the thickness was 8.25 mm. These were cut into 10 mm wide rings using a diamond cutter. As the rings were thick, a hydraulic method was developed. The objective was to pressurize the rings with oil till failure. High strength steel EN24T was used to make the 50 mm thick end plates. On the inner surface of the plates, grooves were machined to hold O-rings and an anti-extrusion ring. This was to prevent the plastic deformation of the O-rings, within the oil cavity, under high pressure. The plates were restrained by six 35 mm bolts, used to withstand tensile stresses while testing. The composite specimen was placed around a concentric Polytetrafluoroethylene (PTFE) ring. The sealing ring had a cavity for the oil. The O-rings and anti-extrusion rings rested on the PTFE rings to prevent any axial load from being applied on the specimen. Within the sealing ring, there was a steel core to withstand the pressure towards the centre. The schematic of the setup is shown in Figure 3.6.

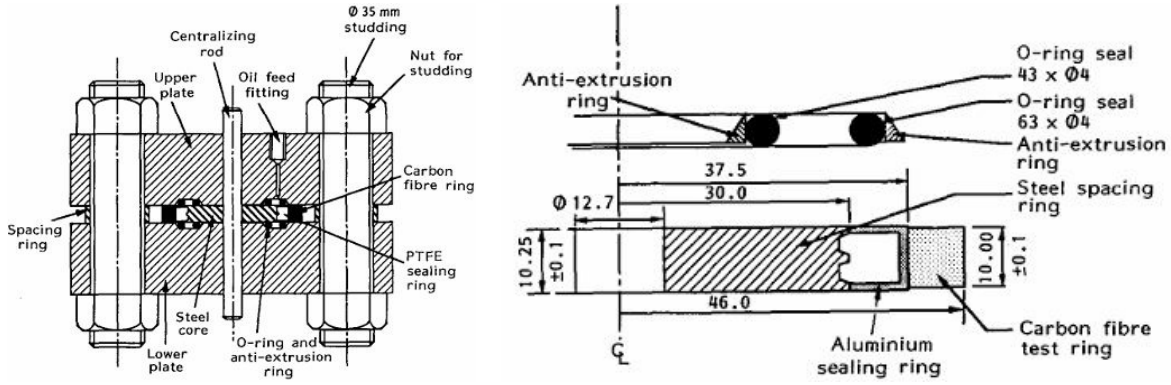

Figure 3.6: Hydraulic Thick Ring Burst Test [33]

The figure mentions Aluminium instead of PTFE as the sealing ring's material. It could be a misprint. The sealing ring had circumferential gaps to introduce oil into the ring's cavity. This then applied hydrostatic pressure to the specimen. An air pump was used to supply the oil. Three strain gauges were used, two in the hoop direction, placed diametrically opposite to each other, and one in the axial direction, to measure the hoop and axial strains, respectively. Five specimens were tested. The average burst pressure was 336 MPa and the average burst strength was estimated to be 1680 MPa. The failure mode was reported to be delamination in the axial direction followed by fibre failure in the hoop direction closer to the edge. An axisymmetric finite model was used to compute the hoop and axial strains for the same internal pressure. The difference with the experimental results was found to be 10%. Some ideas from this test, such as using a steel core, could be used in a fatigue test. It would reduce the

volume needed to be pressurized, but might lead to additional complexity in designing the seals. The hydraulic setup needed to cycle the pressure would still be a challenge to implement.

A hydraulic test was also developed by Hwang *et al.* [34]. The goal was to be able to measure the material properties of filament-wound COPVs. A 500 mm diameter filament wound tube was made from carbon fibre and epoxy, with the layup $[\pm 20^\circ_2, 90^\circ_2, \pm 20^\circ_2, 90^\circ_6]$, having a thickness of 3.1 mm. The test setup comprised upper and lower end plates, and an inner and outer core. A rubber tube, placed between the cores, was pressurized with water to apply uniform internal pressure on the specimen. The schematic is shown in Figure 3.7.

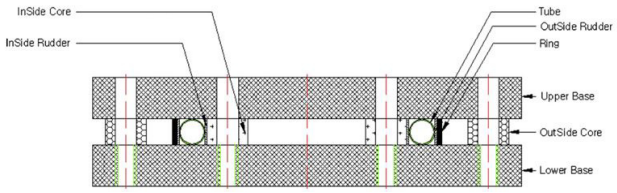

Figure 3.7: Hydrostatic Pressure Test Setup [34]

The pressure inlet for the rubber tube was through an opening in the inner core. Strain gauges were attached to the specimen at 90° intervals to measure the hoop and axial strains. During the test, unexpected failure was observed due to fibre breakage at the edges of the specimen. It was reported to be caused by a non-uniform gap between the specimen edges and the end plates. The rubber tube under squeezed through the gap and caused a stress concentration. Together with defects introduced from machining the specimens, it caused premature failure. The specimens edges were then reinforced. The reinforced specimens were reported to have 16% higher burst strength and their hoop strains were maximum at the centre along the height.

Bujdoso and Mintzas [35] developed a novel small-scale burst test for CF-PVDF pipes. The purpose was to test failure strain and hoop strength of the composite. The inner diameter of the pipe was 185 mm. The specimen used was a 100 mm long section of the pipe, including the barrier. A latex bladder was placed within the specimen and pressurized with water, using a hydraulic pump. This in turn applied uniform radial pressure on the specimen. Rods were used to withstand tensile loads between the end plates, ensuring that the specimen experienced only hoop stress. The pressure inlet was located in the top plate, and it connected to a sealing ring on the latex bladder. Strain gauge rosettes were attached at 90° intervals around the circumference, for data acquisition. The schematic is shown in Figure 3.8.

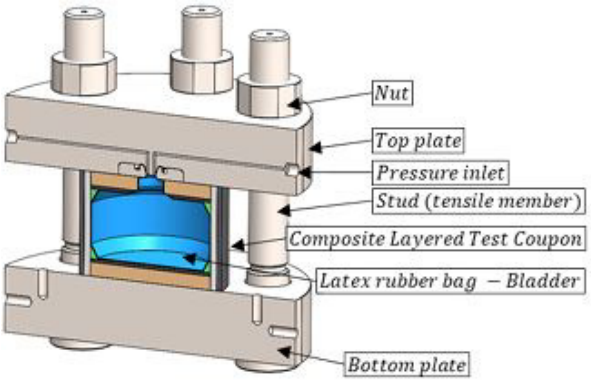

Figure 3.8: Small-scale Burst test Schematic [35]

The pressure was increased linearly, at a rate of 9 MPa/min, until failure. The three types of specimens were $[+85^\circ_4, -85^\circ_4]_2$ (16 layers), $[+85^\circ_4, -85^\circ_4]_3$ (24 layers), and $[+85^\circ_4, -85^\circ_4]_4$ (32 layers). The maximum burst pressures were 83 MPa, 130 MPa, and 145 MPa, respectively. The results from the test were compared against split-disk tests and large-scale burst tests. The same three types of specimens were

used, cut from a manufactured pipe, using the same 12" metal cutting band-saw. These specimens included the barrier layer as well. The ring specimens for the split-disk test were 45 mm wide and were notched. The width of the notched section was 5 mm. The large-scale burst test specimens were 1200 mm long with a gauge length of 884 mm. It was observed that hoop strengths from the small-scale burst tests were within 3% of the results from the large-scale tests. The failure mode for the burst tests were reported to be primarily fibre failure in tension. The split-disk test was shown to under-predict the hoop tensile strength of the composites by more than 10%. The failure mode was a mix of delamination and fibre failure. Hence, the small-scale burst test was a reliable and representative way to test the thermoplastic composite pipes.

However, some challenges were considered. As the specimen expanded radially, it contracted in the longitudinal direction. This created a gap between the specimen and the end plates. The bladder could fail by expanding and bursting through this gap. Hence, steel plates were added to maintain the longitudinal seal between the specimen and the end plates. To maintain the seal radially, rings were added to the outer diameter to constrain the radial expansion at the ends of the specimen [35]. Under fatigue loading, certain challenges may arise, apart from the pressure cycling mechanism. A latex bladder might be susceptible to degradation under cyclic loading. Moreover, constraining the radial expansion towards the ends might lead to cyclic bending stresses at the ends of the pressurized region [32], creating matrix cracks.

Derived Concept and Calculations

The hydraulic system can be replaced with a reciprocating piston. It eliminates the need for pumps and fittings, but also introduces the challenge of sealing the piston against the cylinder. The size of the piston needed to apply the required pressure of 87.5 MPa was calculated using Equation 3.10. As an example, the applied force was limited to 100 kN, as that was the capacity of the fatigue test benches at Syensqo.

$$P_{radial} = P_{applied} = \frac{4F_{applied}}{\pi d_{piston}^2} = 87.5\ MPa \tag{3.10}$$

$$d_{piston} = \sqrt{\frac{4 \times 100000}{87.5 \times \pi}} = 38.15\ mm$$

Hence, for example, a load requirement of 100 kN means that the size of the piston must be less than 38 mm. A potential concept is shown in Figure 3.9.

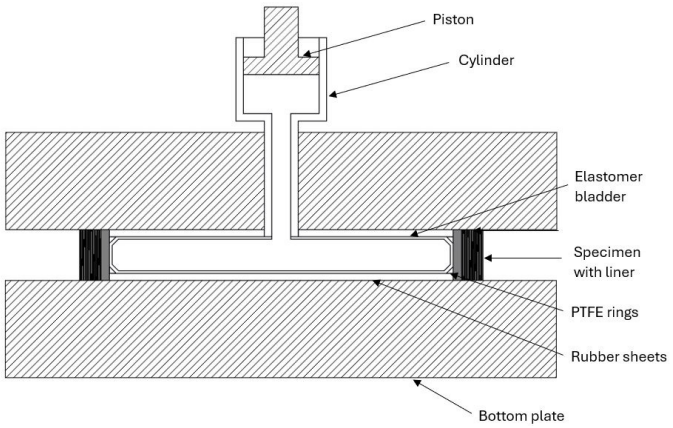

Figure 3.9: Hydraulic Piston Setup Concept

The setup comprises an elastomer bladder to contain the fluid, similar to Bujdoso and Mintzas [35]. A piston diameter of 35 mm was assumed for the following calculations, using the same equations as Equation 3.10. The effective height of the ring considered is 10 mm. However, the total height would be more to accommodate the rubber sheets and PTFE rings. These are required to maintain the seal between the plates and the specimen. Any gaps would cause the elastomer bladder to expand through

the gaps and burst. It was also recommended to prevent loading the edges which would likely have machining defects [35].

$$P_{piston} = \frac{4F_{applied}}{\pi d^2_{piston}}$$
$$P_{piston} = \frac{4 \times 100000}{\pi \times 35^2} = 103.94\ MPa$$

The piston would need sealing rings. Using Equation 3.11 and Equation 3.12, the loss due to friction from the ring was estimated. The calculations are for a ring of inner diameter, $d_{in-seal} = 32\ mm$ and height, $h_{seal} = 2\ mm$. The coefficient of friction for the interface was considered as 0.081[1].

$$F_{sealing} = P_{piston}(\pi d_{i-seal} h_{seal}) \tag{3.11}$$
$$F_{sealing} = 103.94(\pi \times 35 \times 2) = 22857.60\ N$$
$$F_{friction} = \mu F_{sealing} \tag{3.12}$$
$$F_{friction} = 0.081 \times 22857.60 = 1851.47\ N$$

The resulting applied pressure was calculated considering this friction loss. in Equation 3.13. The radial force required was then calculated from it.

$$P_{applied} = \frac{4(F_{applied} - F_{friction})}{\pi d^2_{piston}} \tag{3.13}$$
$$P_{radial} = P_{applied} = \frac{4(100000 - 1851.47)}{\pi \times 35^2} = 102.01\ MPa$$
$$F_{radial} = P_{radial}(\pi d_i h)$$
$$F_{radial} = 102.01(\pi \times 170 \times 10) = 544805.60\ N$$

The mechanical advantage ($F_{radial}/F_{applied}$) from this setup was hence 5.45. The radial displacement was calculated using Equation 3.6 - Equation 3.8. The radial displacement is hence, 0.52. The corresponding change in volume within the specimen was calculated using Equation 3.14.

$$\Delta V = \frac{\pi((d_i + \Delta d)^2 - d_i^2)h}{4} \tag{3.14}$$
$$\Delta V = \frac{\pi(171.04^2 - 170^2)10}{4} = 2785.66\ mm^3$$

An equal volume must be displaced in the cylinder by the piston. The cross-head displacement was then calculated by calculating the height reduction based on the volume displaced.

$$\Delta V_{cylinder} = \Delta V = \pi d^2_{piston} \Delta h \tag{3.15}$$
$$\Delta h = \frac{4 \times 2785.66}{\pi \times 35^2} = 2.89\ mm$$

Elastomer-Hydraulic Combination

To mitigate the high force requirements of the elastomer expansion test, a combination of the hydraulic and elastomer tests was suggested by Dr. Martin Kerschbaum (Toyota Motor Europe). A schematic of this setup is shown in Figure 3.10.

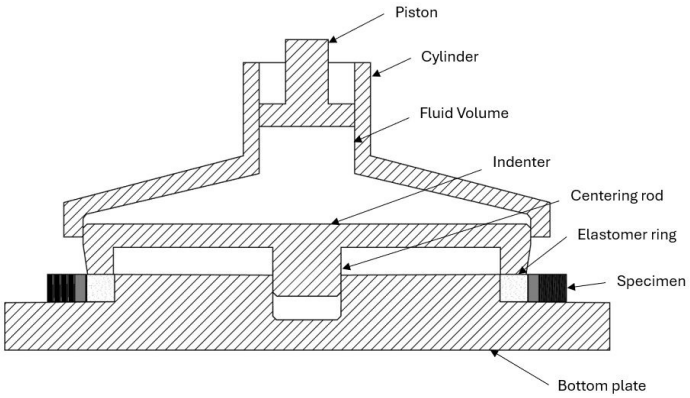

Figure 3.10: Elastomer Expansion through Hydraulic Pressure

The pressure applied by the piston would be transmitted to the indenter surface. The indenter would then push on the elastomer ring. The force applied would increase by the ratio of area of the piston to the area of the indenter. Calculations are shown for a 60 mm diameter piston. Starting from Equation 3.13, the force applied on the indenter was calculated.

$$P_{indenter} = P_{piston} = \frac{4(100000 - 1080)}{\pi \times 60^2} = 34.98\ MPa$$

$$F_{indenter} = P_{indenter} \frac{\pi d_{in}^2}{4}$$

$$F_{indenter} = 34.98 \times \frac{\pi \times 175^2}{4} = 841367.60\ N$$

To account for the friction on the indenter seal, $\mu = 0.081$[1] was considered, similar to Equation 3.11.

$$F_{sealing} = P_{indenter}(\pi d_{in-seal} h_{seal})$$

$$F_{sealing} = 34.98(\pi \times 170 \times 2) = 37363.59\ N$$

$$F_{friction} = 0.081 \times 37363.59 = 3026.45\ N$$

The pressure applied on the elastomer ring and the resulting radial pressure were calculated using Equation 3.13,

$$P_{applied} = \frac{4(F_{indenter} - F_{friction})}{\pi(d_i^2 - d_{core}^2)}$$

$$P_{radial} = P_{applied} = \frac{4(841506.94 - 3026.45)}{\pi(170^2 - 150^2)} = 166.81\ MPa$$

$$F_{radial-ideal} = 41.70(\pi \times 170 \times 10) = 890883.42\ N$$

The friction between the indenter and the elastomer were accounted for, to calculate the radial force using Equation 3.16. From which, the radial pressure was then calculated.

$$F_{radial} = F_{radial-ideal} - 2\mu(F_{indenter} - F_{friction}) \tag{3.16}$$

$$F_{radial} = 890883.42 - 2 \times 0.05(841506.94 - 3026.45) = 807035.37\ N$$

$$P_{radial} = \frac{F_{radial}}{\pi d_i h} \tag{3.17}$$

$$P_{radial} = \frac{807035.37}{\pi \times 170 \times 10} = 151.11\ MPa$$

The radial displacement was calculated using Equation 3.6 - Equation 3.8. The cross-head displacement was calculated using Equation 3.9 and then Equation 3.14 to be 26.76 mm at 100 kN of applied load. This setup gave a mechanical advantage of 8.07. This could be increased by using a smaller piston, but that would increase the cross-head displacement substantially.

3.3.2. Mechanical Setup

The segmented ring burst test setup was developed by Horide *et al.* [36] to test filament wound GRE composites. The goal was to study the fracture behaviour of the damaged specimens under internal pressure. It comprised 12 steel segments which were placed around a tapered rod, which when inserted into the segments, exerted internal pressure on the specimen. A urethane ring was placed between the segments and the specimen to avoid stress concentration. The schematic for this setup is shown in Figure 3.11. The fracture behaviour was then studied using a video camera, strain gauges, and acoustic emission.

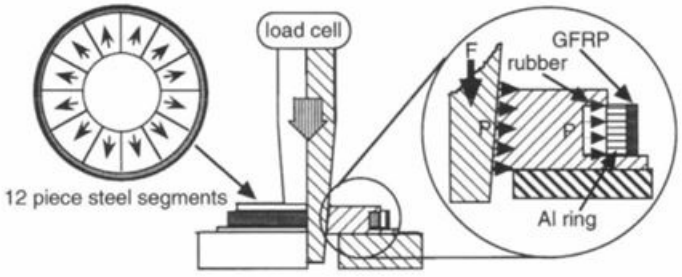

Figure 3.11: Segmented Ring Burst Test Setup [36]

Kim *et al.* [37] modified this ring burst test [36] to the study the burst strength after impact of filament-wound carbon fibre composites. 50 mm high rings were cut from a 158 mm inner diameter tube. The layup was $[\pm 18°_2, 90°_4]$. The specimens were impacted by a 3.4 g projectile, and then half the specimens were temperature cycled from $-75°C$ to $+75°C$. The rings were then tested for burst strength. The test setup comprised 24 tapered segments that were expanded by a tapered cylinder attached to the load cell. A PTFE ring was placed between the segments and the specimen to reduce friction and distribute the stresses more evenly. However, the PTFE rings were observed to bulge at the ends, causing stress concentration. Hence, the some of the specimens were made with glass fibre edge reinforcements to study the effect of this concentration on burst strength. The reinforcement was reported to reduce early failures caused by cracks along the edges of the specimens.

The ring burst setup was further developed by Kim and Kim [38] to evaluate internal pressure resistance of COPVs. The setup was first designed using a finite-element model (FEM). The hoop fracture strain was assumed to be $< 5\%$. A carbon fibre and epoxy tube was made, with a 150 mm inner diameter and 0.5 mm thickness. It was cut into 12.7 mm high rings. From the FEM, the hoop strains were estimated. These were compared against results from a hydraulic internal pressure test. It was observed that on increasing the number of segments, the error percentage reduced. This reduction plateaued beyond 24 segments. Hence, a 24-segment model was designed. Similar to [37], a PTFE ring was placed between the segments and the specimen. It was observed that increasing the thickness of the PTFE ring reduced the effect of stress concentration from the segment edges. The ring thickness that provided the least error was twice the thickness of the composite specimen. Strain gauges were placed at 120° intervals around the circumference of the specimen. The hoop strain was observed to be equal around the specimen. Hence, it was an effective test setup. It was reported that the failure initiated at the edge of the specimen, and propagated in the axial direction, bridged by delamination. The final failure was due to fibre failure across the height of the specimen.

More recently, a similar test method was developed internally at Syensqo. It was observed that under high loads, PTFE rings deformed plastically and extruded through the gaps in the segments. This caused issues with compliance of the test setup as it introduced non-linearity in the strain results. It also required a generous use of lubricant to minimize friction between the tapered rod the the segments. It was also observed that as the segments move radially outwards, the contact area between a segment and the tapered rod reduces to two line contacts. These are at the edges of the segments and it occurs due to the arc radius of the segment face being constant, while the diameter of the tapered rod increases. This creates high concentrated stresses on the tapered rod face. In cyclic loading, the effect of friction and the edge contacts will be exacerbated, affecting the compliance of the setup over the duration of the test.

Calculations

In the wedge setup, the relation between applied force and radial force was derived using free-body diagrams. The angle of the wedge, with respect to the vertical, can be decreased to increase the radial pressure applied. A maximum angle of 7° was required to clear the 100 kN threshold and 5° was chosen. The setup and its forces are shown in Figure 3.12.

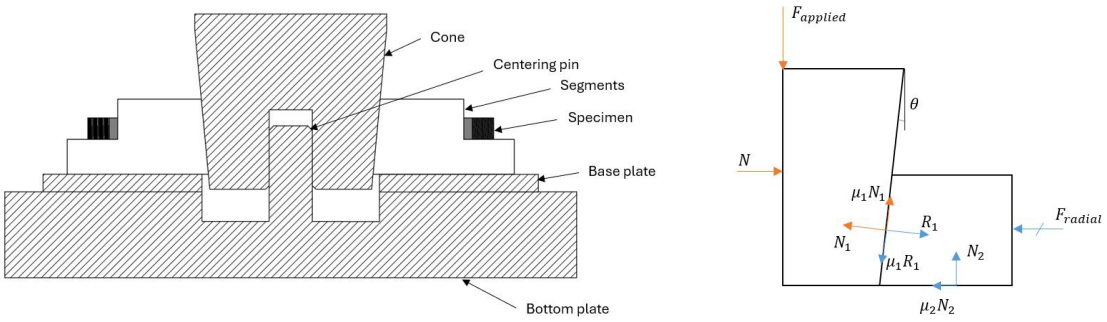

Figure 3.12: Wedge-Segment Setup and Forces

The friction coefficients μ_1 and μ_2 were assumed as 0.081[1]. Equation 3.18 was derived from Figure 3.12. It was then used to calculate the radial force and the radial pressure for a wedge angle of 5°.

$$F_{radial} = F_{applied}\left(\frac{1-\mu_1 \tan\theta}{\tan\theta + \mu_1} - \mu_2\right) \tag{3.18}$$

$$F_{radial} = 100000\left(\frac{1-0.081\times\tan(5°)}{\tan(5°)+0.081} - 0.081\right) = 581206\ N$$

$$P_{radial} = \frac{F_{radial}}{\pi d_i h}$$

$$P_{radial} = \frac{581206}{\pi \times 170 \times 10} = 105.72\ MPa$$

The mechanical advantage was 5.81. The radial expansion at 87.5 MPa was calculated from the hoop stress, as per Equation 3.6 to Equation 3.8. The corresponding cross-head displacement was calculated using Equation 3.19.

$$\Delta h = \frac{\Delta r}{\tan\theta} \tag{3.19}$$

$$\Delta h = \frac{0.52}{\tan(5°)} = 5.94\ mm$$

3.4. Exploring Other Disciplines

Apart from standard tests and non-standard tests, other mechanisms that could be used for radial expansion were explored. These are mechanisms used from other disciplines that a test setup concept can be either directly or indirectly based off of.

3.4.1. CVT (Cones)

From the automotive industry, drum brake and continuously variable transmission (CVT) mechanisms were studied. In a drum brake, hydraulic pressure is used to push twin brake shoes against a rotating drum. In principle, it would work as a split-disk test [7], but actuated by hydraulic pressure. Hence, it would face the same issues of bending and friction. However, it would make it possible to apply substantially higher internal pressures to the specimen for the same applied load. Sealing the hydraulic system and cycling the pressure would still be a challenge.

A CVT assembly uses two pairs of cones that are connected by a belt. The cross-section of the belt is V-shaped to conform to the surface of the wedges. The wedges can move towards or away from

one-another, changing the diameter of the belt, creating a continuous transition between gear ratios. A setup, inspired by this, can be imagined using a single pair of circular wedges mounted on an electromechanical test bench, along their axis. One of the wedges would be fixed, while the other would reciprocate. The specimen would be pushed radially outwards at the edges by the wedge surfaces. However, this will cause bending along the specimen's cross-section. To mitigate this, an elastomer core, between the wedges can be used to apply internal pressure just at the centre of the specimen. A polymer ring, such as the liner, can be used at the top and bottom edges of the specimen, similar to [35], to prevent extrusion of the elastomer through any gaps that may form. The concept is shown in Figure 3.13.

Increasing the angle of the cone, with respect to the horizontal, increases its load applying capability. A minimum angle of 72° was required to cross the threshold and 75° was used. The forces are shown in Figure 3.13. To support the central part of the specimen and prevent it from bending inwards, an elastomer disk could be used to fill the gap between the cones.

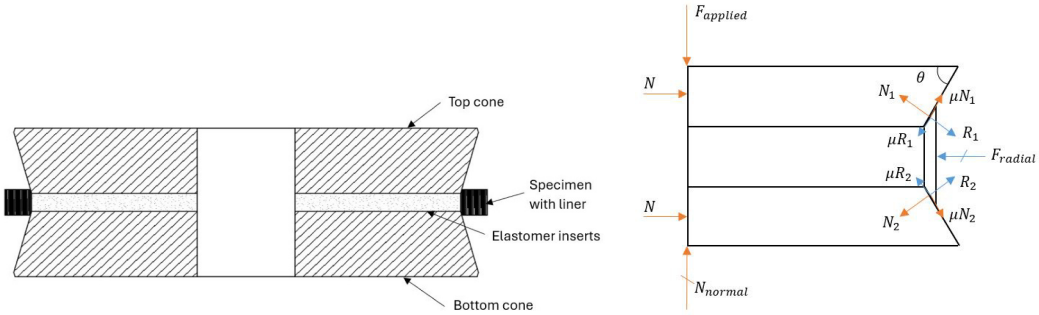

Figure 3.13: Cones Setup and Forces

From Figure 3.13, Equation 3.20 was derived. It was used calculate the radial force and then pressure applied on the specimen. The friction coefficient, μ was assumed to be 0.081[1].

$$F_{radial} = 2F_{applied}\left(\frac{1-\mu\tan\theta}{\tan\theta+\mu}\right) \tag{3.20}$$

$$F_{radial} = 2\times 100000\left(\frac{\tan(75°)-0.081}{1+0.081\times\tan(75°)}\right) = 560709.77\ N$$

$$P_{radial} = \frac{560709.77}{\pi\times 170\times 10} = 104.99\ MPa$$

Hence, the mechanical advantage was 6.21. The cross-head displacement was calculated from the radial expansion, similar to Equation 3.19.

$$\Delta h = \frac{2\times 0.52}{tan(15°)} = 3.45\ mm$$

3.4.2. Umbrella Hinge

An umbrella-like setup was proposed by Prof.dr.ir. René Alderliesten. Rods would extend radially from a central hinge. The rod end towards the specimen would be hinged at segments that will be pushed radially outwards as load is applied by the cross-head. The setup would be symmetric along the specimen's plane. This would add the reaction force generated by the cross-head, doubling the radial load application capability of the setup. It would apply high radial pressures for the same applied load, compared to the aforementioned ring burst test [36]. It would also eliminate the problem of friction. From initial calculations, for it to be effective, the initial angle of the rods must be 20° from the horizontal, or lower. An illustration of this is shown in Figure 3.14.

A potential risk would be that any misalignment between the top and bottom hinges would generate a couple and destabilize the setup. At high applied loads, this could be unsafe. To resolve this half the

setup could be used, with the segments sliding on a flat surface. The required angle would then be 14°, or lower. However, this would reintroduce the friction problem. It is shown in Figure 3.15.

In the umbrella setup, the applied load is transferred from a central hinge to the segments through pushrods. As the pushrods would be hinged, they would only experience compression. The free-body diagram is also shown in Figure 3.14.

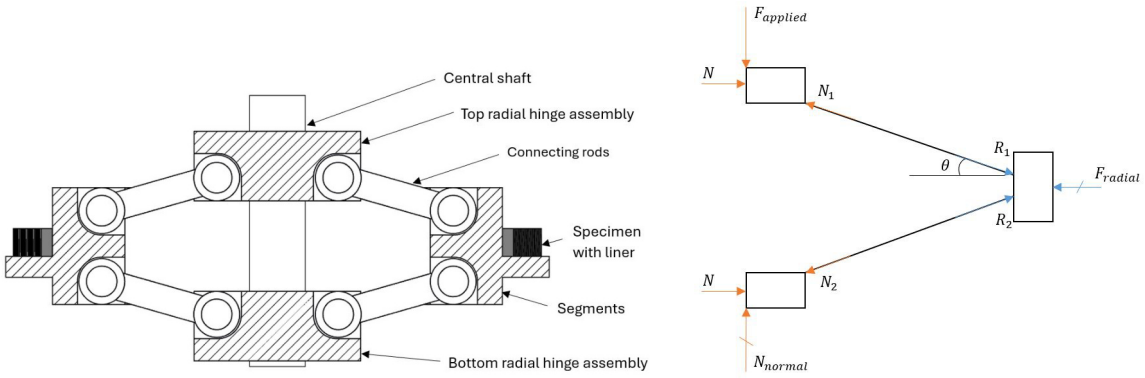

Figure 3.14: Umbrella Setup and Forces

Based on the forces shown in Figure 3.14, the relation between applied force and radial force was drawn in Equation 3.21.

$$F_{radial} = \frac{2F_{applied}}{\tan\theta} \tag{3.21}$$

Due to the challenges with this setup in section 3.4, the half-umbrella setup was designed. The setup and forces are shown in Figure 3.15.

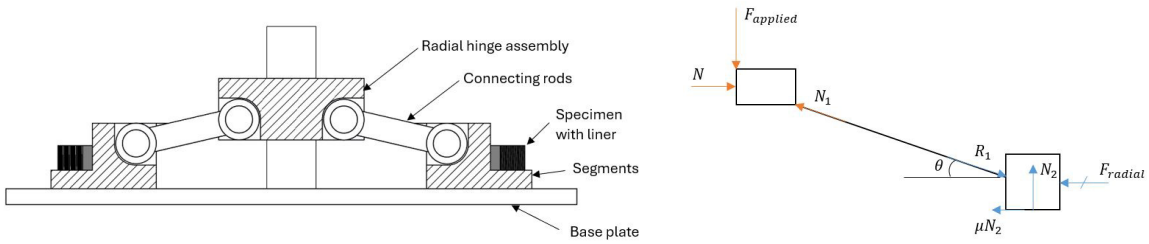

Figure 3.15: Umbrella Setup and Forces

Equation 3.22 was derived from Figure 3.15. It was used to calculate the force, pressure, and displacements as in previous setups. The coefficient of friction, μ was 0.081[1].

$$F_{radial} = F_{applied}\left(\frac{1}{\tan\theta} - \mu\right) \tag{3.22}$$

Equation 3.21 and Equation 3.22 were solved iteratively to get the curves shown in Figure 3.23. As the radial force was inversely proportional the tan of the angle of the pushrods with respect to the horizontal, the forces would increase as the angle decreased. The initial angles for the umbrella and half-umbrella setups were 20° and 14°, respectively. With these angles, the mechanical advantage for the umbrella setup ranges from 5.45 – 6.46, and for the half-umbrella, from 3.93 – 5.35. The file created for all the calculations is in subsection A.1.1.

3.4.3. Camera Aperture

A concept similar to camera apertures was also imagined. Apertures work by moving segments along a groove as their plane is rotated. The segments are shaped to roughly form a circle at each stage of

the aperture setting. They are hinged at a back-plate slide over one-another to adjust the aperture. A reverse mechanism can be imagined, where the outer faces of the segments form a circle. A grooved plate that controls their motion could be attached to a torque tube. As torque is applied to the plate, the segments are pushed along the groove and slide over one-another to expand radially. The challenge of the setup would again be friction between the plates and segments, and between the segments themselves. They would be supported only at two points, the hinge and the groove. When they expand the unsupported section would bend between them. This would lead to the segments having increased thickness, making it a challenge to fit them over other the segments. The expansion, being more at the free edge, would also cause a more polygonal expanded shape than a circular one, causing bending and stress concentration in the specimen.

3.4.4. Cam Lobe

A cam-roller setup to push segments radially outwards can also be used. It would use torque to rotate a cam disk. The cam lobe height would determine the applied increase in diameter, resulting in a constant applied radial pressure. The lobe height can be calculated based on the pressure requirement. Friction would affect this setup as well. Apart from that, the normal force at the contact would be in the direction of the pressure angle, creating a moment. It would need an additional plate to react that moment, else it would cause each segment to rotate in-plane. The setup would not be versatile and it would also not account for the change in compliance of the specimen during the test. A schematic is shown in Figure 3.16.

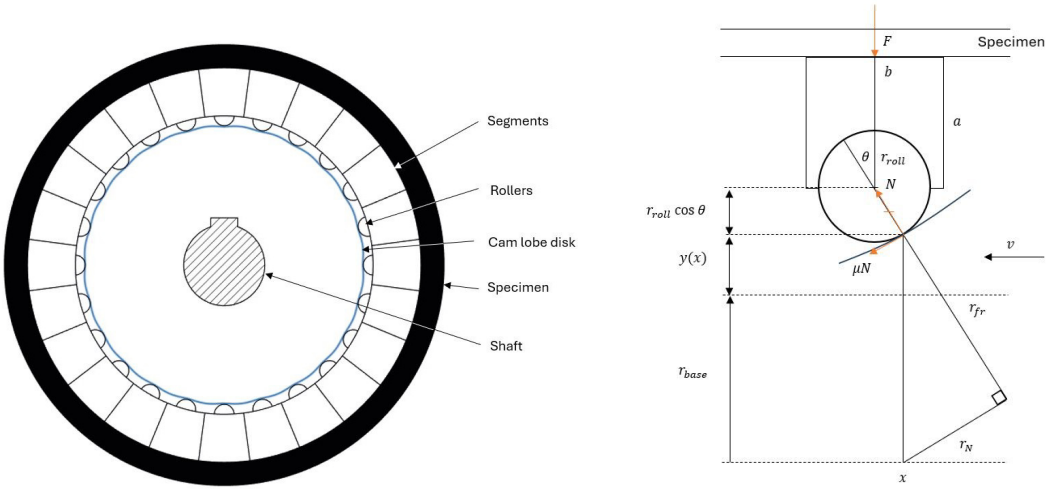

Figure 3.16: Cam-roller Setup and Forces

The cam-lobe setup, shown in Figure 3.16, was designed to apply 87.5 MPa of radial pressure. The height of the lobe required was back-calculated from this pressure. The equation used for lobe profile is shown in Equation 3.23.

$$y(x) = h_{lobe}\, e^{\frac{-x^2}{r_{base}\phi}} \tag{3.23}$$

In the equation, h_{lobe} was the peak height of cam lobe calculated, r was the radius of the base circle, and ϕ was the sweep angle of each lobe. To calculate the lobe height required, Equation 3.6 - Equation 3.8 were used. The sweep angle and arc length were calculated for 24 segments and a base circle diameter of 60 mm. The lobe profile $y(x)$ is shown in Figure 3.17 (a). As the roller would move over the cam profile, the slope of the profile at the point of contact would be given by dy/dx. This would define the pressure angle (θ), shown in Figure 3.17. This pressure angle would create a moment around the rest of the roller segment, pushing into the specimen on one side. The relation between the applied force and the reaction was derived to be Equation 3.24.

$$N = \frac{F}{cos\theta - \mu sin\theta} \tag{3.24}$$

The applied force was calculated from the hoop stiffness of the specimen. This would depend on the radial extension corresponding to $y(x)$. It can be observed that the tangential (horizontal) forces were not balanced. In the design, as the segments would expand, they would no longer be in contact with each other, allowing them to rotate under the tangential component of the force due to the pressure angle. Hence, an additional fixture, such as a groove would be needed to react this bending moment.

Assuming that the unbalanced forces would be reacted externally, the torque required was calculated for a 10 mm high specimen using Equation 3.25. The distribution over the arc length shown in Figure 3.17.

$$\begin{aligned} r_F &= (r_{base} + y(x)) \cos\theta \\ r_{fr} &= (r_{base} + y(x)) \sin\theta \\ T &= (rF + \mu r_{fr})N \end{aligned} \tag{3.25}$$

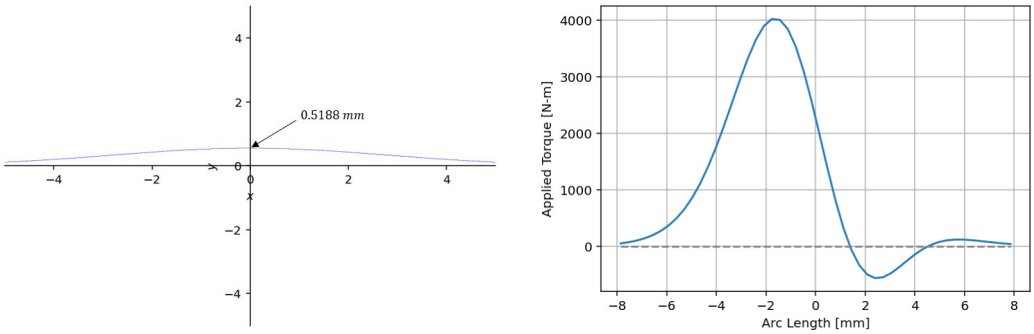

(a) Lobe Profile **(b)** Torque Required

Figure 3.17: Cam Lobe Setup (subsection A.1.2)

It requires almost 4000 Nm of torque to expand 24 segments. This can be reduced by reducing the base circle diameter of the cam. However, this would increase the reaction moment that would be applied on specimen due to the pressure angle.

Cam-Umbrella Combination

To overcome the high torque requirement of the cam lobe setup, an amalgamation of the cam and umbrella setups was devised. It also solved the problem of the complex hinge design by eliminating it from the design. It comprised 24 rocker arms hinged towards the specimen. It would be pushed down by a plunger, rotating the arm around the hinge. The short side of the arm would have a cam lobe, gradually increasing in height. A schematic is shown in Figure 3.18.

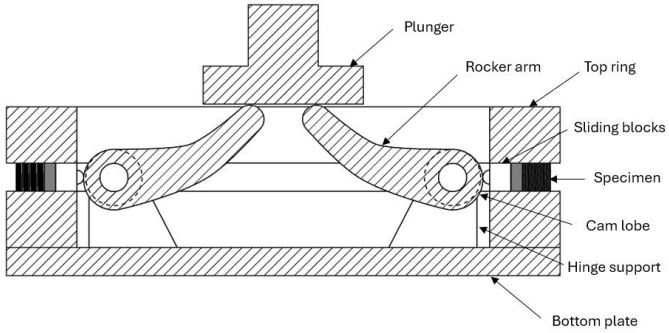

Figure 3.18: Cam-Rocker Arm Setup Concept

Similar to the cam-lobe design, the torque required was calculated. In this case, the lobe profile was chosen to be a linear one, such that it could be used for both fatigue and burst tests. The equation used

for the profile is shown in Equation 3.26.

$$y(x) = \frac{h_{lobe}}{r_{base}\phi}x \tag{3.26}$$

The height of the lobe required for the fatigue test was 0.52 mm, as calculated before. For the burst test, the required radial pressure was 157.5 MPa. Following Equation 3.6 to Equation 3.8, the lobe height required was 0.93 mm. The forces are shown in Figure 3.19.

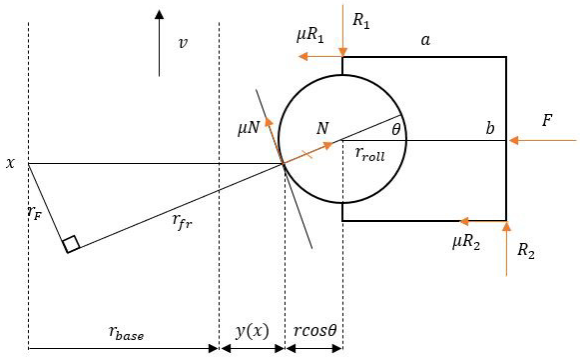

Figure 3.19: Cam Rocker Arm Forces

The horizontal and vertical forces, and the bending moments were balanced. For the bending moments, the segment was approximated to a beam and hence, only the out-of-plane forces were considered. The below equations were derived from Figure 3.19.

$$N(\cos\theta - \mu\sin\theta) = F + \mu(R_1 + R_2)$$
$$N(\sin\theta + \mu\cos\theta) = R_1 - R_2$$
$$R_2 a = N(\sin\theta + \mu\cos\theta) r_{roll}\cos\theta$$

They were solved to derive the relation between the applied force and the normal force, shown in Equation 3.27.

$$R_2 = N(\sin\theta + \mu\cos\theta)\left(\frac{r_{roll}\cos\theta}{a}\right)$$
$$R_1 = N(\sin\theta + \mu\cos\theta)\left(1 + \frac{r_{roll}\cos\theta}{a}\right)$$
$$N = \frac{R}{\cos\theta - \mu\sin\theta - \mu\left(1 + \frac{2r_{roll}\cos\theta}{a}\right)(\sin\theta + \mu\cos\theta)} \tag{3.27}$$

With the linear curve used, the slope and hence, the pressure angle (θ) could be reduced by increasing the maximum sweep angle (ϕ). For a base circle radius, r_{base} of 15 mm, roller radius of 5 mm, and specimen height of 10 mm, the required torque was calculated using Equation 3.25. The torque that could be applied was calculated considering a rocker arm length of 35 mm. The comparison is shown in Figure 3.20.

To reach the burst test pressure of 157.5 MPa within 100 kN, the sweep angle required was 45°. The dotted line corresponds to the fatigue test pressure limit, which was reached at 25°.

At the 45° limit, the cross-head displacement was calculated using Equation 3.28.

$$\Delta h = l_{arm}\sin\theta \tag{3.28}$$
$$\Delta h = 35 \times \sin(45°) = 24.75\ mm \tag{3.29}$$

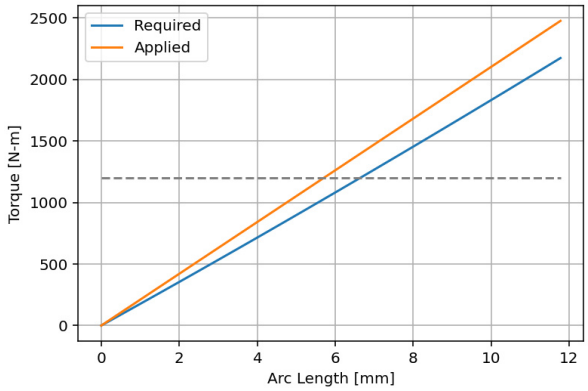

Figure 3.20: Torque Required for the Cam-Umbrella Setup (subsection A.1.2)

The radial displacement of the arms towards the centre of the setup was given by Equation 3.30.

$$l_{arm}(1 - \sin\theta) = 10.25\ mm \tag{3.30}$$

The gap from the centre with the dimensions used was 25 mm. Hence, this could be accommodated. However, to prevent interference due to the thickness of the rocker arms, they would have to be tapered towards the centre.

3.4.5. Storm Surge Barrier Bearing

A concept was also derived from the bearing design of the Maeslantkering storm surge barrier [39]. The bearing uses multiple ultra-high molecular weight polyethylene (UHMWPE) discs, which are each constrained radially by a CF composite ring. The purpose of the UHMWPE discs is to provide a low friction contact, while the composite ring limits the plastic radial deformation of the discs. A test setup can be used where the disc is compressed to load the specimen. using a spherical indenter. The curvature of the indenter ensures its alignment. It also creates a small component of force acting in the radial direction. In principle, it is similar to the elastomer compression test, detailed in [28]. The forces required are also the same. The concept is shown in Figure 3.21

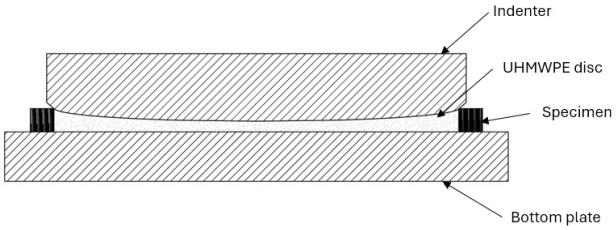

Figure 3.21: Disc Compression Setup

There were two concerns with this setup. First, compressing a 170 mm disc to apply a radial pressure of 87.5 MPa would require 1986.08 kN, as estimated in Equation 3.5. Only the 3500 kN test bench would be capable of performing the fatigue test, while the burst test would not be possible. Second, if a UHMWPE disc is used, it would deform plastically, changing the setup's behaviour in subsequent cycles. Despite its simple construction, the high force requirement meant this was not a feasible option.

The estimations were confirmed by Prof.dr.ir. Wim van Paepegem. A concept was developed in where the effect of the indenter's curvature was studied. It was concluded that the alleviation in force was minimal. It was also mentioned by Prof. Wim that the composite ring in this bearing design was observed to curl when expanded under pressure. It induced through-thickness shear stresses in the composite, which caused matrix failures. In section 5.2, the effect of shear stresses was considered and addressed in section 6.2.

3.5. Assessment

The setups were judged based on their performance, feasibility, and trade-offs. They are shown again in Figure 3.22, for reference.

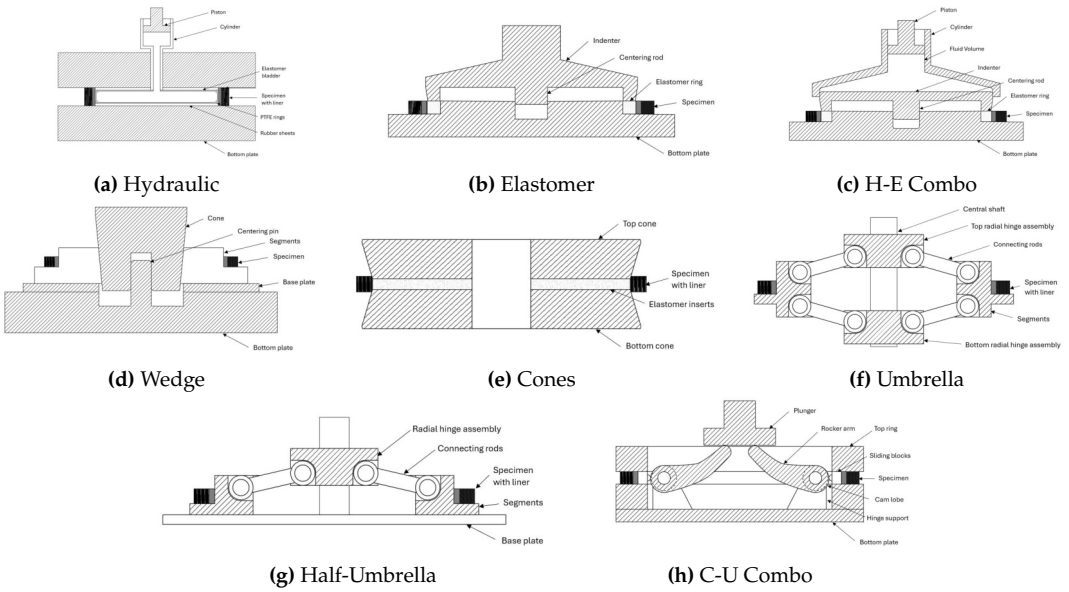

(a) Hydraulic **(b)** Elastomer **(c)** H-E Combo

(d) Wedge **(e)** Cones **(f)** Umbrella

(g) Half-Umbrella **(h)** C-U Combo

Figure 3.22: Test Setup Concepts

3.5.1. Performance

The performance of each potential test setup was determined based on initial calculations. It was essential to see if the setups could meet the 87.5 MPa internal pressure requirement. For comparison, a 100 kN force limit was used for the fatigue tests. The specimen height considered was 10 mm. Assumptions made for the calculations were,

1. The specimen's material is linear-elastic and isotropic, with E = 68.44 GPa.
   Note: It was the E_{xx} of the COPV layup in Table 4.4, calculated using CLT. As the layup was 13.3 mm thick, it was only an approximation.
2. The specimen only deforms in the hoop direction. Out-of-plane and transverse stresses are neglected.
3. The radial load applied in each test is distributed equally to the specimen with a 170 mm inner diameter. The polymer liner is ignored.
4. The hoop pressure is estimated from the radial pressure by approximating the specimen to a thin-walled pressure vessel. The relation between the internal radial pressure and hoop stress is $\sigma_\theta = \frac{Pd}{2t}$, where d is the mean diameter of the specimen.
5. The weights of the individual components are reacted by the test bench and are neglected in the calculations. For hydraulic setups, any losses are neglected.
6. The kinetic friction coefficient, where applicable, was 0.081 for Steel-Steel lubricated interfaces and 0.05 for Steel-Polymer interfaces[1].

The results for a 10 mm-high specimen are shown in Figure 3.23. For the hydraulic setup, the cross-head represents a piston. They are calculated iteratively using the equations in the previous sections.

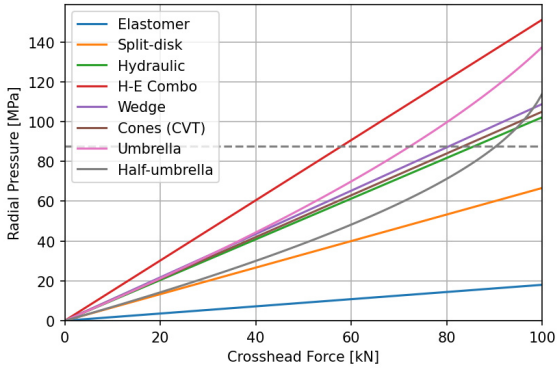

(a) Force Required to Apply 87.5 MPa Radial Pressure

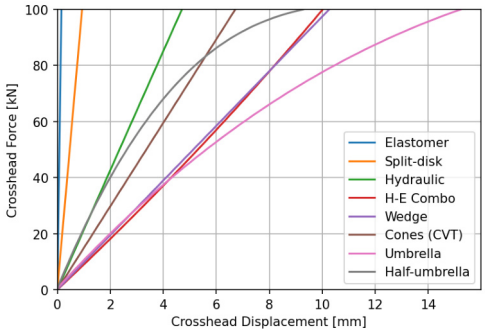

(b) Corresponding Displacement Required

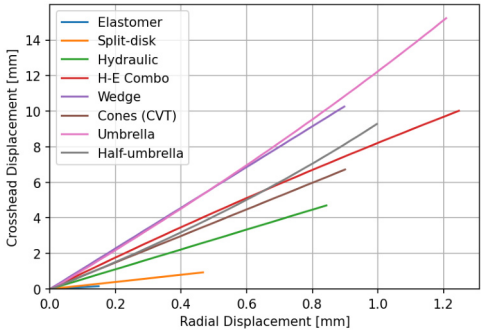

(c) Resultant Radial Expansion

Figure 3.23: Calculated Results for a 10 mm-high Specimen (subsection A.1.1)

3.5.2. Feasibility

The potential challenges and concerns that accompany each concept were assessed. The feasibility was judged based on the complexity of the parts, setup, and materials. These parameters affect the lead time and were crucial to determine whether the development could be completed within the time-frame of the master thesis.

Hydraulic Internal Pressure

This setup would apply uniform pressure across the circumference. The edges would not be pressurized. The short overhangs could minimize the bending. However, there were significant concerns were there regarding the durability of elastomer bladder. There were commercial options to have custom-moulded latex bladders, as they are used regularly for composite part manufacturing. In this process, they are heated and pressurized, but they can only be used for 3 to 5 cycles[2].

Sealing the piston effectively is another challenge. However, off-the-shelf automotive brake systems can also be repurposed for this use. Lastly, how quickly the piston can release the pressure after failure would be crucial for the bladder to not burst under pressure when the specimen fails. Hence, it can be used in burst tests, but for fatigue tests, the durability of the latex bladder under cyclic pressure is not sufficient. This made the concept unviable for a fatigue test.

Elastomer Expansion

The concept seems feasible as it has fewer parts and they can be machined on a lathe. However, the effectiveness of elastomer under cyclic loading needs to be studied before this can be implemented. The initial assumption is that even though the elastomer expands radially, it is still in hydrostatic compression between the pushrods and the specimen. This should prevent crack formation and propagation. Moreover, the scale of radial expansion would be in the $100s$ of microns, further impeding opportunities for crack formation.

[2] https://www.piercanusa.com/natural-rubber-latex-bladders

Further, compared to the split-disks, the design of the pushrods do not need to have holes. This removes areas of stress concentration. This, combined with predominantly compression-compression loading cycles experienced by the pushrods, would ensure the setup does not fail in fatigue.

A challenge foreseen is that the elastomer can squeeze out around the specimen as it is compressed. In the concept, a tapered face is used to reduce the gap that might be created. The actual setup would require careful design choices for it to be effective. Regardless, this was a promising concept.

Hydraulic-Elastomer Combination

The setup poses the combined challenges of the hydraulic and elastomer setups, namely sealing. Using a standard-sized piston would allow the use of off-the-shelf parts, alleviating sealing issues at the piston. However, sealing the indenter against the cylinder would be challenging. Offsets due to orientation and alignment of the indenter can cause further gaps and hence, leakage.

Wedge-Segment

This setup had the benefit of being easy to setup and perform. It was also completely mechanical. However, it was held back by friction. The high number of sliding surfaces and sliding distances would make the parts wear out. To manufacture the components, electrical discharge machining (EDM) would have to be used, which is time-consuming and expensive. At 24 segments, a 5% error in hoop strain would be expected [38].

Cones

A concern with this setup was friction and wear of the components. The setup relies on a polymer ring to transfer the loads from the cones to the specimen. The polymer ring could squeeze through any gaps between the cones as the specimen contracts along its axis. It would also depend on the alignment and orientation of the cones. Lastly, the load was being applied through the edges of the specimen, which is where the machining defects would be. This could affect the results of the test by causing premature failure of the specimen. However, the setup was easy to manufacture, assemble, and test. The mechanical advantage could be increased by bringing the angle closer to 90°, but this would increase the cross-head displacement, creating a risk of the setup bottoming out.

Umbrella

Some challenges could be foreseen with both variations of this setup, stemming from space constraints from the 170 mm inner diameter of the specimen. At a 100 kN of cross-head load, an 11 mm bolt would be needed to withstand the high shear stresses at the hinge. The space constraint would limit the number of rods that could be accommodated in the central hinge to 6. The rod diameters would then have to be at least 10 mm to prevent buckling in fatigue and burst tests. Moreover, the hinge design would also need to avoid sharp design features that could lead to stress concentrations, causing failure of the setup during fatigue tests. Lastly, to minimize the variation in hoop strain around the circumference, 24 segments would be needed [38].

Apart from its complexity and limitations, beyond a certain angle, the force increased exponentially as setup bottomed out, flattening the hinges. It would also apply a variable loading rate to the specimen, accelerating the hoop strain rate at the higher stresses. This could under-predict the fatigue life of the specimen.

Cam Lobes

The cam-lobe design required 4000 Nm of torque. Applying it through a shaft would be impractical. A screw setup can be used that uses a worm gear pushed axially to generate torque. However, this would lead to immense friction and wear and still be impractical.

The can-umbrella combination was an improvement upon the cam lobe design. Although this setup was versatile, it would require complex machining and precise tolerances, increasing the manufacturing time. It could extend beyond the timeline of the thesis. Apart from these challenges, it would introduce a hoop strain error, similar to other segmented ring burst tests [38]. It would also suffer from friction and wear of the sliding surfaces.

3.5.3. Summary

The setups were ranked based on their performance, accuracy, and complexity. The study is presented in Table 3.2. Explanation for each row is mentioned below.

Table 3.2: Trade-off Table Column Descriptions

Column	Description
Governing Parameter	Relevant design values that affect each setup's performance
Mechanical Advantage	Ratio of radial force to cross-head force
Friction loss%	Reduction in radial force applied to the specimen due to sliding friction (estimated by neglecting friction)
Hoop Strain error%	Expected error in hoop strain for segment-based tests, estimated from [38] and [20]
Design Complexity	Complexity of the part and assembly design based on features, connections, tolerances, and materials (1 - low, 5 - high)
Manufacturing Complexity	Estimated time to manufacture based on machining processes required (1 - low, 5 - high)
Setup Complexity	Expected ease of setup assembly, data acquisition preparation, testing, foreseen risks, and disassembly (1 - low, 5 - high)
Wear Volume	Estimated wear volume of the setup for 22,000 loading cycles, based on sliding distance and normal force at the sliding interface
Average Rank	Weighted average rank of each setup based on the afore-mentioned parameters

Additional parameters from which the complexities and wear volumes were estimated are shown in subsection A.1.3. These were not shown for brevity. The trade-off table is shown in Table 3.3.

Each column was given a weight based on the priorities for this thesis. It was decided not to limit the test to 100 kN if it would lead to a more complicated setup. Hence, the machine limit was given less weight. The hoop strain error was given more weight as it was important to have uniform strain distribution around the circumference. Localized high strains due to segments would create areas of stress concentration and adversely affect the fatigue life. The manufacturing complexity had more weight owing to the time constraint of this project. Similarly, to prioritize the longevity of the setup, the wear volume was given more weight.

Table 3.3: Trade-off Table (subsection A.1.3)

	Weight	0.5	1.5	2.0	1.0	2.0	1.0	2.0	
Test Setup	Governing Parameter	Mechanical Advantage	Friction loss%	Hoop Strain error%	Design Complexity (1 - 5)	Manufacturing Complexity (1 - 5)	Setup Complexity (1 - 5)	Wear Volume per 22000 cycles $[mm^3]$	Average Rank
Elastomer	$d_{core} = 150\ mm$	0.96	-10%	0%	2	2	2	0.85	**3.45**
Cones	$\theta = 15°$	6.21	-20%	5%	3	2	5	0.72	3.85
Hyd.-Ela. Combination	$d_{piston} = 60\ mm$, $d_{core} = 150\ mm$	8.07	-12%	0%	4	4	5	0.10	4.15
Wedge [38]	$\theta = 5°$	5.81	-97%	5%	3	4	2	2.71	4.75
Hydraulic	$d_{piston} = 35\ mm$	5.46	-2%	0%	4	4	5	0.87	5.40
Split-disk [18]	NA	0.89	-12%	20%	1	3	1	5.59*	5.45
Cams	$\phi = 45°$	8.38	-107%	5%	5	5	4	1.54	5.45
Half-umbrella	$\theta_{initial} = 14°$	5.35**	-3%	12%	5	5	4	0.02	6.15
Umbrella	$\theta_{initial} = 20°$	6.46**	0%	12%	5	5	5	0.00	6.35

* Wear of the specimen.
** At 100 kN. Mechanical advantage increases with decrease in θ.

Based on the ranking, the elastomer test was the first choice. In terms of design, the parts would not be complex and could be machined with standard turning and milling operations. The tolerances required between the specimen's inner diameter and the indenter surface would have to be 0.81 mm [29]. The elastomer material and hardness must also be able to withstand the cyclic applied pressure. Lastly, the test would need a 500 kN machine to perform the fatigue test and a 1000 kN test bench for the burst test.

3.6. Inherent Challenges

Testing a ring specimen could introduce challenges inherent to its geometry and material. These would affect the results regardless of the test setup. Hence, they might need to either be mitigated during the test, or corrected for while processing the results after the test.

3.6.1. Stress State

Under internal pressure, a pressure vessel experiences both hoop and axial stress. The axial stress is reacted by the ends of the vessel. The area of the fluid volume and the cross-section area of the pressure vessel at its cylindrical region are given by Equation 3.31 and Equation 3.32, respectively.

$$A_{fluid} = \frac{\pi d_i^2}{4} \tag{3.31}$$

$$A_{pv} = \frac{\pi((d_i + 2t)^2 - d_i^2)}{4} = \pi t(d_i + t) \tag{3.32}$$

For a thin-walled pressure vessel, when $d \gg t$. Then, equating the force acting on the fluid volume to the force reacted by the vessel's cap, Equation 3.33 can be derived for the axial stress on the pressure vessel's cross-section.

$$\begin{aligned} A_{pv} &= \pi dt \\ PA_{fluid} &= \sigma_z A_{pv} \\ P\frac{\pi d_i^2}{4} &= \sigma_z(\pi d_i t) \\ \sigma_z &= \frac{Pd_i}{4t} \end{aligned} \tag{3.33}$$

Similarly for hoop stress, for a length l, Equation 3.34 can be derived for the hoop stress in the pressure vessel.

$$\begin{aligned} P(d_i l) &= \sigma_\theta(2tl) \\ \sigma_\theta &= \frac{Pd_i}{2t} \end{aligned} \tag{3.34}$$

The vessel walls will also experience radial stress. However, for a thin-walled vessel, the t/d_i ratio will be low, and hence, the radial stress would be negligible compared to the hoop and axial stresses.

The axial stress in a pressure vessel would also lead to axial strains and Poisson's ratio contraction. Hence, in an actual vessel, the hoop strain for the same internal pressure would be,

$$\epsilon_\theta = \frac{1}{E}(\sigma_\theta - \nu_{12}\sigma_z) \tag{3.35}$$

Hence, in a complete vessel, the wall would experience a biaxial stress state and its radial expansion will be affected by the Poisson's contraction. However, in the test setups shown in section 3.5, the specimen will only experience a hoop stress. Due to the lack of any axial constraints, the hoop strain and radial expansion for the same internal pressure would also be more compared to a pressure vessel. This slightly higher strain might result in the test slightly under-predicting the fatigue life. However, this could be corrected for by reducing the applied pressure by a factor, considering the layup, to match the radial expansion of the complete vessel.

3.6.2. Edge Machining Effects

In composites, the alternating high-stiffness fibres and low-stiffness matrix leads to a machined surface that is rough. Traditional machining processes can also leave critical defects in the composite such as delamination, fibre splinters, and matrix cracks [40]. The specimens for the fatigue test would be cut from a hoop-wound AFP tube. Even though it is hoop-wound, the winding angle would be around $\pm 85° \; to \; 87°$. In every alternate layer, the cut would either be slightly along or against the fibre direction. For the validation tests, the specimens would be cut from a composite tank, which would have hoop-wound as well as $\pm 55°$ layers.

Ramulu [40] observed that when machining along the fibre direction, the fracture was along the fibre-matrix interface. As the tool progressed, the bending of the fibres caused fibre failure perpendicular to cut's direction. For off-axis directions, fibre fracture was due to compression, and cracks along the fibre-matrix interface were induced due to inter-laminar shear. The most damage was observed when cutting against −45° layers. It caused fibre fracture perpendicular to the fibre direction and extensive shear failure along the fibre-matrix interface. The various mechanisms are shown in Figure 3.24.

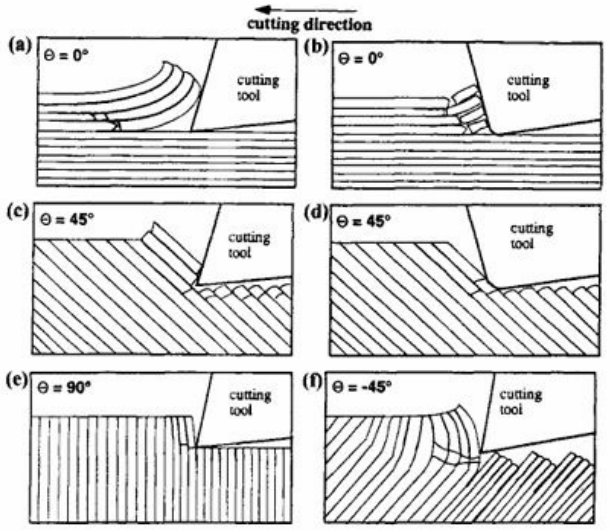

Figure 2. Cutting mechanisms in the orthogonal machining of Gr/Ep. (**a**) Delamination; (**b**) fibre buckling; (**c**) & (**d**) fibre cutting; (**e**) deformation; (**f**) shearing.

Figure 3.24: Damage from Machining Along Different Fibre Orientations [40]

ASTM D3039/D3039M-17 [11] recommends the use of abrasive water-jet or Polycrystalline Diamond (PCD) tools for machining specimen edges. It mentions that rough or uneven surfaces must be avoided. It also advises against inappropriate methods that may cause delamination in the specimen.

Ghidossi *et al.* [41] studied the effect of varying machining parameters on the strength of GRE specimens. Flat notched specimens were produced for Iosipescu tests and ring specimens were made for ring tensile tests. For the rings, side-milling, end-milling, or grinding was done using three different tool materials - Carbide, PCD, and Diamond-coated Carbide. Different machining parameters such as tool rotation speed and feed rate were varied and the surface quality of the resulting specimens were studied under a scanning electron microscope. The performance of the specimens were then tested using the respective Iosipescu and tensile tests. However, it was concluded that no correlation could be drawn between visible surface damage and mechanical performance. This was contrary to what was stated in the ASTM standard [11]. This was attributed results being affected more by damage that had propagated within the specimen and could not characterized from a surface study [41].

Since thermoplastic composite specimens were being used in this project, surface observations could be misleading. As the specimen would be cut, thermoplastic matrix could melt and reform, filling any gaps left by the machining process. This would make the surface appear relatively defect-free. It would also cover up the damage that would have propagated through the depth of the specimen.

Moreover, inherent AFP defects such as gaps, porosities, or delamination could be exacerbated by the machining process used. An ultrasonic scan of the source tube or vessel would therefore be necessary to account for this. The choice of the section location at which the spcimen would be cut from could also affect its properties. Such as, if the location of the fibre overlap area falls on the edge or in the centre of the specimen. The latter could lead to a reinforced edge in case of an overlap, but a weaker edge if there is a gap.

3.6.3. Free-Edge Effect

Pipes and Pagano [42] analysed inter-laminar stresses in laminates under uniaxial tension. It was to study how shear stresses are transferred between layers. An infinite laminate under uniaxial tension would experience a constant axial (σ_x) and shear stress (τ_{xy}). However, for a finite laminate, these stresses must be zero along the free edge. According to the solution from Pipes and Pagano [42], the inter-laminar shear stress (τ_{xz}) increases exponentially near the edges, up to a width equal to the laminate thickness. The distribution across the half-width (b) of the laminate is shown in Figure 3.25. This inter-laminar shear stress existed within the laminate, and zero at the mid-plane and the free surfaces.

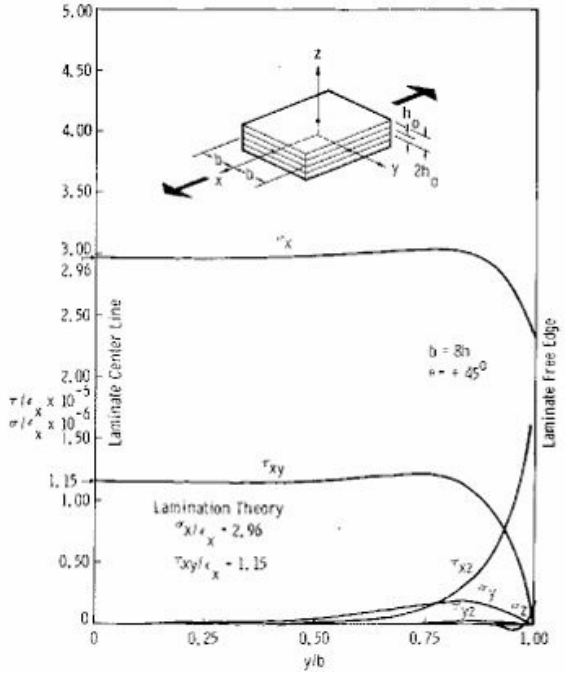

Figure 3.25: Distribution of Stresses along the Laminate Width [42]

The inter-laminar shear stress would cause an additional axial displacement in the direction of the tensile displacement. This would vary across the thickness of the laminate. It would also vary with the layer orientation, as shown in Figure 3.26.

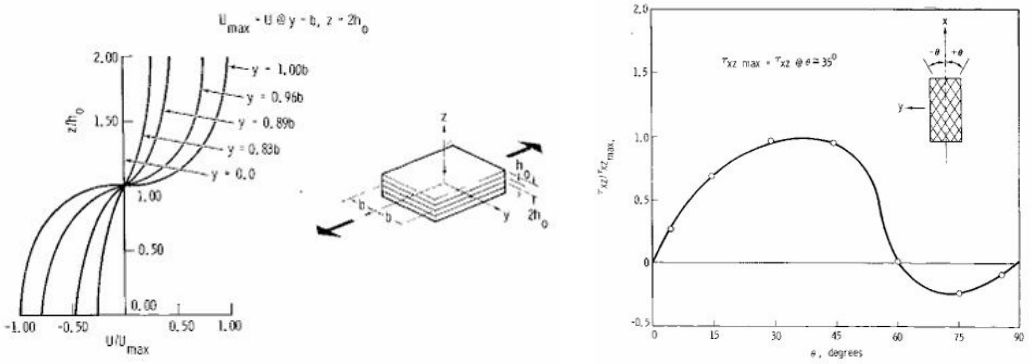

(a) Axial Displacement Caused along Thickness **(b)** With Fibre Orientation

Figure 3.26: Variations in Free-edge Effect [42]

Hence, these high inter-laminar shear stresses exist at the free edge to transfer shear between the laminate layers. They extend along the width up to the thickness of the specimen. The specimens used

in this project would have a thickness of approximately 10 mm and a height of 10 mm as well. The high stress at the free edge, coupled with machining defects, could lead to delamination and early failure of the specimen. However, the layer orientations in the specimen, along the hoop direction, would be close to 0° with the exception of some ±55° layers. Hence, referring Figure 3.26 (b), the free-edge effect might not have a significant effect on the test.

3.6.4. Self-Heating

Katunin [43] studied the self-heating effect in thermoset polymer composites under fatigue loading. The self-heating phenomenon was experimentally observed to follow three phases. The first phase was an exponential increase, followed by temperature stabilization due to damage accumulation, and then rapid increase in temperature when a macro-crack was developed, before leading to failure. It was observed to be critical as it dominated the mechanical fatigue loads as the cause of failure. The experimental observations for a GRE specimen is shown in Figure 3.27.

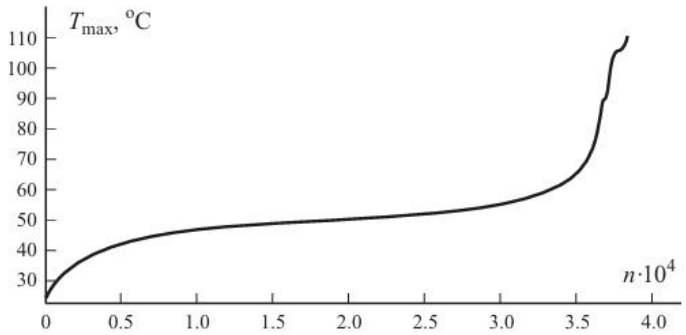

Figure 3.27: Self-heating Effect in Fatigue Tests [44]

This heating effect was attributed to the mechanical energy being dissipated as heat, and due to the poor thermal conductivity of the composite, it led to the increase in the specimen's temperature. It also depended on the magnitude of fatigue load applied.

Peyrac *et al.* [45] and Muller *et al.* [46] conducted self-heating tests on thermoplastic composites. Both used CF/PA66 specimens, which had a glass transition temperature of 70°C. Short loading cycles were applied successively at increasing load levels. The increase in temperature compared to the room temperature was recorded for each lead level. It was observed that the temperature increased linearly up to a certain load. Beyond that, the temperature increase was rapid. The load at which this increase was observed corresponded to the fatigue limit.

Twelve load blocks were applied with 6000 cycles in each block, with a loading rate of 4.72 Hz. It was confirmed that self-heating affected thermoplastic composites the same way as it did for thermosets. Peyrac *et al.* [45] used load blocks of 5000 cycles at 5 Hz each, starting with 50 MPa and going up to 120 MPa. They reported that for 0° layups, the temperature increase in a self-heating test was around 2°C up to the fatigue limit. For ±45° laminates, the temperatures were significantly higher, increasing by more than 80°C.

As mentioned before, the specimens would have primarily hoop-wound layers, with a few diagonal layers. Following the results from [45], the self-heating effect could be expected to lie on the lower end of the temperature increase reported. However, as it was also reported to be dependant on the applied stress [43], the significant radial stress applied in this test could increase this effect.

3.7. Research Proposal

In this thesis, the main research question was: **How can the fatigue properties of wound composites be characterized accurately?**. It led to the following sub-questions:

1. How can the specimen be loaded cyclically, ensuring as uniform as possible hoop strain distribution in the specimen?
2. Can the current standard ring fatigue test be improved upon?

To proceed towards an answer to first sub-question, a thorough assessment was done in section 3.5. Both existing and novel setup concepts were studied. They were then ranked based on their feasibility, expected accuracy, and performance. It was determined that the elastomer expansion concept, shown again in Figure 3.28, was the most promising way forward.

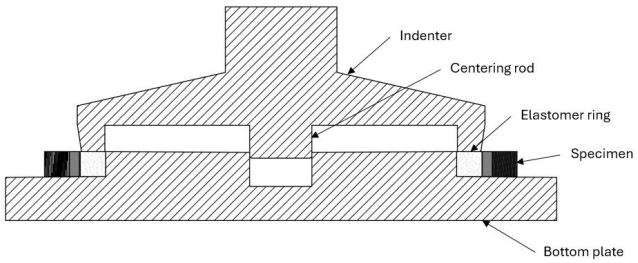

Figure 3.28: Choice of Test Setup - Elastomer Insert Expansion

This choice was based on the merits that it would apply uniform radial pressure, would not be significantly affected by friction, and required simple parts, losing less time in manufacturing, and allowing more time for testing.

There were some foreseen concerns. The setup would require a 500 kN test bench, limiting it to a rare machine. Improper orientation and alignment of the indenter could affect the pressure distribution and the sealing of the elastomer. Lastly, cyclic stresses could lead to crack propagation in the fixture itself.

Owing to the high load requirements in this setup, the height of the specimen was limited to 10 mm. Hence, the second sub-question would lead to a detailed study of factors that could affect the results and repeatability of the test.

The setup could be fine-tuned and calibrated. It could then be compared with results from a split-disk test. The minimum goal for the test development was to be able to test thin ring specimens up to 22000 $cycles$ to demonstrate the setup's capability to apply to consistent fatigue loads. Following which, the next step was to demonstrate that it can perform qualitative tests based on burst-after-fatigue, or residual strength.

From the initial tests, the objective was to demonstrate the setup's potential to characterize the fatigue properties of composite rings. A secondary objective was to demonstrate that rings with a COPV layup can also be tested. It would be carried out based on the EU requirements [9]. It could be used in the future to study the extent to which the performance of a ring could be representative of a vessel, and how gaps between the two could be bridged.

4

Design Methodology

4.1. Requirements

For the test setup's performance, there were three main requirements,

1. To subject the specimen to an as-uniform-as-possible hoop stress state along the specimen's circumference. This would justify the use of this test over the standard split-disk method.
2. To generate a material's SN curve, the setup should be capable of consistently subjecting the specimen to a range of stress levels. This should lead to an accurate study of the specimen's material properties.
3. The setup should be able to test specimens cut from a COPV, up to 87.5 MPa internal pressure in fatigue and 157.5 MPa internal pressure for burst. This meant the setup itself should not fail or deform significantly in these conditions.

From these three points, individual requirements for the setup components, shown in Figure 4.1, were derived.

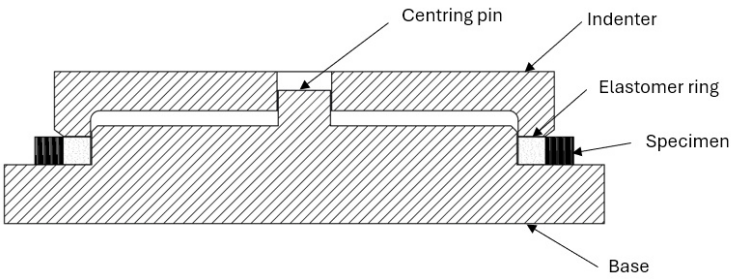

Figure 4.1: Test Setup Initial Concept

The fixture comprising the indenter and the base should not deform significantly during the test. Functionally, it should also remain centred and prevent extrusion of the elastomer ring. This was foreseen as a crucial challenge.

For the ring, the material chosen should be able to withstand the test pressure without disintegrating. For the test to be successful, the material should not deteriorate over the course of the test. This would affect the relation between the applied cross-head force and the measured hoop strain in the specimen, deviating from an initially calibrated setup.

4.2. Material Selection

4.2.1. Fixture

For the fixture, a high-strength steel with good fatigue life was needed. 17-4 PH Steel initially chosen had sufficient strength for the test setup. The material properties are shown in Table 4.1. It was not assured which material specification would actually be delivered. Hence, the lowest available mechanical properties for the 17-4 PH bar were used.

Mechanical Properties

Table 4.1: 17-4 PH Stainless Steel Bar Mechanical Properties, AMS 5643 [47]

Mechanical Property	B-basis Value
E, MPa	196650
E_c, MPa	207000
ν	0.27
F_{TU}, MPa	924
F_{TY}, MPa	793
F_{CY}, MPa	717
F_{SU}, MPa	586
ϵ, %	16

4.2.2. Specimens

The specimens were made from Toray T700 with Huntsman LY1135. It is referred to as T700-Epxoy throughout the text. This was chosen as it was available and had known properties, which had been published by Van Bavel *et al.* [48]. Its mechanical properties are mentioned in Table 4.2.

Mechanical Properties

Table 4.2: T700-Epoxy Mechanical Properties [49]

Mechanical Property	Value at 60% Fibre V_f
E_{11}, MPa	139340
E_{22}, MPa	10590
G_{12}, MPa	4940
G_{13}, MPa	4940
G_{23}, MPa	3782
ν_{12}	0.2600
ν_{13}	0.0198
ν_{23}	0.4000
X_T, MPa	2125
X_C, MPa	1570
Y_T, MPa	45
Y_C, MPa	200
S, MPa	70

Types of Specimens

The specimens were made through wet-winding by Sharp Composites from Herk-de-Stad, Belgium. Two types of specimens were requested, 2 mm ring specimens with a hoop layup and rings cut from a COPV cylinder. The 2 mm specimens are hereby referred to as 'thin' specimens and the latter are referred to as 'tank' specimens.

Thin Specimens

The thin specimens served two purposes. First, to perform benchmark tests against the standard split-disk test and the wedge test setups. A quasi-static comparison would be made, focusing on

the hoop stress distribution and hoop failure strength. The hoop-wound layup would also allow to easily differentiate between fibre and matrix failure modes. Second, for qualitative comparisons of burst-after-fatigue strengths, and quantification of the materials fatigue properties. The layup of the thin specimens is given in Table 4.3. The thickness of each ply was 0.245 mm. The laminate modulus, estimated through CLT was, E_{XX} = 139218 MPa. The nominal height would be 10 mm.

Table 4.3: Hoop-wound T700-Epoxy Ring Layup [Sharp Composites]

Layer	Orientation* [°]	Thickness [mm]
1	88.77	0.49
2	88.77	0.49
3	88.77	0.49
4	88.77	0.49

***Each layer comprises a pair of plies with +/− orientations.**

Tank Specimens

The tank specimens would be used to demonstrate the performance of the test setup up to its limits. The goal of the research was also to find out to what extent a ring specimen could be representative of a tank. The purpose was also to study the performance of the ring, compare it to that of a tank, and see if the two could be linked. The tank layup is shown in Table 4.4. The total thickness was 13.32 mm and the nominal height was 10 mm.

Table 4.4: ConfHy T700-Epoxy Pressure Vessel Layup [Sharp Composites]

Layer	Orientation* [°]	Thickness [mm]
1	88.77	0.49
2	88.77	0.49
3	88.77	0.49
4	71.9	0.499
5	19.4	0.632
6	19.3	0.628
7	23.3	0.628
8	23.1	0.635
9	33.9	0.566
10	37.6	0.562
11	88.84	0.49
12	88.84	0.49
13	88.84	0.49
14	25.8	0.572
15	18.2	0.632
16	23.7	0.566
17	19.6	0.629
18	88.89	0.49
19	88.89	0.49
20	31.6	0.573
21	38.7	0.573
22	70	0.487
23	80	0.48
24	88.92	0.735

***Each layer comprises a pair of plies with +/− orientations.**

For both types of specimens, the setup must be calibrated. It would be necessary to establish a relation between the applied force and the resulting hoop strain. For the test to be effective, this relation must remain intact throughout the test.

4.2.3. Elastomer Ring

For the ring's material, polyurethane (PU) was chosen. This was because of its incompressible nature and superior and mechanical properties compared to other elastomers, such as Neoprene or EPDM. Mosley [29] used PU discs in compression for internal pressure tests on small tubes. In his study, PU with 90 Shore A hardness (90A) was functional up to 50 MPa, while PU 95A was used up to 130 MPa pressure. These were not tested in cyclic loading conditions. However, polyurethane is used extensively, along with other elastomers, in bridge bearings. There it experiences cyclic hydrostatic compressive loading. Hence, it gave some confidence in its use in this case.

It was decided to use PU 90A for the thin specimen tests, as it was cheaper and the test would not exceed it's limit pressure of 50 MPa. The PU 95A rings would be used for the tank specimen tests. This material was harder to procure and more expensive. Hence, it was decided to use it judiciously. An estimate of the costs is mentioned in Table B.1.

Mechanical Properties

Elastic properties for the PU 90A were determined through initial tests, shown in section 4.3.

Table 4.5: PU 90A Elastic Properties

Mechanical Property	Value
E, MPa	39.52 [Equation 4.1]
ν	0.4956 [Figure 4.11 (b)]

At the time of testing, PU 95A samples were not available. It was assumed that its compressibility would be at least equivalent to the tested PU 90A samples. The elastic properties of PU 95A are mentioned in Table 4.6. The test data used is shown in Figure 4.2.

Table 4.6: PU 95A Elastic Properties

Mechanical Property	Value
E, MPa	55 [50]
ν	0.4956*

***assumed same as PU 90A**

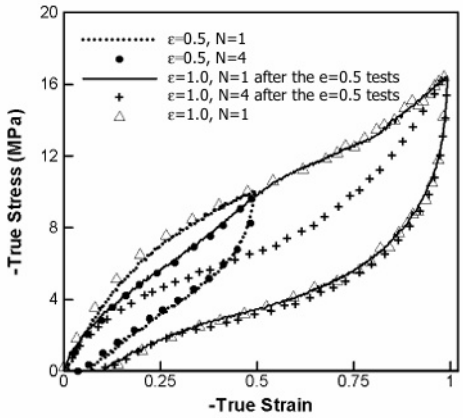

Figure 4.2: PU 94A Compression Test Data at $\dot{\epsilon} = 0.01\ s^{-1}$ ($\epsilon = 1.0,\ N = 1$) [50]

4.2.4. Backup Ring

Although the polyurethane seemed promising, a backup option was prepared in case the PU 95A could not withstand the burst pressure of 157.5 MPa. In that case, ultra-high molecular weight polyethylene (UHMWPE) rings could be used. It had been proven to withstand substantially high pressure without failure, as reported in the work of Van Paepegem *et al.* [51]. It was also available at Vaneflon from Hamme, Belgium. It would have a Shore D hardness of 64 (64D), which is higher than, but comparable to, 95A. The elastic mechanical properties and yield behaviour of the UHMWPE are mentioned in Table 4.7 and Table A.3, respectively.

Mechanical Properties

Table 4.7: UHMWPE Elastic Properties

Mechanical Property	Value
E, MPa	700 [52]
ν	0.46 [53]

The yield behaviour of UHMWPE in compression was studied by Brown *et al.* [54], shown in .

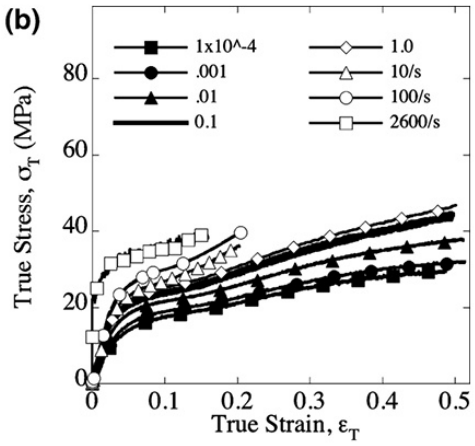

Figure 4.3: UHMWPE Compression Test Data at $\dot{\epsilon} = 0.01\ s^{-1}$[54]

To note, the Poisson's ratio of UHMWPE can vary, but was assumed as 0.46 [53]. The compressive modulus could also be higher than the tensile modulus mentioned [53]. Another challenge with this material is that it would show permanent plastic deformation, mostly in the first cycle.

4.3. Preliminary Tests

Tests were performed to determine the behaviour of the polyurethane. The purpose was to use test data to fit a material model. It was then used for predicting the test behaviour and designing the fixture, through finite-element analyses.

The behaviour of PU 90A was studied through static, cyclic, and creep compression tests. A sample sheet was provided by Van De Wiele Rubber from Kluisbergen, Belgium. Small samples, 24.5 mm in nominal diameter, were stamped out of it using a die cutter. The initial height of the samples was 9.73 mm.

4.3.1. Static Tests

Static compression tests were performed on the PU 90A samples. They were tested up to 0.5 strain on the Instron 5985 test bench at Syensqo. The loading rate was 0.61 mm/s, having an effective strain rate of 0.06 s^{-1}. The setup is shown in Figure 4.4.

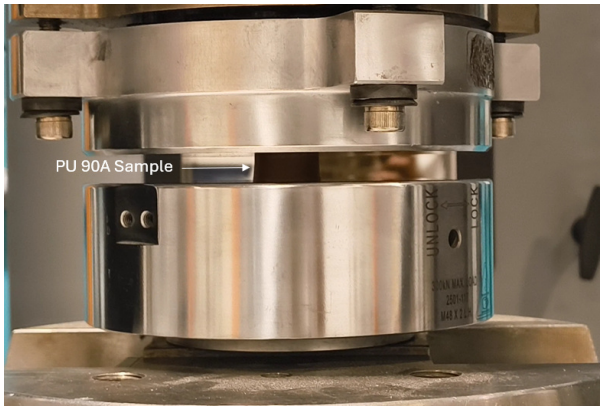

Figure 4.4: Uniaxial Compression Test Setup

The same sample was tested till the behaviour stabilized. The results are shown in Figure 4.5.

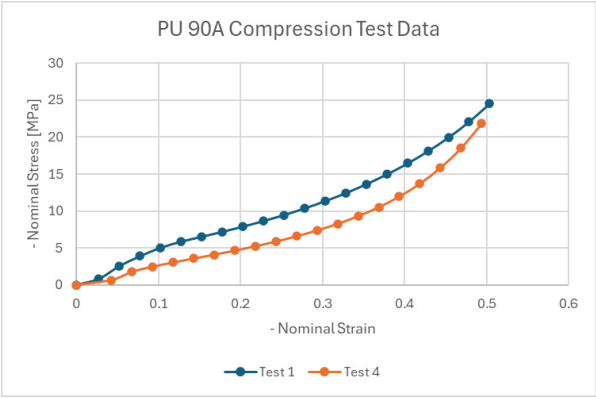

Figure 4.5: Uniaxial Compression Test Results

Softening was observed after the first cycle. The behaviour stabilized after the 3^{rd} cycle, which was then similar to the 4^{th} cycle. It was compared to literature data in Figure A.1 (a). The results were used to fit hyper-elastic material models in the FEM in section 4.5.

The stiffness of the PU 90A was calculated from the initial slope of the force-displacement curve of the compression test. This was termed its 'free stiffness' Its modulus was then calculated using Equation 4.1.

$$k = \frac{F}{d} = \frac{1800}{0.94} = 1914.89\ N/mm$$
$$E = \frac{kl}{A} = \frac{1914.89 \times 9.73}{\pi \times 12.25^2} = 39.52\ MPa \tag{4.1}$$

4.3.2. Creep Test

For the creep test, an Instron 5900R test bench at Syensqo was used, shown in Figure 4.6.

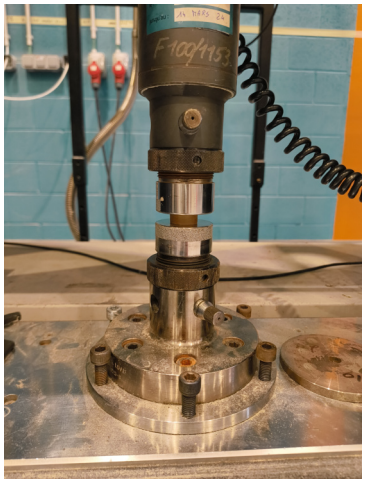

Figure 4.6: Creep Test Setup

A new sample was left between the plates, compressed by 0.5 mm. The specimen was left in the compressed state (t_n) for approximately 18 hours. Afterwards, it was removed from the test bench to recover for approximately 72 hours. Following the nomenclature in [55], t_0 is the specimen's original height, t_n is the specimen's compressed height, t_i is the specimen's final height.

$$t_0 = 9.73\ mm$$
$$t_n = 9.73 - 0.5 = 9.23\ mm$$
$$t_i = 9.58\ mm$$

The compression set of the PU 90A was calculated as per [55], using Equation 4.2.

$$C_B = \frac{t_o - t_i}{t_o - t_n} \times 100 \tag{4.2}$$
$$C_B = \frac{9.73 - 9.58}{9.73 - 9.23} \times 100 = 30\%$$

The compression set estimated from the test was used to determine the initial height of the PU rings. It was assumed that the rings would exhibit the same properties. Using the 30% set and Equation 4.2, the required height of the specimens was calculated in section 5.3, by accounting for the PU ring's height reduction.

4.3.3. Cyclic Compression Tests

Fatigue tests were then performed see if the material could survive 22000 cycles. The test sample and setup are shown in Figure 4.7. A hydrostatic compression test setup was used as it more closely represented the loading condition the polyurethane would face in the ring tests.

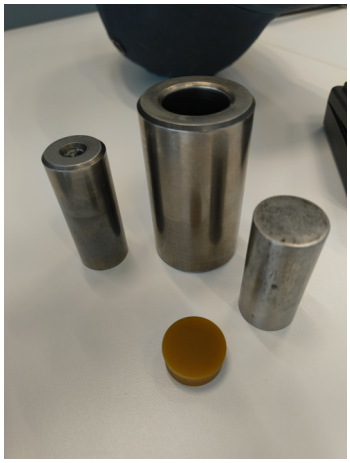

(a) Test Sample and Components

(b) Test Setup

Figure 4.7: Preliminary PU Compression Tests

The sample had the aforementioned nominal diameter and height of 24.5 mm and 9.73 mm, respectively. Based on initial calculations, for thin specimens to reach 0.88% hoop strain, the required force would be close to 150 kN (subsection A.2.2). At that force, the pressure applied on the PU ring was calculated using Equation 4.3.

$$P_{ring} = \frac{4 \times 150000}{\pi(170^2 - 150^2)} = 29.84\ MPa \tag{4.3}$$

To apply the same pressure on the small 24.5 mm samples, the force required was calculated using Equation 4.4. As it was expected to fill the volume during the test, the cross-section area of the setup's cylinder was used.

$$F_{test} = 29.84 \times \pi(12.52)^2 = 14695.35\ N \tag{4.4}$$

A force-controlled test was performed on the 15 kN MTS fatigue test bench at TU Delft. For safety, the force was limited to 14 kN ($R = 0.1$). The average applied force was 13857 N, which was equivalent to an applied pressure of 28.14 MPa on the PU 90A sample. Two sets of data were extracted from this test,

1. Force-displacement behaviour (loading + unloading). This was used to estimate the stiffness. Any variation in stiffness would have appeared as a shift in the slope of the curve. It is shown in Figure 4.8.
2. Piston displacement for each peak and valley in the loading cycle - the displacement or stroke of the piston at each cycle was used to estimate the reduction in the height of the sample over time. It is shown in Figure 4.9.

Figure 4.8 shows the applied force [kN] vs. displacement [mm] curves during the test. The axes are negative, so the curves begin from the top-right side. The initial region of low stiffness existed till the sample filled up the volume completely. The stiffness after that remained constant as the curve was linear. It was termed the 'constrained stiffness'. The constrained stiffness remained constant over 22000 cycles. It meant that the PU 90A would be effective as the ring material in the actual test.

After testing to 22000 cycles, the same sample was tested again for 100 cycles. It was observed that the sample's height immediately reduced to the height it had reached during the previous test. It meant that the sample had reduced free stiffness. However, since the constrained stiffness was intact, it was not expected to impact the test.

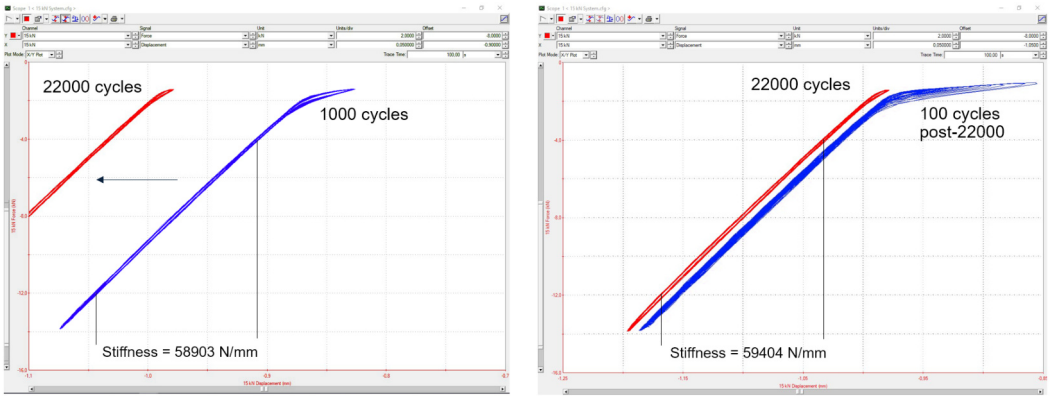

(a) Shift in Displacement over 22000 cycles **(b)** Faster Reduction in Height due to Softening

Figure 4.8: PU 90A Force [kN] vs Displacement [mm] Curves (Negative Axes)

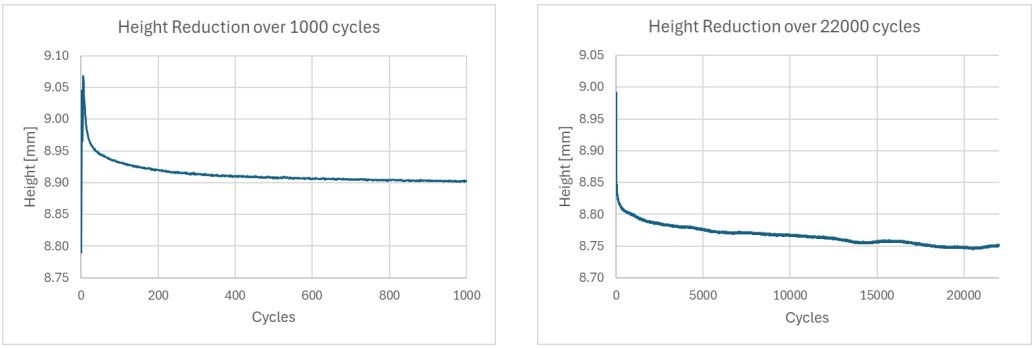

Figure 4.9: PU 90A Height Reduction under Cyclic Compression

From Figure 4.9, the reduction in the sample's height is reflected in the gradual reduction in the displacement of the piston at the end of each cycle (at minimum force). From this, the final height of the sample was calculated. The results are shown in Table 4.8.

Table 4.8: PU 90A Compression Test Results

	After 1000 cycles (mm)	After 22000 cycles (mm)
Initial Peak	9.0685	8.7986
Final Peak	8.9027	8.7504
Height Reduction	0.1658	0.2411
Final Height	9.5624	9.4889
Height Measured	9.61	9.53

After being removed from the setup, the height immediately started to increase. Hence, the height measured was always slightly higher than calculated. The samples were observed to slowly recover their height when left to rest. It hinted that the PU rings might be reusable.

In the tests, the average piston compression at the peak of each cycle (maximum force) was 1.18 mm. Hence, as a function of compression displacement, the height reduction was approximately calculated to be 20% of the maximum displacement in Equation 4.5.

$$\Delta h = \frac{0.2411}{1.18} = 20\% \tag{4.5}$$

4.3.4. Limit Pressure and Recovery Tests

Further tests were performed in a 100 kN fatigue test bench at Syensqo. The purpose of the tests was to go up to the limit of the polyurethane. Three tests were performed on a new sample, at increasing applied forces. The same 'Test' sample was used for all three tests. A test was also performed on the 'Fatigued' sample that had been cycled 22000 times, and allowed to rest for one week. The purpose was to see if the polyurethane had recovered its initial free stiffness. The results are shown in Figure 4.10 (a).

Table 4.9: PU 90A Limit Pressure Tests (0.42 Hz)

Test	Specimen	Force $[kN]$	Cycles	Stiffness $[kN/mm]$
1	Test	14	10	71.53
2	Test	25.5	10	78.85
3	Test	50	10	86.22
4	Fatigued	14	100	73.43

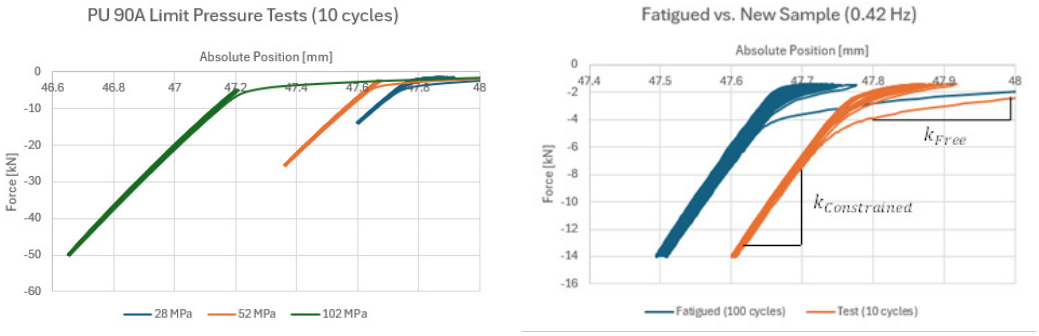

(a) Tests at Increasing Pressures

(b) Test to Assess Recovery

Figure 4.10: PU 90A Disc - Limit and Recovery Tests (Negative Axes)

It was observed that even at pressures as high as 100 MPa, the polyurethane survived the test. With the increase in pressure, the constrained stiffness also increased, as seen in Table 4.9. Hence, in section 5.5, calibration tests were done by loading the specimen close to the maximum load in the fatigue cycles. From Figure 4.10 (b), it was observed that the sample that was fatigued sample did not recover its initial free stiffness (slope of the curve before it goes steep). It's comparison with the new 'Test' sample showed that it went to its last reduced height in the first cycle.

4.3.5. Compressibility Estimation

A finite-element model of the test setup shown in Figure 4.7 was created. It was an axisymmetric model shown in Figure 4.11. The dimensions and details of the same are mentioned in Table 4.10.

Table 4.10: Test Setup Axisymmetric FEM Details

Component	Dimensions	Material	Material Model	Properties	Element Type	Element Size (mm)
Cylinder	$d_{inner} = 25\ mm$ $d_{outer} = 45\ mm$ $h = 50\ mm$	Steel (generic)	Elastic, Isotropic	$E = 197000\ MPa$ $\nu = 0.3$	CAX4R	1
Plungers	$d = 24.96\ mm$ $h = 20\ mm$	Steel (generic)	Elastic, Isotropic	$E = 197000\ MPa$ $\nu = 0.3$	CAX4R	1
Elastomer	$d = 24\ mm$ $h = 9.73\ mm$	PU 90 A	Elastic, Isotropic	$E = 39.52\ MPa$ $\nu = 0.49995$	CAX8RH	1.25

Since the material specification of the test setup components was not known, generic stainless steel properties were assumed[1]. The behaviour of elastomer, during the loading section in the test, was observed to be almost linear-elastic. Hence, elastic material properties were used initially to represent it. The stiffness calculated in Equation 4.1 was used. The initial assumption being that the material was incompressible, the Poisson's ratio chosen was close to 0.5. Force-displacement behaviour was compared between the test and the FEM, shown in Figure 4.11 (b).

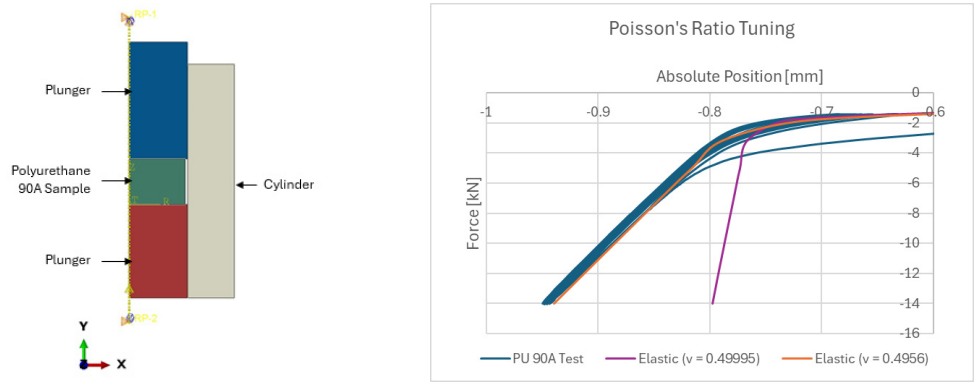

(a) Axisymmetric FEM Components **(b)** Comparison of FEM and Test Results

Figure 4.11: Poisson's Ratio Estimation through FEM Comparison

It was observed that the PU was slightly compressible. This was noticeable in the constrained stiffness (steep part of the curve) bring lower than that for the incompressible assumption. Based on this, the Poisson's ratio for the PU 90A's elastic material model was adjusted till its stiffness matched what was observed in the test. The elastic properties are mentioned in Table 4.5.

Another observation, pointed out by Prof.dr.ir. Wim van Paepegem, was that a 1% change in the Poisson's ratio caused a large variation in the force required. This was explained by the material model reaching the limits of incompressibility, and hence being extremely sensitive close to an asymptotic value.

4.3.6. Summary

The observations from the preliminary static, fatigue, and creep tests are summarized here.

1. The material softens in the initial three cycles, stabilizing from the fourth cycle onwards. The softening behaviour affects its under free compression, but does not affect its constrained stiffness. Hence, it is not expected to affect its performance in the test.
2. Polyurethane shows a permanent compression set of 30%. This can be used to estimate its maximum reduction in height in a high-cycle fatigue test. The height of the specimen can then be calculated from it, to ensure it does not exceed the PU ring's height during the test.
3. The PU disc maintains its constrained stiffness during the cyclic compression tests. It does reduce in height, which should be accounted for by the previous point.
4. It survives up to 100 MPa of pressure tested, albeit for the 10 $cycles$ tested. Its constrained stiffness increases under higher pressures. However, it can still be approximated to a linear relation. Calibration tests should go up to the force expected in the actual tests.
5. The PU has is slightly compressible, with $\nu = 0.495$. The same can be implemented in the hyper-elastic material model. Since it is at the limit of incompressibility, it would make the FEM force predictions sensitive to the Poisson's ratio.

[1] https://asm.matweb.com/search/SpecificMaterial.asp?bassnum=mq304a

4.4. Initial Calculations

A basic design of the indenter and the base was imagined, shown in Figure 4.1. For the desired stress ratio of 0.1, the setup would always be in compression. Hence, on the test bench, compression plates would be best suited to load the setup. This meant that the indenter and base surfaces facing the plates should be flat.

4.4.1. Setup Description

The indenter would have an annular ring protruding from the flat plate to load the elastomer ring. The base would have a recess to house the elastomer ring and to provide a constraint along the inner surface of the ring. The specimen would be placed on the outside of the elastomer ring. The elastomer, when compressed, would apply pressure on its contact surfaces. The specimen having the least stiffness compared to the steel fixture, would deform the most.

4.4.2. Assumptions

To estimate the stresses acting on the setup components in the ring test, initial calculations were performed using an analytical representation of the test setup (subsection A.2.2). The purpose was also to use these calculations to validate finite-element analysis (FEA) results. The assumptions used for these calculations were,

1. The ring material, PU 95A is linear elastic and incompressible, with $E_c = 55\ MPa$ [50].
2. The indenter does not deform radially.
3. The specimen does not deform through-thickness. It only expands radially with a hoop stiffness $= E_{XX}$ of the laminate.
4. The applied pressure is distributed uniformly over the specimen and hence, it does not rotate about its radial cross-section.
5. The friction coefficient is 0.20.

For the fixture, the 17-4 PH properties were used from Table 4.1. The specimen's hoop stiffness was approximated using CLT for the layup shown in Table 4.4. The resulting modulus was $E_{XX} = 68.44\ GPa$ (subsection A.2.1).

4.4.3. Estimated Stresses

In section 3.5, 8 mm was the ring thickness estimated as the maximum required to be within the 500 kN test bench limit. The calculations shown in Figure 3.2.4 were extended to calculate the stresses in the setup components as well. The equations were solved iteratively, accounting for the change in the elastomer's dimensions in each iteration. For a maximum applied pressure of 200 MPa on the specimen, the expected stresses in the fixture are shown in Figure 4.12.

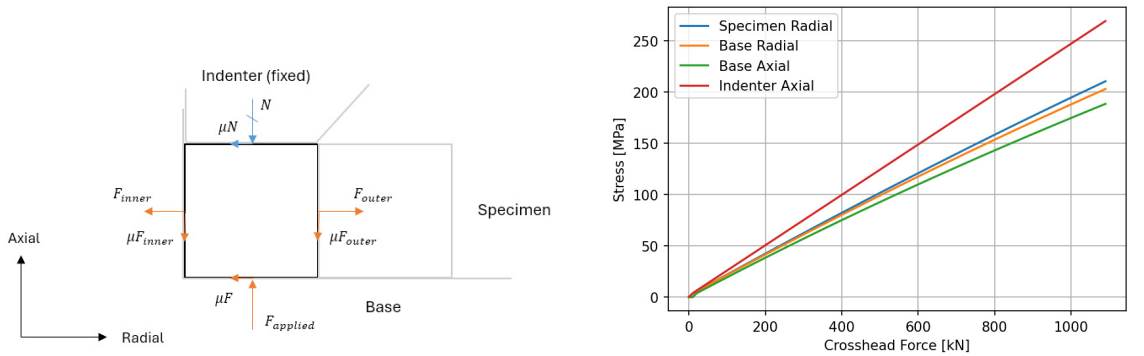

(a) Ring Free-body Diagram

(b) Stresses at 200 MPa Internal Pressure (subsection A.2.2)

Figure 4.12: Initial Stress Estimation on the Setup

To note, a ring, when compressed, would only expand radially outwards. It would not apply any pressure on the inner side. However, in this case, as the expansion is constrained by the specimen, the ring was expected to apply a pressure radially inwards as well.

4.4.4. Expected Stress Concentrations

Two areas of stress concentration were foreseen in this design, shown in Figure 4.13. The first was at the indenter's inner corner. A fillet could be used here to reduce the stress concentration factor. The indenter would be in compression. However, it was also expected to deform radially outwards when compressed. Hence, the expected load case was a combination of compression and bending.

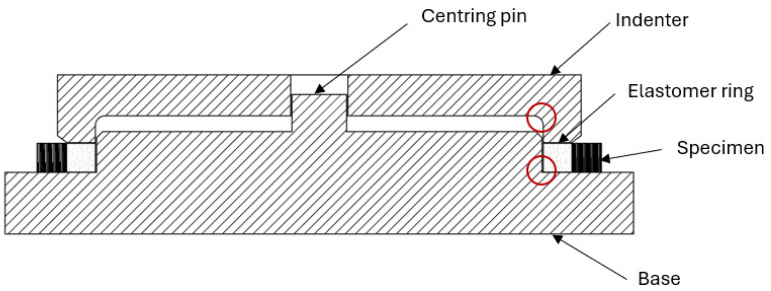

Figure 4.13: Stress Concentrations Expected at Corners

To size the fillet radius at the indenter's inner corner, the effect of stress concentration was estimated. Stress concentration factors for shoulder fillets in tension and bending were compared, shown in Figure 4.14. It was assumed that under axial compression, the effect of stress concentration would be identical to its effect in tension.

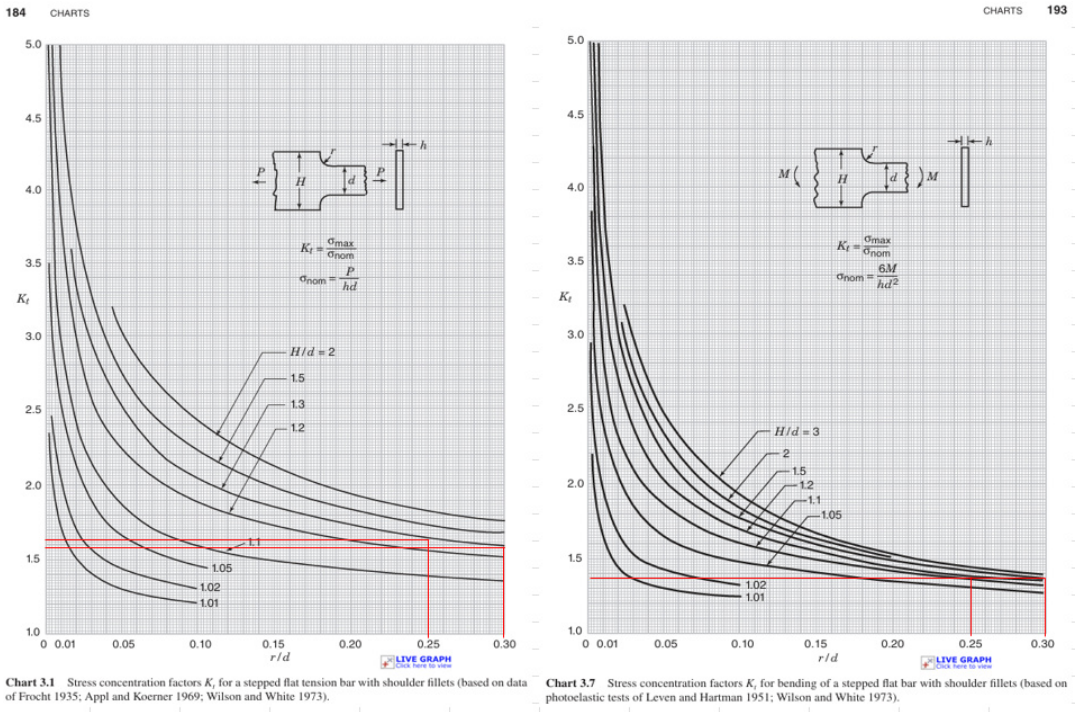

Figure 4.14: Stress Concentration Factors [56]

The size of the fillet radius chosen was 2.5 mm. A larger fillet radius would reduce the stress at the fillet slightly, but it would also limit the depth of the indenter. This trade-off is explained in detail in

subsection 4.6.3. The higher of the axial and bending factors was used. The 2.5 mm radius corresponded to $K_t = 1.6$.

At 200 MPa of radial pressure on the specimen, the stress experienced by the indenter is 261.62 MPa (Figure 4.12). The maximum stress at the indenter fillet was then calculated using Equation 4.6.

$$\sigma_{peak} = K_t \, \sigma_{field} \tag{4.6}$$
$$\sigma_{peak} = 1.6 \times 261.62 = 418.59 \; MPa$$

The second stress concentration point foreseen was at the corner of the recess made for the ring on the base. Under compression, as the ring is constrained from all sides, it would apply equal pressure on its bounding surfaces. At that corner, there would be a radially inward pressure on the vertical surface of the base, and a downward pressure on the horizontal surface. Together, these would create a tensile stress at the corner.

A fillet could not be added at this corner as it would create an additional challenge. The presence of a fillet would offset the seating of the elastomer ring in the recess. To make it fit, the ring's corner would have to be machined with the same fillet radius. Machining the elastomer rings from the inside was not a feasible option owing to its flexibility. A solution was implemented, which is detailed in subsection 4.6.4.

The solution involved splitting the base into two parts to allow for a sharp corner at the recess. It also prevented the stress concentration at the corner by allowing the contact faces at the recess to deform independently of each other. The FEM included this solution, having a sharp corner in the recess of the base.

4.5. Finite-Element Model

As the design was perfectly axisymmetric, no variations were expected around the circumference of the setup. Hence, an axisymmetric FEM was best suited to represent this setup. It reduced the number of elements and computation time, while maintaining accuracy. There were 3 main components that had to be represented accurately in the FEM,

1. Elastomer - for an accurate representation of the test, reliable material models were required for the elastomer.
2. Specimen - to correctly estimate the internal pressure and predict the forces required and the stresses in the specimen, the stiffness of the specimens had to be modelled correctly.
3. Fixture - comprises all the components required in the setup. An accurate representation was required to capture the stress concentrations and correctly size the components to meet the design requirements while not exceeding the materials limits.

The approach for each component is described in their respective sections below. A summary of the the FEMs is shown in subsection 4.5.4.

4.5.1. Elastomer

To represent the elastomer accurately, a hyper-elastic material model was required. Qi and Boyce [50] studied the uniaxial compression behaviour of thermoplastic PU 94A at various strain rates. Their test data was used to create the PU's material model.

Strain Rate Estimation

The initial stiffness of PU was observed to increase with the increase in strain rate [50]. To represent the worst-case performance of the elastomer, the lowest expected strain rate was assumed.

For the thin specimens, the frequency would be 25 $cycles/min$, as per [7]. Hence, depending on the desired stress level, the displacement applied would vary. This would result in different strain rates applied for different stress level tests. For the tank specimens, a frequency of 10 $cycles/min$ would be used up to a fixed stress level. Hence, the strain rate was calculated based on the same.

The maximum expected displacement in the tank specimen fatigue test was close to 1.8 mm. This was calculated using the analytical model of the test setup, attached in subsection A.2.2. The expected force-displacement curve for the test is shown in Figure 4.15.

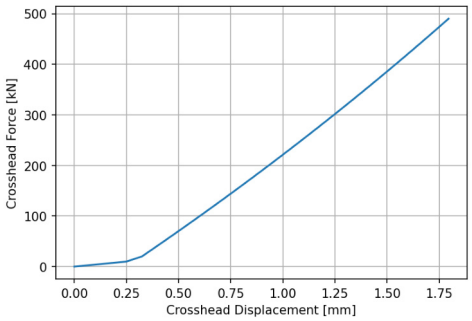

Figure 4.15: Expected Cross-head Displacement of 1.8 mm (subsection A.2.2)

The lowest frequency for the fatigue test was 10 $cycles/min$ or 0.17 Hz [9]. The strain on the PU rings was then estimated using Equation 4.7.

$$v = 2f \times d = 2 \times 0.17 \times 1.8 = 0.612\ mm/s$$
$$\dot{\epsilon} = \frac{v}{h} = \frac{0.612}{10} = 0.0612\ s^{-1} \tag{4.7}$$

A lower stiffness would mean a worse-case scenario. It would require a larger displacement to apply the same force. The displacement estimated would then drive the geometrical requirements of the indenter. Hence for the design, $\dot{\epsilon} = 0.01\ s^{-1}$ was chosen. The maximum expected strain was less than 0.20 in the fatigue test and up to 0.40 in the burst test.

Compression Test Data

A hyper-elastic material model was used in Abaqus to represent the polyurethane. The behaviour was defined by test data [50]. For Abaqus, the true stress-strain data was converted to nominal stress-strain, shown in Figure 4.16. The same is tabulated in Table A.1.

To convert nominal stress-strain to true stress-strain in compression, Equation 4.8 and Equation 4.9 were used [53].

$$\epsilon_T = -\ln(1-\epsilon_T) \Rightarrow \epsilon_T = 1 - e^{-\epsilon_T} \tag{4.8}$$

$$\sigma_T = \sigma_N(1-\epsilon_T) \Rightarrow \sigma_N = \frac{\sigma_T}{1-\epsilon_T} \tag{4.9}$$

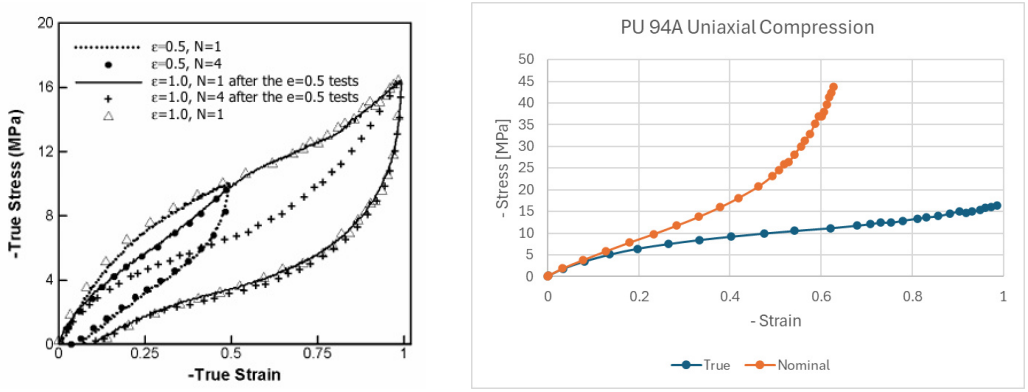

(a) True Stress-Strain Curve (Δ) [50] **(b)** Converted Nominal Stress-Strain Curve for Abaqus

Figure 4.16: Polyurethane Uniaxial Compression at $\dot{\epsilon} = 0.01\ s^{-1}$ [50]

Material Model

The curve was added to Abaqus and the built-in curve-fitting function was used. The default selection of models was tried, as shown in Figure 4.17. The strain limit was set at −0.50, as the maximum expected strain was −0.40 for the burst test (subsection A.2.2).

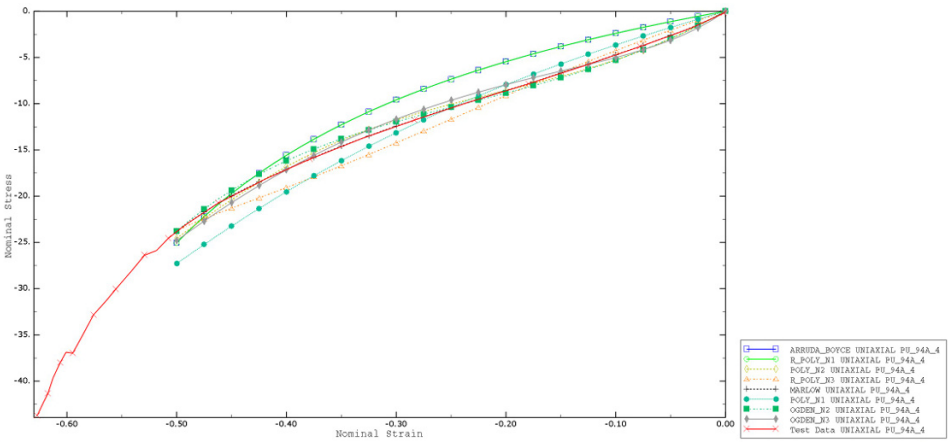

Figure 4.17: Hyperelastic Model Curve-Fitting

For the models compared, fitting errors and stability conditions were checked. The comparison is shown in Table 4.11. Unlike polynomial models that ft curves to the test data, the Marlow model directly calculates strain energy by integrating over the test data [57]. Hence, the fitting error was not applicable to the Marlow model.

Table 4.11: Material Model Analysis Results

Hyper-elastic Model	Fitting Error	Stability
Arruda-Boyce	2.148	Stable
Marlow	-	Unstable
Ogden ($N = 3$)	0.2649	Stable (Uniaxial)
Mooney-Rivlin	1.106	Unstable
Polynomial ($N = 2$)	0.3343	Stable (Test Range)
Neo-Hookean	2.148	Stable
Reduced Polynomial ($N = 3$)	0.7969	Stable

Based on the fitting error and stability, three models were chosen for comparison, shown in Figure 4.18 (b). To study how close the models were to the test data, an FEM representation of the test performed by Qi and Boyce [50] was created. The samples used in the tests were 12 mm in diameter and 3 mm in height. They were modelled using CAX8RH elements, with a element size of 0.5 mm. It was an axisymmetric model with rigid bodies used as compression plates, shown in Figure 4.18 (a).

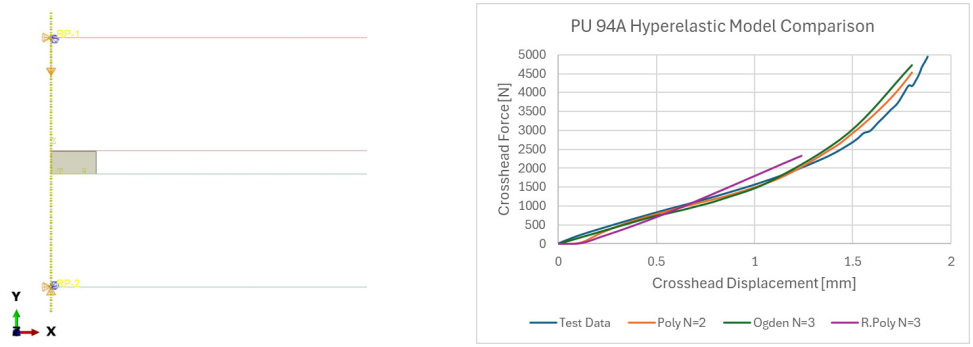

(a) FEM of Compression Test [50]

(b) Force vs. Displacement Curve Comparison

Figure 4.18: PU 94A Hyper-elastic Material Model Fitting

From the comparison, the Polynomial 2^{nd} order model was the closest fit to the disc-sample test data. However, as further shown in section 6.2, the Reduced Polynomial 3^{rd} order model fit better to the actual test. It was also more stable. Hence, it was used in the FEMs. The coefficients for the final hyper-elastic model are shown in Table 4.12. The same was used for PU 90A, detailed in subsection A.2.3.

Table 4.12: Reduced Polynomial ($N = 3$) Hyper-elastic Model Coefficients

D_1	C_{10}	C_{01}		
$1.5469E-03$	6.4861	0		
D_2	C_{20}	C_{11}	C_{02}	
0	−1.8718	0	0	
D_3	C_{30}	C_{21}	C_{12}	C_{03}
0	0.3374	0	0	0

As observed in Figure 4.16 (a), in subsequent cycles, the material showed significant softening. Hence, to complete the material model, elastomer damage through Mullins Effect was modelled. Reis *et al.* [58] characterized the effect through coefficients for PU 85A. Assuming that to be a worse-case scenario for the PU 94A, the same coefficients were used, shown in Table 4.13.

Table 4.13: Mullins Effect Coefficients for PU 85A Damage [58]

r	n	β
2.21	0.30	0.0

Modelling the softening behaviour allowed for an initial estimation of how it would affect the test. As in the preliminary tests, it was observed not to have an effect on the loading behaviour of the PU.

Element Type

The elastomer's element type was CAX8RH (quadratic hybrid elements with reduced integration). Under pressure and friction, the elastomer would bulge at the centre. It would also try to bend around the edge of the indenter. Hence, quadratic elements were required to capture that deformation. As the material was almost incompressible, hybrid formulation was used.

Mesh Convergence

The mesh convergence was done on an initial axisymmetric FEM, which used an Ogden 3^{rd} order model. The indenter and base were modelled as rigid bodies, compressing the ring. The loads and boundary conditions are as shown in Figure 4.12 (a), with the indenter fixed and the base moving up. The convergence study considered the maximum radial expansion and the field stress. The displacements converged faster, but the stress distributions across element boundaries was discontinuous. Hence, the convergence study was based on von Mises stress in the field region. The FEM and convergence results are shown in Figure 4.19.

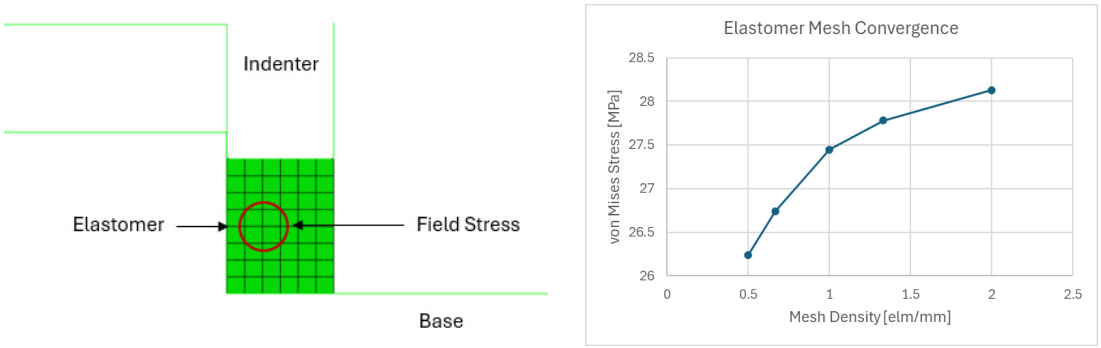

(a) Elastomer Compression Model **(b)** Convergence using von Mises Stress

Figure 4.19: Elastomer Mesh Convergence Study

In all mesh convergence studies, an error $< 3\%$ was chosen as the convergence criteria to balance accuracy with computational cost. From this, element sizes of 1 mm was determined. The deviation from the near-asymptotic value, at the highest mesh density, was 2.4%. To estimate The continuity of stress distribution between elements was checked to ensure it was smooth. To resolve convergence issues due to contact penetration at high forces, the element size was reduced to 0.5 mm.

4.5.2. Specimen

As mentioned in section 4.2, there were two kinds of specimens - thin specimens and tank specimens, whose layups are shown in Table 4.3 and Table 4.4, respectively. Both were made by wet-winding Toray T700-Epoxy uni-directional tape. The mechanical properties of the same are shown in Table 4.2.

Material Models

Two material models were used for two purposes, and led to the creation of two FEMs,

1. By representing the composite as an isotropic material, the hoop stiffness was captured using computationally inexpensive elements. This was used with a deformable fixture model to estimate the stresses in the fixture.

2. An orthotropic material model was used to capture the layup, by assigning a local material orientation to each ply. This method was computationally expensive. It was used to predict the stress distribution in the specimens, with a rigid body representing the fixture.

Elastic Isotropic

To predict the forces required for the test, initially, an isotropic material model was used to represent the specimens. For the thin specimens, E_{XX} was assumed equal to the E_{11} of the T700-Epoxy, from Table 4.3. For the tank specimens, the E_{XX} was calculated through CLT using the layup mentioned in Table 4.4. The properties used are shown in Table 4.14.

Table 4.14: T700-Epxoy Isotropic Approximation (subsection A.2.1)

Specimen	E, MPa	ν
Thin	139340	0.26
Tank	68440	0.21

Elastic Orthrotopic

The ply properties were modelled using engineering constants, shown in Table 4.15. This was used with generalized axisymmetric elements such that each ply could be modelled separately. To capture shear stresses at the ply interfaces, cohesive contact was defined between plies. The stiffnesses were assumed same as the ply through-thickness and shear properties, and are shown in Table 4.16.

Table 4.15: T700-Epoxy Engineering Constants (Table 4.2)

E_{11}, MPa	E_{22}, MPa	E_{33}, MPa	ν_{12}	ν_{13}	ν_{23}	G_{12}, MPa	G_{13}, MPa	G_{23}, MPa
139340	10590	10590	0.26	0.0198	0.4	4940	4940	3782

Table 4.16: T700-Epoxy Cohesive Contact Definition [MPa]

K_{nn}	K_{ss}	K_{tt}
10590	4940	4940

Element Types

The isotropic material model was used with CAX8R elements. These were computationally inexpensive and allowed for use with a deformable mesh of the fixture. Quadratic elements were used to capture bending of the specimen, if any.

The orthotropic material model was used with CGAX8R elements. It was advised by Prof.dr.ir. Wim van Paepagem and Dr.ir. Siebe Spronk. These elements allow axisymmetric torsion, and hence, add additional degree of freedom (DOF) in the circumferential direction. This allowed to define the ply angles accurately in the specimen, shown in Figure 4.20.

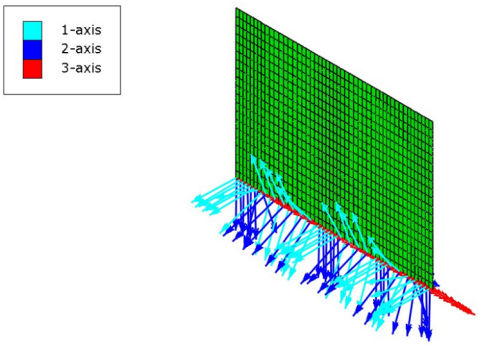

Figure 4.20: Ply Orientations in an Axisymmetric FEM (subsection A.2.4)

Mesh Convergence

The axisymmetric model shown in Figure 4.19 was modified to include the specimen. The isotropic material with torsionless axisymmetric elements was used. The convergence study was done based on the maximum von Mises stress calculated at the element centroid. The FEM and results are shown in Figure 4.21.

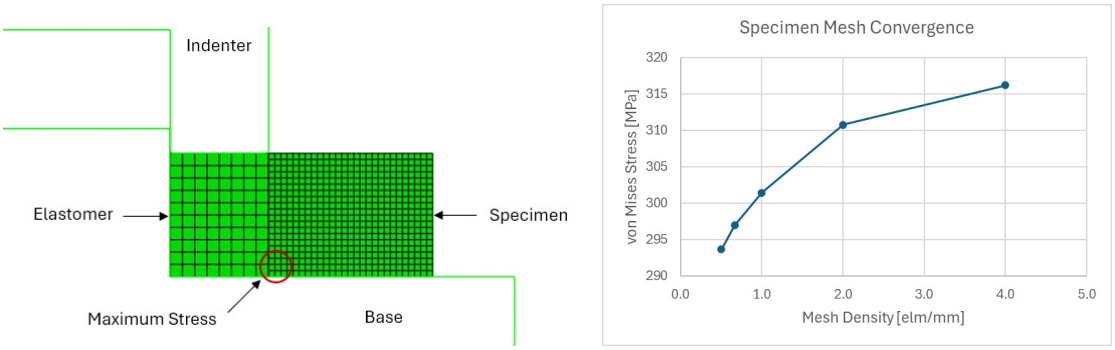

(a) Ring Expansion Model **(b)** Convergence using von Mises Stress

Figure 4.21: Specimen Mesh Convergence Study

From this study, a maximum element size of 0.5 mm was determined. The difference from the near-asymptotic value, at the highest mesh density, was 1.7%. The same was used for the second FEM where the plies were modelled individually.

4.5.3. Fixture

An separate FEM was used for each component of the fixture. It was ensured that the boundary conditions captured the behaviour expected in the test.

Material Model

Since the fixture material was chosen to be steel, a linear-elastic isotropic material model was used. The properties are shown in Table 4.17.

Table 4.17: 17-4 PH Isotropic Properties (Table 4.1)

E_c, MPa	ν
207000	0.27

Element Type

CAX8R elements were used for the fixture. Quadratic elements were used to capture any bending behaviour under compression.

Mesh Convergence

A mesh convergence study was performed using an individual model of the indenter. The boundary conditions represented Figure 4.12 (a). The top edge was constrained in vertical displacement. A maximum force of 1200 kN was applied on the indenter's face. Minimum principal stress calculated at the element centroid was used as the convergence criteria. The mesh and results are shown in Figure 4.22.

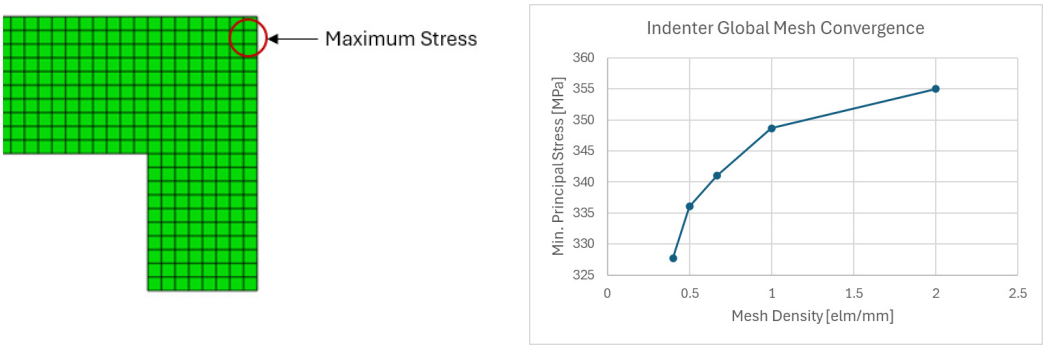

(a) Indenter Compression Model **(b)** Mesh Convergence using Minimum Principal Stress

Figure 4.22: Indenter Global Mesh Convergence

A maximum element size of 1 mm was determined from this study. The deviation from the near-asymptotic stress, at the highest mesh density, was 1.8%. The same element size was used for each fixture component.

Fillet Mesh Convergence

Another mesh convergence study was done on a 2.5 mm fillet radius. The mesh was locally refined and minimum principal stress was used as the convergence criterion. The number of elements along the fillet were increased till the criterion was met. The model and the results are shown in Figure 4.23.

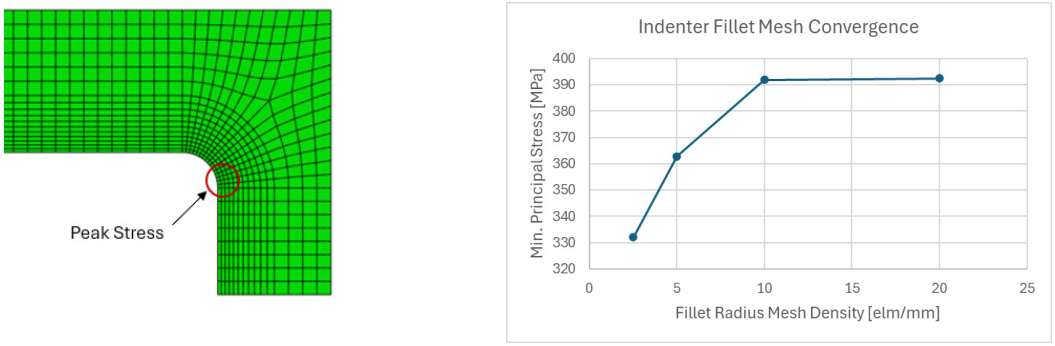

(a) Indenter Compression Model **(b)** Mesh Convergence using Minimum Principal Stress

Figure 4.23: Indenter Local Mesh Convergence

From this study, a maximum element size of 0.25 mm was determined. It was observed an element size $1/10^{th}$ the radius of the fillet was sufficient to capture the peak stress accurately. The same rule-of-thumb was used for the later FEMs. The difference in stress from the asymptotic value was 0.14%.

4.5.4. FEM Details

Combining the aforementioned details, two FEMs were created to increase the efficiency of the analyses. One focused on sizing the fixture, while the other was used for studying and predicting the stress state in the specimens.

Sizing Model

It used a deformable fixture with the purpose of estimating the forces and sizing the components. It had a simplified representation of the specimen which captured only its hoop stiffness. The details are shown in Table 4.18 and the FEM is shown in Figure 4.24. The simplified specimen captured the hoop stiffness of the layup, and was efficient for focusing on the fixture.

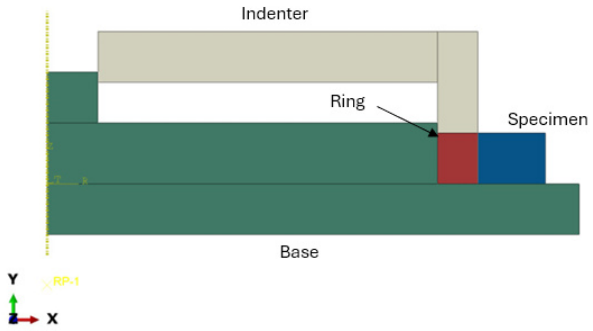

Figure 4.24: Sizing Model

Table 4.18: Sizing Model Details

Component	Material	Material Model	Element Type	Element Size (mm)
Fixture	Steel 17-4 PH	Elastic, Isotropic (Table 4.1)	CAX8R	1
Ring	Polyurethane 95A	Hyperelastic, Isotropic (Table 4.12)	CAX8RH	1
Specimen	T700-Epxoy	Elastic, Isotropic (Table 4.4)	CAX8R	0.5

Prediction Model

The second model was made to predict the stress state in the specimen during the test. It featured individually modelled plies with cohesive contact between each ply. The details of this model are shown in Table 4.19 and the FEM is shown in Figure 4.25. This was termed as the 'prediction model'. The presence of generalized axisymmetric elements made it resource-intensive and to stay within the available memory, rigid body representations of the fixture components were used.

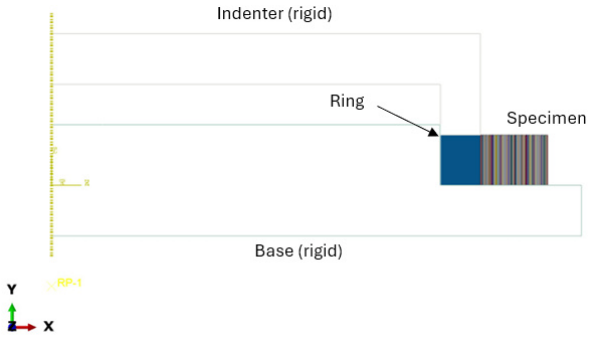

Figure 4.25: Prediction Model

Table 4.19: Prediction Model Details

Component	Material	Material Model	Element Type	Element Size (mm)
Ring	Polyurethane 95A	Hyperelastic, Isotropic (Table 4.12)	CAX8RH	0.5
Specimen	T700-Epxoy	Elastic, Orthotropic (Table 4.2 & Table 4.16)	CGAX8R	0.5

4.5.5. FEM Validation

To ensure the results of the FEM were reliable, it was compared with the initially calculated results. The peak stress from the FEA was compared to the theoretical peak stress. calculated below. The indenter was observed to bend as well as rotate under compression. From Figure 4.14, considering the bending load case, $K_t = 1.39$ was used in Equation 4.10.

$$\sigma_{field} = \frac{F}{A} = \frac{4 \times 1200}{\pi(170^2 - 154^2)} = 294.73\ MPa$$
$$\sigma_{peak} = K_t \sigma_{field} = 1.39 \times 294.73 = 409.68\ MPa \tag{4.10}$$

The peak stress at the integration point in the FEM was 414.67 MPa, using the indenter model from Figure 4.23. The K_t in the FEM was then calculated using Equation 4.6 to be 1.406. The peak stresses from the FEM were just 0.25% higher. This ensured the stresses extracted from the model were reliable.

Further comparisons were done between the force-displacement and force-radial pressure curves, shown in Figure 4.26.

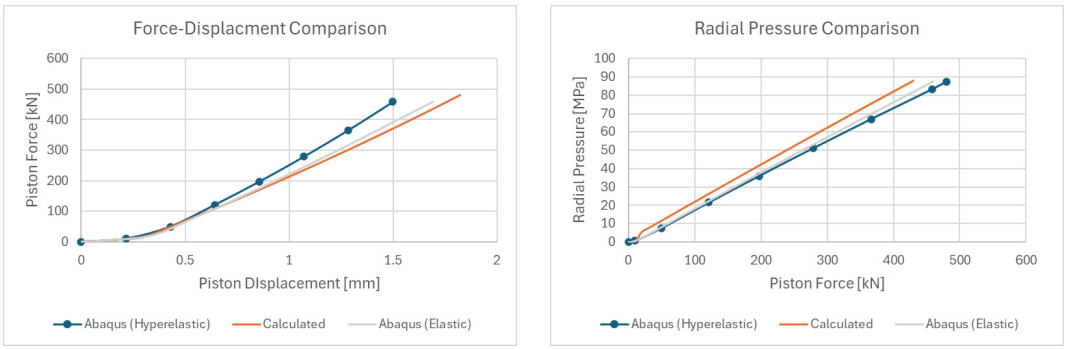

(a) Calculated Force Comparison **(b)** Calculated Performance Comparison

Figure 4.26: Comparison of FEM with Initial Calculations for Tank Specimens

From Figure 4.26 (b), the initial calculations in subsection A.2.2 under-predicted the force required by 12%. It did not capture the non-linear behaviour that was exhibited by the hyper-elastic material model used in Abaqus. However, it was a closer match to the elastic material behaviour. Hence, the calculations could be used for preliminary parameter studies, but the final implementations were done in the FEM.

Finally, the behaviour of the sizing model and prediction model were compared. Both had the same results, as shown in Figure 4.27. Hence, they could be used inter-changeably.

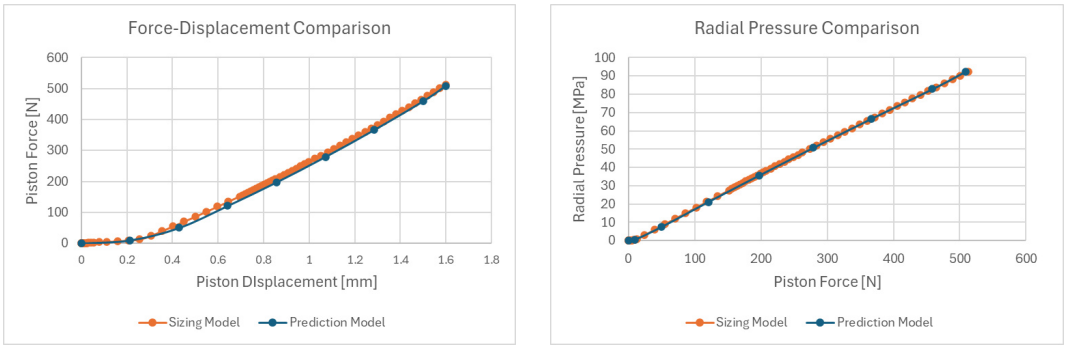

(a) Model Force Comparison **(b)** Model Performance Comparison

Figure 4.27: Comparison of Sizing and Prediction Models

4.6. Design Through Analysis

The sizing model, shown in Figure 4.24 was used as the starting point for the design. The FEMs created were parametric which to allow iterations on the critical dimensions.

The parameters that were designed for are listed in their individual sections. Each parameter was inter-linked and imposed constraints on other parameters. Hence, the order of the following sections is independent of the order in which they were determined. The parameters are also categorized based on the component they belong to.

4.6.1. Functional Design

Crucial parameters such as the height of the specimen and the thickness of the ring had to be determined initially. These parameters greatly controlled the performance and the design of the setup.

While creating the FEMs, two challenges were observed. First, the stress state in the specimen was not uniform across its height. Second, there was a design challenge to prevent the elastomer from squeezing out under pressure. Both were addressed by using taper angles.

Taper Angles

The initial design included a taper angle on the indenter. The idea was to prevent the elastomer from squeezing out by creating a seal between the indenter and the specimen. At the same time, the indenter must not contact the specimen. That would apply high edge stresses, which would detrimental to the specimen and the test.

It was also noticed that putting the taper angle on the indenter, while having a flat base, caused the specimen to twist about its cross-section. The reason was determined to be the uneven loading along the height of the specimen as the test progressed. As the ring got compressed, no load was applied near the top edge, which caused it to twist inward, shown in Figure 4.28 (a).

The twist also pushed the specimen's inner bottom corner into the base, creating additional compressive stresses on that edge. At high displacements, the twist increased, increasing friction as the specimen slid on the base. This would have led to heating and deterioration of the edge in the test.

Both challenges were solved by adding a symmetric taper angle on the base and the indenter. Being geometrically symmetric, the specimen was loaded only at the centre, with no edge stresses. The effect is shown in Figure 4.28 (b).

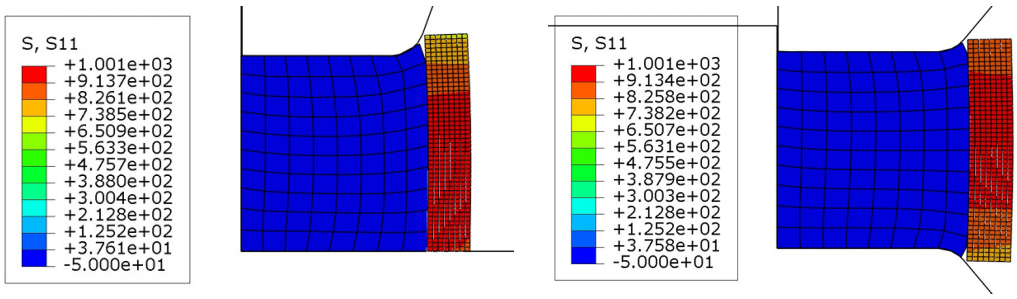

(a) Tapered Indenter, Flat Base **(b)** Tapered Indenter and Base

Figure 4.28: Thin Ring Hoop Stress at 1 mm Piston Displacement

The taper angle was determined as a function of the piston displacement required to cause a certain radial expansion of the specimen. The displacement depended significantly on the radial gaps between the elastomer ring, fixture, and specimen at the start of the test. For the measured radial expansion (u_1) at a known piston displacement (u_2), Equation 4.11 was derived from Figure 4.28 to calculate the taper angle.

$$\epsilon_{xx} = u_2/r$$
$$\epsilon_{yy} = \nu_{xy}\epsilon_{xx} = \nu_{xy}u_2/r$$
$$\theta = \tan^{-1}\left(\frac{u_2 + h\epsilon_{yy}}{2u_1}\right) \tag{4.11}$$

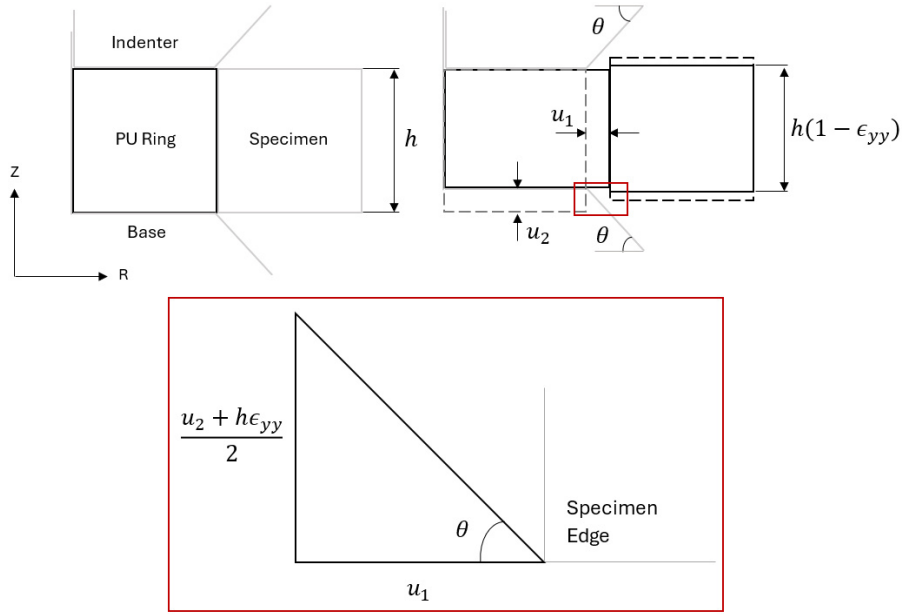

Figure 4.29: Taper Angle Calculation

The relevant radial expansion to measure in this case was u_1 of the inner edge node, minimum of the top and bottom edges. For the case shown in Figure 4.28 (b), $u_2 = 1.00\ mm$ and $u_1 = 0.52\ mm$. With these values, the taper angle was calculated using Equation 4.11.

$$\theta = \tan^{-1}\left(\frac{1 + 0.21 \times \frac{0.52}{85}}{2 \times 0.52}\right) = 43.91°$$

The taper angle was also affected by the polyurethane's stiffness. It was observed from Figure 4.5 that the polyurethane softened over 4 cycles before its stiffness stabilized. This behaviour had a marginal effect on the angle.

A major factor was also the difference between the height of specimen and the ring. It was observed from Table 4.8 that the height of the polyurethane reduced successively under cyclic compression. The angle thus had to accommodate cases where the the height of the ring at the start of the cycle might be lower than that of the specimen.

Hence, the taper angle calculated had to account for,

1. Radial gaps initially present between contact surfaces, which was controlled by the manufacturing tolerances.
2. Specimen's hoop stiffness, which depended on both its material's modulus and layup.
3. Elastomer's constrained stiffness, which was defined by its hardness and compressibility.
4. Successive reduction in the elastomer's height during the test.

The worst case scenario comprised a 0.2 mm radial gap and a PU 90A ring, with a 0.2 mm height reduction. The angle was thus calculated by modelling the worst case scenario in the FEM and measuring the specimen's radial expansion. Accounting for manufacturing tolerances, it was 50°.

Hence, the symmetric taper was added with a slightly higher-than-calculated angle to maintain a gap. With this change, the stress distribution along the specimen's height was more symmetric about its axial mid-plane.

Specimen Height

A higher specimen decreased the effect of free-edge shear stresses on the gauge section, while the magnitude of the stresses remained the same. However, increasing the specimen height would increase the amount of material used in each test, which was to be minimized.

The shear stress distribution is shown in Figure 4.30. The 20 mm specimen experienced higher bending, leading to slightly higher ply shear stresses. The effect of increasing the specimen height on the setup's behaviour is shown in Figure 4.31.

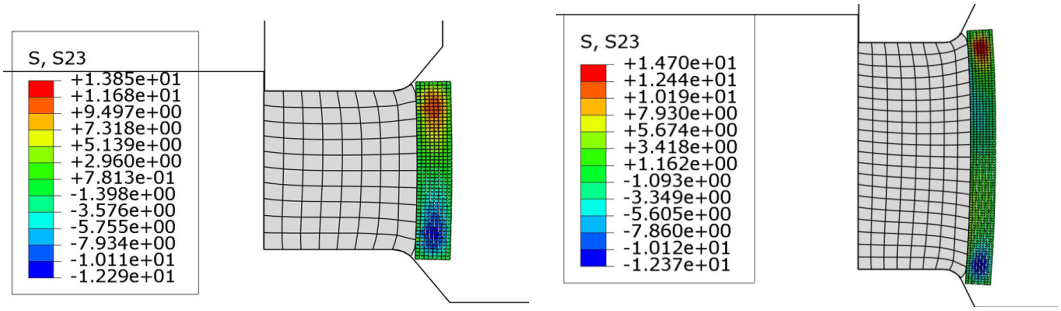

(a) 10 mm Specimen **(b)** 20 mm Specimen

Figure 4.30: Thin Ring Transverse Shear Stress

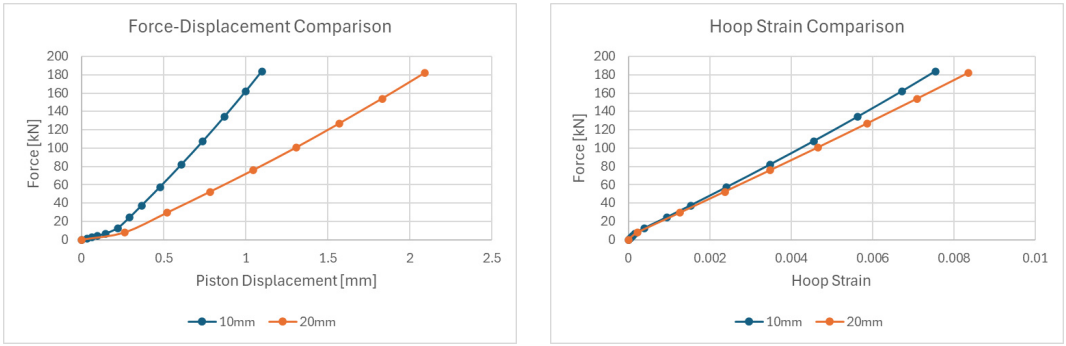

(a) Displacement Required **(b)** Forces Required

Figure 4.31: Effect of Specimen Height on Performance for Thin Rings

While at the same applied force, the 20 mm specimen experienced 11% higher hoop strain, the displacement required was 90% higher, from 1.1 mm to 2.1 mm. For a tank specimen burst test, the setup would exceed the 4 mm displacement limit set by the indenter depth. The depth, in turn, was controlled by the ring thickness and the indenter's taper width. It cannot be increased without compromising its stiffness and strength. These constraints are explained in detail in subsection 4.6.3.

Hence, to stay within the displacement limit and to reduce material usage, the specimen height of 10 mm was chosen.

Ring Thickness

As per the requirements, the forces in the test had to stay within the 500 kN test bench limit. This limit would be reached only when testing the tank specimens. The parameter which had the greatest effect on the required force was the elastomer ring thickness. It was the difference between the outer and inner

radii of the polyurethane ring. To reduce the thickness, the inner diameter of the rings was increased. Its effect on the setup's performance and force requirements are shown in Figure 4.32. The forces shown in Figure 4.32 (b) were required for the tank specimen fatigue tests. For that, the ring was required to apply 87.5 MPa of radial pressure on the specimen.

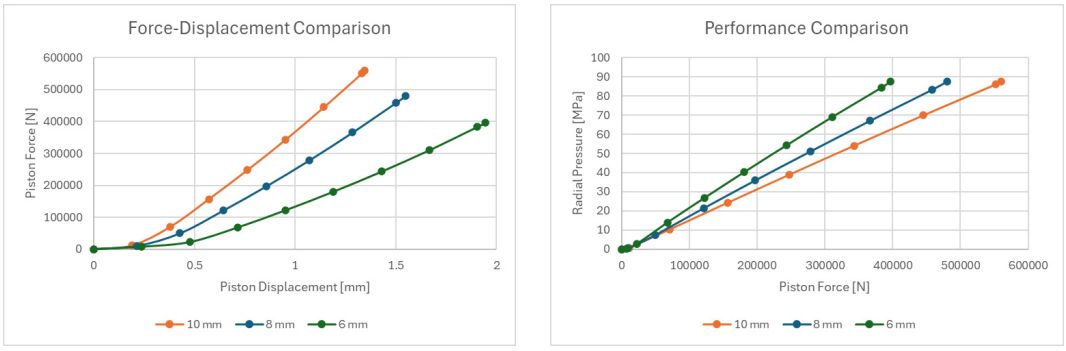

(a) Displacement Required

(b) Forces Required

Figure 4.32: Effect of Ring Thickness on Performance for Tank Specimens

A thickness higher than 8 mm was predicted to exceed the test bench limits. Even though it led to a safer design, the higher force requirement made it unviable. A 6 mm thick ring was safely within the 500 kN limit. However, it posed a series of challenges. The higher displacement required a deeper indenter. Since the indenter must match the ring thickness, it led to a thinner, deeper indenter design. This reduced its stiffness which led to much higher bending stresses reacted at the fillet corner. This risked an unsafe design.

Hence, the ring thickness chosen was 8 mm. It was predicted to stay within the 500 kN limit and, as shown in subsection 4.6.3, it led to a safe design of the indenter.

Ring Height

The ring was expected to reduce in height in subsequent cycles. Its height had to account for the compression set of 30%, estimated in Equation 4.2. From Figure 4.32 (a), the compressed height was estimated as $t_n = 9\ mm$. After the ring was relieved of compression, it should ideally recover to the specimen height $t_i = 10\ mm$. Starting from Equation 4.2, the compression set of 30% was used. The initial ring height, t_o, was then calculated in Equation 4.12.

$$
\begin{aligned}
C_B &= \frac{t_o - t_i}{t_o - t_n} \\
t_o = \frac{t_i - C_B\, t_n}{1 - C_B} &= \frac{10.0 - 0.30 \times 9.0}{1 - 0.30} \\
t_i &= 10.43\ mm
\end{aligned}
\tag{4.12}
$$

Hence, in the worst case, the initial height of the ring should be 10.43 mm to account for a permanent compression set. In fatigue, the height recovery after a loading cycle was expected to be quicker. Extending the results from Table 4.8, the height reduction after every cycle was expected to be proportional to the compressed height.

4.6.2. Sizing Loads

Before proceeding to detailed design, the sizing loads for static and fatigue cases were determined. The maximum forces expected during the tests were estimated through the FEM, shown in Table 4.20.

Table 4.20: Maximum Test Bench Forces Required

Specimen	Fatigue (kN)	Burst (kN)
Tank	480	900
Thin	315**	350*

*Assuming 2000 MPa hoop tensile strength.
**Assuming low-cycle fatigue at 90% of hoop strength.

The highest forces were required to reach the target fatigue and burst pressures on the tank specimens. In these conditions, the fixture's surfaces contact with the PU ring would experience contact pressures higher than the target pressure applied on the specimen.

However, with an increase in force, the relation between the specimen radial pressure and the pressure on the contact faces was linear. Since the FEM faced convergence issues at high displacements, these linear relations or factors were used to scale up the contact pressures for the burst pressure case. These pressures, shown in Table 4.21, were used to estimate the margin of safety for the fixture's parts.

Table 4.21: Fixture Contact Pressures for Tank Specimen Tests

Contact Face	Fatigue (MPa)	Burst (MPa)	Factor
Specimen Radial	87.5	157.5	-
Indenter Axial	114	205	1.302
Base Axial	112	201	1.275
Base Radial	85	145	0.973

4.6.3. Indenter Design

The indenter was made of 17-4 PH steel. The properties shown in Table 4.1 were used for the strength estimation. It was designed as a flat plate with a protruding annular ring. It included a hole to accommodate the centring pin on the base. A schematic drawing of the indenter and its parameters is shown in Figure 4.33.

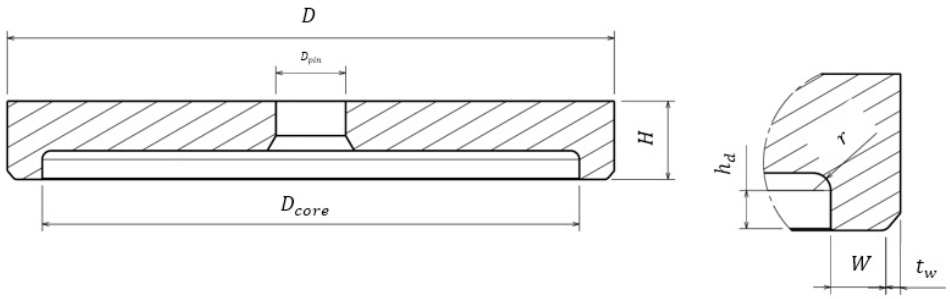

Figure 4.33: Indenter Dimension Nomenclature

The main parameters that ensured its effectiveness were its taper width (t_w) and depth (h_d). The width (W) must match that of the ring, which was determined to be 8 mm. The taper angle was determined in subsection 4.6.1.

The depth was designed to be sufficient for a burst test using the backup UHMWPE ring. The maximum displacement predicted with the sizing model was 3 mm. The fillet radius (r) was added to the depth. However, several factors could affect the maximum displacement. The piston could have an impulse due to the sudden failure of the specimen. If the specimen had a lower stiffness, it would also lead to higher displacements. To account for these cases, the depth was made as large as possible without having an adverse effect on the bending behaviour.

Increasing the depth, however, increased the outward bending of the indenter, shown in Figure 4.34 (a). The bending induced tensile stresses at the fillet corner, which were not desirable in fatigue.

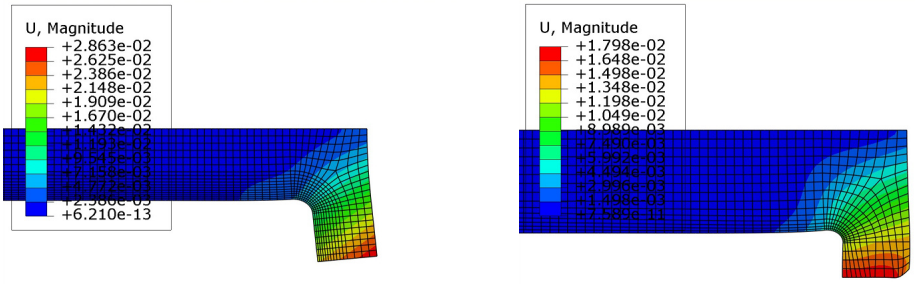

(a) Initial Concept **(b)** Final Design

Figure 4.34: Deformation at Maximum Contact Pressure (Scale: 100×)

The bending was balanced by the tapered edge. The taper width (t_w) added on the outside limited the outward bending. The added material increased the stiffness. However, at higher loads, the elastomer ring curved around the edge of the indenter. It applied pressure on the tapered edge and caused it to bend inwards.

The required width was estimated by calculating the maximum increase in diameter of the two specimens. For thin specimens, considering a hoop tensile strength of 2400 MPa, the radial expansion was calculated using Equation 3.7 and Equation 3.8.

$$\epsilon_\theta = \frac{X_T}{E_{11}} = \frac{2400}{139340} = 0.0172$$
$$\Delta d = \epsilon_\theta d_{initial} = 0.0172 \times 170 = 2.92$$

For the tank specimens, the increase in diameter was calculated at the burst internal pressure of 157.5 MPa, using Equation 3.6, Equation 3.7, and Equation 3.8.

$$\sigma_\theta = \frac{P d_{mean}}{2t} = \frac{157.5 \times 183}{2 \times 13.32} = 1081.93\ MPa$$
$$\epsilon_\theta = \frac{\sigma_\theta}{E_{xx}} = \frac{1081.93}{68440} = 0.0158$$
$$\Delta d = \epsilon_\theta d_{initial} = 0.0158 \times 170 = 2.69\ mm \tag{4.13}$$

The taper width was determined in Equation 4.14 based on the maximum radial expansion.

$$\Delta r_{max} = \frac{2.92}{2} = 1.46\ mm$$
$$t_w \geq = \Delta r_{max} = 1.5\ mm \tag{4.14}$$

The total height H was 22.5 mm. It was determined as the minimum required to effectively accommodate the centring pin.

Static Strength Estimation

The static strength was determined for the indenter at the burst contact pressure, from Table 4.21. The nodal stress were compared to estimate the strength. The stress is shown in Figure 4.35.

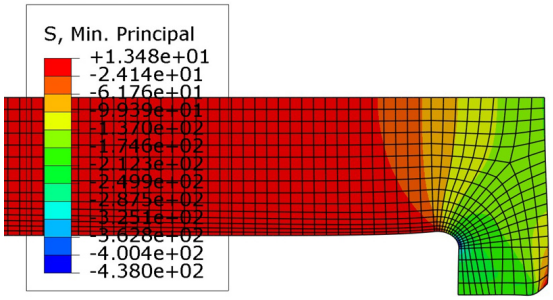

Figure 4.35: Nodal Min Principal Stress at Tank Burst Pressure (Table 4.21)

The margin of safety was calculated in Equation 4.15 by comparing it to the yield strength in compression, from Table 4.1.

$$MS = \frac{F_{CY}}{\sigma_{minP}} - 1 = \frac{717}{438} - 1$$
$$MS = +0.63 \tag{4.15}$$

Fatigue Life Estimation

The SN curve for the material was estimated from the F_{CY} of the 17-4 PH Steel, using the Basquin relation approximation. The considerations made for notched steel specimens in tension were assumed to be applicable in compression as well [59].

The endurance limit (σ_f) of steel is usually 0.5× its ultimate tensile strength (F_{TU}). It was assumed that in compression, a similar relation would hold with the yield compressive strength (F_{CY}). At $R = -1$, the endurance limit was calculated in Equation 4.16.

$$\sigma_f = 0.5 \times F_{CY} = 0.5 \times 717$$
$$\sigma_{f,\,\sigma_m=0} = 358.5\ MPa \tag{4.16}$$

Correcting for mean stress effect, at $R = 0.1$, the mean and amplitude stresses were calculated in Equation 4.17 and Equation 4.18, respectively.

$$\sigma_{max} = F_{CY} = 717\ MPa$$
$$\sigma_{min} = R\ F_{CY} = 0.1 \times 717 = 71.7\ MPa$$
$$\sigma_m = \frac{\sigma_{max} + \sigma_{min}}{2} = 394.35\ MPa \tag{4.17}$$
$$\sigma_a = \sigma_{max} - \sigma_m = 322.65\ MPa \tag{4.18}$$

For steel, the Goodman correction is more applicable [59]. Hence, the fatigue limit was calculated using the same in Equation 4.19.

$$\frac{\sigma_f}{\sigma_{f,\,\sigma_m=0}} = 1 - \frac{\sigma_m}{F_{CY}} \tag{4.19}$$
$$\sigma_f = \sigma_{f,\,\sigma_m=0}\left(1 - \frac{\sigma_m}{F_{CY}}\right)$$
$$\sigma_f = 358.5 \times \left(1 - \frac{394.35}{717}\right) = 161.325\ MPa$$

To account for the expected machined surface roughness, a reduction factor, $\gamma = 0.78$, was used for steel, shown in Figure 4.36.

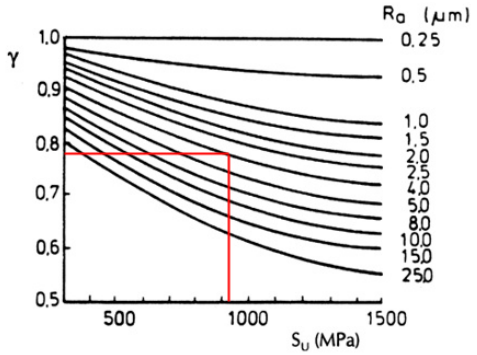

Figure 4.36: Surface Roughness Reduction Factor for Steels [59]

The final endurance limit, including the reduction factor was calculated in Equation 4.20.

$$\begin{aligned} \sigma_f &= 0.78 \times 161.325 \\ \sigma_f &= 125.83\ MPa \end{aligned} \tag{4.20}$$

Under fatigue loading, the maximum forces were expected during the tank specimen tests, shown in Table 4.20. The corresponding nodal stress at the fillet surface is shown in Figure 4.37.

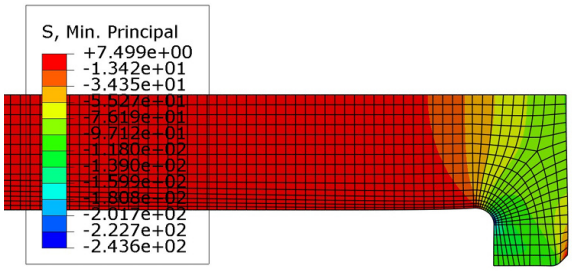

Figure 4.37: Nodal Min Principal Stress at Tank Fatigue Pressure (Table 4.21)

As the stress considered was at the fillet surface, it accounted for the effect of stress concentration. In section 4.5, the stress results at the fillet region were validated. From the critical nodal stress, at $R = 0.1$, the mean and amplitude stresses were calculated Equation 4.17 and Equation 4.18, respectively.

$$\begin{aligned} \sigma_{max} &= 243.60\ MPa \\ \sigma_{min} &= R\ \sigma_{max} = 24.36\ MPa \\ \sigma_m &= \frac{\sigma_{max} + \sigma_{min}}{2} = 133.98\ MPa \\ \sigma_a &= \sigma_{max} - \sigma_m = 109.62\ MPa \end{aligned}$$

The margin of safety was calculated by comparing the maximum amplitude stress to the endurance limit in Equation 4.21

$$MS = \frac{\sigma_f}{\sigma_a} - 1 = \frac{125.83}{109.62} - 1 = +0.14 \tag{4.21}$$

A visual representation of the calculations, using Basquin's relation, is shown in Figure 4.38. As shown, the indenter was predicted to be safe from failure within the fatigue test envelope. Repeated tank

specimen burst tests, at $\sigma_a = 219\ MPa$ ($R = 0$, $\sigma_{max} = 438\ MPa$), could still shorten the life of the indenter to 10000 burst cycles.

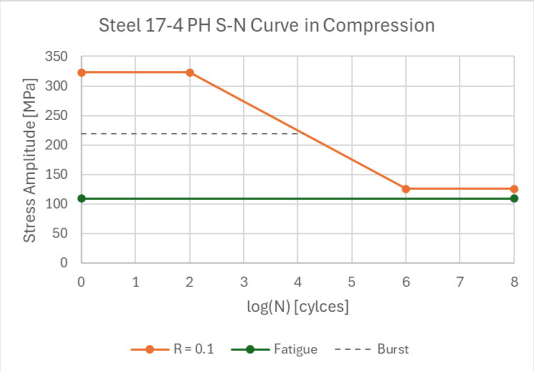

Figure 4.38: Indenter Fatigue Life Estimation

4.6.4. Base Design

The function of the base was to provide a constraint for the polyurethane ring. The base also needed to provide centring support for the indenter. Lastly, it had to effectively support the ring and specimen without excessively deforming itself.

When compressed axially, the ring would first expand radially outwards. However, when pressed against the specimen, it would have to fill up the volume before it could pressurize the specimen internally. The base was designed in two parts, shown in Figure 4.39.

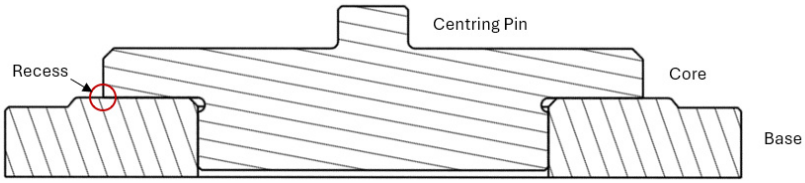

Figure 4.39: Base Assembly and Recessed Corner

Split Parts

A recess was designed to house the ring. It created a closed volume between the fixture's contact surfaces and the specimen. The ring had a rectangular cross-section with sharp corners. To house it in the recess without having to machine the ring's edges, the recessed corner also had to be sharp, marked in Figure 4.39.

This created a challenge as that corner was a stress concentration region. Since the axial and radial faces would be under pressure, the corner faced an opening stress. For a small fillet radius, the tensile stress at the surface during a burst test would exceed the tensile strength of the steel, shown in Figure 4.40.

Hence, the corner was at risk of yielding. After which, crack formation and progression would happen. To prevent this, a fillet radius of at least 0.6 mm was required. The ring edge would have to be machined for it to sit flush in the recess. This was a challenge as the thin elastomer ring was flexible.

To solve this, the top half of the base was made into a separate part - the core. The two parts were designed to be connected by a screw thread. It allowed for the core to be a modular part, for future design iterations. It also accounted for a practical problem where the ring might get stuck in the recess.

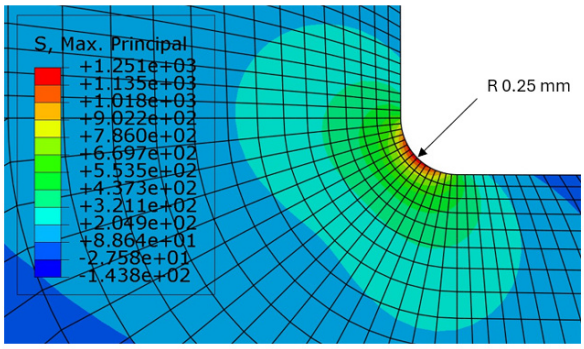

Figure 4.40: Recess Corner Stress Concentration at Tank Burst Pressure (Figure 4.39)

Base Dimensions

The base was designed to be wide enough (D) to accommodate the tank specimens. Hence, a diameter of 210 mm was chosen. It allowed enough gap to allow for a protective shield to be attached to its outside, leaving room for the specimen. A schematic is shown in Figure 4.41.

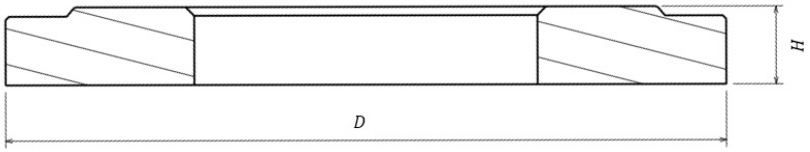

Figure 4.41: Base Design

The height (H) was determined considering the stress distribution through the thickness. It was ensured that an effective threaded depth could be accommodated. It was 22.5 mm, symmetric with the indenter. It was also required to accommodate $M8$ holes along the outer circumference. The holes were required for gripping during assembly, and to attach the protective shield.

Core Design

The core was the central part of the fixture. It ensured the indenter was aligned and provided a radial constraint for the ring. A schematic is shown Figure 4.42.

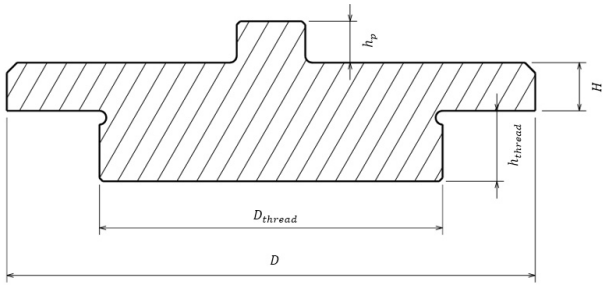

Figure 4.42: Core Design

For the thread diameter (D_{thread}), a standard $M100 \times 2.0$ thread was chosen. The thread depth (h_{thread}) was 20.5 mm. The flange extending from the thread diameter up to the core diameter (D) acted as a cantilevered plate. By adjusting the thread diameter, the vertical deflection of the plate was reduced. It also reduced the stresses reacted at the thread transition chamfer.

For the centring pin, the height was 12 mm. It was sufficient to ensure there was a 4 mm overlap with the indenter hole at the start of the test. Its height was limited by the height of the indenter (H). It was designed to not go past the indenter, else it would directly contact the compression plate.

The core height (H) included a chamfer to accommodate the fillet radius on the indenter. The height facing the ring was 11 mm. It was designed to accommodate a ring that was higher than the specimen. The larger height was needed to account for the compression set of the polyurethane.

The core diameter (D) matched the inner diameter of the ring and had a sliding fit with the indenter. The centring pin diameter was sized such that it is outside the maximum deformation zone. Hence, the stresses induced at the fillet corner were lower. The deformation behaviour is shown in Figure 4.43.

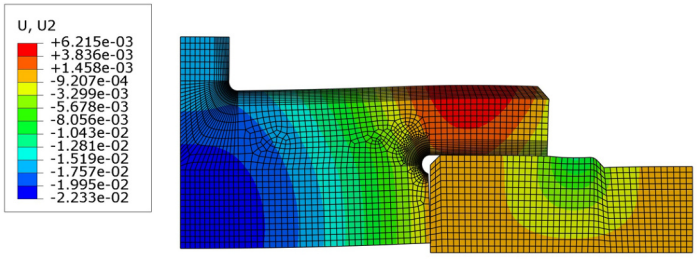

Figure 4.43: Base Assembly Deformation Behaviour at Tank Burst Pressure (Table 4.21, Scale: 50×)

The plate tends to bend up near its centre. The side facing the ring tends to bend down, pushing into the base. The vertical deformation is restrained by the screw thread.

Static Strength

Similar to the indenter, the core is sized to withstand the tank specimen burst test, from Table 4.20. The critical stress location was at the screw thread fillet, shown in Figure 4.44.

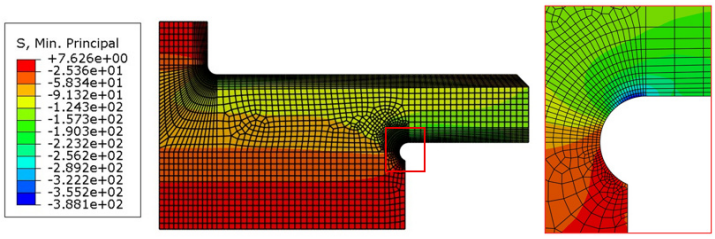

Figure 4.44: Core Nodal Stresses at Tank Burst Pressure (Table 4.21)

The critical nodal stress was compared to the yield strength in compression to calculate the margin of safety in Equation 4.22.

$$MS = \frac{F_{CY}}{\sigma_{minP}} - 1 = \frac{717}{388} - 1 = +0.84 \tag{4.22}$$

Similarly, for the base, the critical stress is shown in Figure 4.45.

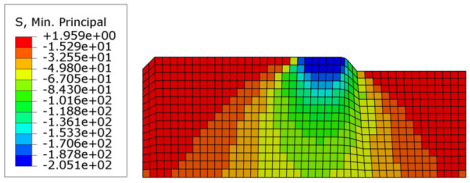

Figure 4.45: Base Nodal Stresses at Tank Burst Pressure (Table 4.21)

The margin of safety for the base was calculated in Equation 4.23,

$$MS = \frac{F_{CY}}{\sigma_{minP}} - 1 = \frac{717}{205} - 1 = +2.49 \tag{4.23}$$

The core and the base had sufficient strength to withstand the maximum stresses predicted. The indenter's fillet region was most the critical point in the design.

Fatigue Life Estimation

Between the two components, the core was more critical in terms of stresses. The fatigue life was estimated for the same. The critical stress in the core is shown in Figure 4.46.

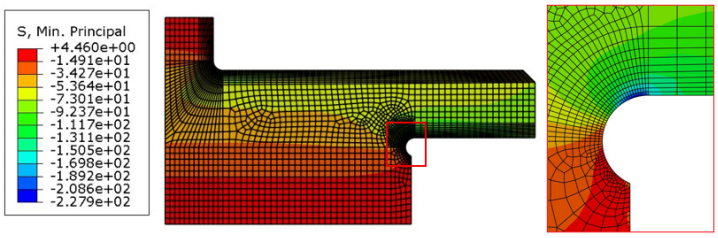

Figure 4.46: Core Nodal Stress at Tank Fatigue Pressure (Table 4.21)

The S-N curve approximation shown for the indenter was applied to the core as well. Continuing from Equation 4.20, the applied stresses were calculated. At $R = 0.1$ the mean and amplitude stresses were calculated using Equation 4.17 and Equation 4.18, respectively.

$$\sigma_{max} = 227.90\ MPa$$
$$\sigma_{min} = 22.79\ MPa$$
$$\sigma_m = \frac{\sigma_{max} + \sigma_{min}}{2} = 115.345\ MPa$$
$$\sigma_a = \sigma_{max} - \sigma_m = 102.555\ MPa$$

The margin of safety was calculated in Equation 4.24, using the endurance limit from Equation 4.20. The same is shown visually in Figure 4.47.

$$MS = \frac{\sigma_f}{\sigma_a} - 1 = \frac{125.83}{102.55} - 1 = +0.22 \tag{4.24}$$

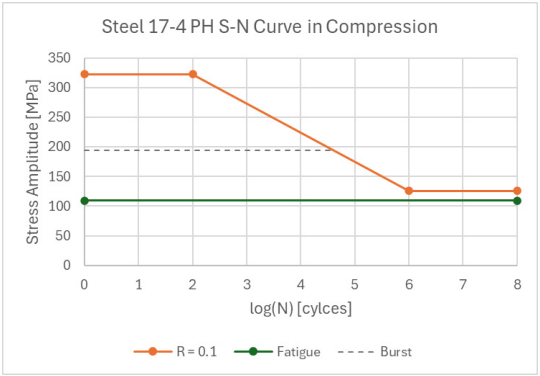

Figure 4.47: Core Fatigue Life Estimation

The σ_a was considered from the fillet region, and hence, included the effect of stress concentration. The σ_f accounted for a reduction factor due to surface roughness. With these considerations, the core was also predicted to be safe from failure within the fatigue test envelope. For repeated burst tests, it could reduce the life to 60000 cycles.

4.6.5. Design for Contingencies

Considerations were made during the design phase to account for contingencies such as jamming, sudden collapse, and collateral damage from burst tests. These were addressed while designing the setup and ensured that they did not affect the strength of the components.

Jamming

The centring pin and its hole on the indenter could get jammed if they were misaligned. This could be caused by the compression plates of the test bench not being perfectly parallel to each other. This was a concern as the 500 kN test bench did not have an adjustable cross-head.

The tightest tolerance was at the centring pin (20 $H7/f7$). For 4 mm of overlap at the start of the test. For 20 $H7/f7$, the minimum and maximum radial gaps were 0.010 mm and 0.031 mm, respectively. With the axial overlap and the radial gap, the allowable misalignment was calculated.

$$\theta_{min} = \tan^{-1}\left(\frac{0.010}{4.5}\right) = 0.13^\circ$$

$$\theta_{max} = \tan^{-1}\left(\frac{0.031}{4.5}\right) = 0.39^\circ$$

Any misalignment past this range could cause the setup to jam. An additional part was added to the design, the un-jammer. It was a plate with a central $M10 \times 1.5$ threaded hole. Three holes surrounded it at a radius of 50 mm, 120° apart. These were $M8$ holes without a thread. It is shown in Figure 4.48.

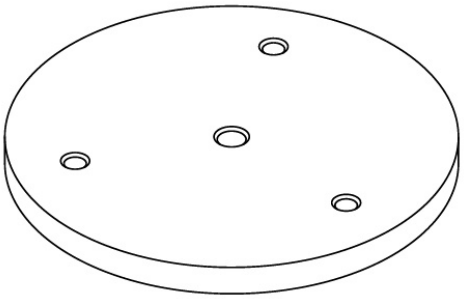

Figure 4.48: Un-jammer

The central hole was aligned with the indenter's centring pin hole. Three identical $M8 \times 1.5$ holes were made on the indenter to fit the un-jammer.

In case the indenter jammed on the core's centring pin, the un-jammer could be attached to the indenter through the three holes. Then, an $M10$ bolt could be screwed into the un-jammer. The bolt would rest on the centring pin of the core, pushing the indenter up as it is turned.

Collapse

If under high load, the specimen suddenly broke, the ring would be free to expand radially, which could collapse the fixture onto itself. This could damage the contact surfaces, especially the fillet corners on the indenter and the core.

To avoid this, axial contact surfaces were designed to ensure a secondary load path in case the setup bottomed out. The primary and secondary load paths for the fixture are shown in Figure 4.49.

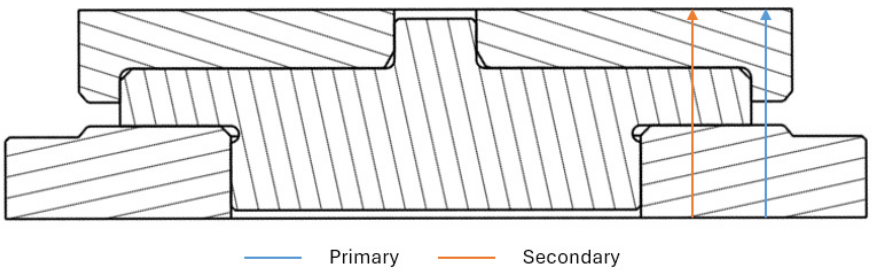

Figure 4.49: Secondary Load Path For Collapse

In that case, the loads would get transferred directly through the core. The surface area in contact, being much higher, would reduce the stresses acting on the fixture. The chamfers were sized to avoid contacting and damaging the fillet corners in any case.

Debris Containment

Upon failure, the specimen could burst, spreading carbon dust and debris around the test bench. To prevent safety issues that might arise due to that, a containment shield was designed. It included a window to allow for DIC and holes around the circumference at each quarter, to pass strain gauge wires. The schematic is shown in Figure 4.50.

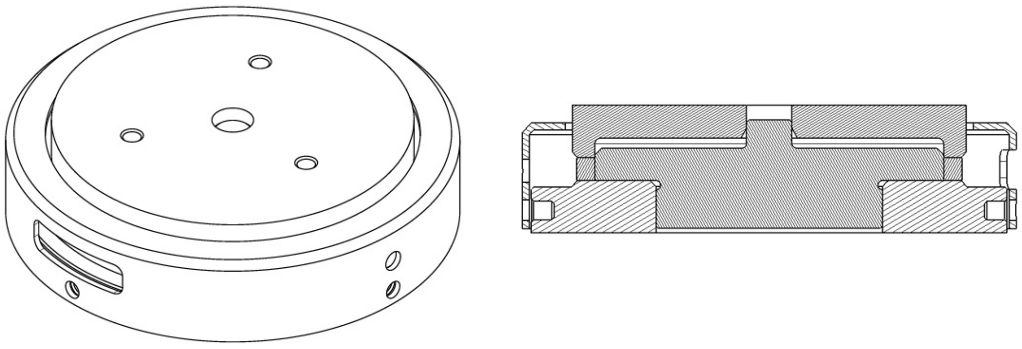

(a) Assembled Setup **(b)** Cross-section View

Figure 4.50: Shell Design

There was 1 mm of radial gap between the base and the shell. $M8$ holes were used to fix them together. Hence, they would move together. It was designed to rest 1 mm above the base and 1 mm below the indenter's limit, so it can not contact the compression plates. This was done to prevent shearing of the pins or bearing failure on the shell's holes at high loads.

The height of the DIC window was kept at 17 mm to accommodate the relative movement of the specimen. The width was a projected 60 mm to allow for a wide for a stereo setup. This was also required to allow sufficient light to illuminate the DIC pattern.

4.6.6. Design for Manufacturing and Assembly

To save time and cost for machining, the features in the components were kept simple. The parts were designed to be machined almost entirely by turning. Holes were added to the base and core to allow for assembly and disassembly using standard tools.

Fillets were only used where absolutely necessary, such as on the inner corner of the indenter. On the core, the fillet between the flange and the screw thread was required to prevent stress concentration. It was made deeper for the effectiveness of the screw thread and to ease machining. Fillets were also used on the tapered faces. This was required to have a smooth surface for the ring to move over. It was also required to prevent shearing and damaging the ring at high forces. Standard chamfers, holes, and tolerances were specified everywhere else.

Tolerances

Tolerances to defined to ensure a sliding fit between the fixture's surfaces. The dimensional tolerances used are listed in Table 4.22.

Table 4.22: Dimensional Tolerances

Indenter-Core	Indenter (hole)	Core (shaft)	
Tolerance Field	H7	f7	Gap
Min (mm)	154.000	153.957	0.043
Max (mm)	154.040	153.917	0.123
Centring Pin	**Indenter (hole)**	**Core (shaft)**	
Tolerance Field	H7	f7	Gap
Min (mm)	20.000	19.980	0.020
Max (mm)	20.021	19.959	0.062

Based on the defined tolerances of the indenter-core sliding interface, the tolerances for the ring material were defined. The maximum acceptable gap between the surfaces was 0.2 mm. The maximum gap that the taper angles were designed for was 0.4 mm. A minimum gap of 0.04 mm was specified to maintain a sliding contact. Based on assumed specimen diameter tolerances, the dimensional tolerances for the ring are shown in Table 4.23.

Table 4.23: Ring Dimensional Tolerances

Inner Diameter	Ring	Core	Gap
Min (mm)	153.997	153.957	0.040
Max (mm)	154.117	153.917	0.200
Outer Diameter	**Spec.**	**Ring**	**Gap**
Min (mm)	170.000	169.900	0.040
Max(mm)	170.100	169.960	0.200

These were specified to the polyurethane 95A rings supplier, Airlant, from Loncin, Belgium. Additionally, to account for the compression set of 30%, a height tolerance of $10^{+0.60}_{+0.35}$ mm was specified. An alternative PU 90A bar was ordered to be able to machine rings from it.

Surface finish tolerances were specified as $Ra = 0.4$ μm for the sliding interfaces. A flatness tolerance of 0.02 mm was specified for the surfaces that would contact the compression plates of the test bench. The final drawings were prepared by a colleague from Syensqo's workshop to send for machining.

4.6.7. Final Design

Steel 17-4 PH bars were ordered from Caseo based in Antwerp, Belgium. It took five weeks for the 3 pieces to be delivered. The parts were machined by Mecarudi in Brussels, Belgium. The final parts were machined in two weeks. The components and the assembly are shown in Figure 4.51.

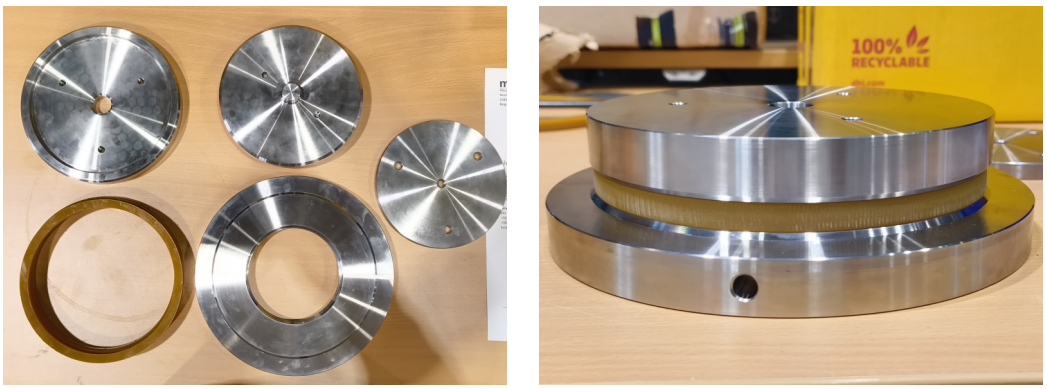

(a) Individual Parts **(b)** Assembled Setup

Figure 4.51: Final Setup

Rings

The initial PU 90A rings were cut from a sheet using the water-jet cutter at Syensqo. The dimensions were within the tolerances required. However, the cut surface had significant ridges. The PU 95A rings were received later. They seemed to be machined and had a smoother surface finish. Both are shown in Figure 4.52. The requested and actual dimensions are compared in Table 4.24.

The PU 90A rings were not within the specifications requested. Its inner and outer diameters exceeded the minimum and maximum tolerances, respectively. It made it challenging to fit the ring in setup along with the specimen. A work-around was tried where the setup was used to push the ring into place. However, it required caution as initial misalignments can cause the setup to jam.

(a) PU 90A **(b)** PU 95A

Figure 4.52: Polyurethane Rings and Surface

Table 4.24: Requested and Received Ring Dimensions (mm)

	Requested	PU 90A	PU 95A
Inner Diameter	154 (+0.117/−0.003)	153.67	154.04
Outer Diameter	170 (−0.04/−0.10)	170.36	169.50
Height	10 (+0.60/−0.35)	9.78	10.48

Un-jammer

The un-jammer was made from the Steel left over from the parts production. It is shown in action in Figure 4.53. Three $M8$ bolts and an $M10$ bolt were required for it as well.

(a) Assembly **(b)** Functioning

Figure 4.53: Un-jammer in Use

The $M8$ nuts were only required to fix it to the indenter. The central $M10$ bolt went through to the core, which then lifted the un-jammer, pulling the indenter with it. If it was jammed to a particular side, the $M8$ bolt on that side could be turned to push it against the core there.

Containment Shield

The shield was made from a 2 mm thick Steel sheet with unknown specification or properties. Holes were milled out on the flat sheet. It was then rolled into a cylinder and spot-welded. The top cap was also milled out from the sheet and spot-welded. This was done by a colleague in Syensqo's workshop. It is shown in Figure 4.54.

(a) Assembled with two 8 mm Pins **(b)** View through the DIC Window

Figure 4.54: Preliminary Containment Shield

Two 8 mm pins that were used to assemble the core and base could also be used to fix the shield. Two $M8$ bolts could also be used. The shield could also just be used without being fixed to the base. In that case, the compression plates must be large enough for the shield to rest on.

5

Fatigue Test Development

5.1. Preliminary Tests

Compression tests were performed on the PU rings without any specimens to study their behaviour. The tests were performed on the 250 kN Instron 5985 static test bench at Syensqo. The test bench had 150 mm diameter compression plates.

5.1.1. Free Compression Test

All tests were performed at a strain rate of 0.06 s^{-1}. The rings did expand radially outwards, as shown in Figure 5.1. The response was measured using a force-displacement curve, shown in Figure 5.2.

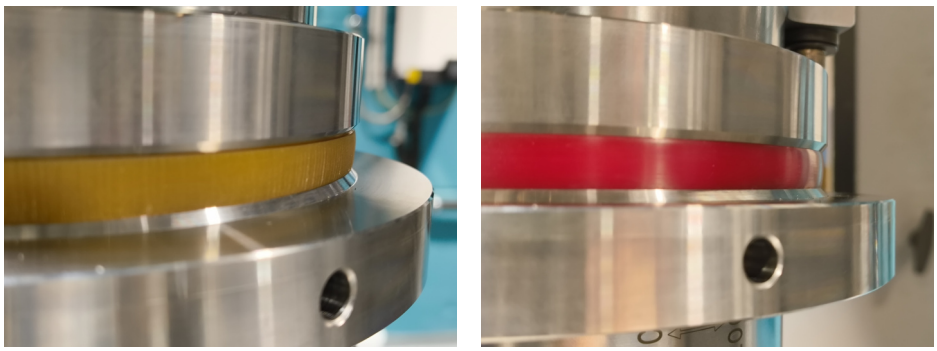

(a) PU 90A Ring **(b)** PU 95A Ring

Figure 5.1: Polyurethane Rings in Free Compression

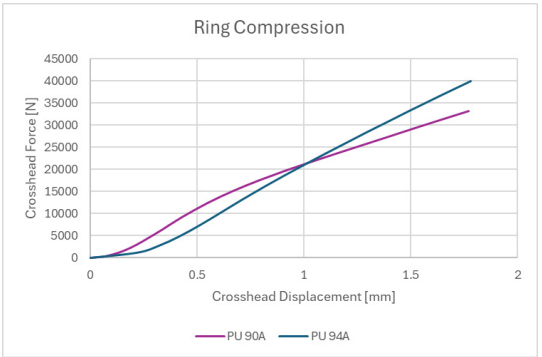

Figure 5.2: Ring Compression Behaviour Comparison

Both PU 90A and 95A showed the same initial stiffness. Past 10 kN, the 90A ring showed a linear softened behaviour. The 95A ring showed a more gradual softening, being approximately linear within the applied 1.8 mm of compression.

In the test, the free compression comprised the initial preload phase, when the ring would fill up the volume. The behaviour after that would be governed by the stiffness of the specimen. Hence, it was decided to that an actual specimen test would also be required to tune the material model.

5.1.2. Softening Test

To study the behaviour of the rings under repeated loading, 5 cycles each were applied to the PU 90A and the 95A rings. The tests were done up to 40 kN of cross-head force. The test results are shown in Figure 5.3.

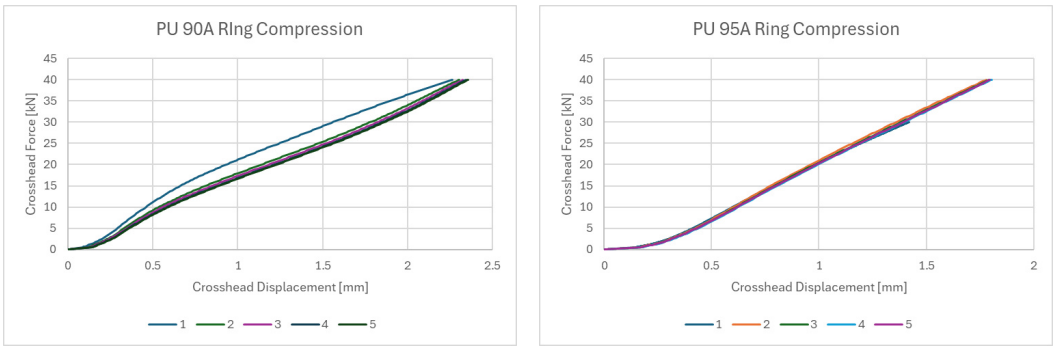

(a) PU 90A Ring **(b)** PU 95A Ring

Figure 5.3: Free Compression and Softening Behaviour

The 95A ring maintained its initial stiffness over the cycles. The first cycle was up to 30 kN. It showed minimal softening behaviour and an average displacement of 1.79 mm. The 90A ring showed immediate softening after the first cycle, which stabilized after 4 cycles. Towards the end, past 30 kN, the 90A ring seemed to revert to its initial stiffness. The softening effect was related to the applied compression displacement. This behaviour was expected to affect the loading of the specimen as well.

5.1.3. Proof-of-Concept Test

An initial test was performed as a proof-of-concept to see if the test worked. It was a basic setup with cross-head readings as outputs. Details of the specimen and test setup are shown in subsection A.3.1.

The initial test was up to 100 kN, to study the loading stiffness. The second test was up to burst. The force-displacement behaviour is shown in Figure 5.4

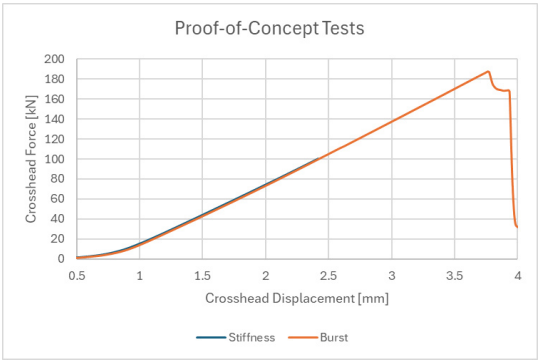

Figure 5.4: Test Results

The test was recorded using a mobile phone camera. Stills from the video were extracted in an attempt to study the failure progression. The stills and failed specimen close-ups are shown in Figure 5.5.

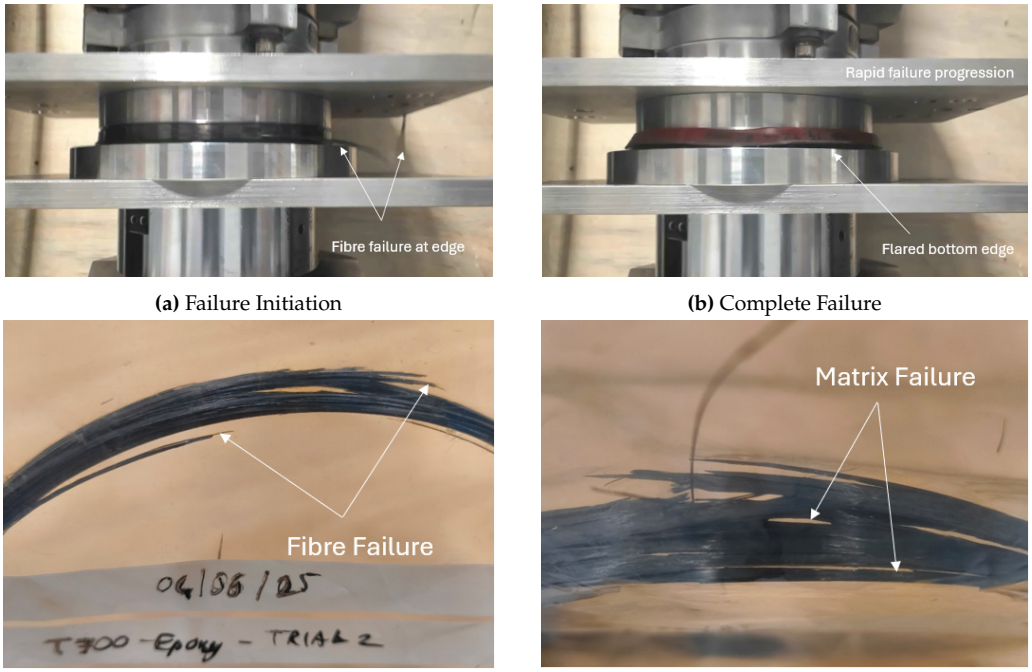

(a) Failure Initiation

(b) Complete Failure

(c) Fibre Breakage across Height

(d) Matrix Crack across Height

Figure 5.5: Specimen Failure and Close-ups

The first observation was that the ring flared at the bottom edge. Molybdenum Sulphide grease was used while fitting the ring and specimen around core of the fixture. This grease was also on the bottom face of the ring. Hence, the bottom face experienced much lower sliding friction than the top face. This caused it to flare out. This was likely the cause of the failure initiation at the specimen's bottom edge.

5.2. Stress State Predictions

Before proceeding to the tests, factors that could influence the results were predicted. The stress state induced in the test was studied. It was compared against two cases - an infinite cylinder and a ring specimen, both under uniform internal pressure.

The specimen was modelled using the script in subsection A.2.4. The ring boundary conditions were imposed on the model, by constraining cross-section rotation ($UR3 = 0$) on the inner edge of the first ply. The cylinder was simulated using symmetric boundary conditions ($U2 = UR2 = UR3 = 0$) on the top and bottom edges of the specimen. They were loaded with an internal pressure of 40 MPa, the average contact pressure expected in the thin specimen fatigue tests.

5.2.1. Thin Specimens

The pressure distribution along the specimen's height peaked at the centre of the specimen. It is compared the cylinder's case in Figure 5.6. The peaks at the edges were artefacts of the model.

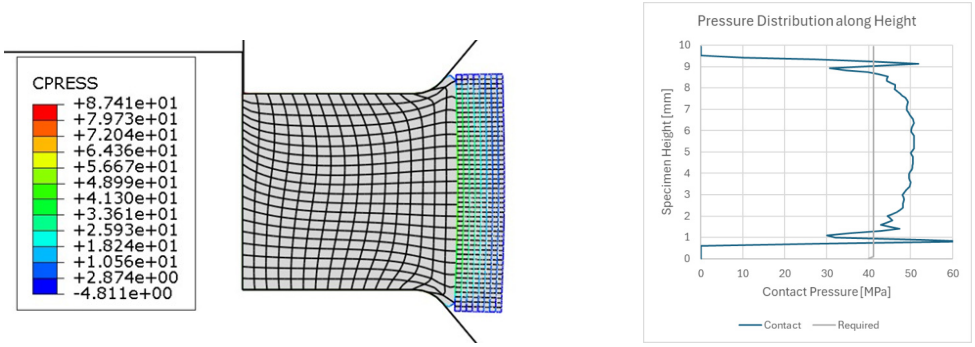

Figure 5.6: Contact Pressure Distribution in Thin Specimens

The hoop tensile stress distribution in each case was compared. Proportional to the pressure distribution, the hoop stress also peaked at the centre of the specimen's height. The comparison is shown in Figure 5.7.

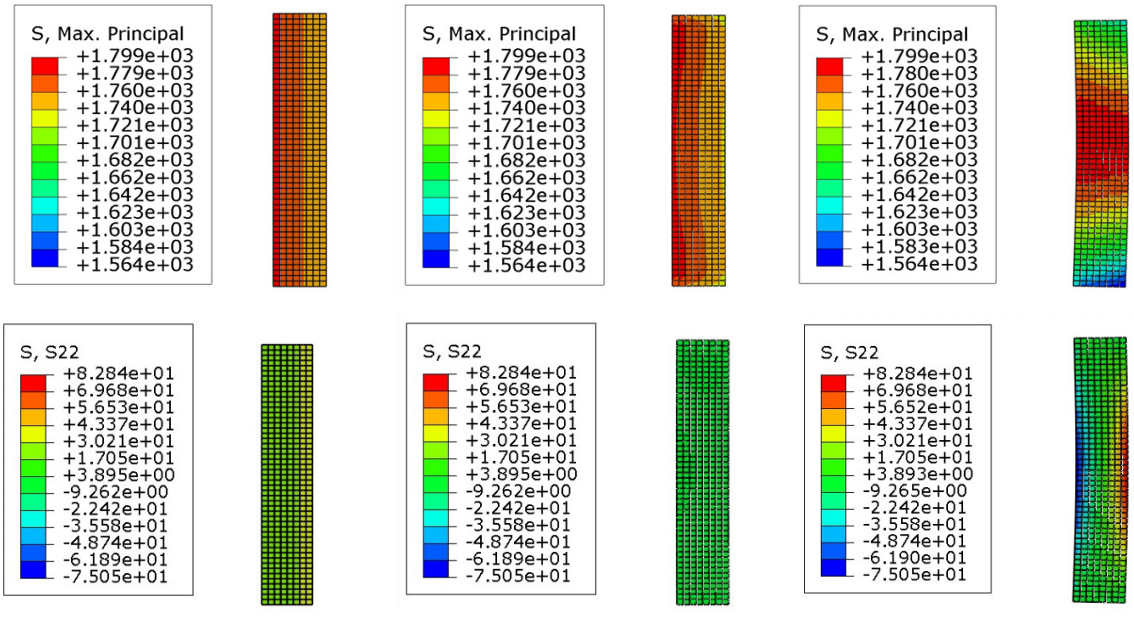

(a) Cylinder under Uniform Pressure **(b)** Specimen under Uniform Pressure **(c)** Specimen under Test Pressure

Figure 5.7: Hoop and Axial Stress Distribution in Thin Specimens

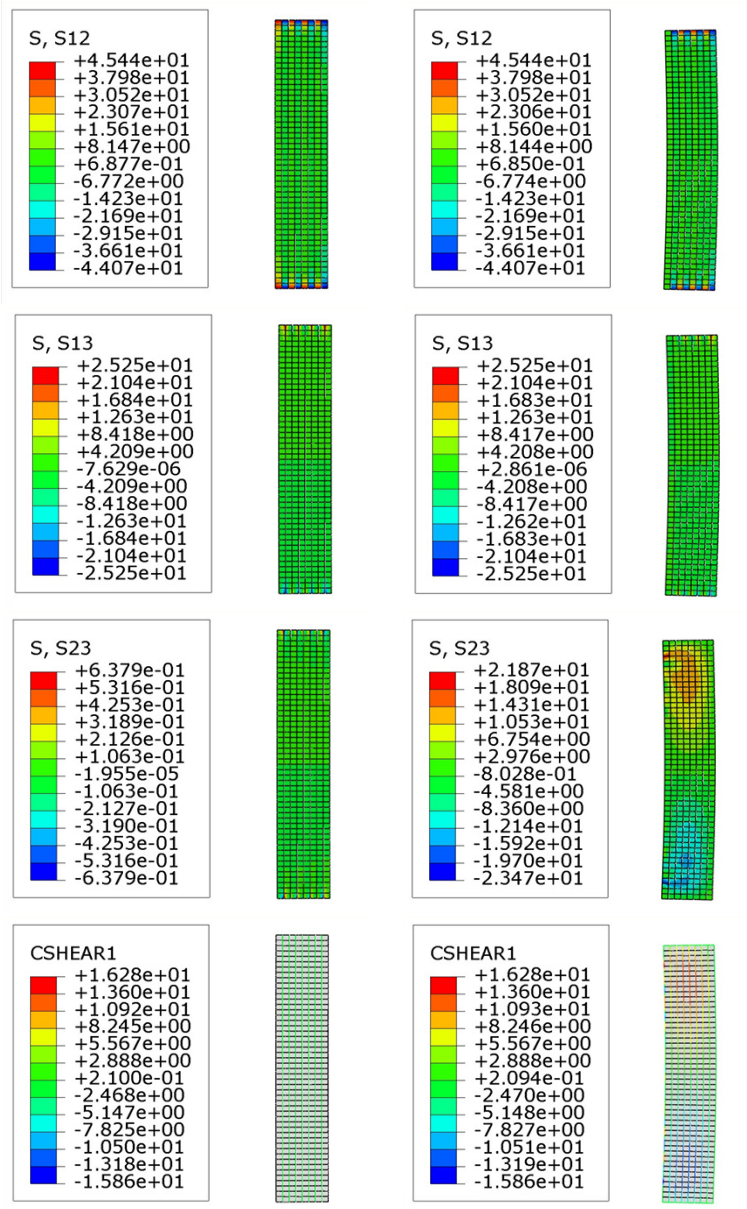

(a) Specimen under Uniform Pressure **(b)** Specimen under Test Pressure

Figure 5.8: Shear Stress Distribution in Thin Specimens

The matrix and interface shear stresses were also compared between the uniform pressure and test pressure cases. They are compared in Figure 5.8. The shear stresses in the cylinder were negligible and are not shown.

The shear stresses at the edges in the uniform pressure case were identical to the test case. These were due to the through-thickness shear transfer due to the free-edge effect [42]. The slight bulging in the test, however, induced transverse shear stresses in the specimen. These were also reflected in the increased interface shear stresses in the same region, as shown in Figure 5.8 (b).

The tools used to cut the tubes into rings would introduce damages such as fibre splits and matrix cracks. This was expected to be exacerbated by the hoop and shear stresses at the edges. These stress could directly interact with the cracks to initiate failure. This was observed in the segmented ring burst test, as shown in Figure 5.9.

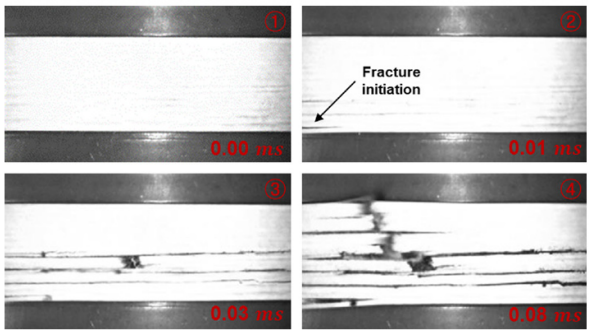

Figure 5.9: Failure Initiation in the Segmented Ring Burst Test [38]

In the current test developed, the hoop stresses would be concentrated at the centre, away from the edges. This was expected to reduce the chance of failure due to crack propagation from the edges. However, the transverse shear stresses could interact with the edge shear stresses to create matrix cracks or delamination within the specimen. This could have an effect on the hoop stiffness of the specimen.

However, a cause for concern was the high transverse tensile stress in the thin specimens. The ring central bulging of the ring would apply a combination of both hoop and axial tensile stresses on the specimen. For a hoop-wound specimen, this could cause early matrix cracking and failure. This must be taken care of by practical solutions such as lubricated surfaces which would allow for a more even expansion of the ring along its height. This was further explored in section 6.2.

5.2.2. Tank Specimens

The pressure distribution for tank specimens is shown in Figure 5.10. It peaked at the centre, similar to the thin specimens. It was also asymmetric about the mid-plane, causing a slight rotation of the specimen about its cross-section.

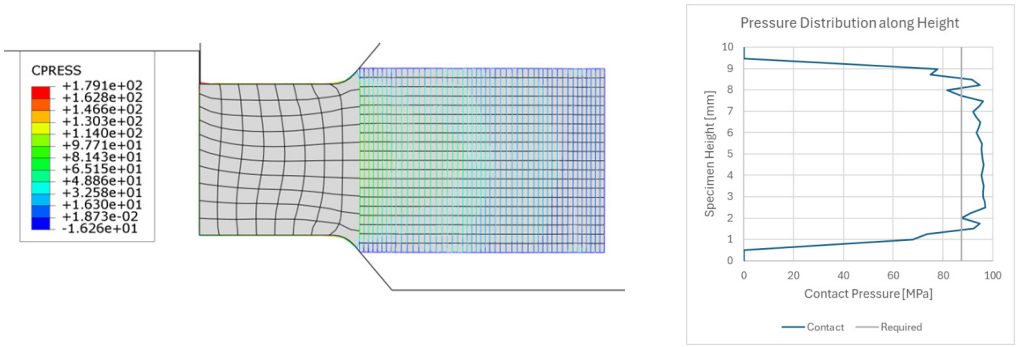

Figure 5.10: Contact Pressure Distribution in Tank Specimens

The hoop stress distribution was compared with the case of the cylindrical section of a tank, and with a ring section. Both were simulated with a uniform internal pressure of 87.5 MPa. The comparison is shown in Figure 5.11.

It was observed that at the same internal pressure, the ring deformed more, hence experiencing higher stress. This was explained through its lower radial stiffness, with no surrounding material to restrain its radial expansion. The specimen in the test case had the least stress owing to a lower average contact pressure and lower radial expansion. The effect of the slight curling of the cross-section could also be observed in Figure 5.11 (c).

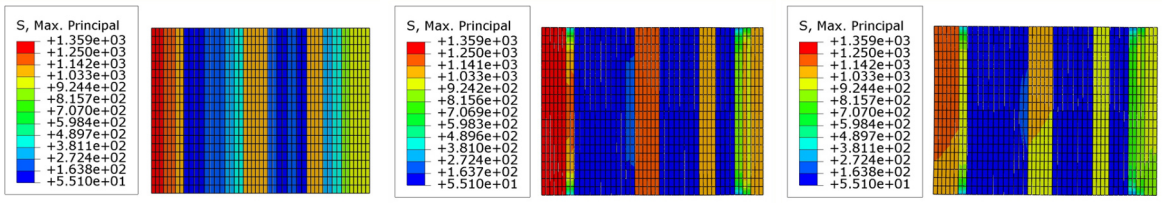

(a) Cylinder under Uniform Pressure **(b)** Specimen under Uniform Pressure **(c)** Specimen under Test Pressure

Figure 5.11: Hoop Stress Distribution in Tank Specimens

The shear stress distribution in the tank specimens could not be captured accurately in the model. Contrary to the hoop-wound thin specimens, the tank layup had helically-wound plies. In the filament winding process, this meant that there were both +/− orientated tapes in the same layer. This is shown on the right in Figure 5.12[1].

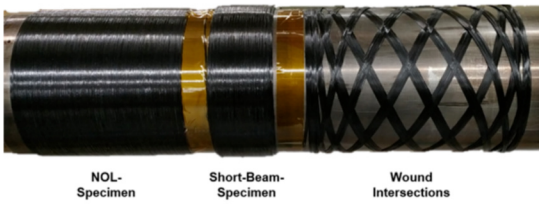

Figure 5.12: Filament Winding of Hoop and Helical Layers[1]

To capture this in the FEM, an effective hoop stiffness would have to be defined for the helical layers. However, in doing so, the shear stresses would not be captured. Hence, an approximate representation was attempted by modelling +/− layers as adjacent and separate [60]. The matrix and interface shear stresses are shown for the three cases in Figure 5.13.

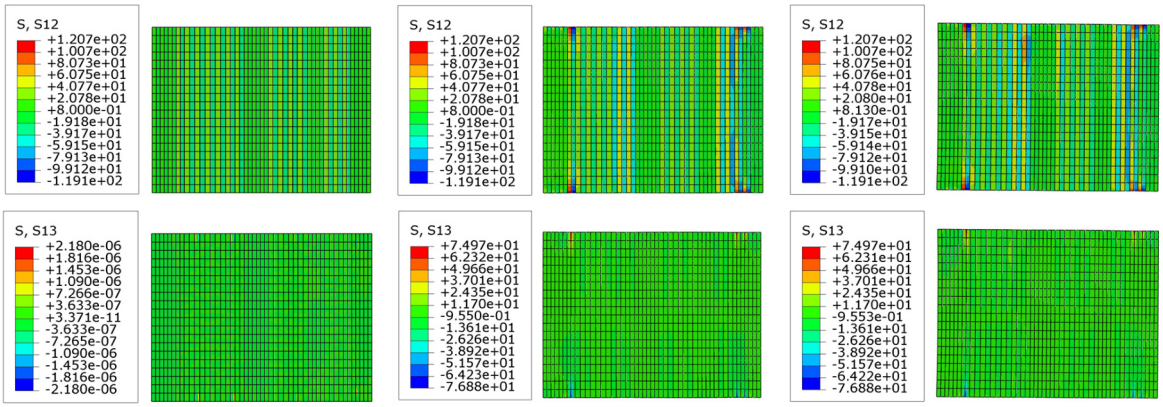

(a) Cylinder under Uniform Pressure **(b)** Specimen under Uniform Pressure **(c)** Specimen under Test Pressure

Figure 5.13: Shear Stress Distribution in Tank Specimens

[1] https://www.ivw.uni-kl.de/en/news/details/process-optimization-innovative-combination-of-adapted-resin-system-and-winding-process

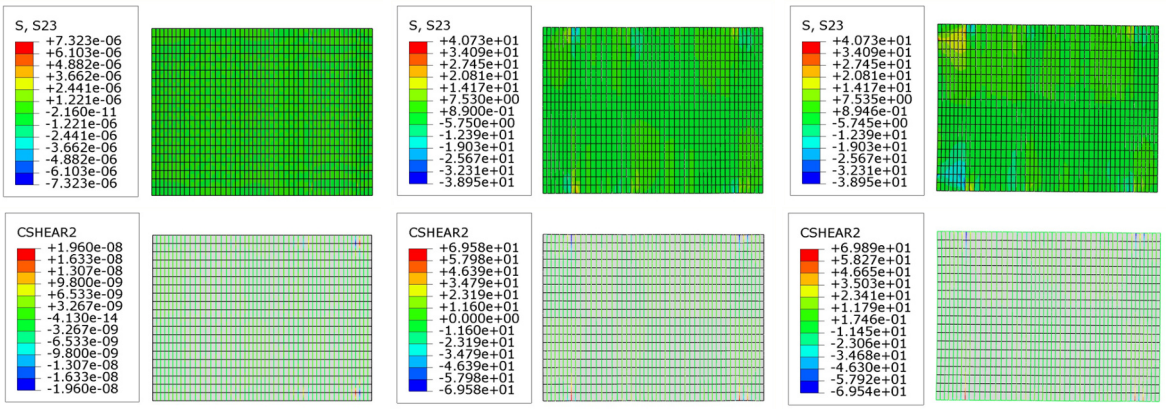

(d) Cylinder under Uniform Pressure **(e)** Specimen under Uniform Pressure **(f)** Specimen under Test Pressure

Figure 5.13: Shear Stress Distribution in Tank Specimens

High matrix and interface shear stresses were observed in layers that were sandwiched between hoop and helical layers, as per Table 4.4. It was expected that these could initiate cracks at the edges of the specimens. However, the crack initiation could relieve the shear stresses.

The order of failure could be determined from the matrix shear stresses. The inner 70° layer should crack first, followed by the outer layers. The purpose of the prediction was to see if the same failures were visible in the actual tests.

5.3. Test Development Methodology

5.3.1. Test Plan

The following 6 sets of tests were planned. They are listed below in the order of their priority. Since the PU 90A rings did not meet the dimensional requirements (Table 4.24), only the PU 95A rings were used in the tests.

0. Fine-tuning - To study what affects the tests and arrive at the optimal setup.
1. Calibration - Tests to establish a relation between the applied force and the hoop strain in the specimen using 3D DIC.
2. Quasi-static tests - 3 or more tests to determine the burst strength of the specimens. It was planned to use DIC to monitor the tests.
3. Burst-after-fatigue tests - 3 specimens were planned to be tested up to 22000 cycles at 25 $cycles/min$, followed by a burst test. This test was meant to establish that the setup could be used to perform comparative tests for different materials.
4. Benchmark - Tests using the split-disk and the segmented ring-burst setups were planned. The split-disk test served to directly estimate the specimen's stiffness. In addition to that, the purpose of the two tests was to provide a comparison for the specimen's hoop tensile strength.
5. Validation - If time permitted, fatigue tests up to 11000 cycles at 10 $cycles/min$ could be performed on specimens with the COPV layup. It also depended on if the specimens could be prepared on time.

Out of the 5 numbered tests, the first 4 were necessary to establish the complete test method and compare it to the standard. They would also be used to tune the FEM for more accurate predictions. The last test served to determine the setup's full capability. The test plan with the specimens and rings are summarized in Table 5.1. The test matrix in Table 6.10 summarizes all the ring expansion tests performed.

Table 5.1: Test Plan

Specimen Type	Layup	D_{inner} (mm)	Tests	Samples	PU 95A Rings	Test Bench	Location
Thin	$[\pm 88.77°]_4$ (Table 4.3)	170	Fine-tuning	01-08	P01-P08	MTS 810 500 kN	TU Delft
			Calibration	09-13			
			Burst	10, 12			
			Burst-after-fatigue	09, 11, 13			
Benchmark	$[\pm 88.77°]_4$ (Table 4.3)	146	Wedge	B1-B3	-	Instron 5985 250 kN	Syensqo
			Split-disk	B4-B6			
Tank	COPV (Table 4.4)	170	Calibration	T1-T3	P09-P10	MTS 810 500 kN	TU Delft
			Fatigue	T1-T3			

5.3.2. Specimen Preparation

Tubes made using wet-winding were generously provided by Sharp Composites, based in Herk-de-Stad, Belgium. They were made using wet-winding of T700-Epoxy. The tubes were then cut into rings colleagues at Syensqo's internal workshop.

Thin Specimens

An approximately 450 mm long tube was provided by Sharp Composites. It had an inner diameter of 170.04 mm. It was made of T700-Epoxy and had a hoop-wound layup, mentioned in Table 4.3. It was cut into rings by a brave colleague with an angle grinder at Syensqo's workshop. The rough edges were removed and the heights were adjusted using a manual polishing machine. The tube and specimens are shown in Figure 5.14.

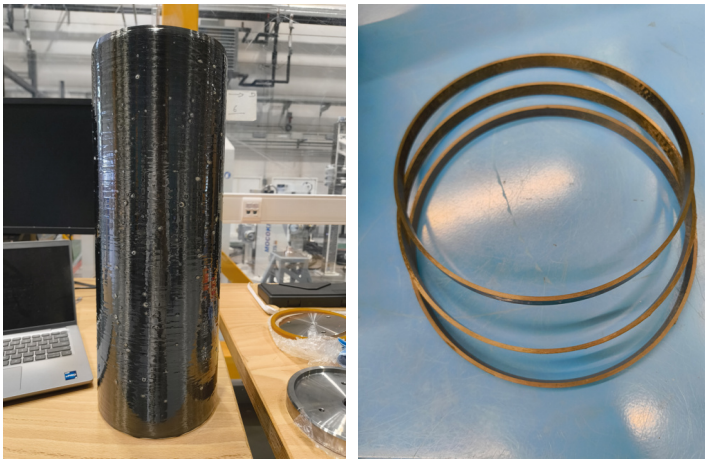

(a) 450 mm-long Tube **(b)** Ring Specimens

Figure 5.14: T700-Epoxy Hoop-Wound Tube and Specimens

The initial height of the PU 95A rings, on average, was 10.48 mm. The maximum expected compression was 3.5 mm (Figure 5.4). The compression set had been estimated to be 30% in Equation 4.2. The same was used to calculate the final height (t_i) of the PU rings, using the compression set (C_B) and the initial height (t_0).

For the PU 95A rings received, $t_0 = 10.48\ mm$ and $t_n = 10.48 - 3.50 = 6.48\ mm$. Rearranging Equation 4.2, the final height of the PU rings was estimated.

$$t_i = t_o - C_B(t_o - t_n)$$
$$t_i = 10.48 - 0.30 \times (10.48 - 6.48)$$
$$t_i = 9.28\ mm$$

Hence, the height of the first set of specimens was approximately 9.30 mm. From a later comparison of the two test benches in Figure 5.31, it was realized that the compression distance was overestimated due to the Instron test bench's compliance. The height of the specimens was then **corrected to** 10 mm, based on results shown in Figure 5.34.

Benchmark Specimens

A tube with a 146.25 mm inner diameter was provided again by Sharp Composites. It used the same materials and layup as the thin specimens. A tool had previously been developed at Syensqo to cut 146 mm AFP tubes into rings. It comprised an expanding mandrel to support and grip the tube from the inside. It included a groove for the diamond saw to cut the tube. The tool and cutting setup are shown in Figure A.6. The rings were cut from the tube and then polished down to a height of 10 mm. The dimensions of each specimen are shown in Table 6.1.

The rings were cut to 10 mm height to fit the wedge test setup at Syensqo. The same height of the rings was used for the split-disk tests.

Tank Specimens

A 14.5 mm thick, 400 mm long tube was provided by Sharp Composites. It was wound to the layup mentioned in Table 4.4. It was cut using the same tool on the lathe. A rubber tube was used to fill the gap between the 146 mm diameter tool and the 170 mm inner diameter tube. The setup and the specimen are shown in Figure A.7.

The rings were cut to a height of 10 mm. As this was a make-shift setup, it introduced defects in the specimens. The height was also not uniform and had to be corrected on a milling machine.

Microscopy and Assessment

An initial benchmark specimen was submitted for microscopy at Syesnqo, by Dr.ir. Siebe Spronk. A resin burn-off test request for fibre volume fraction was also requested to determine fibre volume fraction. It was done simultaneously with the mechanical tests at TU Delft.

The microscopy was performed by a colleague in Syensqo's lab. Hence, the complete process details were not known. An initial image of the specimen's cross-section was available at the time of writing. It is shown in Figure 5.15.

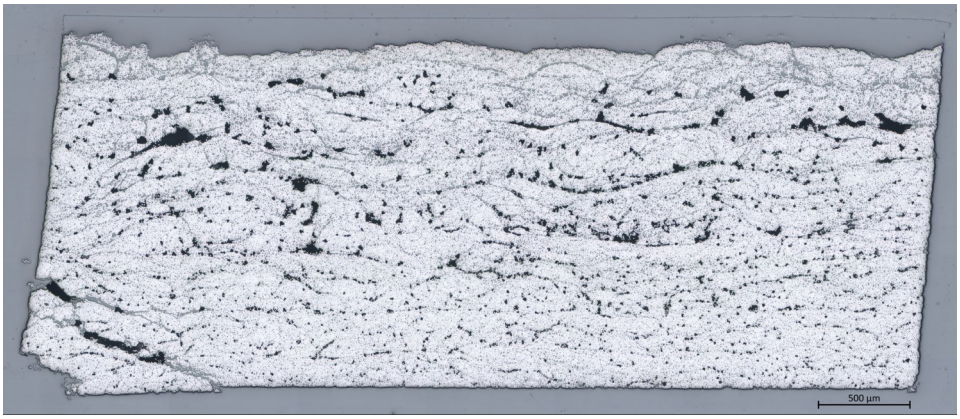

Figure 5.15: Specimen Cross-section (white - fibres, grey - matrix, black -voids)

The results of the burn-off test were also not available. Hence, an estimation was attempted using the cross-section's image to calculate the fibre V_f. A MATLAB code was shared by an independent researcher. It was modified to adapt it to the microscopy image, and is attached in subsection A.3.3. The embedding resin was masked and greyscale thresholds were used to distinguish between fibre, matrix, and voids.

The percentage of pixels detected as fibres were used to estimate the fibre content in the cross-section. Assuming the same content throughout the tube, the fibre V_f was approximated to 63%. The void volume was 4.7%. The visualization is classification are shown in Figure 5.16.

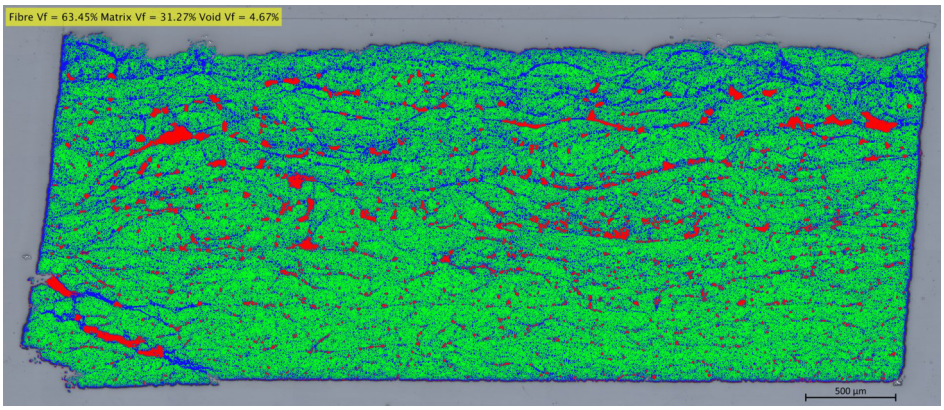

(a) Volume Fraction Estimation through Greyscale Thresholds

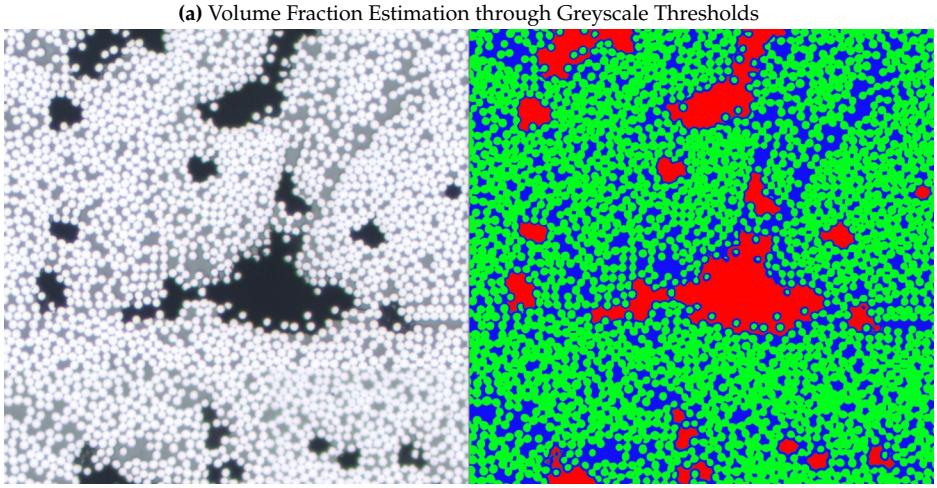

(b) Fibre (green), Matrix (blue), and Void (red) Classification from the Scan

Figure 5.16: Fibre Volume Fraction Estimation from Microscopy

5.3.3. Test Benches

The Instron 5985 250 kN test bench at Syensqo, pictured in Figure 5.17 (a), was used for initial static tests. As shown in Figure A.5, additional plates were required to prevent the setup from yielding under the 150 mm diameter compression plates. The cross-head was equipped with a hemispherical bearing to ensure that the plates were parallel to each other.

Fatigue tests were performed at TU Delft, using the MTS 500 kN fatigue test bench. This machine, shown in Figure 5.17 (b), was equipped with 350 mm diameter compression plates. However, since the cross-head was not adjustable, it required careful alignment before testing. The relative inclination was checked by bringing the plates together. Then, feeler gauges were used to estimate the gaps around the circumference. The inclination was calculated by considering the smallest and largest gaps against the 350 mm diameter of the plates. The angle was 0.036°, which was within the acceptable limit of 0.130° defined by the gaps in the centring pin.

(a) MTS 810 Hydraulic Test Bench (500 kN) **(b)** Instron 5985 Electromechanical Test Bench (250 kN)

Figure 5.17: Static and Fatigue Test Benches Used

5.3.4. Data Acquisition

DIC was used for data acquisition during the tests. Since the tests were planned at TU Delft and Syensqo, the respective setups used are described in this section. More details are shown in subsection A.3.5.

At TU Delft

Two sets of cameras were used, based on their availability. Both are detailed in Table 5.2, marked 'A' and 'B'. The setups are shown in Figure 5.18.

Table 5.2: DIC Equipment at TU Delft

A	Camera	Lens
1	FLIR Grasshopper GS3-U3-51S5M-C	Tamron ($1:1.6/25\ mm$)
2	PointGrey Grasshopper GS3-U3-51S5M-C	Tamron ($1:1.6/25\ mm$)
B	Camera	Lens
1	Limess AVT Pike F421B	Tamron ($1:2.8/50\ mm$)
2	Limess AVT Pike F421B	Tamron ($1:2.8/50\ mm$)

Setup 'A' used 5 MP cameras with a resolution of 2448×2048 pixels, whereas setup 'B' used 4 MP cameras with an image resolution of 2048×2048 pixels. Both were calibrated using a 14×10-dot target with a 3 mm dot spacing. For setup 'B', as the focal length was higher, the larger distance lead to a lower resolution.

As the tests spanned multiple weeks, the positioning of the cameras varied between tests. Setup 'B' was only used for the fine-tuning tests. The calibrated parameters of the cameras are mentioned separately for each test.

VIC3D 8 was used to post-process the results. In all cases, the subset size was 35 px, covering at least 3 black-to-white transitions. A step size of 12 was used, roughly $1/3^{rd}$ of the subset size [61]. The subset is marked by the yellow lines in Figure A.13 (b). Due to undulations on the surface, smaller subset sizes resulted in missing spots. Hence, this size was chosen to average over the gaps in the plot.

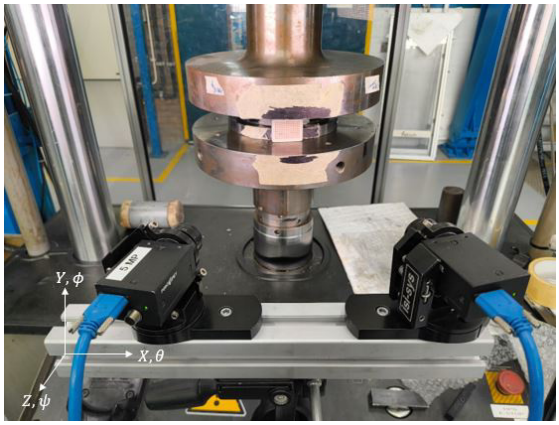

(a) Setup A: 5 MP Cameras with 25 mm Lenses

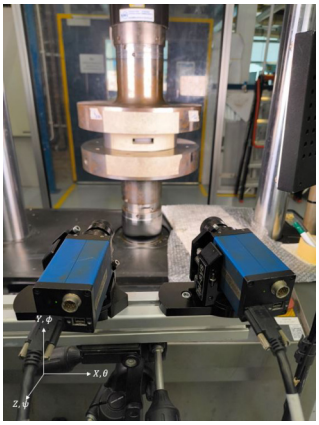

(b) Setup B: 4 MP Cameras with 50 mm Lenses

Figure 5.18: DIC Camera Setups at TU Delft

At Syensqo

The data acquisition setup comprised two 5 MP DIC cameras with 25 mm lenses, detailed in Table 5.3. Their resolution was 2448 × 2048 pixels For DIC, a pattern printed on tattoo paper was used. It was applied on to the specimen by gentle application of water. The complete setup, marked setup 'A' is shown in Figure 5.19. They were calibrated using a 12 × 9-dot target with a 3 mm spacing between dots.

Table 5.3: DIC Equipment at Syensqo

C	Camera	Lens with Polarizing Filter
1	FLIR Blackfly S BFS-U3-51S5M-C	Nikon AF NIKKOR 24-85mm $(1:2.8-4D/64\ mm)$
2	FLIR Blackfly S BFS-U3-51S5M-C	Nikon AF NIKKOR 24-85mm $(1:2.8-4D/64\ mm)$

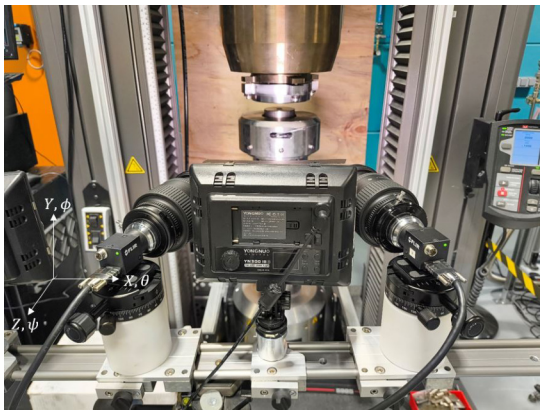

Figure 5.19: Setup C: 5 MP Cameras with 64 mm Lenses

MatchID 2024.2.1 was used for calibration and post-processing. The subset size chosen was 55 px, with a step size of 18 px. The subset covered 3 black-to-white transitions. For both software, the post-processing parameters used are shown in Table 5.4.

Table 5.4: DIC Post-processing Parameters

Software	Subset Weight	Interpolation	Correlation Criterion	Strain Window
VIC 3D	Gaussian	Biquadratic	ZNSSD	15
Match ID	Uniform	Bilinear	ZNSSD	5

5.4. Fine-tuning

To study the parameters that govern the setup, multiple quasi-static and fatigue tests were performed. The 8 trial specimens, listed in Table 5.5, were used. The purpose was to first study the effects of the parameters affecting the test, and then, to establish a relation between the applied force and hoop strain.

5.4.1. Specimens

A first set of 8 trial specimens was cut from the tube shown in Figure 5.14. Their dimensions are listed in Table 5.5.

Table 5.5: Trial Specimen Dimensions

Specimen	Height (mm)	Thickness (mm)
01	9.36	2.45
02	9.40	2.27
03	9.27	2.26
04	9.13	2.24

Specimen	Height (mm)	Thickness (mm)
05	9.19	2.31
06	9.59	2.28
07	9.27	2.29
08	9.36	2.32

5.4.2. Test Setup

Two DIC setups were used for the tests, based on availability. For static tests on specimens 01 – 03 and on the ring, setup 'A' was used. For fatigue tests on specimens 04 – 08, setup 'B' was used. The camera positions for both setups are shown in Table 5.6.

Table 5.6: Camera Positions for Fine-Tuning Tests

Setup	$X\ (mm)$	$Y\ (mm)$	$Z\ (mm)$	$\theta\ (°)$	$\phi\ (°)$	$\psi\ (°)$
A	210.526	-1.766	43.807	-0.006	28.470	-0.581
B	134.722	-1.029	12.789	0.214	15.057	1.370

The test programs varied based on the factors being studied. The procedure for each test is mentioned in its respective section.

5.4.3. Strain Rate Effect

In the fatigue tests, the cycling rate was fixed at 0.42 Hz for thin specimens, or 0.17 Hz for the tank specimens. Depending on the maximum amplitude that the specimen would be loaded to, the displacement needed at the rate would also change. This would change the strain rate applied on the ring between tests. Hence, the effect of strain rate on the loading behaviour needed to be understood.

To understand this effect, 5 tests were done from 0.067 s^{-1} (0.7 mm/s) up to the maximum expected strain rate of 0.33 s^{-1} (3.33 mm/s). The observations are shown in Figure 5.20. In the tests, the PU ring was loading the specimen. At higher strain rates, the stiffness of the polyurethane was expected to be higher, as observed by [50].

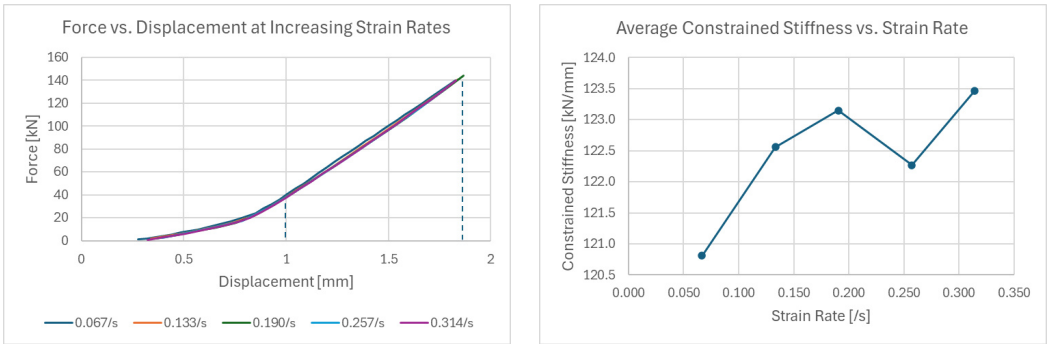

Figure 5.20: Effect of Loading Rate on Calibration

The initial gap in the force-displacement curve is due to the data acquisition starting after the preload is applied. At low strain rates, the loading behaviour is linear. At higher strain rates, there is a slight stiffening. However, the average slope of the curve remains roughly the same. Hence, the stiffness was approximated to a straight line and deemed not to have a significant effect on the calibration.

5.4.4. Effect of Specimen Alignment

In some cases, a gap existed between the ring's outer diameter and the specimen's inner diameter. The specimen then rested loose on the base at the start of the test. It was foreseen that the offset might lead to uneven loading of the specimen along its height. To mitigate it, an additional step was added before the test.

Alignment Procedure

At the start of each test, a preload was applied by manually increasing the displacement. For safety, this was done while the test bench was in low pressure mode. The preload required is a function of the gap that exists initially at both the inner and outer diameters of the polyurethane (PU) ring. It varies between rings. Only when the gaps are filled, the ring starts loading the specimen

For the PU 95A rings used, a preload of $3 - 4\ kN$ was sufficient. It was applied by moving the piston up by $0.4\ mm$. This compressed the ring, which then expanded radially to 'grip' the specimen. While in this position, two thin metallic tabs were used as levers to adjust the specimen's resting height along the ring, as shown in Figure 5.21.

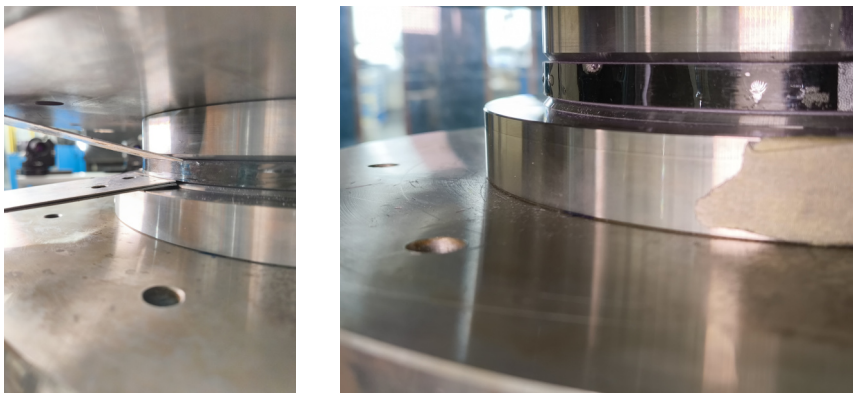

(a) Centring with Preload **(b)** Centred at Test Start

Figure 5.21: Specimen Centring using Thin Plates

The quasi-static tests were then started from that applied pre-load. Ideally, the rings should have a press-fit with the specimens, such that the specimen can be adjusted on to it before being put in the setup. However, due to tolerances in both the production of the ring and the specimen, a preload can be required.

Effect on the Test

The effect of misalignment was visible in the DIC results. A larger gap along an edge created more room for the polyurethane (PU) ring to expand more along that edge. Hence, it induced higher hoop strain along the same. It is shown in Figure 5.22 (a).

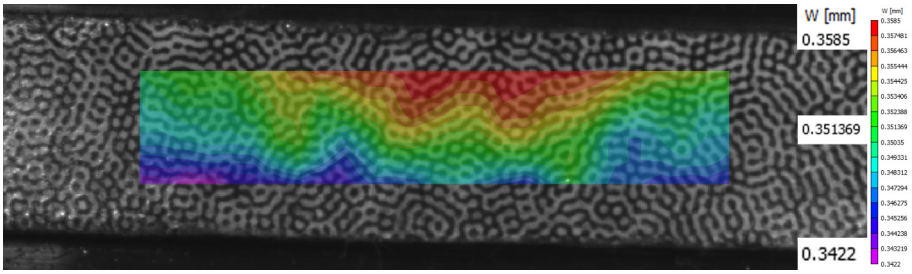

(a) Radial Expansion of specimen 01 at 100 kN of Force (mm) (Max = 0.3585, Min = 0.3422)

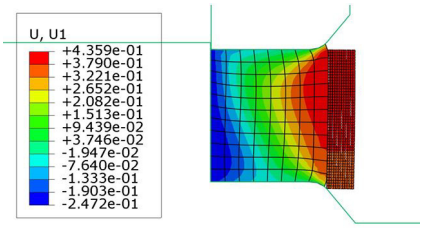

(b) Misalignment Effect in Simulation

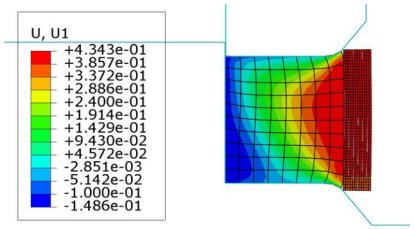

(c) Aligned

Figure 5.22: Effect of Specimen Misalignment

Since the specimens were manually polished after cutting, the height of the specimens was not perfectly uniform around its cross-section. This can lead to difference in the position of the gaps between the specimen and the ring. The edge of the specimen facing the gap tends to expand more. If on one side there is a gap on the top, whereas next to it there is a gap on the bottom, it would cause twisting of the specimen. It would also induce through-thickness shear stresses.

Hence, this is a challenge stemming from specimen preparation methods and having the right height of the specimen in comparison to the height of the ring. The height of the specimen must also account for the height that the ring needs to be compressed to to fill the radial gaps in the setup. Hence, it is a function of the diameters of the ring and the inner diameter of the specimen. By utilizing the ring's Poisson's ratio and the volume that needs to be filled, the right specimen height can be calculated. It is implemented in subsection A.2.2.

5.4.5. Effect of Lubricant

The specimen height was lower than the ring's to account for the reduction in the height of the PU ring over the course of the fatigue test. However, it was anticipated that in the initial cycles, the ring could squeeze out of the gap, based on the specimen's alignment. To mitigate it, one way was to increase the friction at the top and bottom faces of the ring. In the simulations, a friction coefficient of 0.2 was used. It predicted that it would hold back the elastomer from squeezing out at the edges. This is visible in Figure 5.6 (a). Practically, this was achieved by not using any lubricant on the outer surfaces of the ring. The exact friction coefficient was not known.

Effect on Expansion Behaviour

From free compression tests, the PU ring was observed to bulge in the centre and not expand much at the contact faces. This was observed in the DIC results, shown in Figure 5.23. With lubricant, the ring, unconstrained by a specimen, shoots out under load and causes the setup to bottom out. This is not shown.

However, there was a concern that not using any lubricant could cause the ring to heat up during the test. The effect of temperature on the compression behaviour, as reported by Ashrafizadeh *et al.* [62], was detrimental to the strength and stiffness of polyurethane. Over the course of the test, it could alter the ring's behaviour. If it deviated from the initial calibration, the results would be more challenging to process.

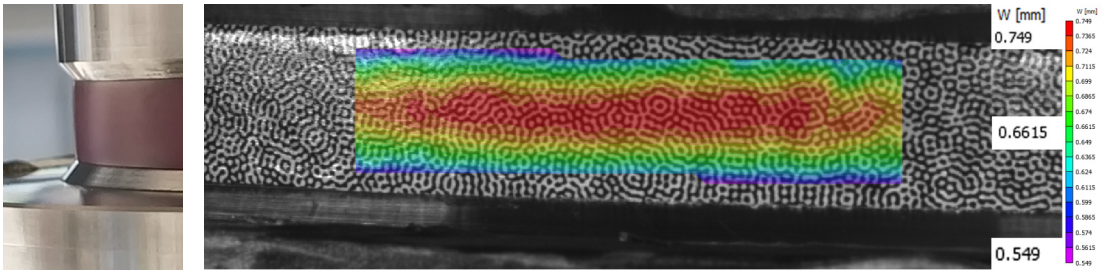

(a) Bulging **(b)** Radial Expansion Plot (mm)

Figure 5.23: PU 95A Ring Dry Expansion

Polyurethane Heating

The temperature increase was studied using a Fluke VT02 Infrared Thermometer. A test up to 1000 $cycles$ was performed, lasting 40 $mins$. Temperatures were recorded at roughly the same 3 points around the circumference of the PU ring, at approximately 10 min intervals. The results are shown in Figure 5.24.

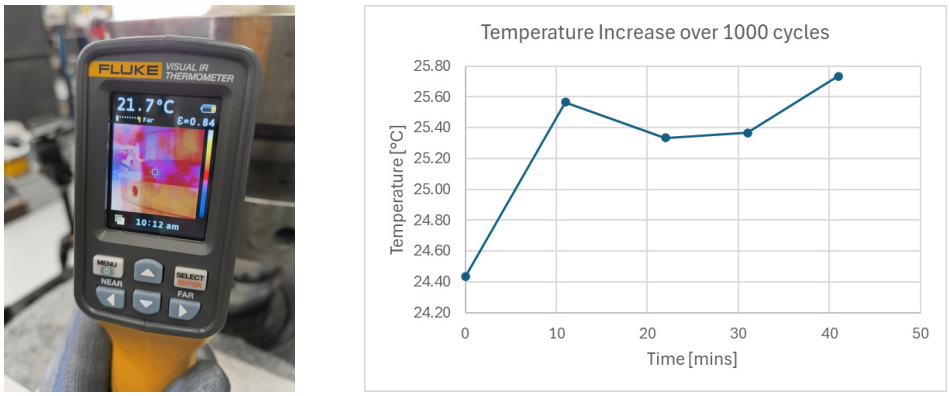

(a) Fluke VT02 IR Thermometer **(b)** Temperature Change over Time

Figure 5.24: PU 95A Temperature Change under Free Expansion

The temperature increase was, on average, 1.30°C. It was marginal and was deemed not to be significant enough to require lubrication. A similar test was performed with the specimen being loaded. Results could not be measured during the test as the ring was completely enclosed. The temperature was measured before and after the test. An increase of 1.37°C was observed, which reinforced the previous conclusion.

Effect on Specimen Stress State

Using lubricant provided a more even expansion of the ring along its height. It created a more uniform pressure and hoop strain distribution in the specimen. For tests where the gap was significant, the ring was at risk of squeezing out. However, at low forces, it should not affect the test. Having a uniform hoop strain distribution was the priority. This was explored further in section 6.3.

5.4.6. Effect of Specimen Surface

The specimen's surface had multiple bubbles and undulations owing to resin squeeze-out in the wet-winding process. This created a challenge while analysing the DIC results. In preliminary DIC strain plots, it was observed that there were mismatches between the radial expansion and the hoop strain of the specimen. An example is shown in Figure 5.25 (b). The dependence of the strain results on the correlation parameters was studied in subsection A.3.5.

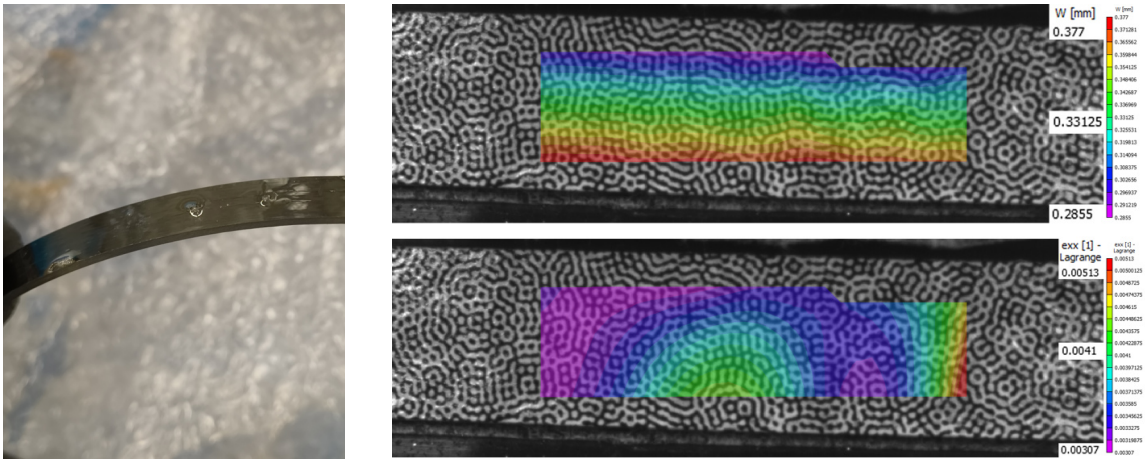

(a) Specimen Surface Bubbles

(b) Specimen DIC Results - Radial Expansion (top), Hoop Strain (bottom)

Figure 5.25: Effect of Undulating Surface on DIC Results for Specimen 2

Cause of Mismatch

To investigate the cause, a specimen's cut surface, was studied. A Keyence VK-X3000 Laser Scanning Microscope was used with a 10× zoom lens. It was a crude microscopy as the specimen's surface was not very well prepared for the scan. However, it was sufficient for the purpose of observing the cross-section. The microscope and the scanned image are shown in Figure 5.26a.

The variation DIC strains was attributed to the resin-rich outer surface of the specimens. The resin undulations in the resin layer could be experiencing varying local strains in response to the global strain of the hoop-wound fibre layers underneath. The local strains could be a result of varying stiffness of the resin layer due to the trapped air.

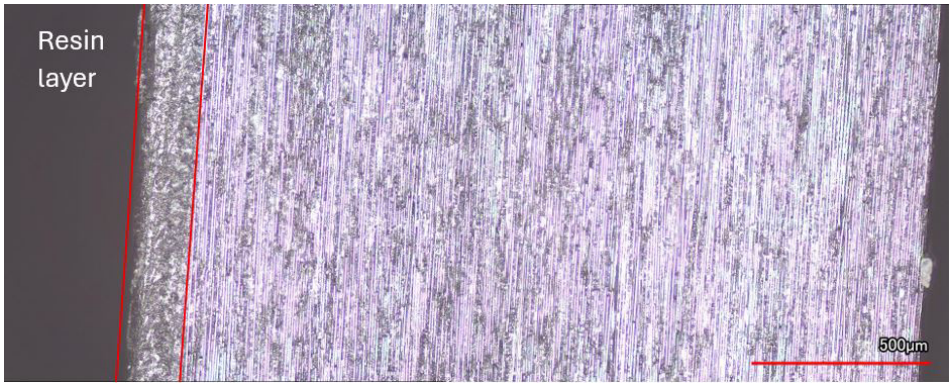

(a) Resin Layer on Specimen 07's Surface

Further Investigation

For the uneven strain distribution, a potential reason was the presence of bubbles or undulations on the surface. To check if it was the case, the topography of the surface was compared with the strain distributions, using DIC. To capture the surface undulations, the DIC results were transformed to

cylindrical coordinates. The built-in fitting transformation tool in VIC 3D 8 was used. However, in some cases, the function predicted incorrect radii. Hence, the radii for the specimens were calculated as the sum of their inner radius and thickness. It was then used for the transformation to cylindrical coordinates.

The comparison was performed for the specimens where the mismatch was most noticeable. Three cases are shown in Figure 5.27.

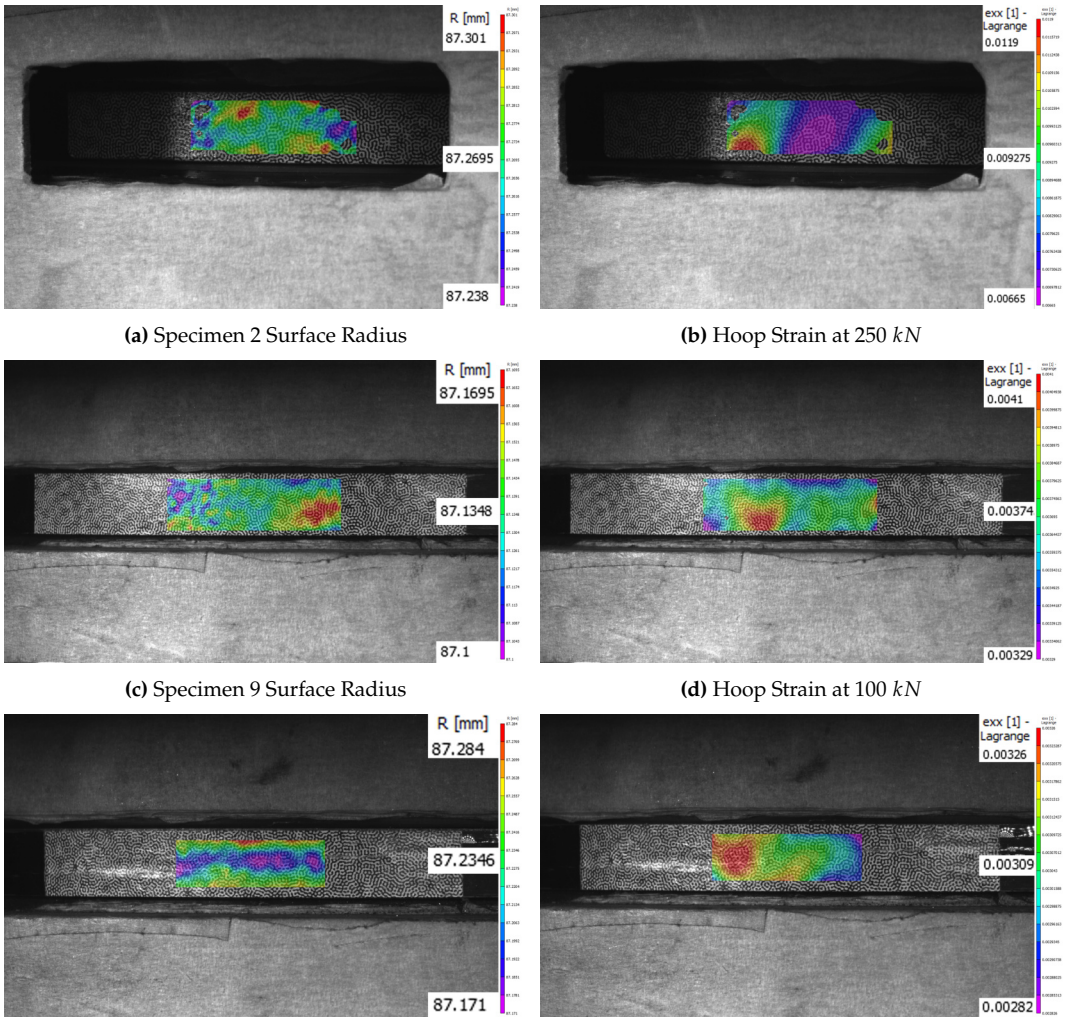

(a) Specimen 2 Surface Radius

(b) Hoop Strain at 250 kN

(c) Specimen 9 Surface Radius

(d) Hoop Strain at 100 kN

(e) Specimen 11 Surface Radius

(f) Hoop Strain at 100 kN

Figure 5.27: Surface Undulations Correlation Attempt with Local DIC Strain Peaks

The bumps on the surface correspond to the red regions in the surface radius plots. It was assumed that the bumps would correspond to the peaks in local strains. However, no such correlation was established through the comparison. The peaks seemed to be influenced by some other factor, but still likely related to the outer resin-rich layer.

The resin-rich layer, shown in Figure 5.26a (c) could have variations in the bond strength between itself and the outer tape layer, creating the peaks. Close-ups of specimen 7's fatigue test are shown below. The cause of failure is discussed in section 6.4. The images in Figure 5.28 show the resin-rich layer and its de-bonding from the inner tape layer.

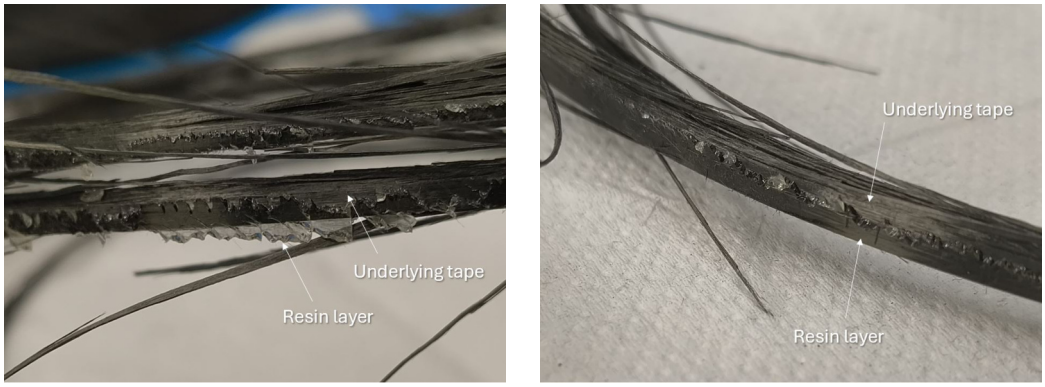

Figure 5.28: Uneven Dis-bonds Between Resin Layer and Tape

An uneven dis-bond is seen between the resin layer and the tape. The strain peaks could indicate regions where the bonding is weak, causing local peaks in strain. The peaks are only apparent in the hoop strain plots. The axial strain plots, shown in section 6.3 have less such variations.

Work-around

To overcome this challenge, the hoop strain was calculated from the radial expansion, using Equation 5.1.

$$\epsilon_{xx} = \frac{\Delta d}{d_i} \tag{5.1}$$

The average hoop strain computed by DIC was compared to strains computed from Equation 5.1, using the average radial expansion. It was also used as a way to validate the DIC strain estimations. It is shown in Figure 5.29, for a loading-unloading cycle.

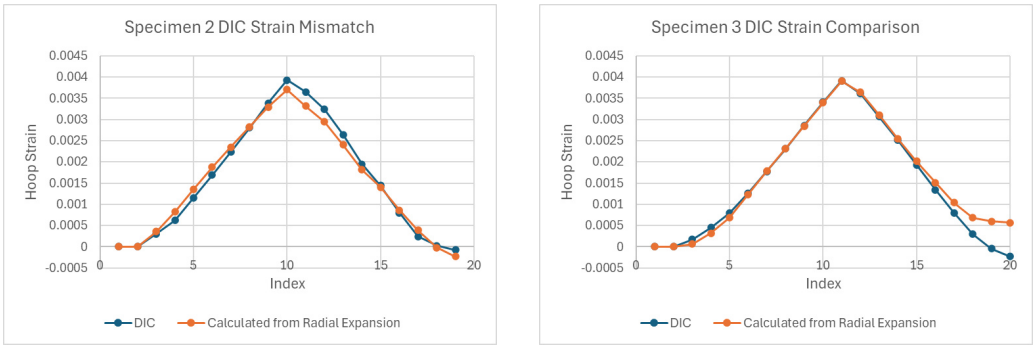

Figure 5.29: Effect of Strain Mismatch

There was up to a 9% increase in the strain estimated due to local effects. This method was also used to validate later DIC strain results.

5.4.7. Effect of Material Variability

The calibration was expected to be subject to variations in the polyurethane ring itself. Different rings were tested against the same specimen. Displacement-controlled tests were performed at 0.7 mm/s till 1.4 mm. The results are shown in Figure 5.30.

The test's behaviour is hence subject to variability in the PU 95A rings. During the tests, a difference of up to 4% was observed in the force vs. hoop strain relation. In the force-displacement curves' slopes, a difference of up to 8% was observed.

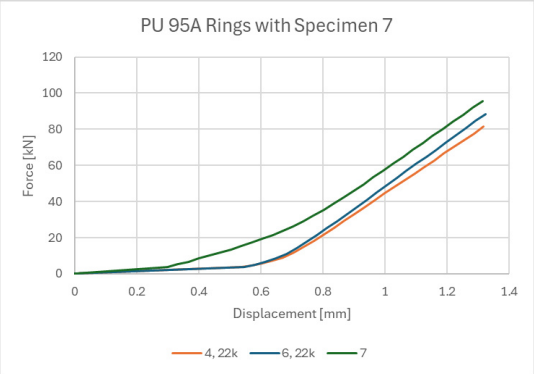

Figure 5.30: Variability in the Test Response

Variations also arise from the different dimensions of the rings. It changes the initial radial gaps in the setup, leading to increased 'grip force' and initial lax displacement. Differences could be inherent to the specimens themselves, owing to variation in its material properties. Hence, owing to these differences, each ring-specimen combination has to be calibrated before starting the test.

5.4.8. Test Bench Compliance

Care must be taken when using displacement readings directly from the test bench. A quasi-static test was first performed on the Instron 5985 test bench at Syensqo. On comparison with later tests on the MTS 810 test bench, a large difference was observed in the displacement readings between the two benches, shown in Figure 5.31. The offsets from the simulation results are due to the initial radial and axial gaps in the test setup.

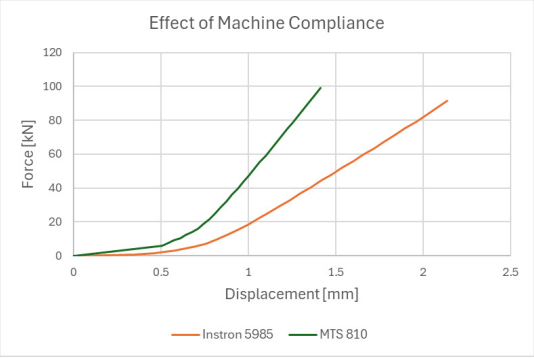

Figure 5.31: Increased Displacement Readings due to Test Bench Compliance

The higher displacement measured in the Instron test bench was attributed to the tall extender used between the load cell and the compression plate fixture, shown in Figure 5.17 (b). It was there to allow for the use of an environmental chamber. However, its length reduced its axial stiffness, leading to increased cross-head displacement readings. Hence, for such test benches, local displacement measurement would be necessary.

Unbeknownst to this effect, results from the initial tests on the Instron 5985 were used to size the height of the specimen. Figure 5.3.2 was used with the higher displacement predictions. This created additional challenges in the alignment of the specimens. On the bright side, it allowed a better test of the limits of the PU ring. Later specimens were prepared to a height of 10 mm to repeat the same tests.

5.5. Calibration

Calibration tests were performed using different ring-specimen combinations. The results of the below tests were used to study the behaviour of the polyurethane ring under free and constrained compression. The results were then combined to tune the polyurethane's hyper-elastic material model in section 6.2.

5.5.1. Specimens

The second set of specimens were cut from the tube shown in Figure 5.14. They were cut to roughly 10 mm in height using the angle grinder, followed by polishing. Their dimensions are listed in Table 5.5.

Table 5.7: Thin Specimen Dimensions

Specimen	Height (mm)	Thickness (mm)
09	10.36	2.21
10	10.06	2.23
11	10.15	2.30
12	9.98	2.21
13	10.09	2.26

The height was restored to 10 mm, following the tests done on the MTS 810 test bench (Figure 5.17 (a)). It showed that the displacements, and hence, compression set were overestimated in the previous tests due to test bench compliance.

5.5.2. Test Setup

For the calibration tests, DIC setup 'A' was used (Table 5.2). The camera positions are shown in Table 5.8. Further tests on specimens 09 – 13 used the same setup.

Table 5.8: Camera Positions for Calibration Tests

Setup	$X\ (mm)$	$Y\ (mm)$	$Z\ (mm)$	$\theta\ (°)$	$\phi\ (°)$	$\psi\ (°)$
A	168.741	3.609	40.026	0.197	-22.482	0.072

Tests were performed at a 0.7 mm/s loading rate. The strain rate test results in Figure 5.20 showed little effect on the ring's behaviour. Hence, a lower loading rate was used to be able to take more images.

5.5.3. Ring Calibration

PU 95A ring 2 was tested under free compression. As shown in Figure 5.23 (a). Grease was not used to prevent the ring from shooting out of the setup. A loading rate of 0.7 mm/s corresponded to a strain rate of 0.067 s^{-1}. The ring's response is shown in Figure 5.32.

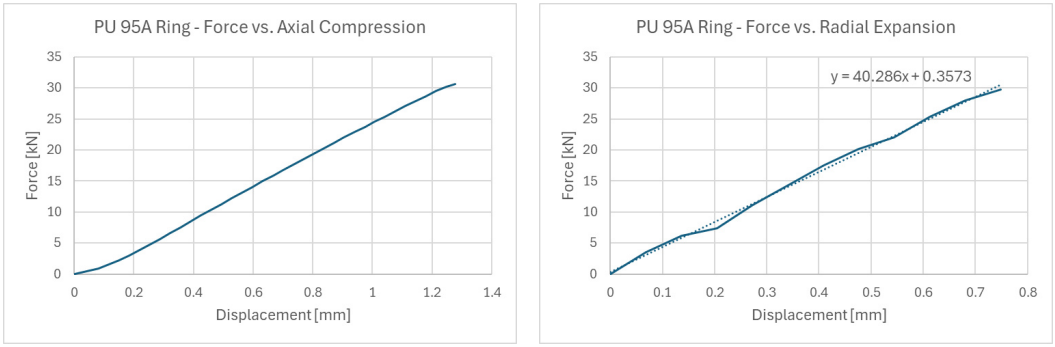

Figure 5.32: PU 95A Ring Response

The force-displacement curve was offset by 0.2 mm to account for the initial axial gap in the test bench. On average, the ring expands radially at 0.0245 mm/kN. The results were used to match the ring's material model in section 6.2.

5.5.4. Specimen Calibration

Specimens 09 - 13 were used (Table 6.10). The tests were displacement-controlled, up to 1.4 mm at a loading rate of 0.7 mm/s. It required approximately 100 kN of force. The maximum applied force varied depending on the initial radial gaps in the setup. This is shown in Figure 5.33. Out of the 5 specimens 11 and 13 are not shown to avoid crowding the plots. In both plots, they overlapped closely with specimens 10 and 12, respectively.

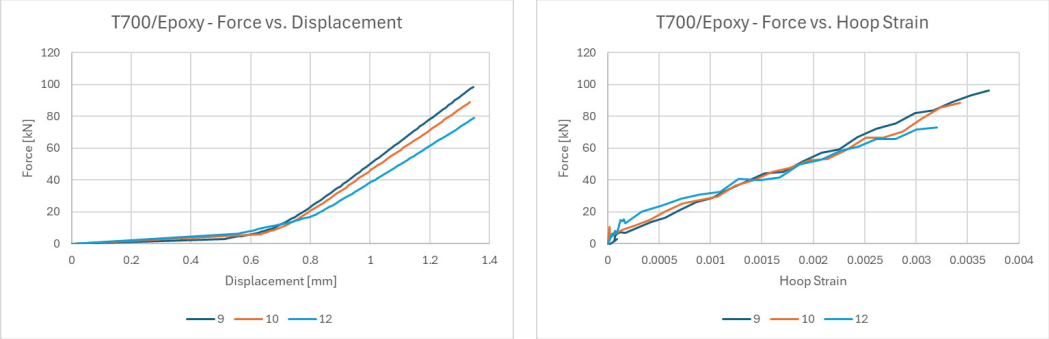

Figure 5.33: T700-Epoxy (Thin Specimen) Response

The roughness of the force-strain curve was due to noise in the analogue voltage signal. The initial offset (y-intercept) in the same is a function of the initial radial gaps between the core, ring, and specimen. In this case, a force of approximately $5 - 15$ kN was required to compress the ring and, in turn, fill the radial gaps. Only after that stage, the ring starts loading the specimen and the hoop strain increases.

The slopes of the lines in both plots were calculated in their linear regions. In the force-displacement curve, it was past 0.9 mm, and past 0.005 in the force-strain curves. The slopes and maximum variations are shown in Table 5.9.

Table 5.9: Thin Specimen Calibration

Specimen	Stiffness (kN/mm)	Performance ($\mu strain/kN$)
09	140.514	39.0
10	128.629	42.3
11	132.159	42.3
12	115.962	51.7
13	113.394	52.2
Mean	126.132	45.5
S.D.	11.348	6.1

On average, the hoop strain in the specimen increases with the applied force by 45.5 $\mu strain/kN$. It shows the extent of variation in the performance and response of the rings. There was a maximum variation of 24% in the stiffness and a maximum of 33% difference in the performance. It further demonstrated the need to separately calibrate ring-specimen combinations before testing.

5.5.5. Consistency Throughout Cycles

Fatigue tests were performed to check if the initial response of the test held true for cyclic loading. 22000 $cycles$ were applied at 25 $cycles/min$ (0.42 Hz) [25]. A sine wave displacement pattern was used for smoother loading-unloading transitions, which was safer for the test bench. The cycling was done with a force-controlled test, between $14 - 140$ kN ($R = 0.1$). The maximum strain applied was

approximately 0.6%, extrapolated from Figure 5.33. Three parameters of interest were defined, and are listed below.

Height Reduction

Displacements peaks of the loading cycles were recorded. The troughs were subtracted from the initial height of the specimen to estimate the height of the ring at the start of each loading cycle. The effect of cyclic compression on the ring's height is shown in Figure 5.34.

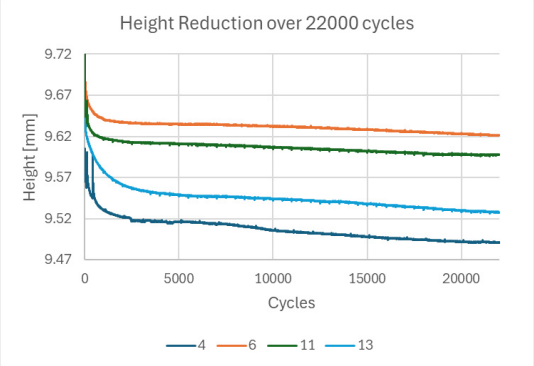

Figure 5.34: PU 95A Ring Height Reduction

On average, the reduction in height, measured as the difference between the height in the first and last cycles, was at maximum 0.115 mm. In the tests, the piston moved by 1.8 mm. Accounting for the initial lax displacement, the ring was compressed by approximately 1.4 mm. Extending the results from Equation 4.5, the expected reduction was 20% of 1.4 mm = 0.28 mm. Hence, it was over-estimated. The difference could be attributed to PU 95A having better recovery than the 90A samples initially tested.

The initial height of the PU 95A rings, accounting for the height reduction, was estimated to be 10.43 mm (Equation 4.12). The height of the rings received was, on average, 10.48 mm. However, there was an initial radial gap that was larger than specified. It increased the displacement required to apply the minimum grip force to 0.3 – 0.4 mm. Hence, the ring height of 10.48 mm matched a specimen height of 10 mm.

Specimen Movement

To check if the specimen shifted around during the test, a fatigue test was programmed to dwell every 1000 $cycles$ at 1 mm of piston displacement. DIC was used to measure the rigid-body displacements in the specimen. The concern was that if the specimen moved, it would affect the hoop strain distribution, as shown in Figure 5.22. The vertical displacement over 22000 $cycles$ is shown in Figure 5.35. The horizontal displacement was negligible.

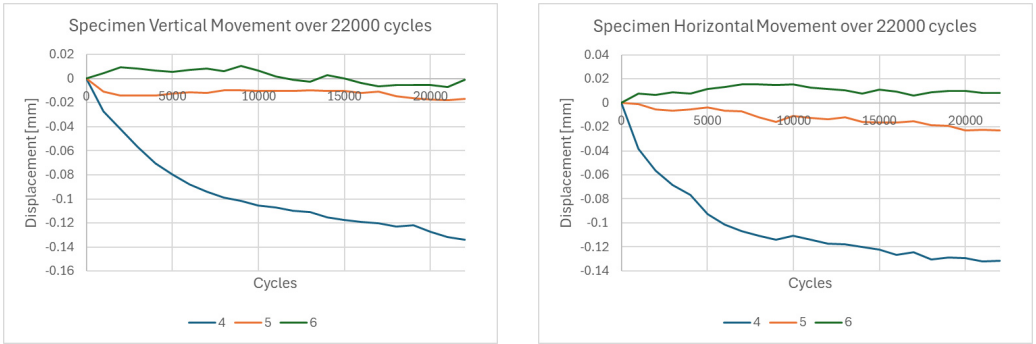

Figure 5.35: Specimen Movement During Fatigue Tests

In two out of the three tests, the specimen stayed almost level since the start of the test. Its sliding down in the third case was attributed to two possible reasons. First, the load required to fill the radial gaps might be more than the force applied at the minimum point. Hence, there was not enough expansion of the ring to grip the specimen. Second, as the specimen sat lower than the ring at the start of each cycle, the expansion of the ring through the gap at the top pushed the specimen down further. Both effects could also work together to cause the vertical displacement.

Performance through Fatigue

A fatigue test was done for 22000 $cycles$ up to a maximum force of 140 kN ($R = 0.1$) at 25 $cycles/min$. It was programmed to dwell every 500 $cycles$ at the mean load of 77 kN. The purpose was to see the variation in the radial expansion in the specimen throughout the fatigue test. The results are shown in Figure 5.36. The reference image was also taken at 77 kN at the first cycle. The subsequent cycles were compared to the same. Hence, the the plot shows the expansion relative to the first cycle.

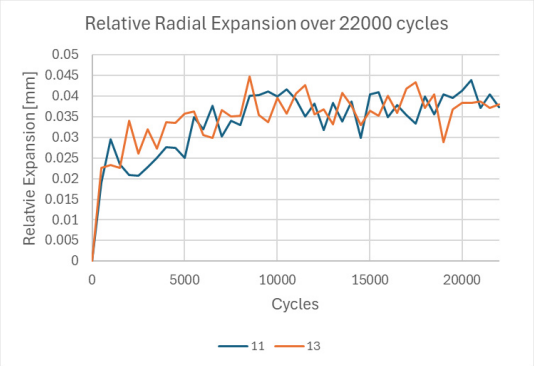

Figure 5.36: Average Radial Expansion Compared at Mean Load in Fatigue

Considering the low magnitude difference between cycles, the radial expansion stays level throughout the test. The initial increase can be attributed to the increase in the constrained stiffness of the PU 95A ring as it gets subsequently compressed. It corresponds to its initial reduction in height, shown in Figure 5.34.

Performance After Fatigue

The calibration tests done for each fatigued specimen was repeated after their fatigue test. The comparison for specimens 11 and 13 are shown in Figure 5.37. The increase in constrained stiffness of the fatigued PU 95A ring was observed. There was a minimal drop in the performance of the ring. Comparing the more visible drop for specimen 13, it strain-force ratio reduced by up to 9.9%.

The tests were performed till 140 kN, leading to 1.8 mm of compression. Tests at higher forces, which lead to higher compression and strains, would likely show degradation in performance. This was observed in the burst tests in Figure 5.38.

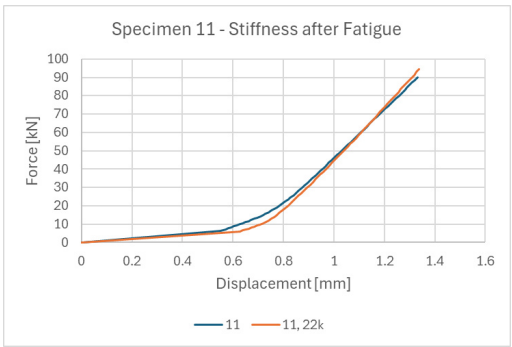

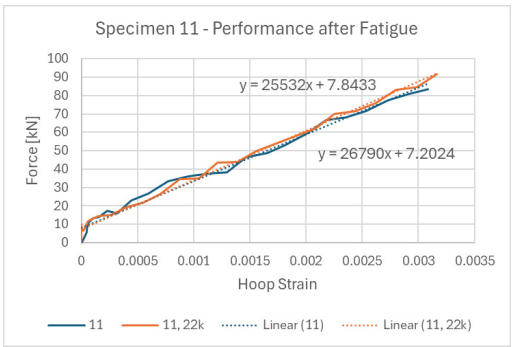

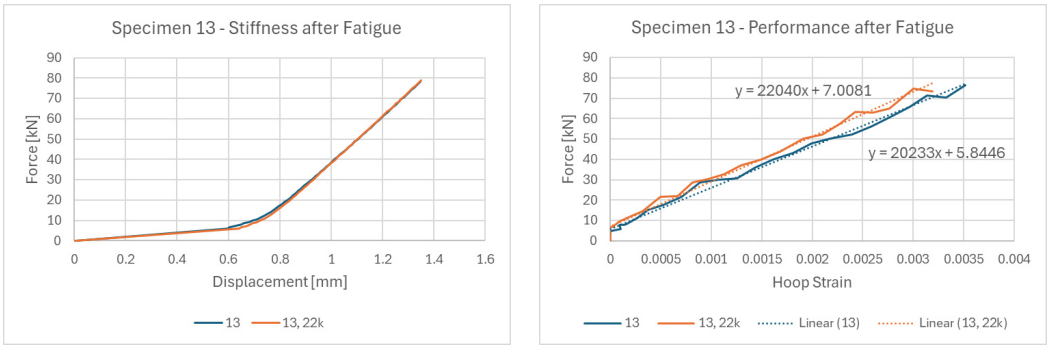

Figure 5.37: PU 95A Ring Performance after Fatigue

Performance after Burst

When the same ring was subjected to larger strains in the burst test, it was expected to soften, as shown in Figure 4.2. To see its effect on the ring, the behaviour and performance of the same ring was compared before and after a burst test. The results for the ring used in the burst-after-fatigue test for specimen 6 are shown in Figure 5.38.

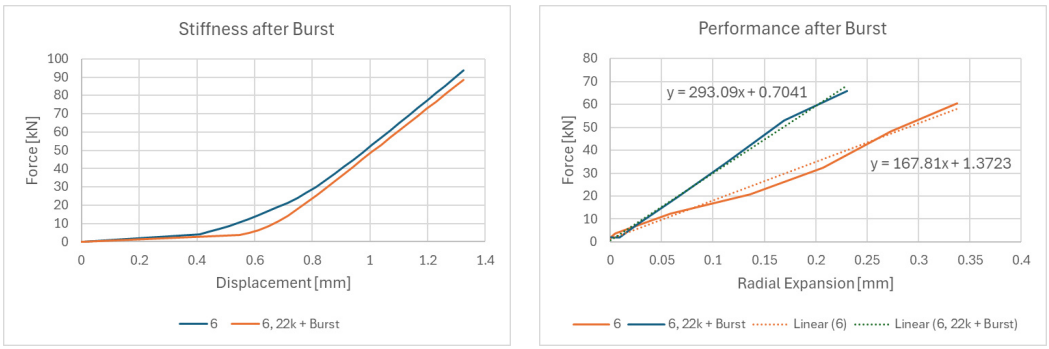

Figure 5.38: PU 95A Ring Performance after Fatigue and Burst

In the force-displacement results, the increased displacement was attributed to the height reduction. The performance was quantified by the rate of radial expansion of the specimen in mm/kN. It reduced from 0.0054 to 0.0034 mm/kN, a decrease of 37%.

The ring tested with specimen 4 was allowed to rest for 2 days before being tested again. The same comparison is shown in Figure 5.39. Specimen 7 was again used for the test after the rest period. The performance seemed to recover after the fatigue cycle and at least 2 days of rest. It implied that the rings could be re-used.

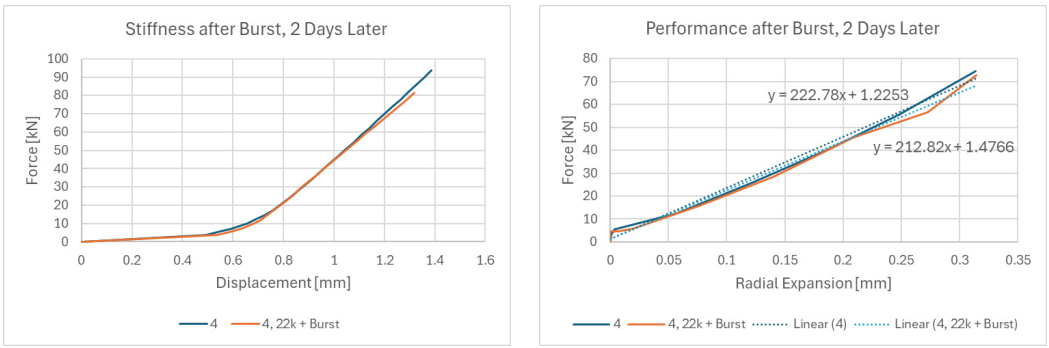

Figure 5.39: PU 95A Ring Performance after Fatigue, Burst, and Rest

5.6. Summary

For ease of reference, the observations and features of the ring expansion test are summarized below,

1. The effect of loading rate on the test is minimal. The lowest expected rate in the fatigue tests ($0.7\ mm/s$) can be used for calibration, to allow for sufficient data capture.
2. Specimen alignment with the ring can change the hoop strain distribution along the specimen's height. Getting the ideal strain distribution is possible but tricky. It is discussed in more detail in section 6.2.
3. Not using a lubricant between the ring and the fixture reduces the ring's tendency to squeeze out of the gaps between the specimen and the fixture. It does not have a significant effect on the heating up of the ring in fatigue tests. However, it's use is preferred for a more uniform pressure distribution along the specimen's height, ensuring a more fibre-dominated failure mode.
4. The filament-wound specimens can have an undulating surface. It affects DIC strain measurements by creating local strain peaks. This is caused by a roughly 100 μm thick outer resin-rich layer. For validation, the strain can be calculated from the radial expansion.
5. The test bench compliance must be accounted for before using displacement readings directly. A local displacement measurement should be set up.
6. Owing to variability in the ring's stiffness and compressibility, all ring-specimen combinations must be calibrated before starting the test.
7. The PU ring's height reduces over the fatigue cycles. This is accounted for in the initial height determined for the ring. The height reduction is accompanied by an slight initial increase in stiffness. Its effect on the radial expansion applied throughout the tested fatigue cycles is minimal.
8. To prevent the specimen from sliding down during the test, the minimum force applied should be greater than the preload used to 'grip' the ring. This varies between rings based on the radial gaps it leaves between the fixture and the specimen.
9. The rings can be reused, but should be allowed to rest for at least 2 days between burst tests.

6

Results and Discussion

6.1. Benchmarks

Tests were performed with two existing setups, the split disk test [7] and the wedge test [36]. They were both available at Syensqo. The purpose of the tests was to find the stiffness of and strength of the T700/Epoxy material. The resulting stiffness was used for calculating the strength of the 170 mm specimens from the DIC strains. The strengths were used as a benchmark for the strengths predicted by in the burst tests in section 6.3.

6.1.1. Specimens

Rings were cut from the 450 mm long tube provided by Sharp Composites, shown in Figure A.6. The inner diameter of the tube was measured to be 146.25 mm. The measured dimensions of the specimens are shown in Table 6.1.

Table 6.1: Benchmark Specimen Dimensions

Wedge Test		
Specimen	Height (mm)	Thickness (mm)
B1	10.066	2.136
B2	10.068	2.104
B3	10.068	2.048

Split-Disk Test		
Specimen	Height (mm)	Thickness (mm)
B4	10.024	2.082
B5	9.998	2.064
B6	10.016	2.144

6.1.2. Split-disk Test

The split-disk test was performed according to ASTM D2290-19a [7] Procedure A. The purpose was to establish a benchmark for the ring expansion test and estimate the hoop tensile modulus of the composite.

Test Setup

The test was performed on the Instron 5985 at Syesnqo. The two split disks were aligned by eye. No lubricant was used between the specimen and the disk surface. ASTM D2290-19a [7] suggests range of loading rates for the test is 2.5 – 12.7 mm/min. In the tests, a loading rate of 12 mm/min was used. It was decided to be as close as possible to the 0.7 mm/s used in the ring expansion test, while staying within the limits defined by the standard.

DIC setup 'C' (Table 5.3) was rotated clock-wise by 90° to align with the hoop direction of the specimen. The test setup and the DIC setup are shown in Figure 6.1. The relative camera positions are shown in Table 6.2.

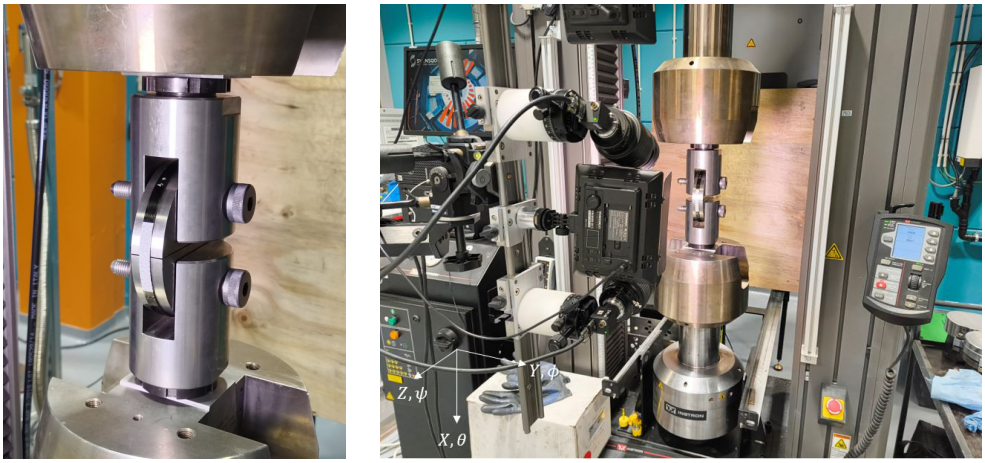

(a) Split-Disk Test Fixture **(b)** Rotated DIC Setup 'C' and Coordinate System

Figure 6.1: T700/Epoxy Split-Disk Fixture and DIC Setup at Syensqo

Table 6.2: Camera Positions for the Split-Disk Test

Setup	$X\ (mm)$	$Y\ (mm)$	$Z\ (mm)$	$\theta\ (°)$	$\phi\ (°)$	$\psi\ (°)$
C	-247.483	-3.261	26.725	0.137	29.652	0.342

A complete Region of Interest (ROI) of $1080 \times 270\ px$ was used, with a density of approximately $27\ px/mm$. A subset size of $55\ px$ was used, with a step size of 18. Both are shown in Figure 6.2.

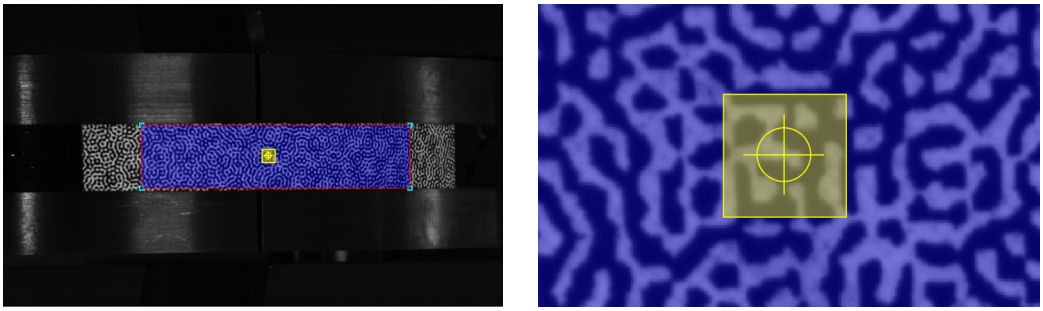

(a) Complete Region of Interest ($40 \times 10\ mm$) **(b)** Subset Size (Yellow Box, 55×55 pixels)

Figure 6.2: Split-Disk Test DIC ROI and Subset Size

Test Results

Specimens B4-B6 were tested till failure in the split-disk tests (Table 6.10). The standard suggests to use the test only to estimate the specimen's strength. To estimate the modulus of the composite from the test, Zhao *et al.* [20] concluded that the strain should be measured 10° away from the split. This avoids the region of low hoop strain at the split where the specimen bends to become flat. The hoop strain plot for the complete ROI is shown in Figure 6.3 (a). From the plot, the average strains were considered at a cropped ROI, shown in (b).

As per the ASTM D2290-19a [7], the strength was calculated using Equation 6.1. The peak force recorded in the test was considered as the failure point of the specimens.

$$\sigma = \frac{F}{2ht} \tag{6.1}$$

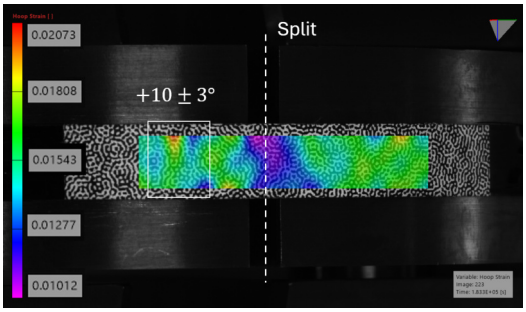

(a) Hoop Strain over Complete ROI (Avg : 0.0149)

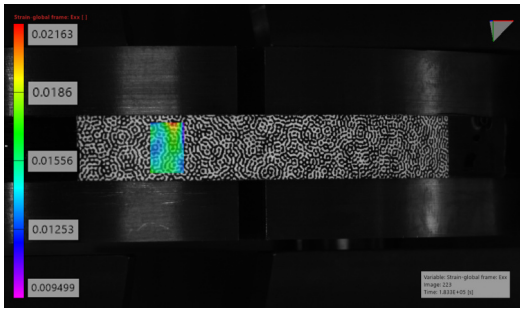

(b) Hoop Strain at 10 ± 3° (Avg : 0.0151)

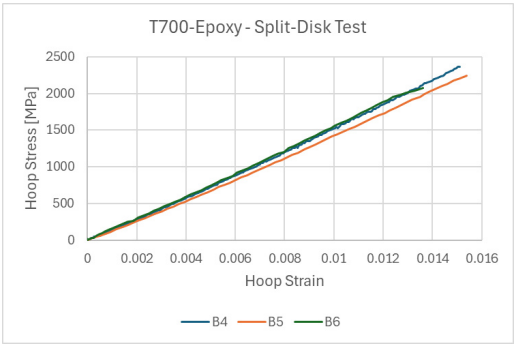

(c) Split-disk Test Results

Figure 6.3: T700/Epoxy Split-Disk Test

The DIC strains were transformed to cylindrical coordinates in MatchID to get the hoop strains. The software's built-in tool was used to fit the cylinder's radius to the specimen. It was cross-checked with the specimens' measured diameter, and was within 2% of the actual outer radius.

The hoop stress-strain curve is shown in Figure 6.3 (b). The modulus of the specimen was estimated from the slopes of the same in the range of 0.1 − 0.3% strain [11]. The results are shown in Table 6.3.

Table 6.3: T700/Epoxy Hoop Tensile Properties from the Split-disk Test

Specimen	X_T (MPa)	E_{XX} (MPa)
B4	2362.39	140958
B5	2239.26	133504
B6	2078.00	140895
Mean	2226.55	138452
S.D.	116.45	3499

The average modulus was estimated at 138.45 GPa. Zhao *et al.* [20] performed similar tests to estimate modulus with 1.5 mm and 1.7 mm thick specimens. The winding angle was ±89.5° and the material used was T700-TW104. For a fibre V_f of 62 − 63%, the modulus estimated in their study was 131 − 132 GPa. The hoop tensile strengths were in the range of 1780 − 2070 MPa.

Comparing with the results of Zhao *et al.* [20], the modulus estimated was 5%, while the average strength estimated was approximately 7% higher. The strength was also 5% higher than the data-sheet value of 2125 MPa (Table 4.2). From a communication from Toray, shared by Dr. Martin Kerschbaum, they had claimed a 10% increase in strength in their T700 fibres. The difference between the work of Zhao *et al.* [20], published in 2021, and the current tests, could stem from this increased strength. However, it can also be an effect of friction, as discussed in subsection 6.1.4.

6.1.3. Wedge Test

The wedge test, first demonstrated by Horide *et al.* [36], had been developed at Syensqo by Dr. Siebe Spronk. As described in section 3.3, it improved on the split-disk test by distributing the split distance around the circumference of the specimen. The setup is shown in Figure 6.4. The camera positions are shown in Table 6.4.

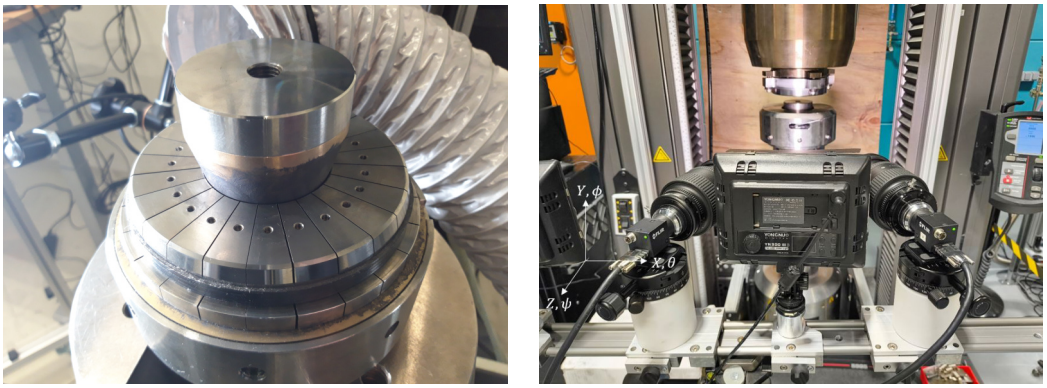

(a) Wedge Test Setup Developed at Syensqo **(b)** DIC Setup 'C' and Coordinate System

Figure 6.4: Wedge Test Developed and its DIC Setup

Table 6.4: Camera Positions for the Wedge Test

Setup	$X\ (mm)$	$Y\ (mm)$	$Z\ (mm)$	$\theta\ (^\circ)$	$\phi\ (^\circ)$	$\psi\ (^\circ)$
C	-254.022	-1.292	51.795	0.195	29.139	0.485

The setup used a PTFE ring between the specimen and the fixture. It was used to distribute the stresses evenly along the specimen's circumference. It further mitigated the effect of stress concentration due to the gaps.

Calibration to Estimate Strength and Modulus

To be able to estimate the modulus, the setup had been calibrated using a steel ring. As the modulus of the steel was known, it was used to relate the DIC strains to the hoop stress. With the specified cross-section area of the ring, a relation was established between the hoop force and the cross-head force. A medium carbon steel was used to ensure a larger elastic region.

The tests were monitored with DIC to measure the strain in the steel ring. 5 tests were done applying 60 kN on the setup, to stay within the elastic region. The hoop strain was measured. Since the modulus was known from the steel's supplier, the hoop stress was calculated from the same. Molybdenum grease was used to coat the sliding surfaces to reduce friction.

With a defined cross-section area of the steel ring, the hoop force was calculated from the stress. The ratio between the applied force and the hoop stress was averaged over the 5 tests. This experimentally determined factor for the steel rings was $F_\theta / F_{applied} = 0.3927$.

Due to difference in dimensions of the steel calibration ring and the specimen, this ratio would need to be adjusted. It can be arrived at analytically using Equation 3.18, rearranged and shown again in Equation 6.2. The parameters governing the ratio are the friction coefficient and the dimensions of the specimen. It is independent of its material properties.

$$\frac{F_{radial}}{F_{applied}} = \frac{1 - \mu \tan\theta}{\tan\theta + \mu} - \mu \tag{6.2}$$

The steel ring had an inner diameter, $d = 146.23\ mm$, height $h = 10.05\ mm$, and a thickness, $t = 6.74\ mm$. Its four edges were chamfered and its resulting cross-section area, $A = 67.10\ mm^2$. Using Equation 3.34, first, F_θ / F_{radial} was derived in Equation 6.1.3.

$$\begin{aligned} P &= \frac{F_{radial}}{\pi d h} \\ \sigma_\theta &= \frac{P d_{mean}}{2t} \\ F_\theta = \sigma_\theta A &= \frac{F_{radial}}{\pi d h} \frac{d_{mean}}{2t} ht \\ \frac{F_\theta}{F_{radial}} &= \frac{d_{mean}}{2\pi d} \\ \frac{F_\theta}{F_{radial}} &= \frac{152.97}{2\pi \times 146.23} = 0.1665 \end{aligned} \tag{6.3}$$

It was then used to calculate $F_{radial}/F_{applied}$ in Equation 6.4. Substituting the ratio in Equation 6.2 and rearranging it gave a quadratic equation, which was solved for μ.

$$\begin{aligned} \frac{F_{radial}}{F_{applied}} = \frac{F_\theta}{F_{applied}} \times \frac{F_{radial}}{F_\theta} &= 0.3927 \times \frac{1}{0.1665} = 2.3586 \\ \mu^2 + (2 \times \tan\theta + 2.3586)\mu + (2.3586 \times \tan\theta - 1) &= 0 \\ \mu &= 0.122 \end{aligned} \tag{6.4}$$

As the same grease was used in the calibration tests, the friction coefficient was assumed to be the same. The specimens had an inner diameter of 146.25 mm and an average thickness of 2.10 mm. Starting from Equation 6.2, the ratio between hoop force and applied force was calculated using Equation 6.5.

$$\begin{aligned} \frac{F_{radial}}{F_{applied}} &= 2.3586 \\ \frac{F_\theta}{F_{radial}} = \frac{d_{mean}}{2\pi \times d} &= \frac{148.35}{2\pi \times 146.25} = 0.1614 \\ \Rightarrow \frac{F_\theta}{F_{applied}} &= \frac{F_\theta}{F_{radial}} \times \frac{F_{radial}}{F_{applied}} \\ \frac{F_\theta}{F_{applied}} &= 0.1614 \times 2.3586 = 0.3808 \end{aligned} \tag{6.5}$$

The factor calculated through Equation 6.5 was corrected for difference in the thickness of the steel calibration ring and the specimens tested. It was used to estimate the modulus of the specimens, independent of the results from the split-disk tests.

Test Setup

The wedge test was set up on the Instron 5985 electromechanical test bench at Syensqo (Figure 5.17). A loading rate of 22 mm/min was used. For the wedge angle of 15°, it applied close to a 12 mm/min radial expansion rate on the specimen. This rate was chosen to match the rate used in the split-disk tests, in subsection 6.1.2.

DIC setup 'C' (Figure 5.19) was used to measure strains the specimen. Match ID was used to post-process the images. The Region of Interest (ROI) was $890 \times 340\ px$, with a density of approximately 34 px/mm. The ROI and subset are shown in in Figure 6.5. The setup was covered with a shield to contain the debris. The DIC window was through the opening in the shield. A plexiglass barrier was placed around the setup for safety.

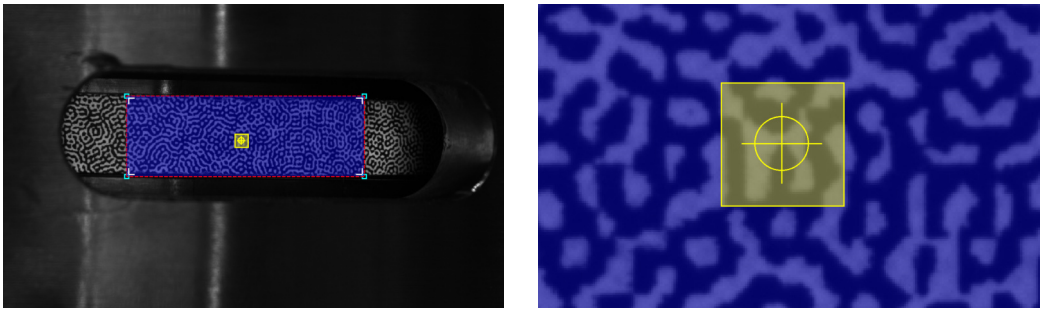

(a) Region of Interest ($26 \times 10\ mm$) **(b)** Subset Size (Yellow Box, 55×55 pixels)

Figure 6.5: Wedge Test DIC ROI and Subset Size

Test Results

Specimens B1-B3 were tested with this setup. The purpose was to estimate the hoop tensile strength and modulus of the material. The hoop strain was calculated by transforming the results to cylindrical coordinates using Match ID's built-in functions. The hoop stress was calculated from the hoop force, which in turn, was calculated through the 0.3808 factor in Equation 6.5. The hoop stress-strain curve for the tests are shown in Figure 6.6.

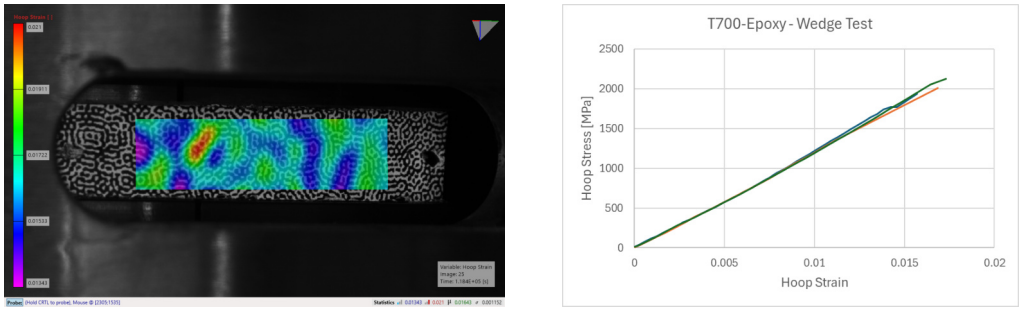

(a) DIC ϵ_{xx} Plot **(b)** Wedge Test Results

Figure 6.6: T700/Epoxy Wedge Test Strain Distribution and Results

The DIC strain plot shows the same local peaks. From the 3 tests, the Young's modulus (E) and hoop tensile strengths were determined. The E_{XX} was estimated from the slope of the stress-strain curve between $0.1 - 0.3\%$ hoop strain. The highest recorded force was used to calculate the hoop strength, using Equation 6.5. The estimated properties are listed in Table 6.5.

Table 6.5: T700/Epoxy Hoop Tensile Properties from the Wedge Test

Specimen	$X_T\ (MPa)$	$E_{XX}\ (MPa)$
B1	1936.38	114243
B2	2011.81	119411
B3	2130.08	115837
Mean	2026.09	116497
S.D.	97.63	2646

6.1.4. Reason for Difference

The specimens in both tests were cut from the same tube, and hence, had the same layup and material properties. Ideally, the strength predicted by the wedge test should be higher as it mitigates the split-disk test's stress concentrations due to bending [37]. The failure strains were compared between the two tests in Table 6.6.

Table 6.6: T700/Epoxy Failure Strain Comparison

Wedge Test	
Specimen	ϵ_{XX}
B1	0.0157
B2	0.0169
B3	0.0164
Mean	0.0163
S.D.	0.0006

Split-Disk Test	
Specimen	ϵ_{XX}
B4	0.0151
B5	0.0154
B6	0.0143
Mean	0.0149
S.D.	0.0005

On average, the failure strains were 9.4% higher in the wedge test. With the same modulus, the strengths would also be higher. Hence, the difference in modulus must originate from the hoop stress calculation. In both tests, friction could have affected the results, and hence, its effect was studied.

Friction in Wedge Tests

In the wedge test, the force transferred from the cross-head to the specimen is sensitive to friction. For instance, if the friction coefficient used to arrive at Equation 6.5 was 0.081[1], the resulting $F_\theta/F_{applied}$ would be 0.4394. The estimated modulus would then increase to 141 GPa. Although the same grease was used in both calibration and burst tests, difference in its application can change the friction coefficient. This effect on the factor is shown in Figure 6.7 (a).

Friction in Split-Disk Tests

The modulus from the split-disk tests (Table 6.3) were closer to the results obtained by Zhao *et al.* [20] for hoop-wound T700-Epoxy. The initial microscopy image (Figure 5.15) showed high void content, from which lower strengths were expected. However, the resulting strengths were higher than the data-sheet value of X_T = 2125 MPa (Table 4.2). The hypothesis was that the results were dependent on friction.

From initial analyses in subsection A.4.1, the required force increased with friction. It created a gradient in the hoop strain distribution around the disk, as shown in Figure A.19 (a). With the hoop strain measured 10° away from the split, the modulus estimated increased by 6% compared to its theoretical value. The dependence on friction is shown in Figure 6.7 (b).

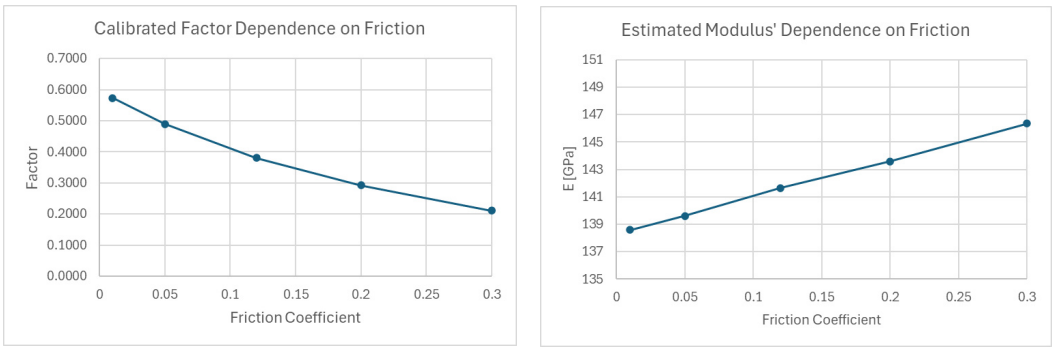

(a) Effect on $F_\theta/F_{applied}$ in Wedge Tests (Table A.6)

(b) Effect on E_{XX} in Split-Disk Tests (Table A.5)

Figure 6.7: Variation of Results with Friction

Choice of Comparison Metric

The modulus estimated independently between the two benchmark tests differed by 19%. There were uncertainties in quantifying the effects of friction in both tests' results. Hence, to avoid inaccurate strength estimations, strain-to-failure (ϵ_{XX}) was used to compare the three test setups. The theoretical modulus in Table 4.2 was retained in the FEM.

6.2. Finite-Element Model Tuning

The estimated modulus of the specimen, from section 6.1, and the test results of the ring and specimen calibration, from section 5.5, were combined to refine the FEMs developed.

6.2.1. Hyper-elastic Model Refinement

Under free compression, the loading condition of the PU 95A ring was different than in the test. Hence, the force-displacement results, from Figure 5.2, were compared with the results from Abaqus, simulating the same free compression of the ring. It is shown in Figure 6.8 (a). The performance comparison was checked for fitting in (b) but the effect of compressibility could not be discerned under free compression loading.

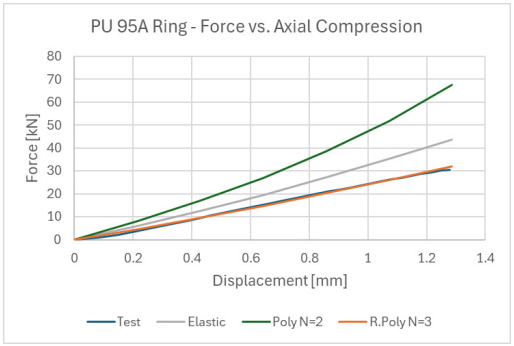

(a) Hyper-elastic Material Model Choice

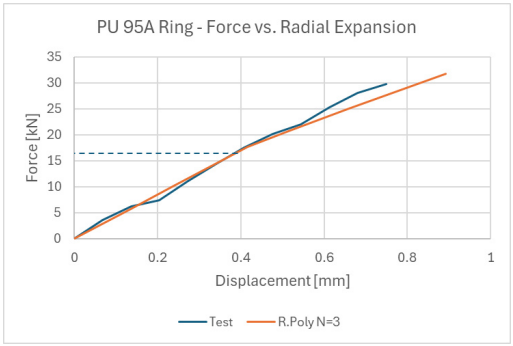

(b) R. Poly (N=3) Performance Comparison

Figure 6.8: PU 95A Material Model Comparison and Fitting under Free Compression

Initially, the Polynomial 2^{nd} order model was used as it fit well in the initial small sample compression tests, as shown in Figure 4.18. The Reduced Polynomial 3_{rd} order model had a worse fit and was unstable, failing to converge to the applied displacement. However, comparing the ring test results, the opposite was observed. The Reduced Polynomial 3^{rd} order model more accurately represented the ring's stiffness in free compression. However, it was still unstable at high compressive strains.

The two models were then compared for the thin specimen test case. The effect on force-displacement and hoop strain were compared, shown in Figure 6.9.

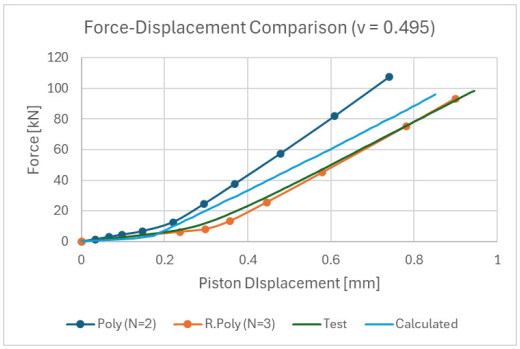

(a) Stiffness Comparison

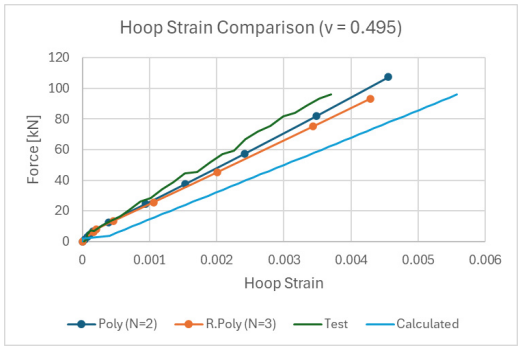

(b) Performance Comparison

Figure 6.9: PU 95A Material Model Comparison for a Thin Specimen Test

The re-fit Reduced Polynomial 3^{rd} order model predicted 10.9% better performance at the same applied force. However, it also predicted 35.6% higher displacement at the same force. The simulations shown in section 5.2 were partially updated. For the tank specimen tests, the Polynomial 2^{nd} order model was still used, owing to convergence issues in the Reduced Polynomial model. Since the results of the Polynomial model were still within 10% of the tests, the simulations were deemed valid for comparison.

The initial calculations, attached in subsection A.2.2, were also compared. As it assumed linear-elastic behaviour of the polyurethane ring, there was a 21.4% difference in the predicted performance. However, it could still be used to estimate the required compression displacement and the effect of radial gaps on the same.

6.2.2. Model Prediction Comparison

The simulations were compared to the specimen calibration tests done in section 5.5. The comparisons are shown in Figure 6.10.

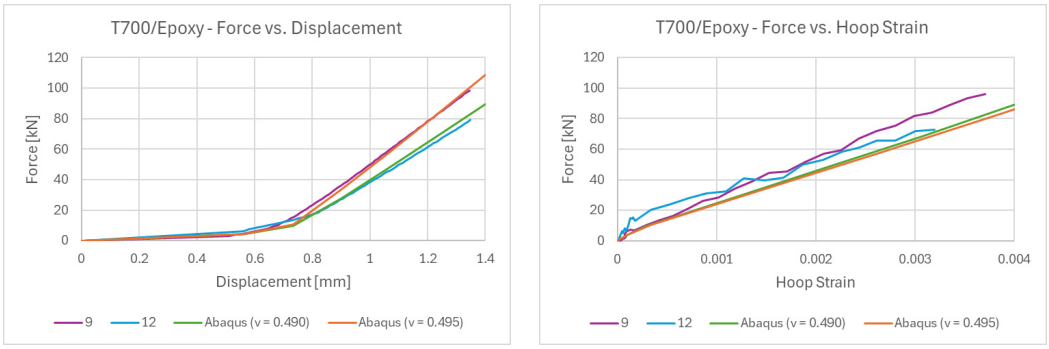

(a) Stiffness Comparison

(b) Performance Comparison

Figure 6.10: PU 94A Material Model Comparison for a Thin Specimen Test

The force-displacement curves from Abaqus are offset by 0.4 mm to have a better visual comparison with the test results. The offset exists due to initial gaps in the test, which would need to be measured accurately to be captured in the model. The Poisson's ratio of the material model governed its force-displacement behaviour. It was observed that the variation in the test results corresponded to a range of $\nu = 0.490\ to\ 0.495$. This could be attributed to tolerances in the hardness of the PU 95A material. The general tolerances specified by the suppliers were roughly $\pm 5A$ in Shore hardness.

The height of the PU ring governed the force-strain behaviour. A shorter PU ring was more effective in producing higher hoop strain. The compressibility had only a slight effect in the range of Poisson's ratios tested. The height of the PU rings in the simulations was 10.5 mm to match the average height of the actual PU rings.

The results also depended on the modulus of the composite. A specimen with a lower hoop stiffness would show a lower slope in the force-strain curve. A sensitivity study was performed in subsection A.4.5 to study its effects. It was challenging to isolate the effect of each variable. The variation in modulus of the thin specimens was not known. Hence, only the PU ring's Poisson's ratio was used as a variable to tune the FEM.

From the results, the constrained stiffness and performance of the simulations were compared with the tests. Table 5.9 was extended to include the simulation results.

Table 6.7: Material Model Tuning using Specimens 9-13

Continued from Table 5.9...		
Results	Stiffness (kN/mm)	Performance ($\mu\epsilon/kN$)
Mean	126.132	45.5
S.D.	11.348	6.1
Abaqus (ν = 0.490)	127.601	45.5
Abaqus (ν = 0.495)	154.129	47.4

Hence, the FEM was tuned, by adjusting the PU's Poisson's ratio, to closely predict the test results. It was then used to virtually develop solutions for the alignment and friction challenges in the next section.

6.2.3. Stress State Improvements

The concern was that the transverse tensile stresses (Figure 5.7) along with the through-thickness shear stresses (Figure 5.8) would lead to matrix-dominated failures in the test. This was later seen in section 6.4.

For the ideal stress state, the specimen should not bulge. That would eliminate transverse tensile stresses on the outer surface. It would also eliminate through-thickness shear stresses. The bulging behaviour depends on two factors, shown in Figure 6.11.

1. The friction between the ring and setup surfaces.
2. The positioning of the specimen with the ring.

.

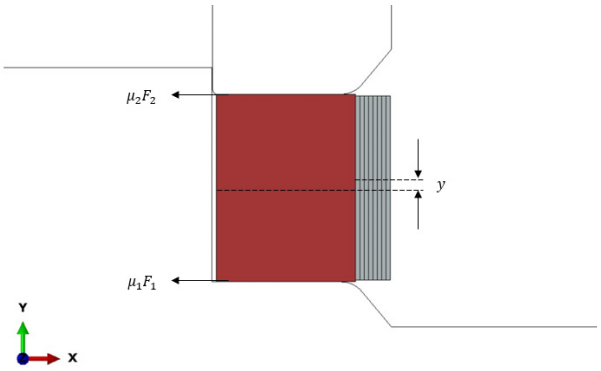

Figure 6.11: Factors Affecting Specimen Stress State

A way to fix it was to have gaps between the specimen and the fixture. It would allow the ring to expand through the gap, loading the specimen at its edges as well. It could make the stress along the height more uniform. For this to work, the friction coefficient must be low. Through trial and error, the results shown in Figure 6.12 were achieved in the simulations. The local peak in the transverse stress (S22) in (a) was neglected. It was likely an artefact of contact penetration.

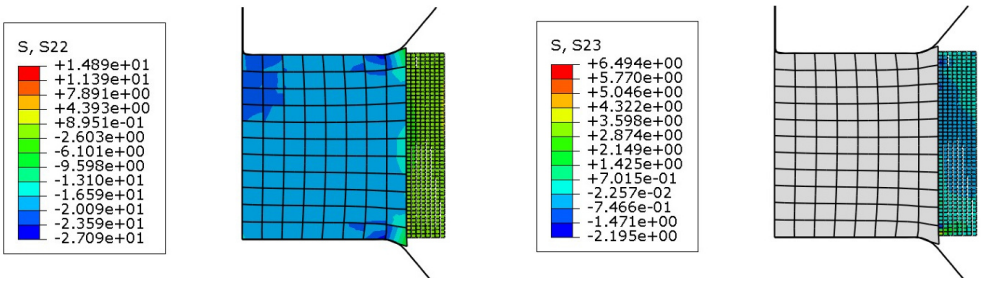

(a) Transverse Stress (Max < 1 MPa) **(b)** Through-thickness Shear Stress

Figure 6.12: Ideal Stress State with 1 mm Total Gap

For a ring height of 10.5 mm, a specimen height of 9.5 mm worked best. A friction coefficient of $\mu = 0.05$ and $y = \pm 0.1$ mm was ideal for achieving a uniform stress state. However, for the FEM, it introduced convergence issues. The nodes at the edges of the ring going past the specimen's edges created excessive penetration. In the earlier simulations, $\mu = 0.2$ prevented this issue entirely.

Practical Attempts

Theoretically, the ideal state seemed possible. Practically, however, it was tricky to achieve. A few attempts were made with specimen 10. No lubrication was used. Different vertical positions of the specimen were tried along the height of the ring. The specimen was also flipped to see if it's inherent stiffness variations affected the results. The radial expansion plots are shown in Figure 6.13.

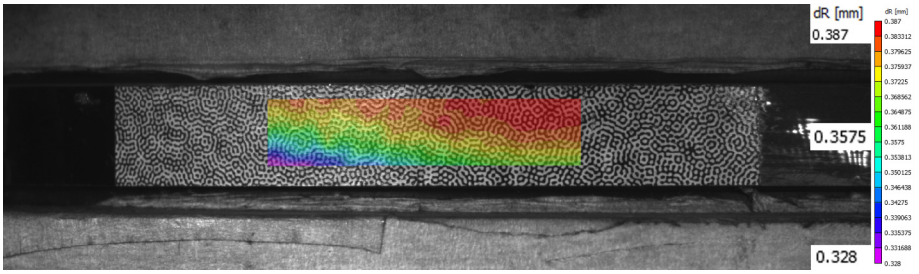

(a) Low (mm) $(Max : 0.387,\ Min : 0.328)$

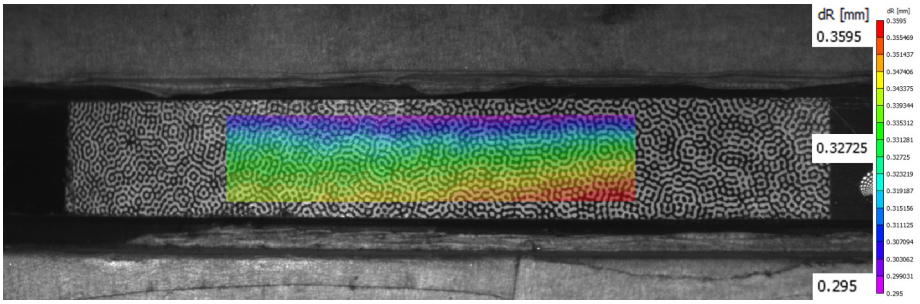

(b) Low, Flipped (mm) $(Max : 0.359,\ Min : 0.295)$

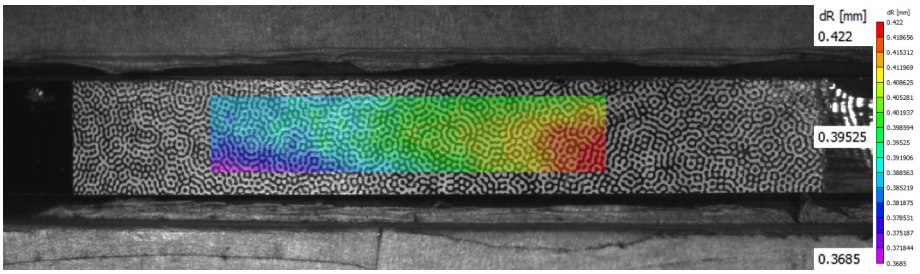

(c) Centred (mm) $(Max : 0.422,\ Min : 0.369)$

Figure 6.13: Stress State Improvement Attempts with Specimen 10 at 1.4 mm Displacement and 100 kN Force

In all tests, a slight twisting behaviour was observed, visible in the radial expansion varying along the circumference. It could be attributed to variations in the friction caused by the uneven application of grease. The specimen's position, height, as well as orientation could also have affected its expansion behaviour.

The lowest variation along the height achieved was 14.3% in attempt (b). In the same case, the transverse strains still were negligible, reaching a maximum of +0.06% (Figure A.21 (b)). This was observed to happen where the specimen's height matched that of the PU ring. The ring would then be confined within the fixture and the specimen's edges, and bulge at the centre. As the specimens' heights after polishing were not uniform, this effect varied along the circumference, as shown in (c).

Without the effect of bulging, the axial strain distribution should be negative due to the specimen's Poisson's ratio. Hence, whether the specimen is close to the ideal stress state could be determined by the variation in its radial expansion and an overall negative axial strain.

Hence, to improve the stress state in the specimens, a gap could counteract the bulging. However, friction must also be low to evenly load the specimen along it's height.

6.3. Burst Tests

Tests were performed to compare the ring expansion test's performance with the benchmark test results. The MTS 810 hydraulic test setup was used at TU Delft. The expected forces required were around 350 kN, as estimated in Table 4.20. A loading rate of 0.7 mm/s was used, consistent with the calibration tests. The test was programmed to stop if the force dropped to $< 75\%$ of the maximum.

6.3.1. Test Setup

The tests were monitored using DIC setup 'A' (Figure 5.18 (a)). An ROI of 620×190 mm was used, with a subset size of 35 px. The step size was 12. The pixel density was approximately 19 px/mm. The containment shield was placed over the setup and the images were captured through the window. It is shown in Figure 6.14.

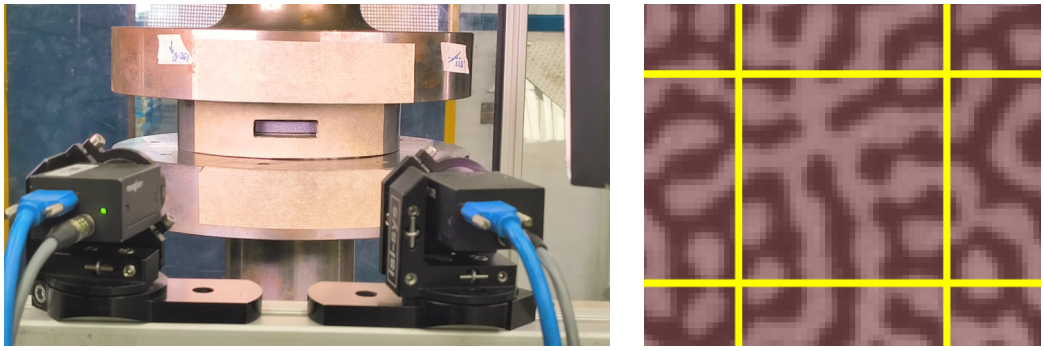

(a) ROI View Through Cameras **(b)** Subset Size (Yellow Box: 35×35 px)

Figure 6.14: Burst Test DIC Setup and Subset Size

The camera positions were as mentioned in Table 5.8. The DIC cameras were supplied with extra power. It was needed to run them at 20 Hz to be able to capture more images.

6.3.2. Stress State

Specimens 10 and 12 were tested in burst in pristine conditions. Specimen 10 was carefully aligned. The surfaces of the ring were not greased. Specimen 12 was tested with greased surfaces.

Effect of Bulging

Specimen 10 failed through matrix cracking. It was likely caused by the transverse tensile stresses developed due to the ring bulging. The correlation can be seen in Figure 6.15. This had to be fixed for specimen 12. Ideally, the entire axial strain distribution should be negative.

The bulging initiated a crack which followed the region between subsequent tape layers. There were bridging fibres observed. The crack followed the tape interface and its progression was stopped by the test bench detecting a failure through a drop in force. The failed specimen and the close-up of the crack is shown in Figure 6.16.

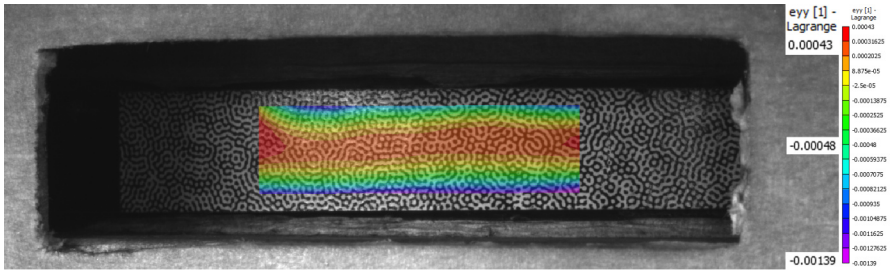

(a) Axial Strain Before Cracking in Specimen 10 (Max : 0.00043, Min : −0.00139)

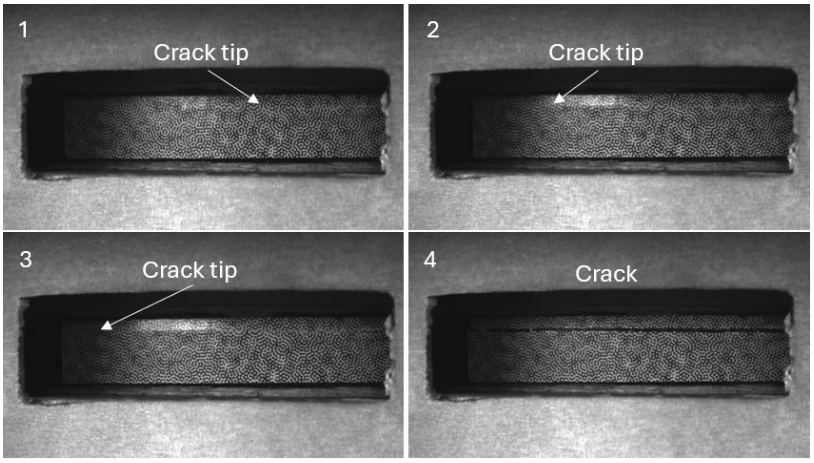

(b) Matrix Crack Progression

Figure 6.15: Matrix Cracking in Specimen 10 due to Transverse Tensile Stress

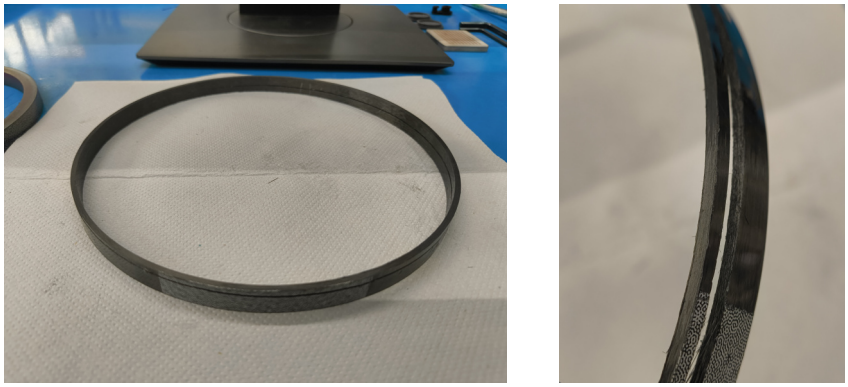

(a) Failure Through Matrix Cracking **(b)** Close-up of the Failed Region

Figure 6.16: Matrix Crack Observations for Specimen 10

Effect of Lubricant

For specimen 12, to reduce the effect of bulging, the surfaces of the ring were lubricated with Molybdenum grease. This ensured a more uniform radial expansion of the specimen. However, achieving equal expansion on the top and bottom faces was challenging. The resulting stress state, however, avoided the tensile axial strains. The axial strain plot for specimen 12 is shown in Figure 6.17. It shows a negative axial strain distribution due to the Poisson's ratio contraction. This was also effective in fatigue, as shown in section 6.4.

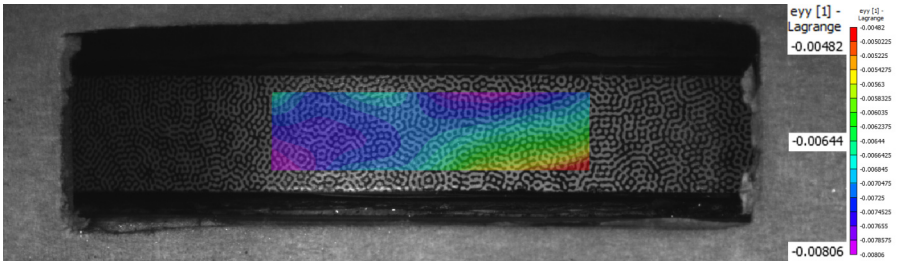

Figure 6.17: Favourable Axial Strains in Specimen 12 (Max : −0.0048, Min : −0.0081)

6.3.3. Test Results

Out of the two burst tests performed, only one exhibited the desired failure mode. Specimen 12 was tested with the greased ring to have an improved stress state. The radial expansion and the hoop strain results are shown in Figure 6.18.

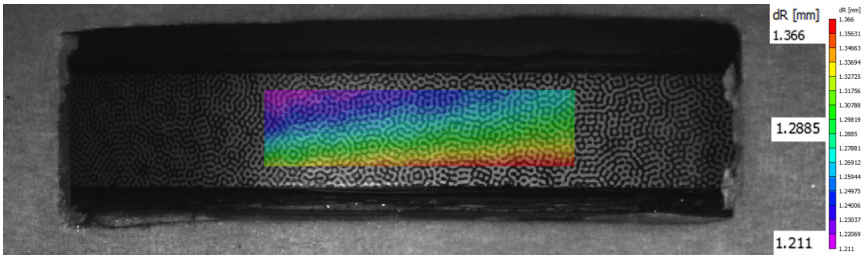

(a) Radial Expansion (mm) (Max : 1.366, Min : 1.211)

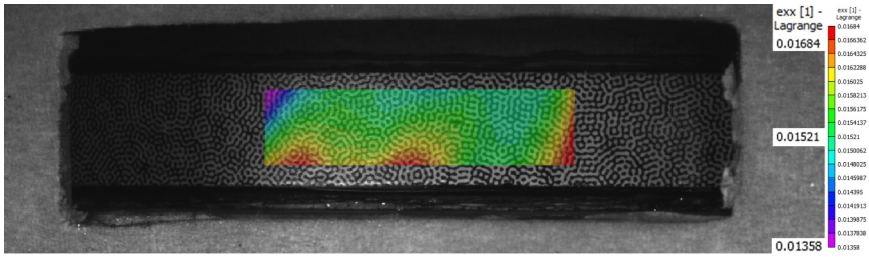

(b) Hoop Strain (Max : 0.0168, Min : 0.0136)

Figure 6.18: Specimen 12 Before Burst

The large variation in the hoop strain (red-green-red) were consistent throughout the test. It could have been caused by cutting defects at that location. If cracks formed along the edges from the defects, it could expand locally, causing the outer resin layer to stretch over that gap. The average hoop strain was considered for the results shown in Figure 6.19. The burst strength and corresponding hoop strain were 1965.44 MPa and 1.55%, respectively.

The failed specimen is shown in Figure 6.20. Mixed-mode failure was observed, namely fibre failure, matrix cracking, and delamination. The initiation is difficult to differentiate in the force-displacement curve. With the setup being covered by the containment shield, it was difficult to capture the exact failure initiation.

The force required was close to the prediction of 350 kN for the thin specimen burst test. However, due to challenges in specimen preparation, and depleting all produced specimens, further tests were not possible within the timeline to establish a more robust strength prediction.

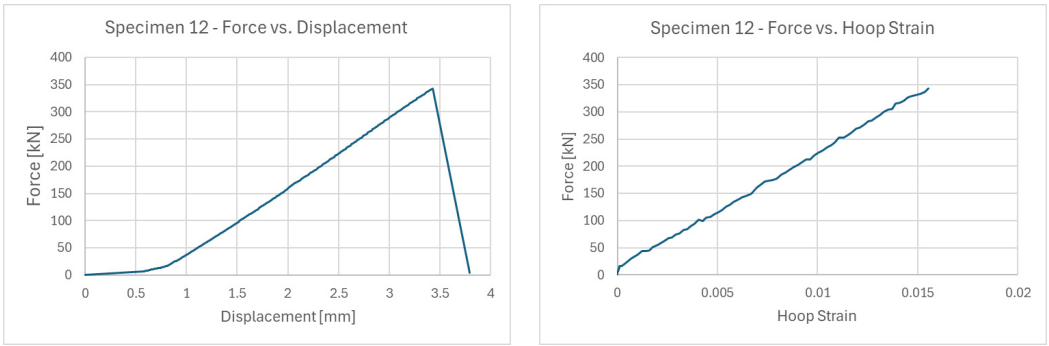

Figure 6.19: Specimen 12 Burst Test Results

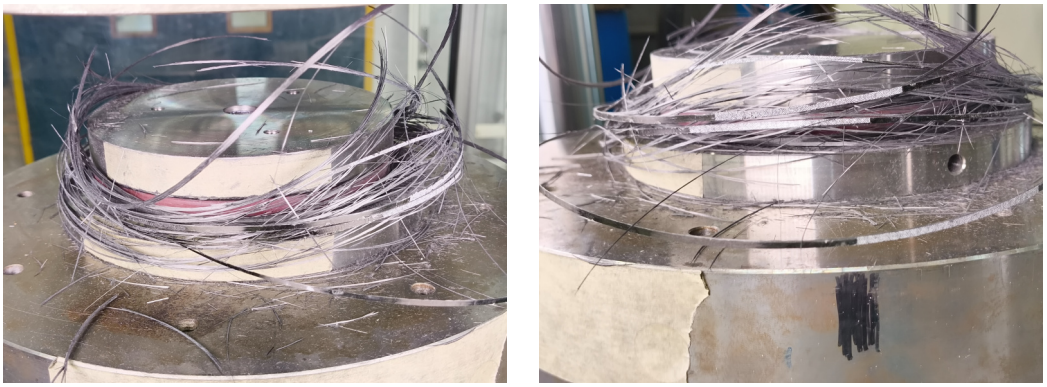

Figure 6.20: Specimen 12 After Failure

Comparison with Benchmark

The single result was compared with the two benchmark tests shown in section 6.1. The comparison is shown in Figure 6.21. As mentioned in section 6.1, due to inconsistencies in the modulus estimation, the failure strain was used as metric for comparison. As the material and layup were the same, the modulus was also expected to be the same. Hence, the strengths should be proportional to the strains.

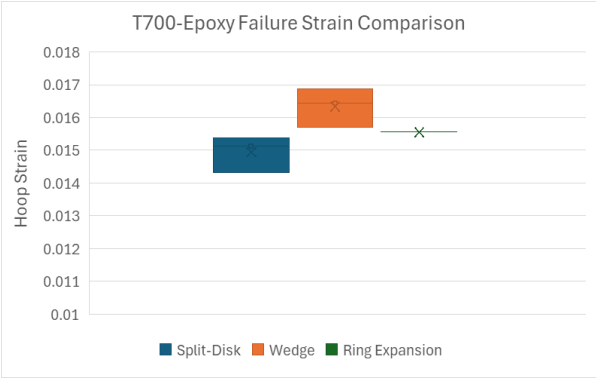

Figure 6.21: Results and Comparison with Benchmark

The test seemingly improved on the split-disk test. Comparing the failure strains, there was an average improvement of 2.6%. However, the uneven loading along the height of the specimen could have initiated fibre splits at the cut surfaces and led to early failure. Notwithstanding, for an initial comparison, the results were promising and there was still room for improvement. Ideally, the test should perform comparably to the wedge test.

6.4. Burst-After-Fatigue Tests

The same setup described in section 6.3 was used for the fatigue and burst-after-fatigue tests. The purpose was to see if the test was able to produce the fatigue damage in the specimens, as predicted by the simulations in section 5.2.

6.4.1. Fatigue Test Setup

22000 $cycles$ were applied at 25 $cycles/min$ (0.42 Hz). The cycling rate was as suggested in standard pipe fatigue tests [25]. Since the standard described an internal hydraulic pressure cycling, a sinusoidal loading curve was used to more closely represent the cycling. It was also safer and less intense for the test bench.

The DIC cameras were used to take images every 500 $cycles$ during the programmed dwell time. Two types of tests were performed, one dwelled at a constant piston displacement of 1 mm. The other dwelled at a constant force of 77 kN, which was the mean force for the loading cycles. The purpose was to study the test setups behaviour over fatigue cycles, as shown in section 5.5.

The force applied was 140 kN at $R = 0.1$ [25], which was lower than the initially decided limit. In the tank layup, at the fatigue pressure of 87.5 MPa, the hoop strain in the 90° (hoop) layers was between $0.7 - 0.9\%$. Ideally, the same was to be applied during the fatigue test of the thin specimens. However, after early failure in initial tests, to ensure the specimens can be tested for burst-after-fatigue strength, the test was limited 0.6%. It also prevented permanent deformation of the limited PU rings, allowing them to be reused.

6.4.2. Fatigue Failures

Although the goal was to apply fatigue cycles and study their burst strength after, some specimens failed during the fatigue tests. For hoop-wound specimens, this failure was mostly matrix dominated and it indicated the effect of shear or transverse stresses being induced by the test. Fibre-splitting at the edges was also observed as an artefact of the ring cutting process. These are shown below as examples of what constitutes an unsuccessful test.

Shear Failure

In earlier trial tests, a trial specimen was tested up to 1% hoop strain, where it failed in 75 $cycles$. The failure seemed to be matrix dominated, as the specimen predominantly split along the fibre direction. The failed specimen is shown in Figure 6.22. As it failed before the first dwell cycle, no images were taken to study the strains. However, it was likely caused by through-thickness shear stresses in combination with transverse tensile stresses.

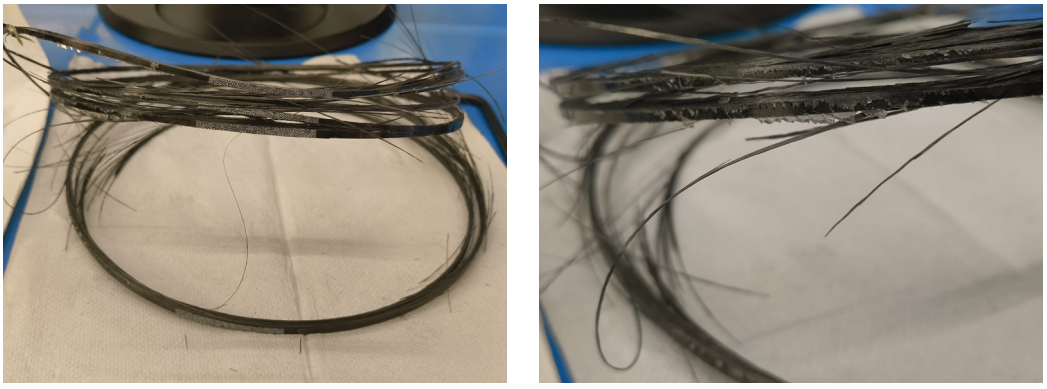

Figure 6.22: Specimen 7 Fatigue Failure after 75 $cycles$ (240 kN, $R = 0.1$, 0.42 Hz)

Fibre Splitting

A lower strain was tried by cycling the specimen up to 200 kN. Sets of 1000 $cycles$ were applied and the specimen was inspected visually between subsequent sets. After 3000 $cycles$, fibre splitting was

observed at the cut surface. These were likely tape edges that were trimmed off while cutting the rings, leaving behind a loosely bound fibre bundle. These were likely exacerbated by the ring loading the specimen more along the edge. It is shown in Figure 6.23.

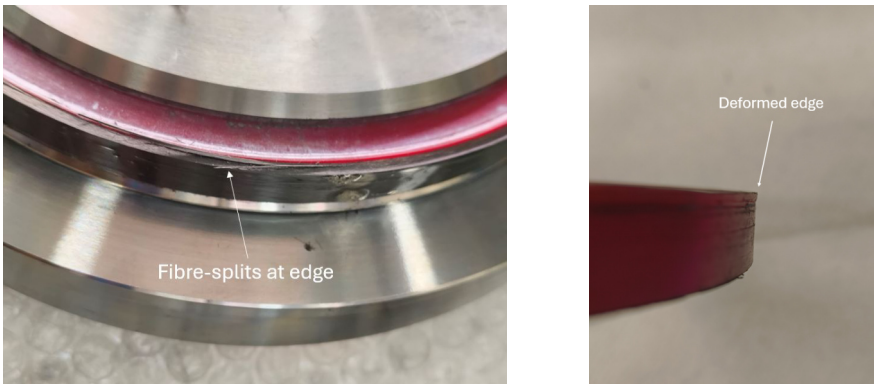

(a) Fibre-splitting **(b)** Permanently Deformed Ring

Figure 6.23: Specimen 8 Fibre Splitting Observed after 3000 $cycles$ (200 kN, $R = 0.1$, 0.42 Hz)

The presence of fibre-splitting on one edge, however, indicated that that edges was being loaded more. The specimen was inverted after 3000 $cycles$ and the split fibres were not observed to propagate.

Also observed as shown in Figure 6.23 (b), was that as the rings expanded through the gaps, they started deforming permanently at high forces. This was not the case at 140 kN. As the number of rings and specimens was limited, the remaining fatigue tests were carried out till 0.6% hoop strain to allow for burst-after-fatigue tests.

Matrix Cracking

Specimen 9 failed in fatigue due to matrix cracking. The transverse strains were tensile when observed in DIC. It is shown in Figure 6.24. At roughly 100 kN, the specimen is shown after the fatigue test in Figure 6.25.

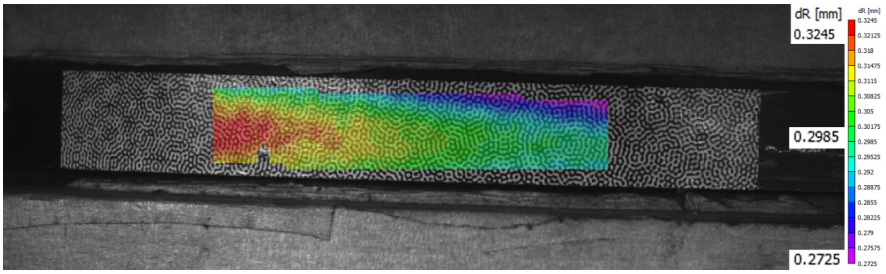

(a) Radial Expansion (mm) (Max : 0.3245, Min : 0.2725)

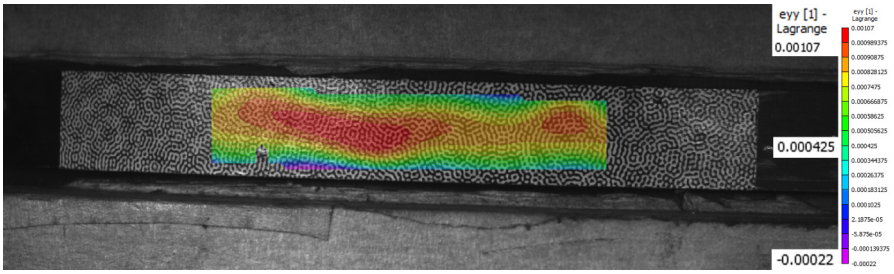

(b) Axial Strain (Max : 0.0011, Min : −0.0002)

Figure 6.24: Specimen 9 Calibration Before Fatigue

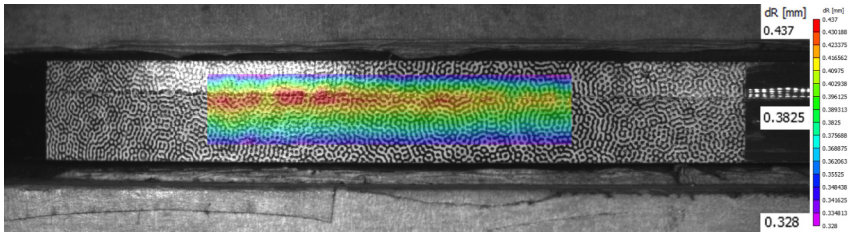

Figure 6.25: Specimen 9 Radial Expansion (mm) After 22000 Cycles till 140 kN, $R = 0.1$ (Max : 0.437, Min : 0.328)

This was also observed with specimen 10, as shown in Figure 6.15 (a). A pattern noticed was that when the specimen's height was same as that of the ring, it bulged in the centre causing the transverse tensile strain on the specimen. Allowing some gap at the top and bottom edges and applying uniform grease along the faces of the ring was used to mitigate this.

Fatigue Test

The above challenges were mitigated while testing specimen 13. The faces of the PU ring were greased and a better alignment was ensured. The resulting strain distributions are shown in Figure 6.26. Although a slight gradient still existed, the transverse tensile strains were avoided. However, interaction with shear stresses was still expected.

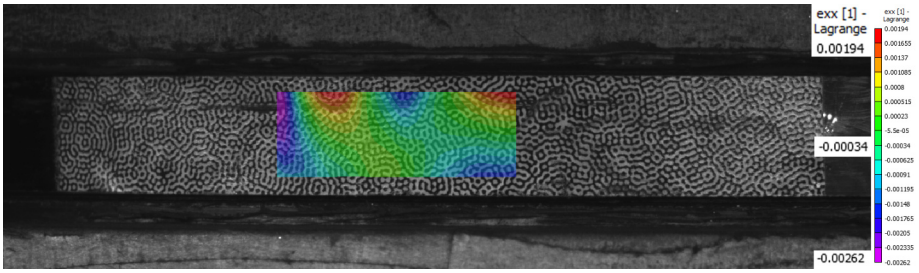

(a) Relative Hoop Strain (Max : 0.0019, Min : −0.0026)

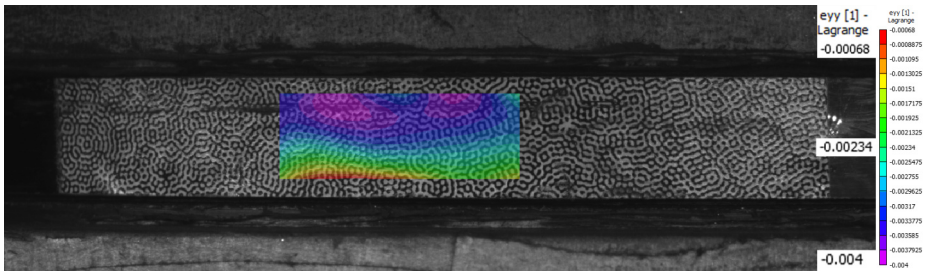

(b) Relative Axial Strain (Max : 0.0007, Min : −0.0040)

Figure 6.26: Specimen 13 After 22000 Cycles till 140 kN, $R = 0.1$

The specimen survived the fatigue test with no visible cracks. It was tested with a second calibration test after fatigue to check for stiffness reduction. The comparison of the ring-specimen combination before and after fatigue is shown in Figure 5.37. The plots showed negligible variation in stiffness, which likely meant the specimen was not damaged. The performance reduction was attributed to the ring. The setup also did not make contact with the specimen, as there was no damage to the edges after the test. It is shown in Figure 6.27.

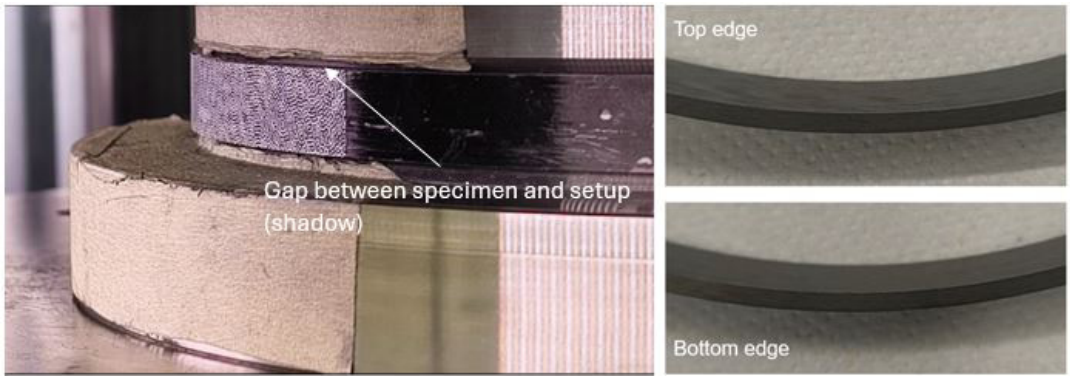

Figure 6.27: Gap Between Specimen and Edge Conditions After Test

6.4.3. Burst After Fatigue

The same test program as the burst tests was used. The rings from the respective specimens' fatigue tests were reused. Out of specimens 9, 11, *and* 13 tested in fatigue, only specimen 13 showed more fibre failure. The burst specimen is shown in Figure 6.28.

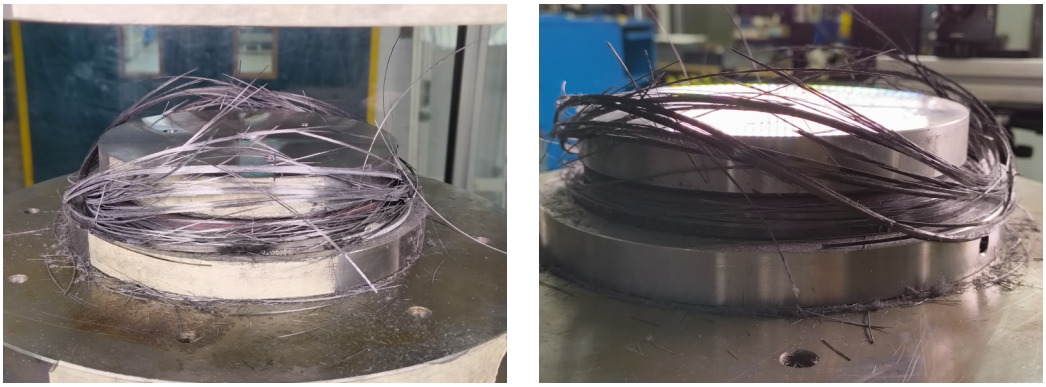

Figure 6.28: Specimen 13 Burst After Fatigue

The DIC plots are shown in Figure 6.29. The grease partly mitigated the bulging effect. Hence, to avoid the formation of transverse tensile strains, the specimen was placed at the slightly below the centre of the ring. The intention was to control the PU ring's expansion through gaps, preventing it from bulging at the centre. However, it was lower than intended and increased loading on one edge.

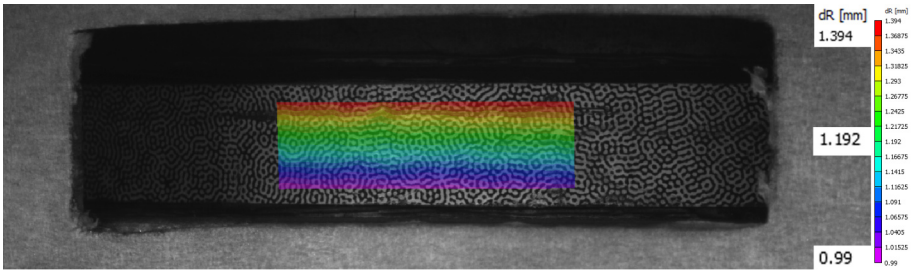

(a) Radial Expansion (mm) $(Max : 1.394,\ Min : 0.990)$

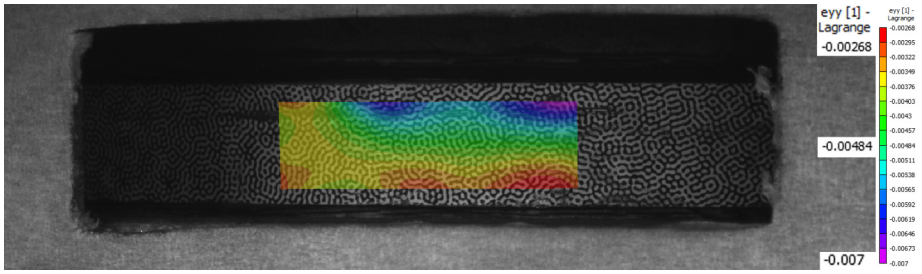

(b) Axial Strain (Max : 0.0016, Min : −0.0109)

Figure 6.29: Specimen 13 Expansion and Strains

6.4.4. Test Results and Comparison

The burst strength of specimen 13 after fatigue was compared to the burst strength of specimen 12. The comparison are shown in Figure 6.30.

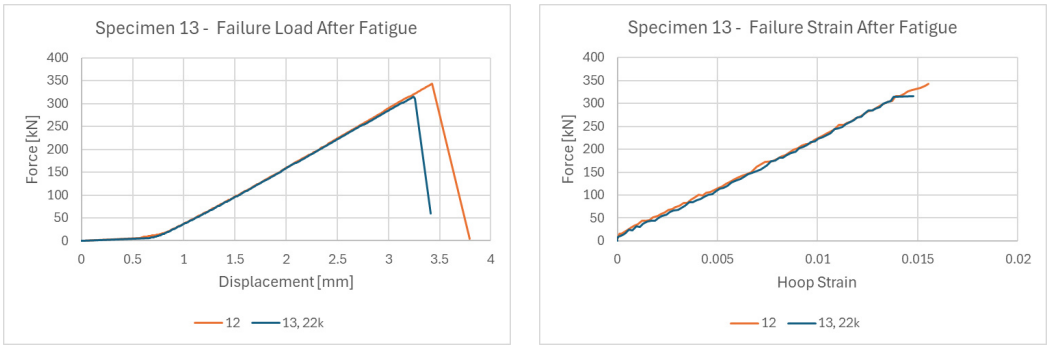

Figure 6.30: Strength Before and After Fatigue

After fatigue, the burst strength was 1868.32 MPa and the corresponding hoop strain was 1.48%. There was a reduction in strength of 5.2%. It followed the expectations. However, there not were enough data points to make a clear distinction between the effect of fatigue loading and the effect of material variability.

6.5. Tank Specimen Fatigue Tests

Preliminary tank specimen tests were performed on the MTS 810 hydraulic test bench at TU Delft. The goal was to test the limits of the setup. It would also demonstrate whether it could be used to test tank specimens in fatigue. The sequence of thin specimen tests were performed again for the tank specimens.

6.5.1. Specimens

The tank specimens were cut from tube shown in Figure A.7 by a colleague at Syensqo. As reported by him, cutting it on a lathe introduced challenges in finding the right cutting speed and stop point. Each specimen was cut on a lathe and took 1 hour. They were then ground down to polish the cut faces. The resulting specimens' dimensions are shown in Table 6.8.

Table 6.8: Tank Specimen Dimensions

Specimen	Height (mm)	Thickness (mm)
T1	10.062	13.834
T2	10.160	13.718
T3	9.954	13.746

Three specimens were produced. The cut section and edges of specimen T1 are shown in Figure 6.31. The edges also showed split fibres. The same was observed in specimens T2 and T3 as well.

(a) Surface Scratches **(b)** Pits and Voids **(c)** Layer Waviness

Figure 6.31: Tank Specimen T1 Cross-section and Defects

6.5.2. Test Setup

For the all tank specimen tests, DIC setup 'A' was re-used. The camera positions are shown in Table 6.9. The specimen and setup are shown in Figure 6.32.

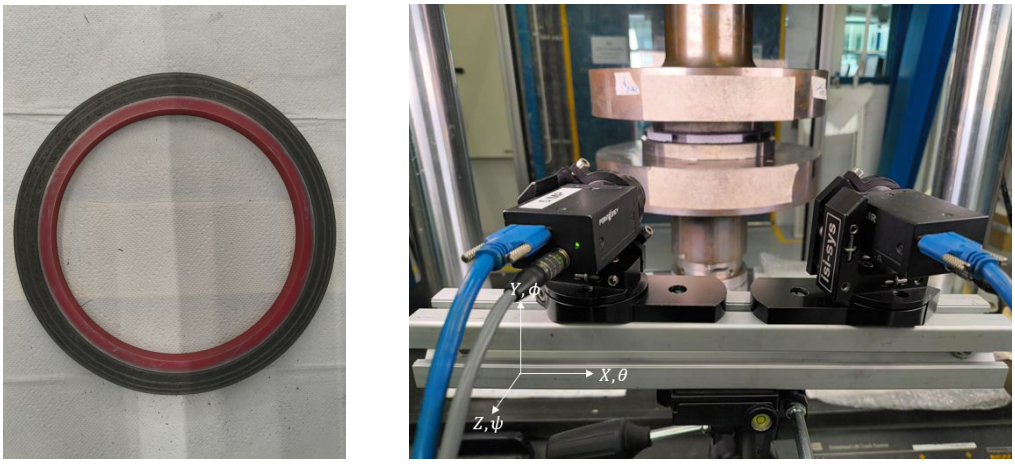

(a) Tank Specimen with PU 95A Ring **(b)** DIC Setup 'A' and Coordinate System

Figure 6.32: Tank Specimen and DIC Setup

Table 6.9: Camera Positions for Tank Specimen Tests

Setup	$X\ (mm)$	$Y\ (mm)$	$Z\ (mm)$	$\theta\ (°)$	$\phi\ (°)$	$\psi\ (°)$
A	160.219	4.121	40.000	0.769	-24.927	-1.218

6.5.3. Calibration

Static tests were done with each specimen prior to the fatigue tests, to get the initial relation between the applied force and hoop strain. Unused PU rings 9 and 10 were used. 240 kN of force was applied at 0.7 mm/s. The results of the test are shown in Figure 6.33.

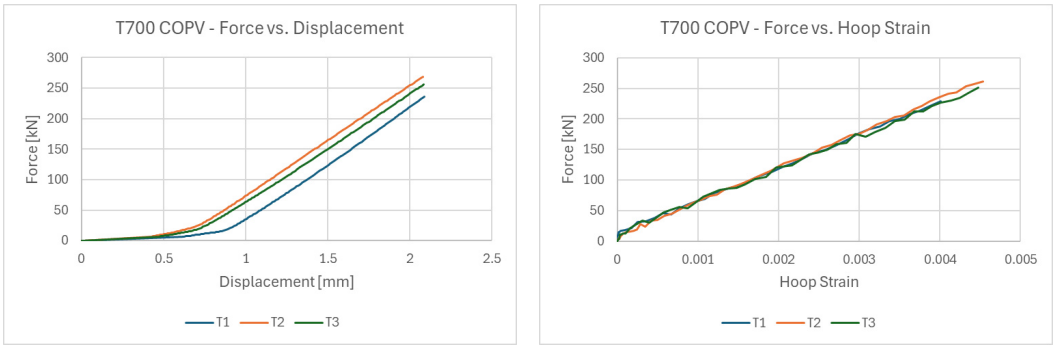

Figure 6.33: Tank Specimen Calibration

The hoop strain distributions on specimen T1 and T3 are shown in Figure 6.34. Due to their thickness, the strain distribution showed less of a gradient compared to thin specimens. However, as seen for specimen T2, it was still influenced by the alignment with the ring.

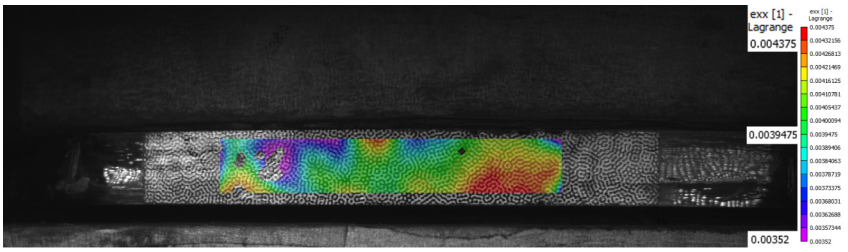

(a) T1 (Max : 0.0044, Min : 0.0035)

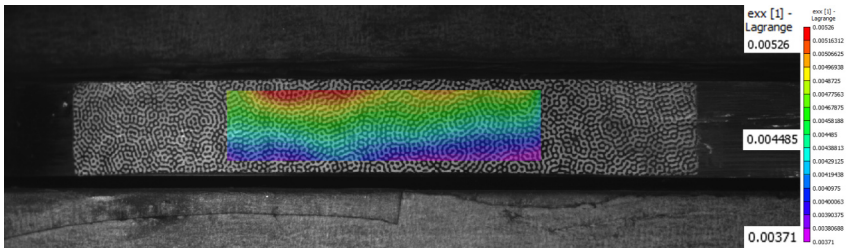

(b) T2 (Max : 0.0053, Min : 0.0037)

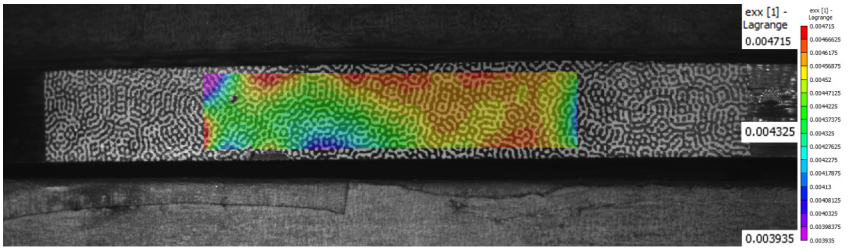

(c) T3 (Max : 0.0047, Min : 0.0039)

Figure 6.34: Tank Specimen Hoop Strain Distributions, Centred

The results were compared to the Abaqus model, shown in Figure 6.35. The Abaqus force-displacement plot was offset by 0.6 mm to match the initial gap in the test setup.

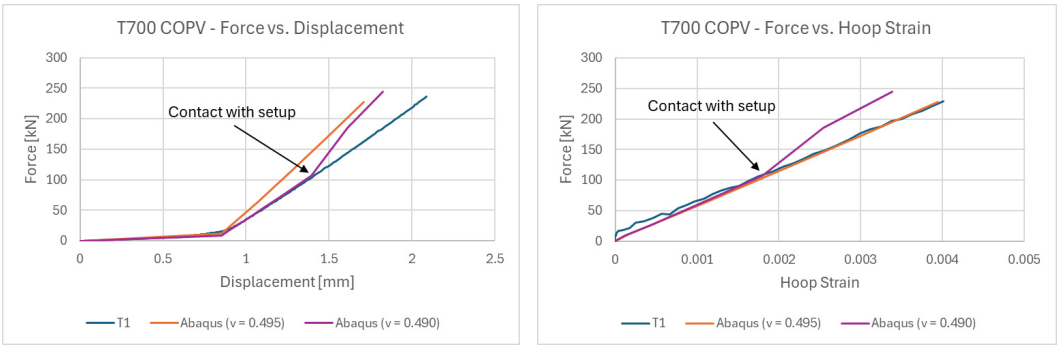

Figure 6.35: Test Comparison with Abaqus

At higher compressibility ($\nu = 0.490$), the tapered faces contacted the specimen. The forces were predicted to increase significantly as the setup would directly load the composite specimen. There would also be a reduction in the performance of the setup as it would no longer load the specimen as much radially through the PU ring. In the static tests, the initial height of the ring was higher than the specimen's. Hence, the contact was not observed. The effect of contact was also not seen in the tank specimen fatigue tests. It could mean that the variation in the slopes could be stemming from a lower effective modulus of the specimen itself.

In the FEM, a perfect model of the composite was assumed, which resulted in its ideal effective hoop tensile modulus. In the tests, the effect of the voids, waviness, and fibre splits would reduce that modulus, causing it to expand more at the same force. It could be why contact predicted by the simulation was not observed in the tests.

Limit Test

A static test was performed up to 400 kN, close to the test bench's limit. Its purpose was to find out whether the force-hoop strain relation remained linear up to that limit. The results were then used to establish the relation between the hoop strain and internal pressure by comparing it to the Abaqus results. The hoop strain distribution is shown in Figure 6.36.

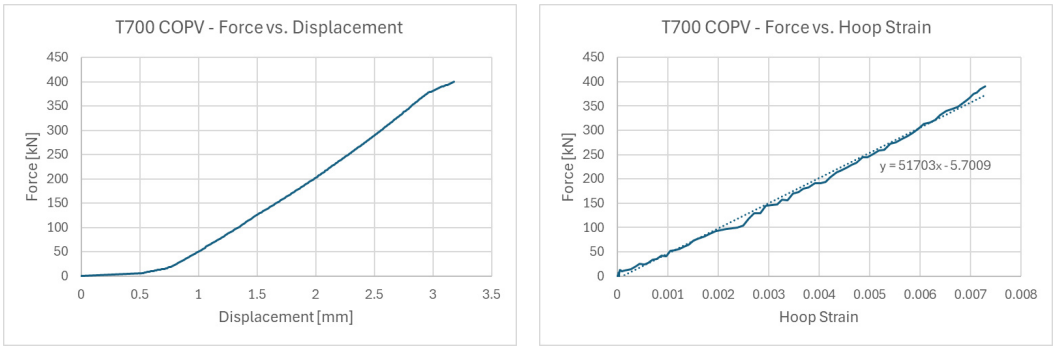

Figure 6.36: Limit Test Relation

The kink towards the end in the both the curves indicated a sudden jump in displacement without much increase in force or radial expansion. It could be because of the PU ring squeezing out of a gap, suddenly creating an extra volume for the indenter to fill.

As per the simulation, at an average contact pressure of 90 MPa on the inner face, the hoop strain on the outer hoop layers was 0.0067. This is shown in Figure 6.37. From the test results, an applied force of approximately $350 - 400$ kN should be sufficient to reach that strain, and hence, internal pressure.

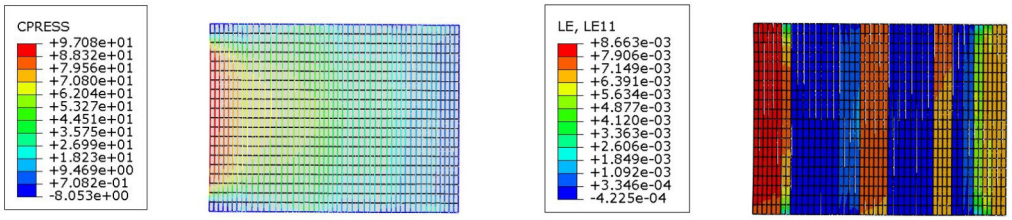

(a) Average Contact Pressure of 88 MPa **(b)** Outer Layer Hoop Strain, $\epsilon_{xx} = 0.0067$

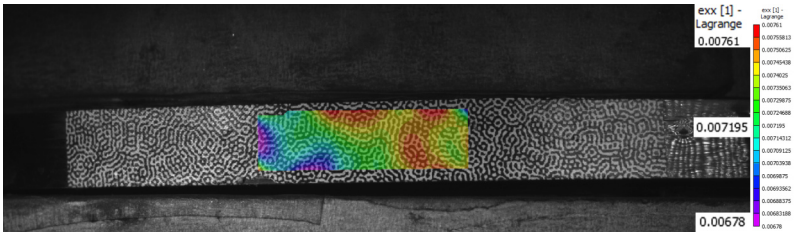

(c) T3 Hoop Strain Distribution (Max : 0.0076, Min : 0.0068)

Figure 6.37: Simulation Correlation with Tests

6.5.4. Fatigue Tests

Specimens T1 and T3 were tested in fatigue. Specimen T2 was only used for calibration (Table 6.10). Specimen T1 was tested till 11000 $cycles$ at 10 $cycles/min$. The maximum force applied was 300 kN which corresponded to a hoop strain of 0.5%, extrapolating from Figure 6.33. Specimen T3 was tested at 450 kN to test the limits of PU 95A.

Ring Height Reduction and Deformation

For specimen T1, at 300 kN ($R = 0.1$), the ring's height reduced by 0.40 mm. Specimen T3 was tested till 450 kN with an unused ring. After 27 $cycles$, the height reduced by 0.42 mm. It caused the total stroke exceed 3.9 mm, which was set as the test bench's displacement limit. This was owing to the 4 mm compression limit of the indenter's design. The height reductions are shown in Figure 6.38.

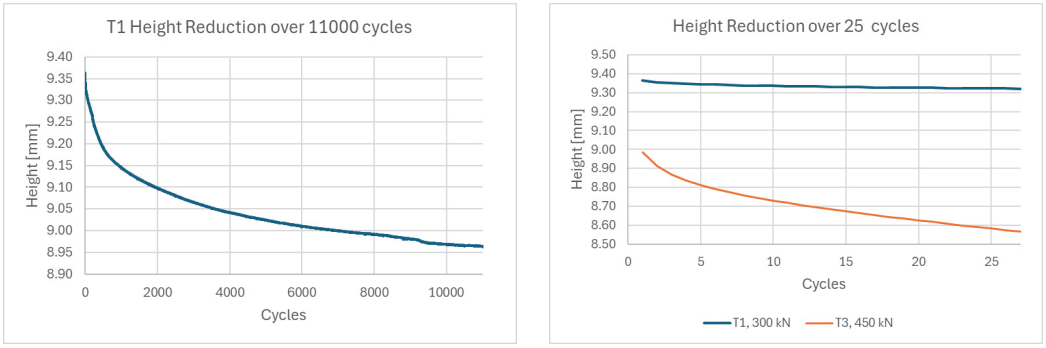

Figure 6.38: Ring Height Reduction for Specimens T1 and T3

As the ring's height reduced to below that of the specimen, it eroded the specimen's and the ring's edges. The ring was also permanently deformed. These are shown in Figure 6.39. The deformed shape of specimen T3's ring conformed to the oblique position of the specimen at the start of the test.

(a) Ring 9 Dust from Erosion

(b) Ring 9 after 11000 $cycles$ at 300 kN

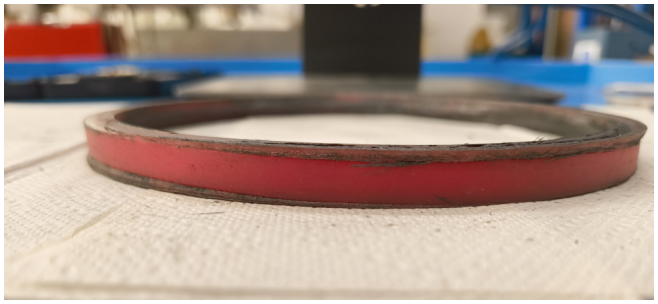

(c) Ring 10 after 27 $cycles$ at 450 kN

Figure 6.39: PU 95A Ring Deformation and Damage

Performance During and After Fatigue

The test was programmed to dwell at the mean load of 165 kN every 250 $cycles$ to take images for DIC. The reference image was also taken at 165 kN at the first cycle. Hence, the strain and displacement results shown in Figure 6.40 are relative.

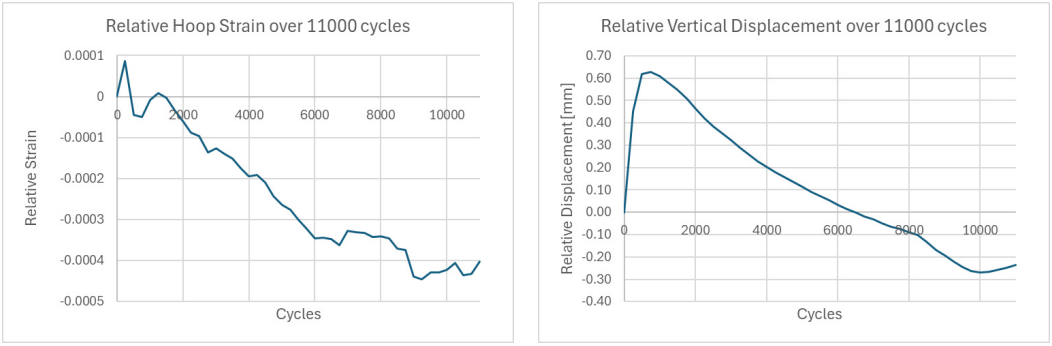

Figure 6.40: PU 95A Performance During Fatigue at 300 kN

The hoop strain applied on the specimen, at the mean force, reduced over cycles. The initial increase was due to the compression stiffening of the PU ring. The subsequent decrease in performance could be due to the ring getting compressed significantly. Over cycles, the specimen's vertical displacement should have increased corresponding to the reduction in height.

The downward movement could not have been due to contact with the indenter. It was fixed so it could not have pushed it down further than its initial height. The decrease was attributed to the PU ring squeezing in between the indenter and the specimen. The extruded lip of the ring shown in Figure 6.39 (b) could have gone in between the gap. As it was compressed, it would have squeezed out more,

pushing the specimen further down in every cycle. This would also explain the dust formed along the top edge of the ring.

The reduction in hoop strain over time was attributed to the increase in compressibility of the PU ring. In the force-controlled test, it resulted in lower radial expansion at the limits. A larger fraction of the force applied was then being used in the compression of the PU ring than for loading the specimen. This behaviour was also seen after the thin specimen burst tests in Figure 5.38, and to some extent in the fatigue tests in Figure 5.37.

Specimen Damage

The damage on the specimens shown in Figure 6.41 could be due to the PU ring squeezing out and eroding the edges through friction.

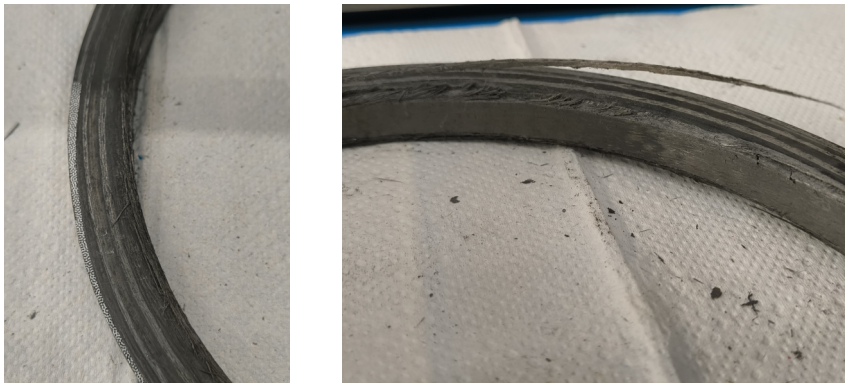

(a) T1 after 11000 $cycles$ at 300 kN **(b)** T3 after 27 $cycles$ at 450 kN, Chamfered Edges

Figure 6.41: Specimen Damage

Both specimens showed frayed edges and fibre splitting. For specimen T3, the edge became chamfered, conforming to the tapered edges of the indenter on one side. The effect of height reduction on the force displacement behaviour is shown in Figure 6.42. In case of direct contact, an increase in the slope should have been visible in curve, similar to Figure 6.35.

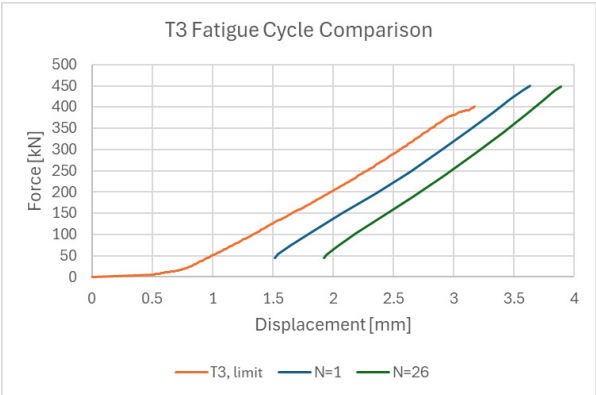

Figure 6.42: T3 Fatigue Cycle Comparison

The actual load cycle only had a 2 mm stroke. The rest was covered in expanding the PU ring to fill the axial and radial gaps. Hence, the fatigue test seemed possible by using rings which adhered better to the tolerances specified. The excessive height reduction at high forces might be overcome by increasing the initial height of the ring. However, it could exacerbate the permanent deformation at the edges.

Table 6.10: Test Matrix and Summary

Tests	Specimens				PU Rings	Test Cycles					Notes	
Thin Specimens	Number	Height (mm)	Thickness (mm)	D_{inner} (mm)	Number	Calibration*	Burst	Fatigue (Load (kN), Frequency (Hz))**	After Fatigue*	Burst After Fatigue	Fail Load (kN)	Failure Mode
Fine-tuning	1	9.36	2.45	170.04	1	4	1	-	-	-	308	Mixed-mode
	2	9.40	2.27		2	3	1	-	-	-	252	Matrix-dominated
	3	9.27	2.26		4	3	1	-	-	-	306	Mixed-mode
	4	9.13	2.34		4	1	-	24000 (140, 0.42)	-	1	287	Matrix-dominated
	5	9.19	2.31		5	1	-	22000 (140, 0.42)	-	1	340	Mixed-mode
	6	9.59	2.28		6	2	-	22000 (140, 0.42)	-	1	353	Mixed-mode
	7	9.27	2.29		7	6	-	76 (240. 0.42)	-	-	-	Matrix cracks
	8	9.36	2.32		8	1	-	3000 (200, 0.42)	-	-	-	-
Calibration, Burst, Burst-After-Fatigue	9	10.36	2.21		6	3	-	22000 (140, 0.42)	1	-	-	Matrix crack
	10	10.06	2.23		3	10	1	-	-	-	237	Matrix crack
	11	10.15	2.30		1	1	-	22000 (140, 0.42)	3	1	276	Matrix-dominated
	12	9.98	2.21		4	3	1	-		-	343	Fibre-dominated
	13	10.09	2.26		2	3	-	22000 (140, 0.42)	2	1	315	Fibre-dominated
Benchmark Wedge Test#	B1	10.07	2.14	146.25	-	-	1	-	-	-	109	Mixed-mode
	B2	10.07	2.10		-	-	1	-	-	-	112	Mixed-mode
	B3	10.07	2.05		-	-	1	-	-	-	115	Mixed-mode
Benchmark Split-Disk#	B4	10.02	2.08		-	-	1	-	-	-	99	Mixed-mode
	B5	9.99	2.06		-	-	1	-	-	-	93	Fibre-dominated
	B6	10.02	2.14		-	-	1	-	-	-	90	Mixed-mode
Tank Specimens	T1	10.06	13.83	170.07	9	2	-	11000 (300, 0.17)	1	-	-	Edge erosion
	T2	10.16	13.72		10	3	-	-	-	-	-	-
	T3	9.95	13.75		10	3	-	25 (450, 0.17)	-	-	-	Edge erosion

* Calibration and After Fatigue tests were displacement-controlled, up to 1.4 mm at 0.7 mm/s. It applied approximately 100 kN of force depending on the gaps. For tank specimens, calibration tests were up to 2.1 mm at 0.7 mm/s, applying approximately 250 kN of force.
** Fatigue tests applied a stress ratio, $R = 0.1$. The maximum load is mentioned.
# Split-disk tests were performed at a cross-head rate of 12 mm/min. For the wedge tests, to apply 12 mm/min on the specimen, the equivalent cross-head rate was 22 mm/min, calculated for the 15° wedge angle.

6.6. Discussion

All ring expansion tests performed are summarized in Table 6.10. The key observations and challenges are summarized in this section. The capabilities and limitations of the test developed are then discussed.

6.6.1. Thin Specimen Tests

The thin specimen were used to fine-tune and calibrate the setup. Static and fatigue tests were then performed to establish that the setup can be used for the same. The tests were meant to demonstrate the setup's capability to perform burst, fatigue, and residual strength tests. The minimum goal was to be able to perform comparative tests to distinguish material based on their residual strength.

Observations

The setup depended on the properties and performance of the PU 95A rings. The rings were in near-hydrostatic compression. Hence, its capability to load the specimen depended on its compressibility. In the calibration tests in section 5.5, there was a variation in the loading stiffness of the polyurethane. Correlating with the material model in the FEM, the variation was linked to the material's Poisson's ratio.

The hyper-elastic material model was based on the test data from Qi and Boyce [50]. It was fit using a polynomial equation. The only variable that could be adjusted in the model was the Poisson's ratio. Hence, based on the FEM results, the test was sensitive to the material's compressibility. However, in the actual test, factors such as the hardness of the ring and the modulus of the specimen could also caused the variation in the force-displacement curves.

The supplier, Airlant, had not provided a hardness tolerance. However, other suppliers such as Artech Rubber had quoted a tolerance of $\pm 5A$. From the modulus estimation, using the split-disk test, in section 6.1, variations of up to 18 GPa were observed between specimens.

Challenges

The specimens had an outer resin-rich layer, as shown in Figure 5.26a. It caused artefacts while post-processing the DIC strain results. A work-around was implemented using the radial expansion data to calculate strains, wherever necessary.

Initial static tests showed a uniform hoop strain distribution along the circumference of the specimens. However, the distribution along the specimen's height had a gradient. It depended on the specimen's positioning with respect to the ring and friction at the ring's top and bottom faces, as shown in Figure 6.11.

Aligning the specimen at the start of the test proved challenging as it had to be precise, within a tolerance of few hundred microns. This was exacerbated by the uneven specimen height from polishing. The height of the specimen with respect to the ring also affected the stress state. Through simulations, the conditions to achieve the ideal stress state were shown in Figure 6.12. Allowing the ring to expand around the edges of the specimen should created a more uniform loading along the height. It avoided interactions with transverse and shear stresses.

Finally, some PU rings showed performance reduction by up to 10% over 22000 $cycles$ (Figure 5.37). However, it can also be compensated for by the initial increase in the ring's stiffness as it got compressed. For a force-controlled fatigue test, it meant that strain applied over the test could reduce by up to 0.03%.

6.6.2. Tank Specimen Tests

The tests were deemed as nice-to-have, if possible within the timeline of the thesis. The purpose of the tests were to demonstrate whether the setup could test representative COPV specimens. The minimum goal was to check if a proof-of-concept could be established. If successful, it could enable future studies to link representative specimen tests to a full COPV's performance.

Observations

The tests required forces up to 400 kN to apply an equivalent of 87.5 MPa of internal pressure through the PU ring. At this force, the ring was compressed by up to 3.2 mm, resulting in a strain > 30%. The ring showed excessive reduction in height, almost reaching the setup's compression limit in 27 $cycles$. The higher reduction could also have been due to the volume of the ring that got squeezed out around the specimen's edges, as shown in Figure 6.39. It showed permanent deformation and hence could not be used for further tests.

Tests at a lower force of 250 kN showed that the reduction in height was 4 times that of the thin specimen tests, which were at 140 kN. In this case, even though the ring was deformed permanently. it still retained its performance. The relative hoop strain reduced by 0.04%.

Challenges

Cutting the specimens from the approximately 14 mm thick tube was a challenge. As a result, the heights could not be adjusted precisely. The heights of the specimens could not be adjusted to account for the increased reduction in the height of the ring.

The tests demonstrated the limitations of the PU 95A material. From the results of Qi and Boyce [50], the material was expected to withstand up to 130 MPa without degradation. However, those results were for small disc specimens under uniform compression. The rings used were subject to high edge stresses around the fillet region of the setup which likely resulted in the permanent deformation observed.

6.6.3. Capabilities

Despite the aforementioned rough edges, the burst test showed a higher failure strain than the standard split-disk tests in Figure 6.21. Hence, by overcoming the challenges, there was potential room for improvement. The initial result was promising and demonstrated that the test could improve upon the standard.

In fatigue, the PU ring showed almost consistent performance throughout the 22000 $cycles$ applied at 140 kN. It's height reduced over time reaching an asymptotic value, but it did not result in a performance decrease. Hence, the setup achieved its minimum goal, which was to perform qualitative residual strength tests.

For the design, by accounting for the ring's reduction in height, the setup did not make contact with the specimen during the fatigue tests. This was evident by studying its edges after the test, in Figure 6.27. With over 160,000 $cycles$ applied on the setup itself, it did not show any signs of wear over the sliding surfaces or damage at the stress concentration regions. Hence, from a design standpoint, it was a success, and reached its minimum goal. The results showed potential to perform tests for an increased number of cycles to be able to generate S-N curves.

6.6.4. Limitations

The setup's fillet edges applied a stress concentration on the ring as it bent around it. The tapered faces were designed to reduce the effect while containing the ring within the specimen. However, the increased stress still exceeded the polyurethane's limits. At forces > 200 kN, it started to cause permanent deformation. The corresponding pressure on the PU ring was 49 MPa. Even though the effect on performance for 11000 $cycles$ was minimal, it affected the reusability of the rings.

As per the design, the setup cannot be compressed past 4 mm, else it will bottom out. In the tank specimen tests, the required displacements at forces > 400 kN (98 MPa) quickly approached that limit. Hence, even though the setup reached the 87.5 MPa internal pressure requirement, its maximum allowed compression can limit the number of cycles that can be applied.

7

Conclusions

The primary objective of this thesis was to **enable a more accurate characterization of the fatigue properties of wound composites**. The first sub-question it led to was how can the specimen be loaded cyclically, emulating uniform internal pressure. To answer the same, a detailed literature review was performed covering standard and non-standard tests, and novel ideas. Based on an extensive trade-off study, the result was a concept which was termed the 'ring expansion test'.

It was designed and developed from scratch through detailed finite-element analyses. Test data from literature and preliminary tests were used for material selection and to arrive at a final design. Initial tests were used to fine-tune the setup. The test developed indeed applied a uniform circumferential stress on the specimen, successfully answering the first sub-question.

The second sub-question was whether the standard split-disk test could be improved upon. The split-disk test has shortcomings, mainly stress concentration and friction, which affects the test results. These are only exacerbated in fatigue. The wedge test overcomes these limitations in static tests, but would itself deteriorate from friction in a fatigue test. To answer the second sub-question, the ring expansion test had to overcome these limitations. It was compared to the aforementioned setups through quasi-static tests.

Due to challenges in assessing the modulus of the material, and hence, its strength, failure strains were compared. The ring expansion test estimated a 2.6% higher average failure strain, even with its multiple challenges. Compared to the wedge test, which was 6.9% higher, there was still room for improvement. In fatigue, it showed consistent performance over the 22000 $cycles$ tested, for thin specimens. Hence, the test improved upon the split-disk test in quasi-static conditions. It also showed potential for the same improvement in a fatigue test, answering the second sub-question.

The main advantages of the new setup developed are,

1. It uses parts that have relatively simple construction. Hence, being easy to procure/produce. It also allows for quick assembly and disassembly. It only needs to placed between compression plates, requiring no special mounts.
2. The design has features to ensure alignment. It also accounts for contingencies where the setup might get jammed due to misalignments. For burst tests, it includes a shield to contain dust and debris, while allowing for DIC and strain gauges.
3. The setup loads the specimen uniformly along the circumferential direction, without causing stress concentrations. Thus, predicting a higher strain-to-failure for the material compared to the standard.
4. Through controlled specimen and ring dimensions, the steel parts does not make direct contact with the specimen, loading it exclusively through the ring. The tapered faces prevent excessive squeeze-out of the ring under compression.

5. The ring maintains its performance over the coarse of a fatigue test. Its successive reduction in height can be accounted for by adjusting the specimen's height.
6. The specimen is not affected by friction wear at its contact surface, as compared to the split-disk test.

However, in its current state, there are challenges that still need to be overcome. These can further improve the test results, making it a more accurate test for mechanical characterization.

1. Although friction does not wear out the specimen, uneven friction on the ring has an indirect effect. Uneven friction between the top and bottom faces and create a stress gradient along the specimen's height. High friction at the top and bottom faces can cause bulging. It creates transverse tensile stresses which cause matrix cracks.
2. The stress distribution is also dependent on the alignment of the ring and the specimen.
3. As the test involves concentric parts, gaps between their diameters must be within specified tolerances. This ensures the setup performs as intended. It requires extra care when machining or choosing suppliers for the rings.
4. The material of the ring can introduce variability in the test's performance. Hence, it would be required to calibrate each ring-specimen combination as a preliminary step before testing.

The setup is also faced with limitations, which stem from a combination of the choice and polyurethane and the setup's tapered design.

1. At forces $> 250\ kN$, stress concentration around the fillet causes permanent deformation of the ring. It can degrade the ring's performance at high cycles. For thin specimens, it can limit the maximum hoop strain in fatigue tests to $\leq 1.2\%$ (75% strength).
2. At forces $> 400\ kN$, it sees excessive height reduction, reaching the setup's compression limit of $4\ mm$. Hence, for fatigue tests on COPV specimens, it can limit the maximum internal pressure that can be simulated to $\leq 70\ MPa$.

Despite the challenges faced in the tests, it still showed an improvement in the failure strain over the split-disk test. The ring expansion test also showed potential for the same improvement in fatigue tests. The challenge in achieving the ideal stress state is a practical one, and can potentially be overcome, as discussed in chapter 8. Hence, to answer the main research question, the ring expansion test developed can enable a more accurate characterization of fatigue properties of composite rings.

8

Recommendations for Future Work

Several factors could have affected the test results and setup design. Due to practical limitations, not all of them could be addressed. Hence, recommendations for future work are listed below, starting from the specimens.

8.1. Specimens

Variations in the test results could stem from the specimens itself. Its preparation and accurate assessment of its properties can help better understand the test results.

8.1.1. Preparation

A major challenge was to cut the specimens from the filament-wound tubes. Ideally, composites are machined using PCD tools or water-jet cutting. Thin, hollow tubes also need to be supported from the inside to prevent them from caving in while cutting. The equipment to do this was available for the standard 146 mm inner diameter tubes, but not for the 170 mm ones. Hence, specimens were cut by hand using an angle grinder and then polished.

For future specimens, a tool to grip the tube would be safer for the operator. It would save time and result in more precise cuts. For the test, it would ensure the specimen height remains same along its circumference. It would avoid uneven gaps with the setup, which can lead to slight variations in the hoop stress distribution.

8.1.2. Assessment

Due to practical limitations, it was not possible to perform ultrasonic C-scans on the filament-wound tubes. For future tests, a C-scan of the pristine tube can be used to assess internal damage that could potentially influence results.

The location of the cut rings can also be tracked by demarcating a reference scale on the tube before cutting. That way, the rings can be traced back to a certain location and the results might be correlated with the existing defects. If possible, the ring can also be scanned after cutting to assess the damage caused by the cutting process.

Along with non-destructive techniques, fibre volume fraction and microscopy tests can also help relating the results to the properties of the specimens.

8.2. Test Setup

The major challenges affecting the test were specimen alignment and friction at ring-setup interface. The limitations were linked to forces, where beyond 250 kN, the ring started deforming permanently.

8.2.1. Alignment

To address alignment issues, a tool can be used to ensure centring of the specimen with the ring. The tool should be fixed to the specimen, with a gauge length of the PU ring's height. Its working principle must be that it moves exactly half the distance to which the setup is compressed. A potential concept is discussed in subsection A.5.1.

8.2.2. Friction

In the tests, both molybdenum sulphide grease and graphite powder were tried as lubricants. Graphite powder was recommended for use with polyurethane. Both partially squeezed out or were challenging to apply evenly throughout the circumference. The grease collected at the edge of the ring. The graphite powder collected at the base.

To ensure uniform and equal friction, PTFE sheets can be used, cut into rings. The sheets need to extend past the ring to maintain the low friction as the ring expands around the fillet edge. An illustration is shown in Figure 8.1.

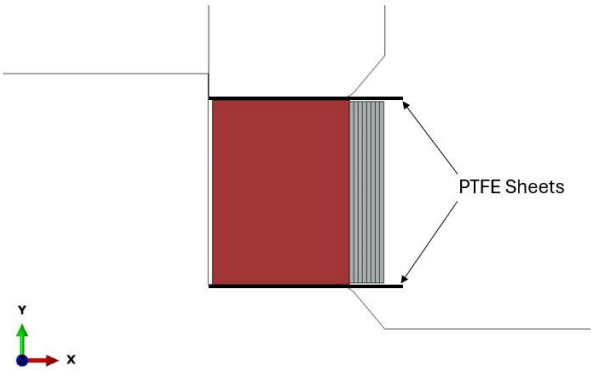

Figure 8.1: PTFE Sheets For Low, Uniform Friction

Under compression, the PTFE sheets can also get squeezed out. However, a thin residual will still be enough to reduce friction. In comparison to grease and powder, it should be more uniform and consistent throughout the test.

8.2.3. Dimensions

The 170 mm inner diameter was chosen as per the design of the pressure vessel being developed by the ComfHy consortium. However, for a more practical setup design, it can be adapted to 146 mm specimens. For material characterization using thin specimens, it would require approximately 15% lower force to apply the same hoop strain. However, at the same force, the stresses on the setup would increase by 17%. For thin specimen tests, it would not be an issue.

The advantages would be that standard 146 mm specimens can be used for tests, reducing the amount of material used. As the tools for cutting and preparing 146 mm specimens are available, it would make specimen preparation easier. The results could then provide a better comparison with literature and validation tests, as the specimens could be cut from the same tube.

8.2.4. Materials

The limitations in the tank specimen tests stemmed from the PU 95A ring. The backup material, UHMWPE, could be used to overcome this limitation (subsection 4.2.4). It was shown to work under

similar loading conditions in the work of Van Paepegem *et al.* [51]. As it is a plastic material, it could face challenges with extrusion as well. However, it was expected to stay level after the initial height reduction in the first few cycles. The drawback would be a higher force requirement owing to its more compressible nature. A comparison performed in Abaqus is shown in Figure 8.2. The compressibility of UHMWPE was seen to vary from $\nu = 0.40$ to 0.46 [53].

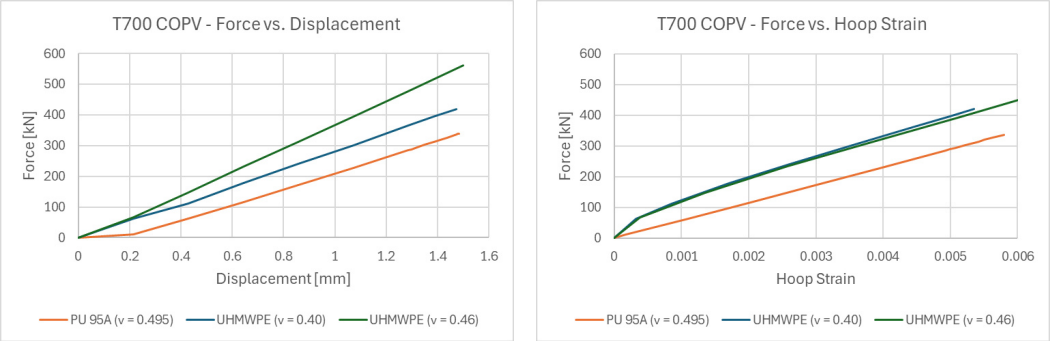

Figure 8.2: Comparison of PU 95A and UHMWPE in Abaqus

Owing to the higher displacement requirement, the taper angle on the setup will have to be increased to 60°. In its plastic state, the height reduction would depend on whether or not the UHMWPE ring gets squeezed out. From a design perspective, the behaviour would be easier to simulate, owing to its plastic behaviour for which there is more test data. Practically, it should be easier to procure and machine. However, challenges could arise from the variability in the properties of the UHMWPE rings itself.

8.2.5. Modulus Estimation

As seen in section 6.1, estimating the modulus, and hence, the strength of the composites was a challenge. The split-disk test and the wedge test resulted in a 20% difference in the estimation. It had the same effect on the strength estimations. The modulus from the split-disk and wedge tests are not yet reliable. They depend on the effect of friction. In the split-disk test, it causes an inaccurate strength estimation. In the wedge test, friction changes the ratio between the applied force and the hoop force, which also affects the strength estimation.

The ring expansion test developed could be used to estimate the same independently. Similar to the wedge test calibration, a steel ring can be used. It should have a known modulus and the same dimensions as the thin specimens. For consistency, the same PU ring should be used between the steel ring and the specimen tests.

Quasi-static tests can be performed on the steel rings, staying within its yield limit. The DIC strains could be used to get the hoop stress. For a known cross-section area, the hoop force can be calculated. The ratio between the hoop force to the applied force can then be estimated.

In the ring expansion test, friction only affects the surfaces of the ring. Using the PTFE sheets should result in an even and predictable friction coefficient in the test. The results of calibration tests should be more consistent. Hence, the ratio established for the steel ring can be applied more reliably to the specimen's test. It could provide a better estimation of the modulus of the wound composite material.

References

[1] H. Council, "Path to hydrogen competitiveness: A cost perspective," *Intelligence*, 2020. [Online]. Available: https://hydrogencouncil.com/wp-content/uploads/2020/01/Path-to-Hydrogen-Competitiveness_Full-Study-1.pdf (visited on Jan. 2, 2025).

[2] B. C. Tashie-Lewis and S. G. Nnabuife, "Hydrogen production, distribution, storage and power conversion in a hydrogen economy - a technology review," *Chemical Engineering Journal Advances*, vol. 8, p. 100 172, 2021, ISSN: 2666-8211. DOI: https://doi.org/10.1016/j.ceja.2021.100172. [Online]. Available: https://www.sciencedirect.com/science/article/pii/S2666821121000880 (visited on Jun. 21, 2025).

[3] X. Li, Q. Huang, Y. Liu, B. Zhao, and J. Li, "Review of the hydrogen permeation test of the polymer liner material of type iv on-board hydrogen storage cylinders," *Materials*, vol. 16, no. 15, 2023, ISSN: 1996-1944. DOI: 10.3390/ma16155366. [Online]. Available: https://www.mdpi.com/1996-1944/16/15/5366 (visited on Jan. 3, 2025).

[4] E. Rivard, M. Trudeau, and K. Zaghib, "Hydrogen storage for mobility: A review," *Materials*, vol. 12, no. 12, 2019, ISSN: 1996-1944. DOI: 10.3390/ma12121973. [Online]. Available: https://www.mdpi.com/1996-1944/12/12/1973 (visited on Jan. 2, 2025).

[5] A. Air, M. Shamsuddoha, and B. Gangadhara Prusty, "A review of type v composite pressure vessels and automated fibre placement based manufacturing," *Composites Part B: Engineering*, vol. 253, p. 110 573, 2023, ISSN: 1359-8368. DOI: https://doi.org/10.1016/j.compositesb.2023.110573. [Online]. Available: https://www.sciencedirect.com/science/article/pii/S1359836823000768 (visited on Jan. 3, 2025).

[6] M. A. Kinna, "Nol ring test methods," Naval Ordnance Lab, White Oak, Maryland, Tech. Rep., 1964. [Online]. Available: https://apps.dtic.mil/sti/pdfs/AD0449719.pdf (visited on Jan. 18, 2025).

[7] D2290-19a, "Standard test method for apparent hoop tensile strength of plastic or reinforced plastic pipe," ASTM International, Tech. Rep., 2019. [Online]. Available: https://www.astm.org/d2290-19a.html (visited on Jan. 7, 2025).

[8] W. van Paepegem, "Comfhy - composite solutions for future hydrogen storage tanks [presentation]," Department of Materials, Textiles, and Chemical Engineering, Ghent University. (visited on Feb. 7, 2025).

[9] E. Union, "Regulation no 134 of the economic commission for europe of the united nations (un/ece) — uniform provisions concerning the approval of motor vehicles and their components with regard to the safety-related performance of hydrogen-fuelled vehicles (hfcv) [2019/795]," *Official Journal of the European Union*, no. L 129, 2019. [Online]. Available: http://data.europa.eu/eli/reg/2019/795/oj (visited on Jan. 2, 2025).

[10] D3479/D3479M-19, "Standard test method for tension-tension fatigue of polymer matrix composite materials," ASTM International, Tech. Rep., 2023. [Online]. Available: https://www.astm.org/d3479_d3479m-19.html (visited on Jan. 7, 2025).

[11] D3039/D3039M-17, "Standard test method for tensile properties of polymer matrix composite materials," ASTM International, Tech. Rep., 2017. [Online]. Available: https://www.astm.org/d3039_d3039m-17.html (visited on Jan. 7, 2025).

[12] E. I. 527-5:2021, "Plastics - determination of tensile properties - part 5: Test conditions for unidirectional fibre-reinforced plastic composites," CEN (Comité Européen de Normalisation), Tech. Rep., 2021. [Online]. Available: https://connect.nen.nl/Standard/Detail/3660055?compId=10037&collectionId=0 (visited on Jan. 14, 2025).

[13] E. I. 13003:2003, "Fibre-reinforced plastics — determination of fatigue properties under cyclic loading conditions," CEN (Comité Européen de Normalisation), Tech. Rep., 2003. [Online]. Available: https://connect.nen.nl/Standard/Detail/93227?compId=10037&collectionId=0 (visited on Jan. 14, 2025).

[14] C. Venkatesan, F. Zulkifli, and A. Silva, "Effects of processing parameters of infrared-based automated fiber placement on mechanical performance of carbon fiber-reinforced thermoplastic composite," *Composite Structures*, vol. 309, p. 116 725, 2023, ISSN: 0263-8223. DOI: https://doi.org/10.1016/j.compstruct.2023.116725. [Online]. Available: https://www.sciencedirect.com/science/article/pii/S0263822323000697 (visited on Jan. 7, 2025).

[15] E. Oromiehie, B. G. Prusty, P. Compston, and G. Rajan, "Automated fibre placement based composite structures: Review on the defects, impacts and inspections techniques," *Composite Structures*, vol. 224, p. 110 987, 2019, ISSN: 0263-8223. DOI: https://doi.org/10.1016/j.compstruct.2019.110987. [Online]. Available: https://www.sciencedirect.com/science/article/pii/S0263822319308281 (visited on Jan. 10, 2025).

[16] A. Kastenmeier, V. Schmid, and I. Ehrlich, "Specimen preparation and material characterization of filament wound composite tubes," *Athens Journal of Technology and Engineering*, vol. 4, no. 3, pp. 191–205, Sep. 2017, ISSN: 2241-8237. DOI: https://doi.org/10.30958/ajte. [Online]. Available: https://www.athensjournals.gr/technology/2017-4-3-2-Kastenmeier.pdf (visited on Jan. 13, 2025).

[17] P. Shabani, F. Taheri-Behrooz, S. Maleki, and M. Hasheminasab, "Life prediction of a notched composite ring using progressive fatigue damage models," *Composites Part B: Engineering*, vol. 165, pp. 754–763, 2019, ISSN: 1359-8368. DOI: https://doi.org/10.1016/j.compositesb.2019.02.031. [Online]. Available: https://www.sciencedirect.com/science/article/pii/S1359836818336461 (visited on Jan. 7, 2025).

[18] D2992-24, "Standard practice for obtaining hydrostatic or pressure design basis for "fiberglass" (glass-fiber-reinforced thermosetting-resin) pipe and fittings," ASTM International, Tech. Rep., 2024. [Online]. Available: https://www.astm.org/d2992-24.html (visited on Jan. 7, 2025).

[19] E. I. 8521:2020, "Glass-reinforced thermosetting plastic (grp) pipes — test methods for the determination of the initial circumferential tensile wall strength," CEN (Comité Européen de Normalisation), Tech. Rep., 2020. [Online]. Available: https://connect.nen.nl/Standard/Detail/3633644?compId=10037&collectionId=0 (visited on Jan. 14, 2025).

[20] Y. Zhao, P. Druzhinin, J. Ivens, D. Vandepitte, and S. V. Lomov, "Split-disk test with 3d digital image correlation strain measurement for filament wound composites," *Composite Structures*, vol. 263, p. 113 686, 2021, ISSN: 0263-8223. DOI: https://doi.org/10.1016/j.compstruct.2021.113686. [Online]. Available: https://www.sciencedirect.com/science/article/pii/S0263822321001471 (visited on Jan. 7, 2025).

[21] H. Mahdavi, G. H. Rahimi, and A. Farrokhabadi, "Fatigue performance analysis of gre composite pipes by conducting tension-tension tests on the rings cut from the pipe," *Journal of Testing and Evaluation*, vol. 49, no. 4, pp. 2767–2778, Jul. 2021, ISSN: 0090-3973. DOI: 10.1520/JTE20180948. eprint: https://asmedigitalcollection.asme.org/testingevaluation/article-pdf/49/4/2767/7144500/10_1520_jte20180948.pdf. [Online]. Available: https://doi.org/10.1520/JTE20180948 (visited on Jan. 18, 2025).

[22] D1598-24, "Standard test method for time-to-failure of plastic pipe under constant internal pressure," ASTM International, Tech. Rep., 2024. [Online]. Available: https://www.astm.org/d1598-24.html (visited on Jan. 9, 2025).

[23] D1599-18, "Standard test method for resistance to short-time hydraulic pressure of plastic pipe, tubing, and fittings," ASTM International, Tech. Rep., 2024. [Online]. Available: https://www.astm.org/d1599-18.html (visited on Jan. 8, 2025).

[24] E. I. 1167-1:2006, "Thermoplastics pipes, fittings and assemblies for the conveyance of fluids —determination of the resistance to internal pressure — part 1: General method," CEN (Comité Européen de Normalisation), Tech. Rep., 2006. [Online]. Available: https://connect.nen.nl/Standard/Detail/106080?compId=10037&collectionId=0 (visited on Jan. 14, 2025).

[25] D2143-21, "Standard test method for cyclic pressure strength of reinforced, thermosetting plastic pipe," ASTM International, Tech. Rep., 2021. [Online]. Available: https://www.astm.org/d2143-21.html (visited on Jan. 9, 2025).

[26] E. I. 15306:2003, "Glass-reinforced thermosetting plastics (grp) pipes — determination of the resistance to cyclic internal pressure," CEN (Comité Européen de Normalisation), Tech. Rep., 2003. [Online]. Available: https://connect.nen.nl/Standard/Detail/87591?compId=10037&collectionId=0 (visited on Jan. 14, 2025).

[27] H. R. Mahdavi, G. H. Rahimi, and A. Farrokhabadi, "Failure analysis of glass-reinforced epoxy pipes under internal hydrostatic pressure: A comparison with the split disk test method," *Journal of Pressure Vessel Technology*, vol. 140, no. 1, p. 014 501, Nov. 2018, ISSN: 0094-9930. DOI: 10.1115/1.4038484. eprint: https://asmedigitalcollection.asme.org/pressurevesseltech/article-pdf/140/1/014501/6320533/pvt_140_01_014501.pdf. [Online]. Available: https://doi.org/10.1115/1.4038484.

[28] C1819-21, "Standard test method for hoop tensile strength of continuous fiber-reinforced advanced ceramic composite tubular test specimens at ambient temperature using elastomeric inserts," ASTM International, Tech. Rep., 2021. [Online]. Available: https://www.astm.org/c1819-21.html (visited on Jan. 10, 2025).

[29] K. Mosley, "The stressing for test purposes of materials in tubular form using elastomeric inserts—experimental and theoretical development," *Proceedings of the Institution of Mechanical Engineers*, vol. 196, no. 1, pp. 123–139, 1982. DOI: 10.1243/PIME_PROC_1982_196_014_02. eprint: https://doi.org/10.1243/PIME_PROC_1982_196_014_02. [Online]. Available: https://doi.org/10.1243/PIME_PROC_1982_196_014_02 (visited on Jan. 18, 2025).

[30] E. I. 21971:2024, "Fine ceramics (advanced ceramics, advanced technical ceramics) — mechanical properties of ceramic composites at ambient temperature in air atmospheric pressure — determination of hoop tensile properties of tubes," CEN (Comité Européen de Normalisation), Tech. Rep., 2024. [Online]. Available: https://connect.nen.nl/Standard/Detail/3713747?compId=10037&collectionId=0 (visited on Jan. 14, 2025).

[31] M. Xiao *et al.*, "Hoop tensile properties and crack propagation investigation of 2d braided sicf/sic composite tubes: Experiments and simulations," *Journal of Nuclear Materials*, vol. 603, p. 155 433, 2024, ISSN: 0022-3115. DOI: https://doi.org/10.1016/j.jnucmat.2024.155433. [Online]. Available: https://www.sciencedirect.com/science/article/pii/S0022311524005348 (visited on Jan. 10, 2025).

[32] M. Madrid, J. José Humberto S Almeida, T. V. Lisbôa, A. Spickenheuer, R. J. Marczak, and S. C. Amico, "Internal pressure testing of open-ended filament-wound cylinders using radial expansion of elastomeric inserts," *Journal of Reinforced Plastics and Composites*, vol. 0, no. 0, p. 241 228 179, 2024, ISSN: 0731-6844. DOI: 10.1177/07316844241228179. [Online]. Available: https://doi.org/10.1177/07316844241228179 (visited on Jan. 10, 2025).

[33] M. Etemad, E. Pask, and C. Besant, "Hoop strength characterization of high strength carbon fibre composites," *Composites*, vol. 23, no. 4, pp. 253–259, 1992, ISSN: 0010-4361. DOI: https://doi.org/10.1016/0010-4361(92)90185-W. [Online]. Available: https://www.sciencedirect.com/science/article/pii/001043619290185W (visited on Jan. 16, 2025).

[34] T.-K. Hwang, J.-B. Park, and H.-G. Kim, "Evaluation of fiber material properties in filament-wound composite pressure vessels," *Composites Part A: Applied Science and Manufacturing*, vol. 43, no. 9, pp. 1467–1475, 2012, ISSN: 1359-835X. DOI: https://doi.org/10.1016/j.compositesa.2012.04.005. [Online]. Available: https://www.sciencedirect.com/science/article/pii/S1359835X12001340 (visited on Jan. 19, 2025).

[35] *A Novel Test Method for the Assessment of the Hoop Performance of Composite Pipes*, vol. All Days, International Ocean and Polar Engineering Conference, Jun. 2024, ISOPE-I-24–207. [Online]. Available: https://onepetro-org.tudelft.idm.oclc.org/ISOPEIOPEC/proceedings/ISOPE24/All-ISOPE24/ISOPE-I-24-207/546602 (visited on Jan. 15, 2025).

[36] A. Horide, S. Wakayama, and M. Kawahara, "Characterization of fracture process during ring burst test of fw-frp composites with damage," *Advanced Composite Materials*, vol. 8, no. 2, pp. 139–151, 1999. [Online]. Available: https://doi.org/10.1163/156855199X00155 (visited on Jan. 18, 2025).

[37] Y. Kim, C. Choi, C.-G. Kim, and Y.-D. Doh, "Ring burst test of filament wound composites for environmental resistance," *Journal of Composite Materials*, vol. 50, no. 18, pp. 2507–2521, 2016. DOI: 10.1177/0021998315607611. eprint: https://doi.org/10.1177/0021998315607611. [Online]. Available: https://doi.org/10.1177/0021998315607611 (visited on Jan. 18, 2025).

[38] W. T. Kim and S. S. Kim, "Design of a segment-type ring burst test device to evaluate the pressure resistance performance of composite pressure vessels," *Composite Structures*, vol. 242, p. 112 199, 2020, ISSN: 0263-8223. DOI: https://doi.org/10.1016/j.compstruct.2020.112199. [Online]. Available: https://www.sciencedirect.com/science/article/pii/S0263822320307042 (visited on Jan. 18, 2025).

[39] P. Samyn *et al.*, "Fracture assessment of carbon fibre/epoxy reinforcing rings through a combination of full-scale testing, small-scale testing and stress modeling," *Applied Composite Materials*, vol. 13, no. 2, pp. 57–85, Mar. 2006, ISSN: 1573-4897. DOI: 10.1007/s10443-006-9007-x. [Online]. Available: https://doi.org/10.1007/s10443-006-9007-x (visited on Mar. 19, 2025).

[40] M. Ramulu, "Machining and surface integrity of fibre-reinforced plastic composites," *Sadhana*, vol. 22, no. 3, pp. 449–472, Jun. 1997, ISSN: 0973-7677. DOI: 10.1007/BF02744483. [Online]. Available: https://doi.org/10.1007/BF02744483 (visited on Feb. 13, 2025).

[41] P. Ghidossi, M. El Mansori, and F. Pierron, "Edge machining effects on the failure of polymer matrix composite coupons," *Composites Part A: Applied Science and Manufacturing*, vol. 35, no. 7, pp. 989–999, 2004, ISSN: 1359-835X. DOI: https://doi.org/10.1016/j.compositesa.2004.01.015. [Online]. Available: https://www.sciencedirect.com/science/article/pii/S1359835X04000223 (visited on Feb. 13, 2025).

[42] R. B. Pipes and N. Pagano, "Interlaminar stresses in composite laminates under uniform axial extension," *Journal of Composite Materials*, vol. 4, no. 4, pp. 538–548, 1970. DOI: 10.1177/002199837000400409. eprint: https://doi.org/10.1177/002199837000400409. [Online]. Available: https://doi.org/10.1177/002199837000400409 (visited on Feb. 13, 2025).

[43] A. Katunin, "Domination of self-heating effect during fatigue of polymeric composites," *Procedia Structural Integrity*, vol. 5, pp. 93–98, 2017, 2nd International Conference on Structural Integrity, ICSI 2017, 4-7 September 2017, Funchal, Madeira, Portugal, ISSN: 2452-3216. DOI: https://doi.org/10.1016/j.prostr.2017.07.073. [Online]. Available: https://www.sciencedirect.com/science/article/pii/S2452321617301658 (visited on Oct. 15, 2025).

[44] A. Katunin, "Evaluation of criticality of self-heating of polymer composites by estimating the heat dissipation rate," *Mechanics of Composite Materials*, vol. 54, no. 1, pp. 53–60, Mar. 2018, ISSN: 1573-8922. DOI: 10.1007/s11029-018-9717-9. [Online]. Available: https://doi.org/10.1007/s11029-018-9717-9 (visited on Feb. 14, 2025).

[45] C. Peyrac, T. Jollivet, N. Leray, F. Lefebvre, O. Westphal, and L. Gornet, "Self-heating method for fatigue limit determination on thermoplastic composites," *Procedia Engineering*, vol. 133, pp. 129–135, 2015, Fatigue Design 2015, International Conference Proceedings, 6th Edition, ISSN: 1877-7058. DOI: https://doi.org/10.1016/j.proeng.2015.12.639. [Online]. Available: https://www.sciencedirect.com/science/article/pii/S1877705815045580 (visited on Feb. 14, 2025).

[46] L. Muller *et al.*, "Experimental monitoring of the self-heating properties of thermoplastic composite materials," *Procedia Engineering*, vol. 213, pp. 183–191, 2018, 7th International Conference on Fatigue Design, Fatigue Design 2017, 29-30 November 2017, Senlis, France, ISSN: 1877-7058. DOI: https://doi.org/10.1016/j.proeng.2018.02.020. [Online]. Available: https://www.sciencedirect.com/science/article/pii/S1877705818302443 (visited on Feb. 14, 2025).

[47] B. M. Institute, *Metallic Materials Properties Development and Standardization (MMPDS-16)*. Battelle Memorial Institute, 2021, ch. 17-4PH. [Online]. Available: https://app.knovel.com/hotlink/khtml/id:kt012L77S5/metallic-materials-properties/17-4ph (visited on Mar. 12, 2025).

[48] B. Van Bavel, O. Shishkina, D. Vandepitte, and D. Moens, "Reliability-based composite pressure vessel design optimization with cure-induced stresses and spatial material variability," *Computer Methods in Applied Mechanics and Engineering*, vol. 432, p. 117 463, 2024, ISSN: 0045-7825. DOI: https://doi.org/10.1016/j.cma.2024.117463. [Online]. Available: https://www.sciencedirect.com/science/article/pii/S0045782524007187 (visited on Feb. 18, 2025).

[49] "Torayca t700s data sheet - rev. 4," Toray Industries, Inc., Tech. Rep., 2018. [Online]. Available: https://www.toraycma.com/wp-content/uploads/T700S-Data-Sheet-4.22.2025.pdf (visited on Feb. 18, 2025).

[50] H. Qi and M. Boyce, "Stress–strain behavior of thermoplastic polyurethanes," *Mechanics of Materials*, vol. 37, no. 8, pp. 817–839, 2005, ISSN: 0167-6636. DOI: https://doi.org/10.1016/j.mechmat.2004.08.001. [Online]. Available: https://www.sciencedirect.com/science/article/pii/S0167663604001140 (visited on Feb. 27, 2025).

[51] W. Van Paepegem *et al.*, "Fast characterization of carbon/epoxy rings for use in the ball-joints of the maeslant storm surge barrier," *Composite Structures*, vol. 78, no. 3, pp. 359–367, 2007, ISSN: 0263-8223. DOI: https://doi.org/10.1016/j.compstruct.2005.10.009. [Online]. Available: https://www.sciencedirect.com/science/article/pii/S0263822305002965 (visited on Mar. 19, 2025).

[52] "Vaneflon uhmwpe data sheet, version: B," Vanéflon N.V., Tech. Rep., 2024. [Online]. Available: https://www.vaneflon.com/content/uploads/2024/05/UHMWPE.pdf (visited on Mar. 13, 2025).

[53] L. G. Malito, S. Arevalo, A. Kozak, S. Spiegelberg, A. Bellare, and L. Pruitt, "Material properties of ultra-high molecular weight polyethylene: Comparison of tension, compression, nanomechanics and microstructure across clinical formulations," *Journal of the Mechanical Behavior of Biomedical Materials*, vol. 83, pp. 9–19, 2018, ISSN: 1751-6161. DOI: https://doi.org/10.1016/j.jmbbm.2018.03.029. [Online]. Available: https://www.sciencedirect.com/science/article/pii/S1751616118304077 (visited on Mar. 13, 2025).

[54] E. N. Brown *et al.*, "Influence of molecular conformation on the constitutive response of polyethylene: A comparison of hdpe, uhmwpe, and pex," *Experimental Mechanics*, vol. 47, no. 3, pp. 381–393, Jun. 2007. DOI: 10.1007/s11340-007-9045-9. [Online]. Available: https://doi.org/10.1007/s11340-007-9045-9 (visited on May 13, 2025).

[55] D0395-18, "Standard test methods for rubber property—compression set," ASTM International, Tech. Rep., 2025. [Online]. Available: https://www.astm.org/d0395-18r25.html (visited on Apr. 17, 2025).

[56] W. D. Pilkey, D. F. Pilkey, and Z. Bi, *Peterson's Stress Concentration Factors (4th Edition)*. John Wiley & Sons, 2020, ISBN: 978-1-119-53251-4. [Online]. Available: https://app.knovel.com/hotlink/toc/id:kpPSCFE029/petersons-stress-concentration/petersons-stress-concentration (visited on Mar. 10, 2025).

[57] F. Hüter and F. Rieg, "Extending marlow's general first-invariant constitutive model to compressible, isotropic hyperelastic materials," *Engineering Computations*, vol. 38, no. 6, pp. 2631–2647, Jan. 2021, ISSN: 0264-4401. DOI: 10.1108/EC-05-2020-0251. [Online]. Available: https://doi.org/10.1108/EC-05-2020-0251 (visited on May 16, 2025).

[58] B. P. Reis, L. M. Nogueira, D. A. Castello, and L. A. Borges, "A visco-hyperelastic model with mullins effect for polyurethane elastomers combining a phenomenological approach with macromolecular information," *Mechanics of Materials*, vol. 161, p. 104 023, 2021, ISSN: 0167-6636. DOI: https://doi.org/10.1016/j.mechmat.2021.104023. [Online]. Available: https://www.sciencedirect.com/science/article/pii/S0167663621002519 (visited on Mar. 29, 2025).

[59] J. Schijve, "The fatigue strength of notched specimens," in *Fatigue of Structures and Materials*. Dordrecht: Springer Netherlands, 2009, pp. 171–208, ISBN: 978-1-4020-6808-9. DOI: 10.1007/978-1-4020-6808-9_7. [Online]. Available: https://doi.org/10.1007/978-1-4020-6808-9_7 (visited on Apr. 9, 2025).

[60] M. Hondekyn, N. Ali, and W. Van Paepegem, "Closed-form analytical model for the cylinder region of thick-walled composite pressure vessels for hydrogen storage," *International Journal of Hydrogen Energy*, vol. 87, pp. 457–468, 2024, ISSN: 0360-3199. DOI: https://doi.org/10.1016/j.ijhydene.2024.08.447. [Online]. Available: https://www.sciencedirect.com/science/article/pii/S0360319924036292 (visited on Jul. 31, 2025).

[61] E. Jones and M. Iadicola, "A good practices guide for digital image correlation," International Digital Image Correlation Society, Tech. Rep., 2018. DOI: 10.32720/idics/gpg.ed1. (visited on Jun. 12, 2025).

[62] H. Ashrafizadeh, P. Mertiny, and A. McDonald, "Evaluation of the effect of temperature on mechanical properties and wear resistance of polyurethane elastomers," *Wear*, vol. 368-369, pp. 26–38, 2016, ISSN: 0043-1648. DOI: https://doi.org/10.1016/j.wear.2016.08.008. [Online]. Available: https://www.sciencedirect.com/science/article/pii/S0043164816301831 (visited on Jun. 24, 2025).

A

Appendix

This appendix is divided into sections corresponding to each chapter in the main text. Each section contains data or files relevant to its particular chapter.

A.1. Literature Review

A.1.1. Analytical Comparisons

The attached program was written to perform initial calculations for the setups conceptualized during the literature review. The were used to compare the concepts.

setups.py

A.1.2. Cam Lobe Torque Calculations

The below python file was created to define a cam lobe shape and determine the torque required to rotate the same.

cam.py

A.1.3. Trade-off Matrix

The below excel file contains the complete trade-off table, with data and calculations used to estimate the complexities and setup wear.

Trade-offs.xlsx

A.2. Design Methodology

A.2.1. Classical Laminate Thoery

The author's implementation of Classical Laminate Theory is contained in the below two python files. The file `properties.py` calculates the laminate properties of a given layup through Classical Laminate Theory. The file `clt.py` contains functions required for the calculations. Both files must be in the same folder to run the code.

properties.py
clt.py

A.2.2. Initial Calculations

The below python file was created as an analytical model of the test setup for an initial estimation of the forces, displacements, and stresses.

elastomer.py

A.2.3. Material Models

From the PU 94A and UHMWPE test data, points from the curves were extracted using WebPlotDigitizer (https://github.com/automeris-io/WebPlotDigitizer). The extracted data points are tabulated below.

PU 94A Test Data Extraction

Table A.1: Polyurethane 94A Compression Test Extracted Data-points [50]

- True Strain	- True Stress (MPa)	- Nominal Strain	- Nominal Stress (MPa)
0.0000	0.0000	0.0000	0.0000
0.0014	0.2042	0.0014	0.2045
0.0331	1.8150	0.0325	1.8760
0.0809	3.5273	0.0777	3.8246
0.1363	5.0965	0.1274	5.8409
0.1974	6.4410	0.1792	7.8468
0.2652	7.5198	0.2329	9.8033
0.3329	8.4354	0.2832	11.7676
0.4025	9.2081	0.3314	13.7716
0.4759	9.9398	0.3787	15.9984
0.5417	10.5289	0.4183	18.0990
0.6199	11.1584	0.4620	20.7406
0.6790	11.7478	0.4929	23.1660
0.7086	12.0936	0.5077	24.5633
0.7305	12.4600	0.5183	25.8692
0.7534	12.4183	0.5292	26.3785
0.7792	12.8866	0.5412	28.0879
0.8106	13.3547	0.5554	30.0393
0.8307	13.6396	0.5642	31.3009
0.8574	13.9242	0.5757	32.8188
0.8832	14.5558	0.5865	35.2037
0.9032	14.9836	0.5947	36.9722
0.9184	14.7177	0.6008	36.8725
0.9318	14.9620	0.6061	37.9889
0.9480	15.3491	0.6125	39.6097
0.9605	15.8180	0.6173	41.3305
0.9729	16.0420	0.6220	42.4390
0.9862	16.3067	0.6270	43.7199

PU 90A Material Model

For PU 90A, the nominal stress-strain curve was compared to the PU 94A test data [50]. For 90A, the curve was derived from the force-displacement data (Figure 4.5). The comparison is shown in Figure A.1 (a). The PU 90A (at $\dot{\epsilon} = 0.06\ s^{-1}$) and 94A (at $\dot{\epsilon} = 0.01\ s^{-1}$) test data exhibit a close fit, as shown in Figure A.1 (b).

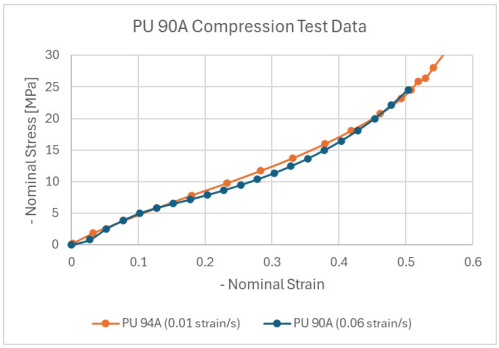

(a) Nominal Stress vs. Strain in Compression

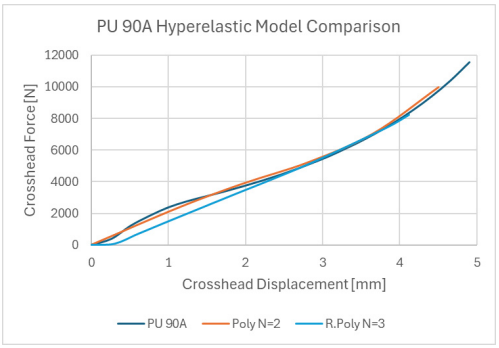

(b) Hyperelastic Material Model

Figure A.1: PU 90A Material Model Fit

Table A.2: Polynomial ($N = 2$) Hyper-elastic Model Coefficients

D_1	C_{10}	C_{01}	
$8.8722E-04$	51.9385	−40.6297	
D_2	C_{20}	C_{11}	C_{02}
0.0000	27.2101	−12.5181	2.6419

Backup Material Model

A plastic material model was used for the backup UHMWPE ring material. The curve for $\dot{\epsilon} = 0.01\ s^{-1}$ was used to model the yield behaviour in Abaqus, as it was closest to the expected strain rate, determined in Equation 4.7. The curve and conversion are shown in Figure A.2. The same is tabulated in Table A.3. ($Plastic\ Strain_n = Total\ Strain_n - 0.0258$).

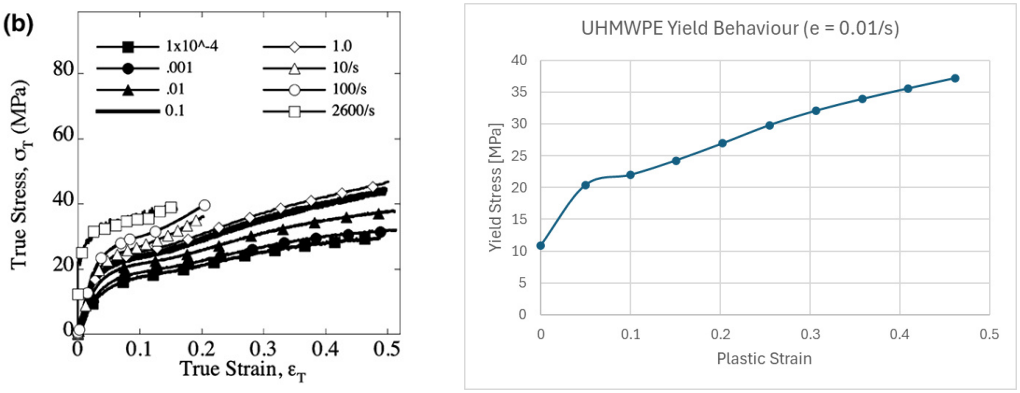

(a) Stress-Strain Curve [54]

(b) Converted Yield Stress-Strain Curve for Abaqus

Figure A.2: UHMWPE Compression Test Data at $\dot{\epsilon} = 0.01\ s^{-1}$

Table A.3: UHMWPE Extracted Plastic Data-points [54]

Yield Stress (MPa)	Plastic Strain	Total Strain
10.82	0.0000	0.0258
20.38	0.0498	0.0756
22.02	0.1003	0.1261
24.28	0.1509	0.1767
26.96	0.2025	0.2283
29.85	0.2553	0.2811
32.12	0.3069	0.3327
33.97	0.3585	0.3843
35.61	0.4090	0.4348
37.25	0.4617	0.4875

A.2.4. FEM Scripts in Abaqus Python

The below scripts were written in Abaqus python. They can be used in any version of Abaqus, through `File, Run Script...`. They create the starting-point FEMs. The `start_dfm.py` file creates the deformable sizing model. The `start_rgd.py` file creates the prediction model. To add the specimen in the prediction model, `specimen.py` needs to be run after `start_rgd.py`.

Each file was made to be parametric. The dimensions, layups, material properties, and so on can be adjusted. When modifying the rigid body geometry, the rigid body constraints might have to be redefined to ensure correct the correct outer face is selected.

start-dfm.py
start-rgd.py
specimen.py

A.3. Fatigue Test Development

A.3.1. Proof-of-Concept Test

Specimen Preparation

An initial sample tube was provided by Sharp Composites with an inner diameter of 169.50 mm. It was from a wet-winding trial and was meant to set up the mould and cure process. The winding angle was approximately ±88° with a average thickness of 1.91 mm. The exact materials and processing conditions used were not known.

Figure A.3: Sample 170 mm Tube and Rough-cut Ring

A ring was cut approximately 15 mm away from an edge of the tube, both shown in Figure A.3. It was cut roughly using an angle grinder by a colleague in Syensqo's workshop. It was then ground down to an average height of 9.10 mm using a manual polishing machine. It was done with the help of a colleague from the microscopy lab at Syensqo.

Test Setup

The test was performed using the 250 kN Instron 5985 static test bench. It was anticipated that the indenter and base could yield around the 150 mm diameter compression plates. This was more critical for the indenter, shown in Figure A.4.

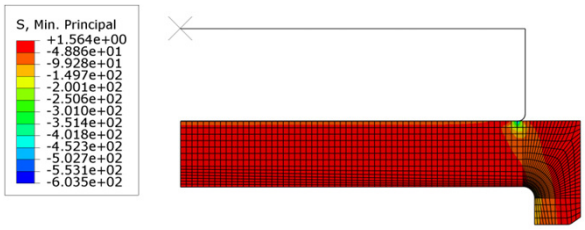

Figure A.4: Indenter Compression against 150 mm Plates at 250 kN

At the applied force, $F = 250\ kN$, the margin of safety for yield in compression was calculated. Since the steel supplier had not provided a technical data-sheet, a safety factor of = 1.5 was assumed for the mechanical properties shown in Table 4.1.

$$\sigma_{min} = -603.5\ MPa$$

$$MS = \frac{F_{CY}}{SF \times \sigma_{min}} - 1 = \frac{717.0}{1.5 \times 603.5} - 1 = -0.21$$

Assuming a linear relation between the cross-head force and the critical surface stress, the maximum safe force was determined. It was back-calculated by setting $MS = 0.01$.

$$\sigma_{min} = \frac{F_{CY}}{SF \times (MS + 1)} = \frac{717.0}{1.5 \times (0.01 + 1)} = 473.3\ kN$$

$$F = \sigma_{min} \frac{\sigma_{min,\,lim}}{F_{lim}} = 473.3 \times \frac{603.5}{250}$$

$$F = 196\ kN$$

Hence, to eliminate the risk of yielding in a static test in the 250 kN test bench, two flat steel plates, 15 mm thick were placed between the fixture and the compression plates. The surfaces were ensured to be parallel to prevent any misalignment. The setup is shown in Figure A.5.

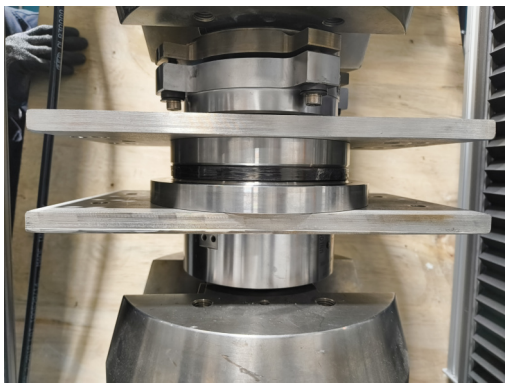

Figure A.5: Test Setup with 'Extended' Compression Plates

For the test, instrumentation was not set up, and only the force-displacement data was recorded. The tests were performed at a cross-head displacement rate of 0.61 mm/s, emulating the lowest strain rate expected in the fatigue test, calculated using Equation 4.7. The displacement limit was set to 4 mm, slightly under what the fixture was designed for. A PU 95A ring was used.

A.3.2. Specimen Preparation

The composite tubes were cut on a lathe using a specially developed mount. It was designed and manufactured by a Syensqo colleague. When pushed by the lathe centre, it expands 4 segments radially outwards to grip the tube from inside. The tube was cut along the groove made in the mount. It can support tubes of 146 mm inner diameter. It is shown in Figure A.6.

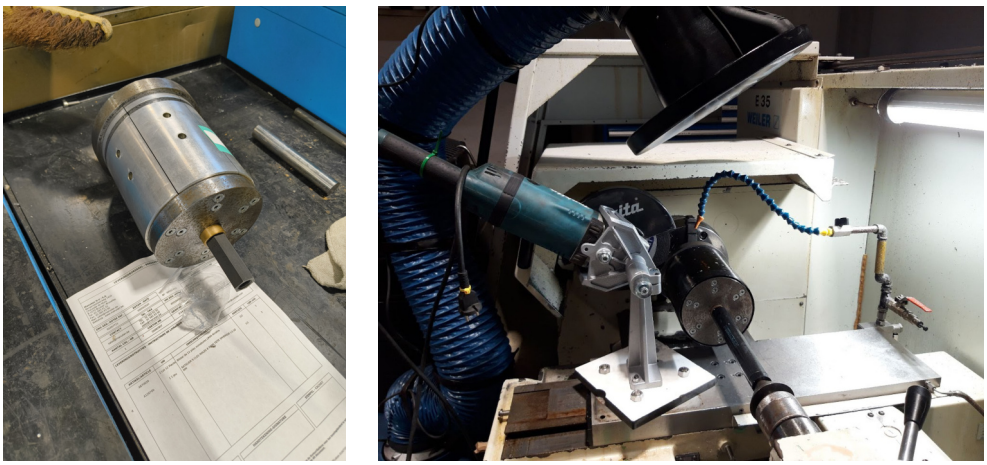

(a) Lathe Mount for Composite Tubes **(b)** Specimen Cutting with a PCD Tool on the Lathe

Figure A.6: T700-Epoxy Benchmark Specimen Cutting Using Specially Developed Mount

To cut the tank specimens using the tool, a rubber sheet was wrapped around the tool. Onto which the specimen was mounted. This was not very reliable as it produced rough edges due to vibrations. The rings were then milled to finish the edges. The cutting process and the specimens are shown in Figure A.7.

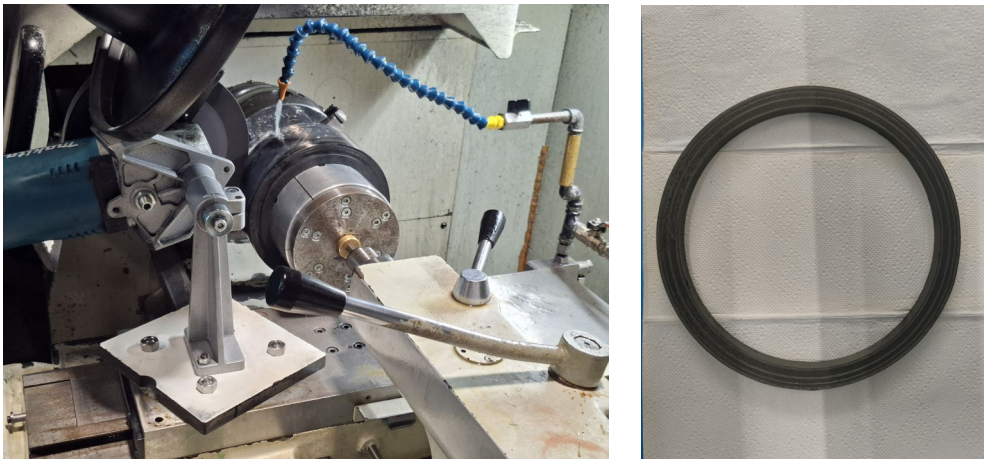

(a) Lathe Mount Adapted using Rubber Filling **(b)** Tank Specimens Cut and Milled

Figure A.7: T700-Epoxy Tank Specimen Cutting on the Lathe

A.3.3. Fibre Volume Fraction Estimation

The below MATLAB code was used to estimate the fibre-volume fraction from the microscopy image. A pixel mask is needed to exclude the embedding resin from being considered in the estimations. The mask can be created in any image processing software. The pixels covered by the mask should be set to a greyscale value that should not get picked up by the thresholds used for the fibre, matrix, and voids.

fvfmicro.m

Figure A.8: Mask for Embedding Resin

A.3.4. Test Bench Setup

PID Tuning

The test bench was set up using MTS' Station Manager. For a force-controlled test, the PID controller had to be tuned. The test was set up with a thin specimen. The PID parameters were adjusted to reduce any mismatch between the force command and the force measured. Up to 50 kN cyclic load was applied at 0.42 Hz. The APC compensator was used after consultation with the technician. The controller was considered tuned when the command and measured forces overlapped. The parameters are shown in Figure A.9.

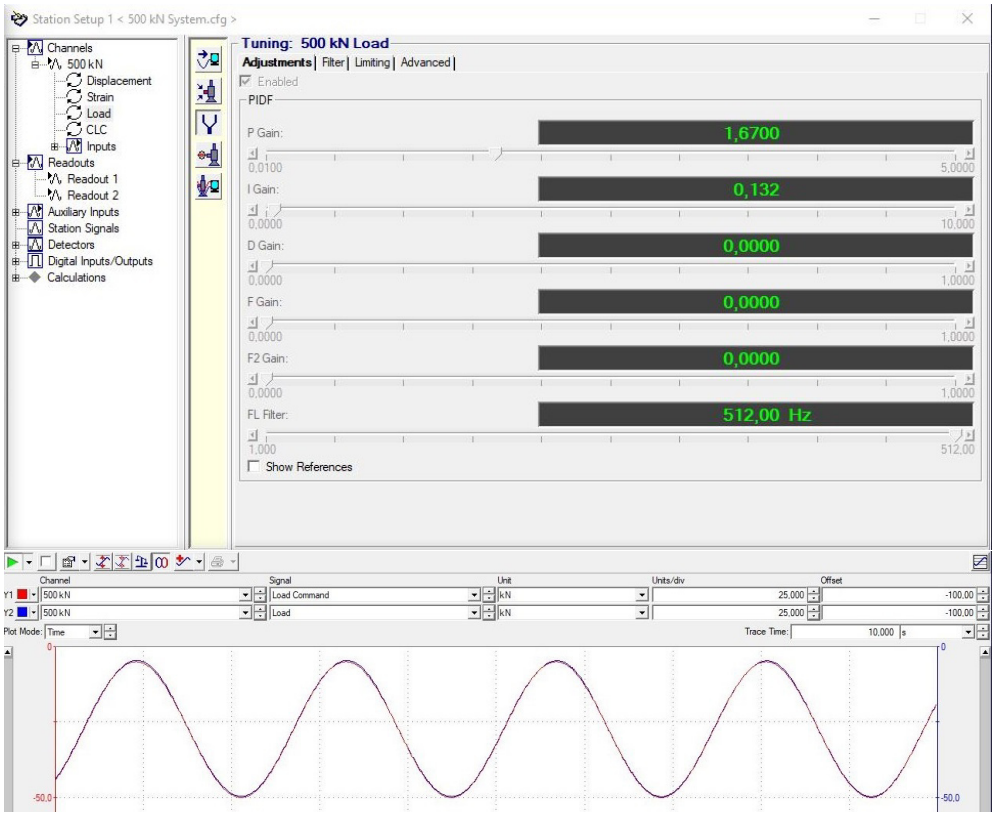

Figure A.9: Force Tuning Parameters and Check (Red - Command, Blue - Measured)

Test Programs

The static and fatigue test procedures were programmed using MPT (legacy). They are shown in Figure A.10 and Figure A.11. The static tests were used for both calibration and burst tests.

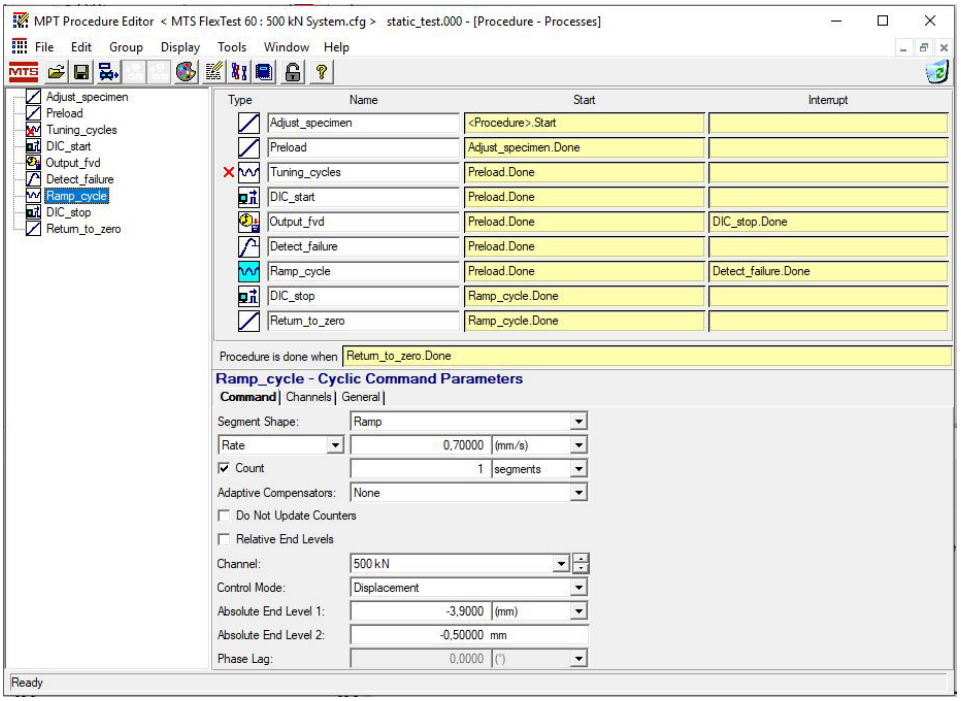

Figure A.10: MPT Static Test Procedure

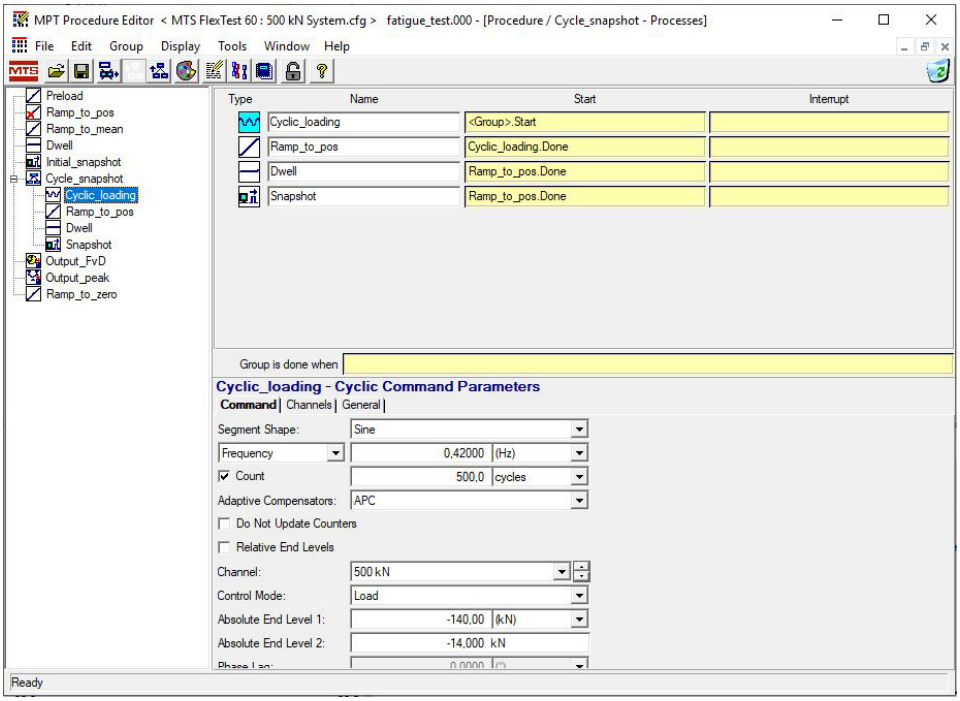

Figure A.11: MPT Fatigue Test Procedure

Data Acquisition Setup

The data acquisition setup comprised coaxial cables to read the test bench's force and displacement values corresponding to the DIC images. The voltage signals had a range of ±10 V. In compression only the negative range was used.

They were scaled to have the correct readings. The displacement range in compression was 76.2 mm. As the maximum displacement was 4 mm, the voltage readout was scaled by 10. The force readout was not scaled up to capture the complete range of 500 kN. The readouts were not offset.

On the data acquisition computer, the displacement signal readout was scaled down by 0.762 to get the displacement readings. The force signal readout was scaled by 50 to get the force readings. However, it also scaled the noise in the force signal which was equivalent to ±3 kN. The data acquisition readings at zero force and displacement are shown in Figure A.6.

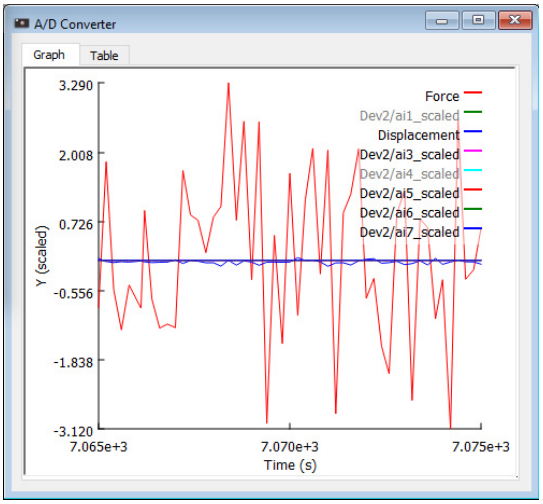

Figure A.12: Signal Noise at Zero Force and Displacement

A.3.5. DIC Setup

DIC Pattern and Subset Sizes

The DIC patterns used were computer-generated. They were printed on tattoo paper and applied on the specimen using water. Care was taken to squeeze out air trapped under the pattern. Leaving bubbles could also create irregular strain readings. The subset size should ideally cover 3 black-to-white transitions to ensure that each subset has a unique pattern.

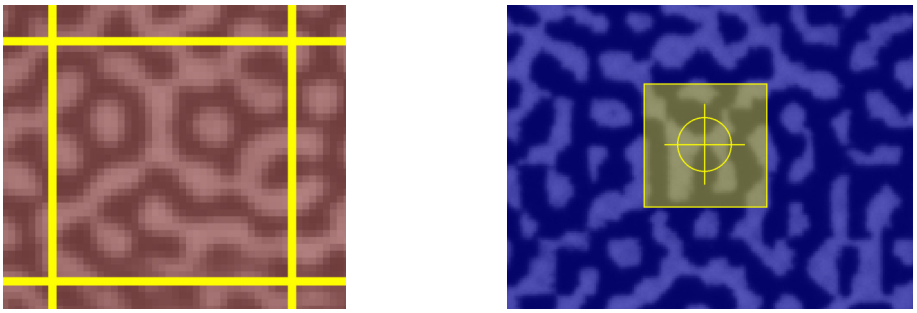

(a) Setup 'B' Subset (Yellow Box, 33 × 33 pixels) **(b)** Setup 'C' Subset (Yellow Box, 55 × 55 pixels)

Figure A.13: DIC Pixel Coverage and Subset Size

DIC Results Sensitivity

To check the sensitivity of the DIC results to the correlation parameters, their effect on the results was checked. The MatchID analyses on specimen B1 was taken as the baseline. The parameters listed in Table A.4 were varied to compare the average hoop strain with the baseline. The corresponding hoop strain distributions are shown in Figure A.14. The default option, Logarithmic Euler-Almansi strain, was used. The subset size was 55 px in each case, as it was determined to cover at least 3 black-to-white transitions. Uniform subset weights were used.

Table A.4: DIC Results Sensitivity with Parameters (Subset Size = 55 px)

Parameter Changed	Shape Function	Strain Window	Interpolation	Step Size	Average Hoop Strain	Figure A.14
Baseline	Affine	5	Bilinear (Q4)	18	0.01526	(a)
Shape Function	Quadratic	5	Bilinear (Q4)	18	0.01523	(b)
Strain Window	Affine	15	Bilinear (Q4)	18	0.01522	(c)
Interpolation	Affine	5	Biquadratic (Q9)	18	0.01520	(d)
Step Size	Affine	5	Bilinear (Q4)	7	0.01523	(e)

The effect of the parameters on the average strain results was negligible. The hoop strain distribution was also similar between parameters, except when increasing the strain window. As a larger set of pixels was used to compute the average strains, it smoothed out the variations around the circumference.

The quadratic shape function also reduced the variations as it also accounted for the bending of the subsets. However, the peaks and troughs in the distribution were still apparent.

Three step sizes were tried, 7, 12, and 18. In the final analyses, a step size of $1/3^{rd}$ the subset size was used. In this case, for a subset size of 55 px, it was 18. On reducing the step size, the variations were captured with higher 'resolution', as the next subset was dependent on the previous one.

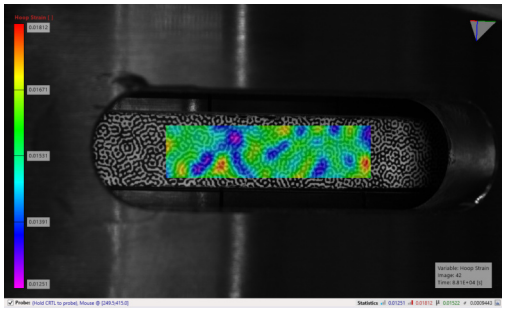

(a) Baseline (Max : 0.0192, Min : 0.0117)

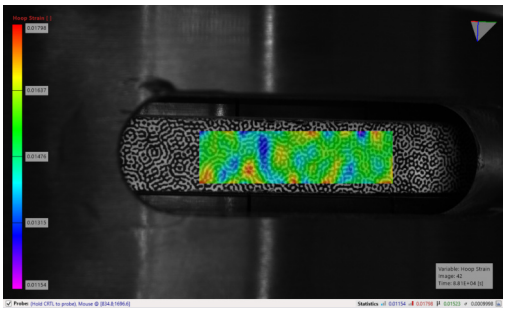

(b) Quadratic SF (Max : 0.0180, Min : 0.0115)

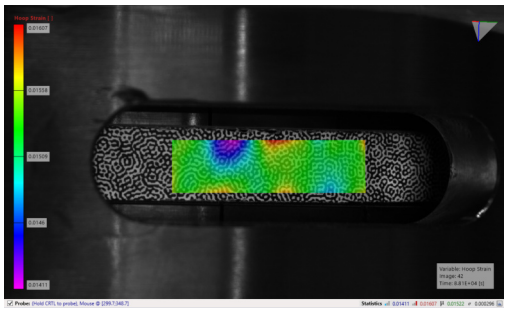

(c) Strain Window (Max : 0.0161, Min : 0.0141)

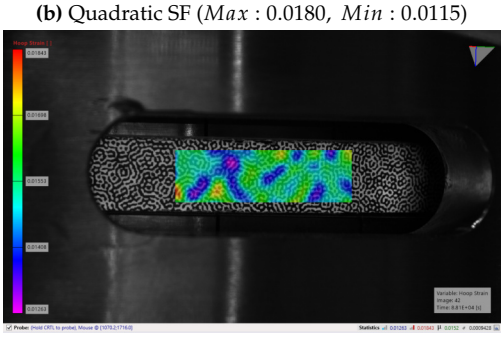

(d) Step Size (Max : 0.0184, Min : 0.0126)

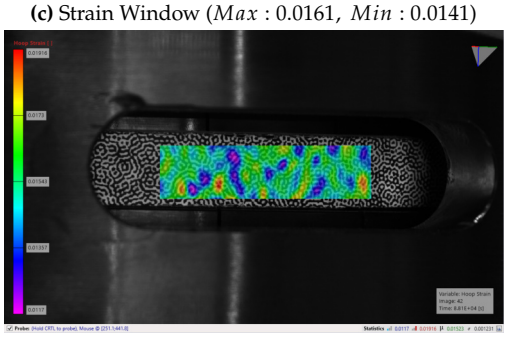

(e) Step Size (Max : 0.0192, Min : 0.0117)

Figure A.14: DIC Hoop Strain Distribution Variation with Parameters (Subset Size = 55 px)

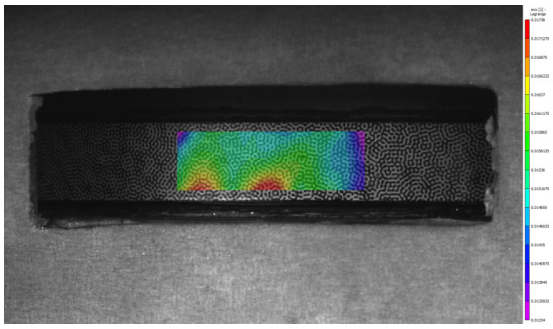

(a) VIC 3D (Max : 0.0174, Min : 0.0133)

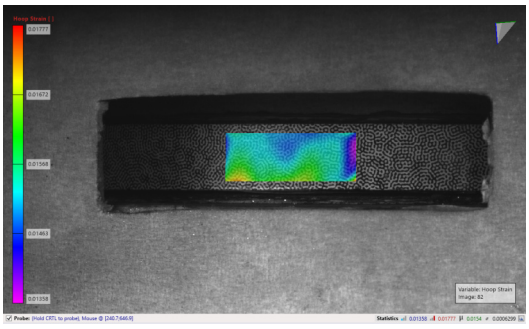

(b) Match ID (Max : 0.0178, Min : 0.0136)

Figure A.15: DIC Hoop Strain Comparison for Specimen 12

To validate the post-processing softwares, Specimen 12's hoop strain results from Match ID 2024.2.1 (Syensqo) and VIC 3D 8 (TU Delft) were compared in Figure A.15. In both cases, a subset size of 35 mm and a step size of 12 was used. The results were transformed to cylindrical coordinates. The correlation criterion was Zero Normalized Squared Differences (ZNSSD). Both used a strain window of 15. Uniform subset weights were used in Match ID compared to Gaussian weights in VIC 3D. The average hoop strain remained comparable, as shown in Figure A.16.

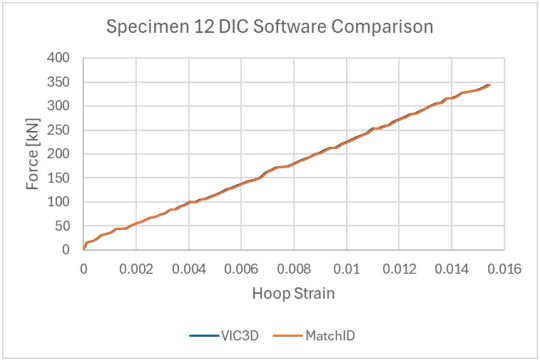

Figure A.16: Hoop Strain Results Comparison for Specimen 12

A.3.6. Fine-tuning Test Results

The camera frame-rate in the fine-tuning tests was 5 Hz. Hence, the failure points in terms of strain were not missed. This was addressed in the later tests. The purpose of the fine-tuning tests was to focus more on the setup. The results of the tests are shown in Figure A.17.

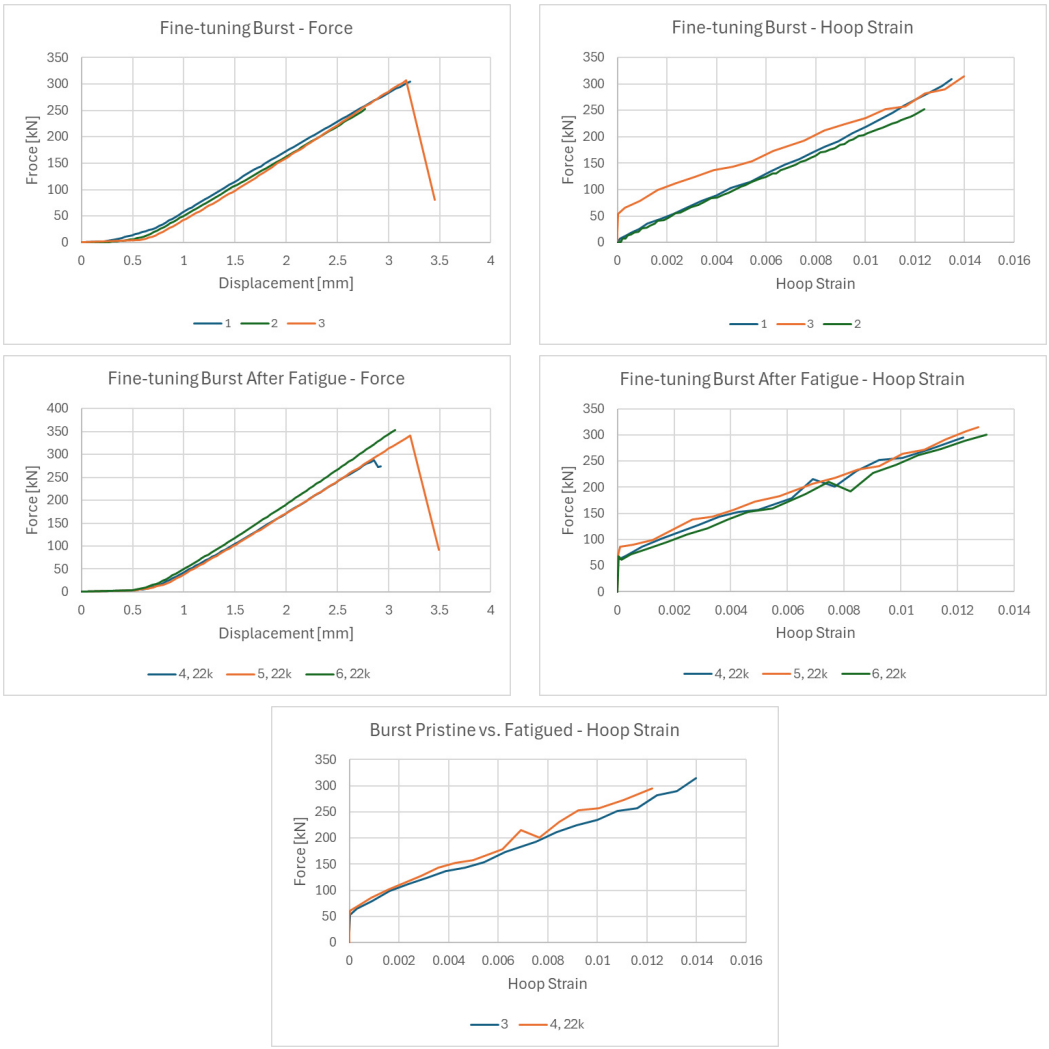

Figure A.17: Test Results for Specimens 01-06

A.4. Results and Discussion

A.4.1. Split-Disk Test FEM

A $1/8^{th}$ finite-element model of the split-disk test was created to study the effect of friction in the test results. The specimen dimensions matched that in the test. It was modelled using C3D8 elements, with a mesh size of $2 \times 2 \times 0.5\ mm$. The disk was modelled as a rigid body. The FEM is shown in Figure A.18.

The specimen was constrained using symmetric boundary conditions. A vertical displacement of $1\ mm$ was applied on the disk. The force was measured at the symmetric point of the specimen. As the cross-section area was $1/4^{th}$ of the actual area being simulated, the force was multiplied by factor of 4.

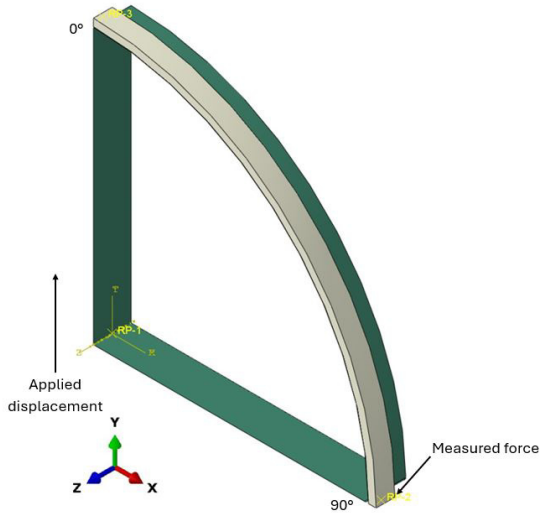

Figure A.18: Split-Disk $1/8^{th}$ FEM with Symmetric Boundary Conditions

The friction coefficient between the specimen and the disk was varied from $\mu = 0.01 - 0.30$. Table A.5 shows the corresponding change in the reacted force, and the resultant change in the estimated modulus. Since the stress is calculated directly from the applied force, the calculated stress increases for the same applied displacement. However, the strain towards the split also increases.

With higher friction, the specimen in contact is more restrained from expansion. The difference has to be compensated for at the split, leading to a proportional increase in stress there. From the strain distribution in Figure A.19 (a), it was observed that the nominal strain is reached between $40 - 45°$ away from the split. However, measuring the corresponding the stress at that point would be a practical challenge in tests.

Table A.5: Effect of Friction on Modulus at the same Applied Displacement

μ	Force (kN)	Stress (MPa)	ϵ_{11} $(80°)$	E_{XX} (MPa)
0.3	50012	1250.3	0.0085	146355
0.2	46544	1163.6	0.0081	143580
0.12	43948	1098.7	0.0078	141646
0.05	41636	1040.9	0.0075	139608
0.01	40392	1009.8	0.0073	138600

The radial pressure distribution was also studied from this FEM. The pressure applied on the $1/8^{th}$ specimen is shown in Figure A.19 (b) at $\mu = 0.2$ and $1\ mm$ displacement. It increases gradually towards the split, where it peaks as it bends around it. Hence, it is not ideal to represent uniform internal pressure.

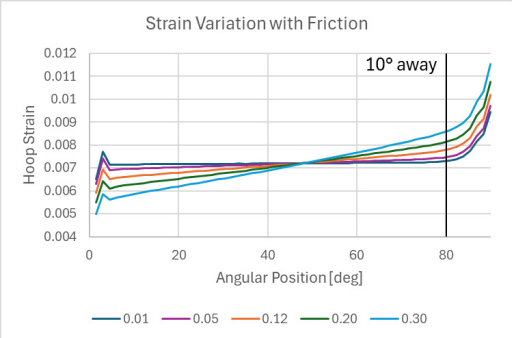

(a) Effect of Friction on Strain Distribution

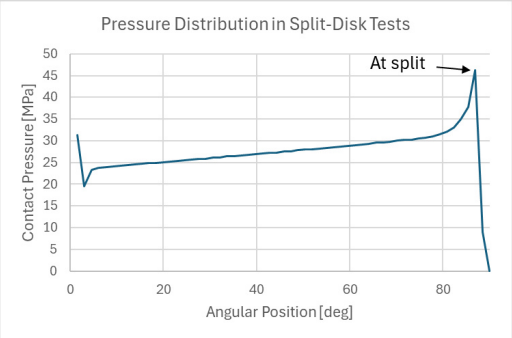

(b) Radial Pressure Distribution

Figure A.19: Studies at 1 mm Displacement in the Split-Disk Test

A.4.2. Wedge Test Friction

Similar to the split-disk tests, the variation of the calculated factors ($F_\theta / F_{applied}$) with the friction coefficient is shown in Table A.6.

Table A.6: Effect of Friction on the Force and Factor at the same Applied Strain

μ	Force (kN)	Stress (MPa)	Strain	E_{XX} (MPa)	Factor
0.3	48388.8	511.5	0.0037	139340	0.2114
0.2	35026.1	511.5	0.0037	139340	0.2920
0.12	26879.9	511.5	0.0037	139340	0.3805
0.05	20908.4	511.5	0.0037	139340	0.4892
0.01	17839.9	511.5	0.0037	139340	0.5734

A.4.3. Benchmark Specimens after Failure

The failed specimens are shown in Figure A.20. The split-disk tests showed mixed-mode failures. Specimen B5 was observed to have a narrower side after polishing. The side was placed facing the cameras. It showed predominantly fibre failure. The specimens in the wedge tests showed consistent mixed mode failures, similar to (d).

(a) Specimen B4 (Split-Disk)

(b) Specimen B5 (Split-Disk)

(c) Specimen B6 (Split-Disk)

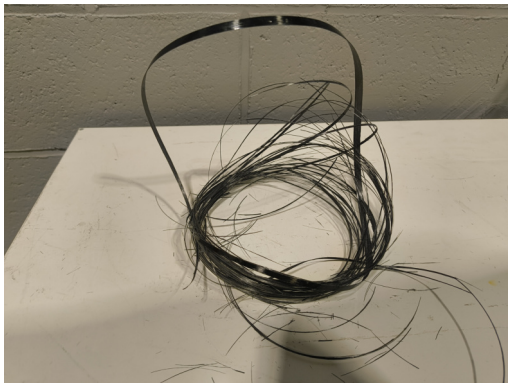

(d) Specimen B1 (Wedge)

Figure A.20: Benchmark Specimens after Burst Tests

A.4.4. Calibration

Axial strain distributions corresponding to Figure 6.13 are shown in Figure A.21.

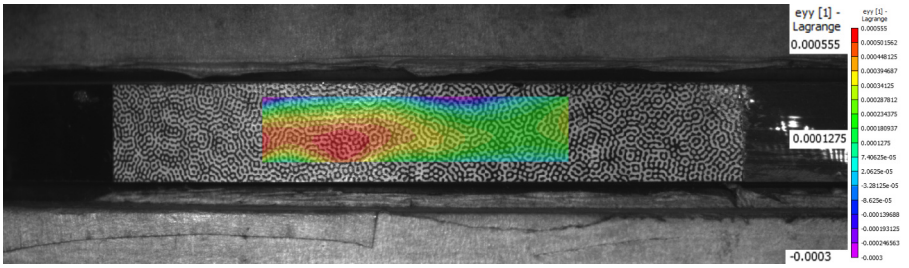

(a) Low (%) (Max : 0.055, Min : –0.030)

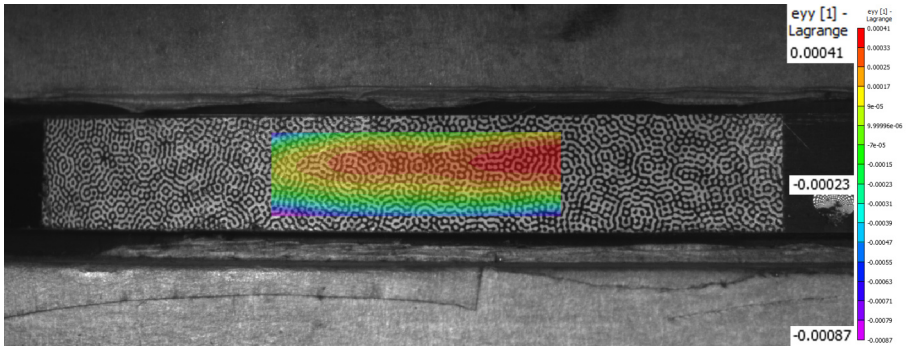

(b) Low, Flipped (%) (Max : 0.041, Min : 0.087)

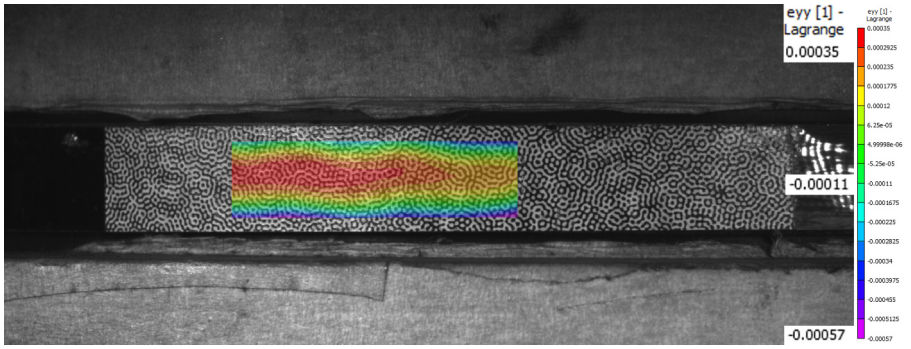

(c) Centred (%) (Max : 0.035, Min : 0.057)

Figure A.21: Axial Strains in Specimen 10 at 1.4 mm Displacement and 100 kN Force

A.4.5. Finite-Element Model Tuning

The sensitivity of the test to the ring's Poisson's ratio and the specimen's modulus is shown in Figure A.22. The Reduced Polynomial 3^{rd} order model was used. Closer to incompressibility limit, the force required for the same compression displacement increases. However, the hoop strain applied on the specimen also increases. Hence, the test results vary based on the compressibility of the PU ring used.

The test results also depend on the modulus of the specimen. However, within a ±10% variation in modulus, there is a ±8% variation in the performance of the test.

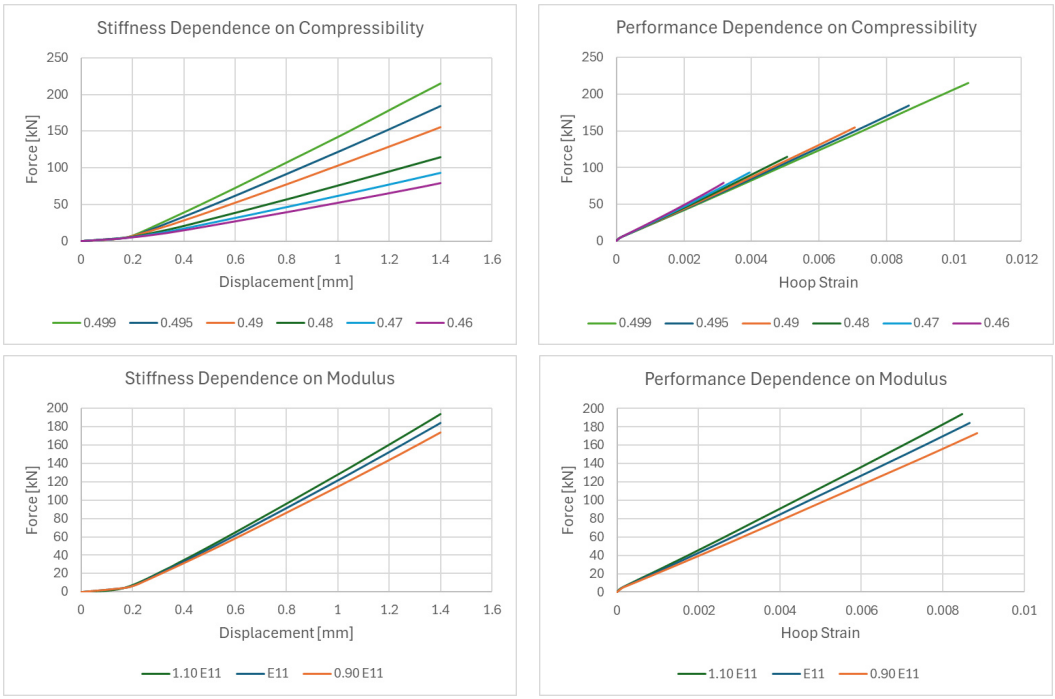

Figure A.22: Test Sensitivity to PU's Poisson's ratio ($E = 139\ GPa$, top) and Specimen's Modulus ($\nu = 0.495$, bottom)

A.5. Recommendations for Future Work

A.5.1. Alignment Tool Concept

The design, shown in Figure A.23, uses a compliant mechanism than can be 3D-printed for trials. The top and bottom flanges should contact the compression plates, while the jaws should hold the specimen. The thin sections act as hinges about which the tool can flex. It can include a vertical spring seated between the top and bottom flanges, if the natural stiffness of the material is insufficient.

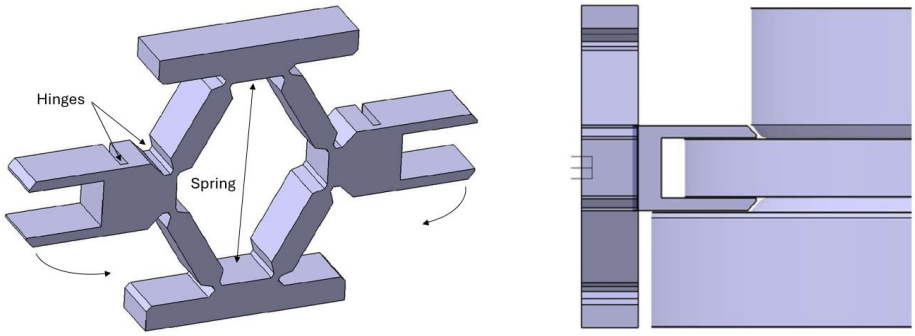

Figure A.23: Alignment Tool Concept (left) and Setup (right)

B

Project Management

B.1. Expenses

An capital expense budget of EUR 20000 was initially estimated for the test development. It included the cost of raw materials, machining, and supplementary tools. The final expenses to create the setup are shown in Table B.1. The values are from the quotations received from the suppliers. The total does not include shipping and packaging, or the operator and overhead costs.

Table B.1: Capital Expenses

Part	Supplier	Quantity	Cost (EUR)
PU 90A Rings	Artech Rubber, Netherlands	10	318
PU 95A Rings	Airlant, Belgium	10	1300
PU 90A Rod	-, Bulgaria	1	300
17-4PH Steel	Caseo, Belgium	3	1500
Machining	Mecarudi, Belgium	4	2056
Lubricant + Tool	Online Retailer	3	110
		Total	**5584**

B.2. Risk Analysis

The critical risks and dependencies of the thesis were analysed. Their impact was assessed and possible mitigations were devised, shown in Table B.2. The impacts were first categorized in a probability-severity matrix. The biggest impacts were assessed and accounted for in the project plan. Mitigations were devised where necessary. The probability-severity matrix used is shown below.

Impact Matrix			Severity				
			Negligible	Minor	Moderate	Major	Catastrophic
			1	2	3	4	5
Probability	Very Unlikely	1	1	2	3	4	5
	Not Likely	2	2	4	6	8	10
	Possible	3	3	6	9	12	15
	Probable	4	4	8	12	16	20
	Very Likely	5	5	10	15	20	25

Table B.2: Risks Analysis and Mitigation

Risks	Impact	Possible Outcome	Mitigation
Manufacturing delays	20	Will have to skip tank specimen tests	Some delay accounted for in the plan
Ring specimen production delays	20	Will have to skip tank specimen tests	Some delay accounted for in the plan
PU 95A ring delivery delays	15	Will have to skip tank specimen tests, or try with PU 90A rings	Alternative to order PU 95A bar and machine it to rings in-house
Elastomer degrades during the test	15	No definite relation between crosshead force and hoop strain	Switch to UHMWPE rings as backup. Fixture can be machined to increase the angle.
Elastomer shows permanent deformation	12	Will increase the crosshead displacement.	Accounted for in the elastomer height.
Test bench and technician availability	12	Delayed testing plan, might have to skip tank specimen tests	Booked test bench from 09/07-20/07, will confirm technician's availability
DIC equipment and license availability	12	Use strain gauges only, misalignment can introduce errors	Can request Syensqo equipment if not available
Elastomer extrusion through the gaps	12	Excessive deformation can cause degradation	Chamfered edges to prevent high corner deformations.
Tank specimen production delays	9	Will have to skip tank specimen tests	-
Higher forces required	9	For tank specimens, 500kN might not be sufficient	Switch to the 3500kN machine
Uneven tolerances in the elastomer	9	Elliptical deformation of the specimen	Check tolerances to qualify elastomer rings before use
Test bench crosshead misalignment	9	Elliptical deformation or jamming	Ensure alignment with the technician. Indenter designed to be unjammed.
Elastomer self-heating due to strain and friction	8	Can degrade the material faster	According to literature, should be safe <1Hz.

B.3. Project Plan

The timeline of the thesis is shown in Table B.3, split across 4 pages. The work was done from 06 January 2025 to 08 August 2025, with no breaks. The work was split between Syensqo in Brussels and TU Delft, requiring occasional travel. Based on the risk analysis, manufacturing was given sufficient time. The only significant delay was during specimen preparation. Since it was partially accounted for, it only shifted the initial plan by a week.

Table B.3: Thesis Timeline

Fatigue Test Development for Composite Rings

TASK	PERSON	PROGRESS	START	END
Kick Off				
Kick-off form	ZAI	100%	03-01-25	03-01-25
Kick-off Meeting	**All**	**100%**	**06-01-25**	**06-01-25**
Thesis proposal approval	RAN	100%	06-01-25	06-01-25
SPA check	ZAI	100%	07-01-25	08-01-25
Agree on timeline, supervision, expectations, and deliverables				
Literature Review				
Standard test methods	ZAI	100%	07-01-25	13-01-25
Non-standard tests	ZAI	100%	14-01-25	19-01-25
Mechanisms from other disciplines	ZAI	100%	20-01-25	26-01-25
Feasibility study and trade-offs	ZAI	100%	27-01-25	07-02-25
Stress state and inherent effects	ZAI	100%	08-02-25	13-02-25
Draft Literature Review	ZAI	100%	14-02-25	16-02-25
Research Proposal Review	**All**	**100%**	**17-02-25**	**17-02-25**
Finite-element modelling techniques	ZAI	100%	18-02-25	21-02-25
Outcome: Agree on test setup concept, research plan, and research activities				

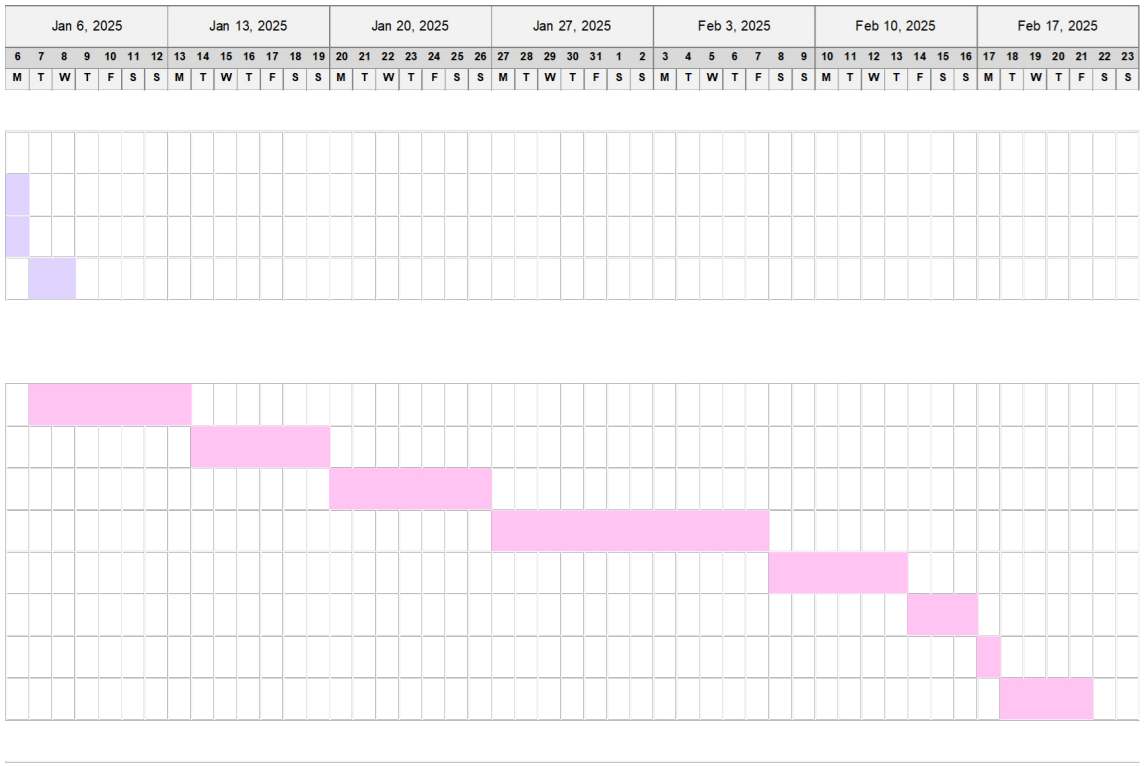

Fatigue Test Development for Composite Rings

TASK	PERSON	PROGRESS	START	END
Research Phase 1 - Design and Analysis				
Parametric FEM setup, mesh convergence	ZAI	100%	24-02-25	28-02-25
Elastomer setup sizing, specimen sizing	ZAI	100%	03-03-25	10-03-25
PE disk setup comparison	ZAI	100%	11-03-25	14-03-25
Initial design	ZAI	100%	17-03-25	21-03-25
Estimate raw material and cost	ZAI, Syens	100%	24-03-25	24-03-25
Design for manufacturing	ZAI, Syens	100%	24-03-25	04-04-25
Final drawings	Syensqo	100%	07-04-25	11-04-25
Procure raw material 17-4PH	Caseo	100%	24-03-25	25-04-25
Elastomer ring production	Artech Rul	100%	31-03-25	11-04-25
Midterm Review	**All**	**100%**	**16-04-25**	**16-04-25**
Outcome: Finalize test setup and specimen design. Agree on risks and trade-offs				

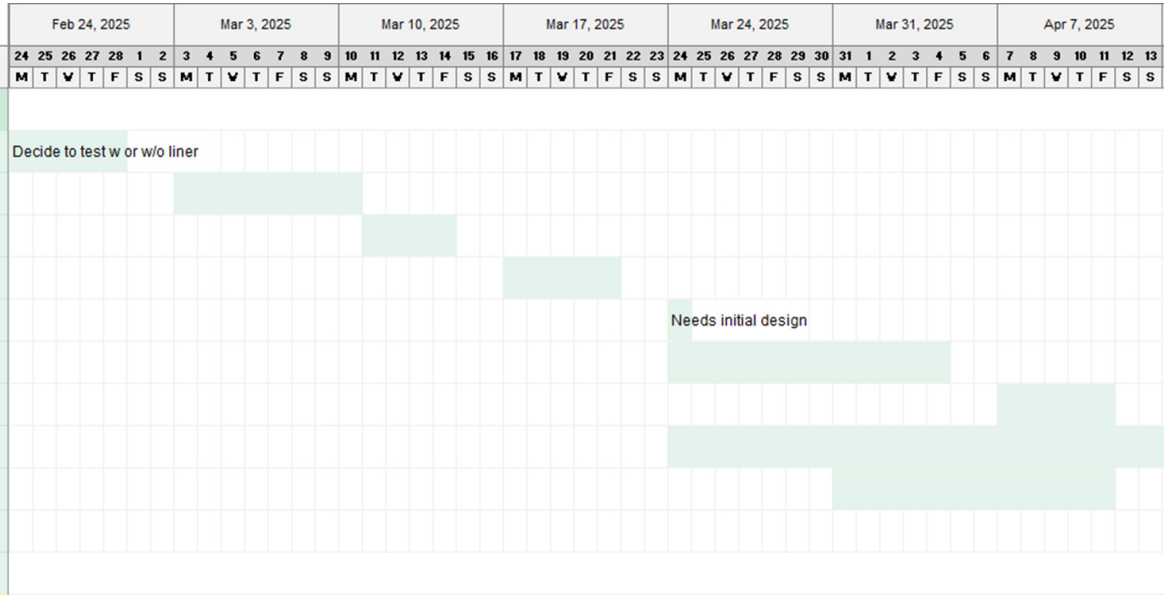

Fatigue Test Development for Composite Rings

TASK	PERSON	PROGRESS	START	END
Procure raw material 17-4PH	Caseo	100%	24-03-25	25-04-25
Elastomer ring production	Artech Rul	100%	31-03-25	11-04-25
Midterm Review	**All**	**100%**	**16-04-25**	**16-04-25**
Outcome: Finalize test setup and specimen design. Agree on risks and trade-offs				
Research Phase 2 - Setup and Testing				
Manufacturing	Syensqo	100%	28-04-25	16-05-25
170 mm tube preparation (TS wet-winding)	Sharp Composites	100%	14-04-25	03-06-25
PU 95A rings production	Airlant	100%	05-05-25	16-05-25
Elastomer testing	ZAI, SSK	100%	14-04-25	18-04-25
Post-processing	ZAI	100%	19-04-25	21-04-25
UHMWPE rings production	Vaneflon	0%	22-04-25	09-05-25
Specimen stress state analysis	ZAI	100%	14-04-25	25-04-25
Specimen progressive damage	ZAI	100%	28-04-25	05-05-25
PU ring static compression tests	ZAI, SSK	100%	19-05-25	23-05-25
Cut rings	ZAI	100%	19-05-25	06-06-25

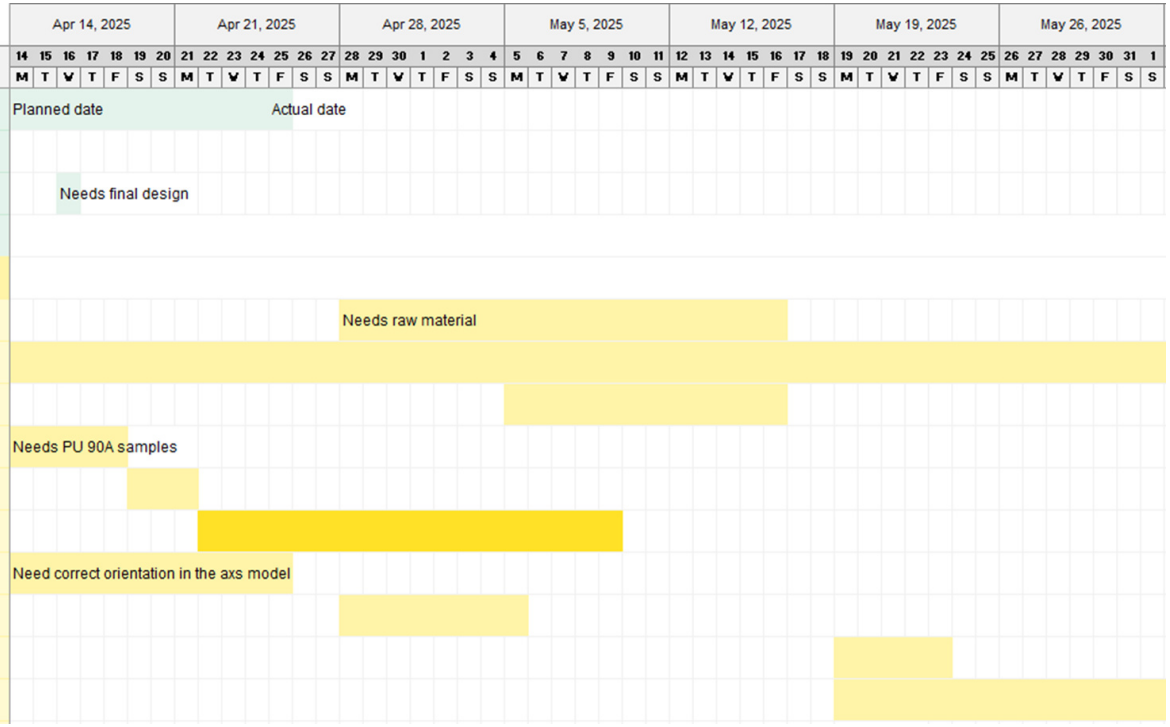

Fatigue Test Development for Composite Rings

TASK	PERSON	PROGRESS	START	END
Proof-of-concept test	ZAI, SSK	100%	04-06-25	06-06-25
Quasi-static tests and calibration	ZAI, SSK	100%	10-06-25	13-06-25
Benchmark tests with split-disk and ring burst setups (146 mm rings)	ZAI, SSK	100%	30-06-25	04-07-25
Shipping to TU Delft	ZAI, SSK	100%	16-06-25	18-06-25
Quasi-static tests (170 mm rings)	ZAI	100%	19-06-25	20-06-25
Post-processing and calibration	ZAI	100%	20-06-25	22-06-25
Thin specimen fatigue tests (TU Delft) + post-processing	ZAI	100%	23-06-25	29-06-25
Tank specimen fatigue tests (TU Delft) + post-processing	ZAI	100%	07-07-25	13-07-25
Outcome: Test setup and results, comparison with the standard				
Research Dissemination				
Draft Thesis Finalization	ZAI	100%	07-07-25	13-07-25
Plaigarism report	ZAI	100%	14-07-25	14-07-25
Submit draft for Syesnqo and ComfHy a	ZAI	100%	14-07-25	14-07-25
Green light review form	ZAI	100%	08-07-25	08-07-25
Green Light Review	**All**	**100%**	**14-07-25**	**14-07-25**